Mécanismes de germination et de croissance d'oxydes d'un acier inoxydable contenant du molybdène et effet de la pré-oxydation sur le comportement du film passif.

Benjamin Lynch

PSL UNIVERSITÉ PARIS

THÈSE DE DOCTORAT
DE L'UNIVERSITÉ PSL

Préparée à Chimie ParisTech

Oxide nucleation and growth mechanisms of a molybdenum-containing stainless steel and the effect of pre-oxidation on passive film behaviour

Soutenue par
Benjamin Lynch
Le 28 Janvier 2022

École doctorale n°388
Chimie Physique et Chimie Analytique de Paris Centre

Spécialité
Chimie Analytique

Composition du jury :

Bernard NORMAND Professeur, INSA Lyon	*Président*
Robert LINDSAY Reader, University of Manchester	*Rapporteur*
Christine BLANC Professeure, Toulouse INP	*Rapporteure*
Mary RYAN Professeure, Imperial College London	*Examinatrice*
Frédéric WIAME Maître de conférences, Chimie ParisTech	*Co-encadrant*
Philippe MARCUS Directeur de recherche, Chimie ParisTech	*Directeur de thèse*

Chimie Paris ParisTech | PSL

Acknowledgements

The work in this thesis was carried out as part of the *Physico-Chimie des Surfaces* (PCS) team in the *Institut de Recherche de Chimie Paris* (IRCP) at *Chimie ParisTech, Université Paris Science et Lettres* (PSL). The project was performed under the supervision of Philippe Marcus, Vincent Maurice and Frédéric Wiame.

I would first like to thank Dr Philippe Marcus, for overseeing the project and welcoming me to his laboratory. His vast experience and contribution to the areas of surface and corrosion science have been the foundation of this research topic, with his invaluable insight benefiting not just the project, but also my own understanding.

Next, I must thank Dr Vincent Maurice, who has played a key role in all aspects of the project from experimental design to data interpretation. His always timely and astute comments, in particular with regards to analysis of the results, have been a major help in maximising the quality of the work.

Thirdly, there is Dr Frédéric Wiame, to whom my gratitude cannot truly be expressed in just a few lines. His day to day, and often minute to minute, guidance and supervision have not only proved to be beyond helpful with regards to the topic, but he has also made me truly appreciate the meaning of what it is to be a scientist. I must also mention his persistence in maintaining that I am in good health, readily supplying me with various fruits (and the occasional Belgian chocolate, to keep me happy).

My fellow PhD students, post-docs and other members of the PCS team, of which there are too many to name, have contributed to creating a welcoming and friendly atmosphere. The wide range of backgrounds has allowed me to learn about different cultures as well as trying new cuisines. Special thanks must go to Martin Weiser and Shova Neupane, post-doctoral researchers, whom I have worked closely with on the project.

My deepest thanks go to my family and loved ones for their unconditional support and love during the three years. Without my mam, dad and brother, as well as all those close to me, I would not have made it to the start of this PhD, let alone to the end. If my family kept me sane, then my wonderful girlfriend, Emma, has made me happy. Always by my side, not a day has gone by where she has not made me laugh or smile.

This project has received funding from the European Research Council (ERC) under the European Union's Horizon 2020 research and innovation program (ERC Advanced Grant No. 741123, Corrosion Initiation Mechanisms at the Nanometric and Atomic Scales: CIMNAS). Région Île-de-France is acknowledged for partial funding of the UHV equipment.

Contents

General introduction

Context

Stainless steels are an inherently useful class of materials. They are everywhere in our daily lives, from cooking utensils to car parts to buildings. The remarkable versatility displayed by these iron-based alloys is owed in part to their high strength and resistance to corrosion, the latter of which is owed to the formation of a thin protective oxide layer known as the passive film. This chromium-rich oxide layer, which is typically only a few nanometres in thickness, efficiently isolates the underlying metallic alloy from the local environment in which it finds itself. The result is a relatively unreactive material that can be placed in a range of conditions without degrading. Not only does this increase the safety of the population, but the long lifetime of the material comes with large economic benefits. One of the most commonly used stainless steels is 304 austenitic stainless steel. It contains iron (balance), chromium (18–20 at%) and nickel (8–10.5 at%) as the main constituent elements. Unfortunately, certain conditions may still result in passive film breakdown and subsequent degradation of the material. However, if one wishes to improve the resistance to corrosion, notably in environments with aggressive anions such as chlorides, small amounts of molybdenum can be added, giving us what is known as 316 austenitic stainless steel. Despite its notoriety for providing corrosion protection benefits, the exact role that molybdenum plays is still debated. Whilst it is generally agreed that it is involved in combatting passive film breakdown, the exact mechanism is unknown. Some suggest that it prevents passive film breakdown in the first place, whilst others say that it promotes re-growth after the breakdown has occurred.

Recent work, pioneered by the Marcus group, has shown that the chromium distribution within the passive film is not homogeneous and that local heterogeneities, that form as a result

of the oxide growth mechanisms prior to passivation, are potential weak spots for localised breakdown. Therefore the initial stages of oxidation, from adsorption to growth, are of key interest if one is to better understand the breakdown on the passive film. Furthermore, it may be possible to improve corrosion resistance if we can better control the heterogeneities that form at the surface.

In this work, a combined surface science and electrochemical approach was applied in order to better understand the oxidation mechanisms that govern pre-passivation of stainless steels and how different oxidation methods may influence passive film performance and corrosion behaviour.

Thesis overview

Chapter one discusses the current state of the literature and aims to provide the reader with the required knowledge such that they can maximise their understanding of the topic at hand. The section begins by outlining the key concepts in corrosion, stainless steels and passivation. From there, oxidation and passivation of the key metallic elements involved in the process are discussed. Finally, the oxidation and passivation of stainless steels is covered in detail, with particular reference made to the role of molybdenum.

In chapter two, the key analytical techniques used over the course of the investigation are detailed. The passage discusses the fundamentals of the four principal techniques used, namely X-ray photoelectron spectroscopy (XPS), time-of-flight secondary ion mass spectroscopy (ToF-SIMS), scanning tunnelling spectroscopy (STM) and low energy electron diffraction (LEED). In addition to this, the various operating modes of each technique are outlined.

The third chapter goes on to provide an overview of the equipment used and the experimental procedures. The treatment of data is discussed in detail, outlining the key principles used in the analysis.

The fourth chapter focuses on understanding an oxide-free FeCrNiMo(100) surface. The section starts by showing the complexities of surface preparation and how seemingly small changes at the surface can have dramatic effects on reactivity and the composition of the oxide. From there, STM and LEED are used to characterise the clean surface, highlighting areas that may be of interest when it comes to reactivity, as well as reconstruction of the surface.

Chapter five uses XPS to follow the nucleation and growth mechanisms of oxidation on the FeCrNiMo(100) surface at both room temperature and 250 °C. The clean stainless steel sample was exposed to ultra-low pressures of oxygen in a controlled and stepwise manner, allowing us to document the mechanism by which the oxide formed. Angular analysis allowed for detailed

information on the in-depth distribution of the oxide.

In the sixth chapter, the role of pre-oxidation at high temperature in a controlled manner, using ultra-low pressures of O_2, on the behaviour of the passive film is investigated. Electrochemical passivation in acidic media is performed, with the composition, thickness and in-depth distribution evaluated using XPS and ToF-SIMS. The pre-oxidised surface is compared with the native oxide which was also subjected to the same electrochemical passivation treatments. Voltametric experiments provide insight into the benefits of pre-oxidising in a controlled environment.

CHAPTER 1

State of the art

1.1 Introduction

1.1.1 Corrosion

Corrosion is, according to International Union of Pure and Applied Chemistry (IUPAC) [1], "An irreversible interfacial reaction of a material with its environment which results in consumption of the material or in dissolution into the material of a component of the environment." This fundamentally leads to the slow destruction of the material, which can result in a loss of strength as well as aesthetic. The process, which arises from the material's reaction with its local environment, is a major issue in a variety of fields, in particular where metal and alloy materials play a large role in the structure and stability of the components being used. Corrosion prevention is of particular importance in the nuclear and aeronautic industries, as any degradation of materials can result in serious issues relating to safety. Corrosion is not just limited to metals, as it can occur in other materials such as polymers and ceramics, however this is more typically referred to as degradation [2, 3]. As well as reducing durability and performance, corrosion has a significant economic cost, with reports of 3 % GDP being lost [4]. Schweitzer states that economic loses can be divided into direct and indirect loses, with the former being concerned with replacement of corroded materials, structures and components, as well as labour and prevention costs. Indirect loses are more difficult to calculate but take into account things such as shutdowns and loss of product etc. [5]. A 2002 US report by Koch et al. identified that the sectors most effected by direct impacts of corrosion were drinking water and sewage systems,

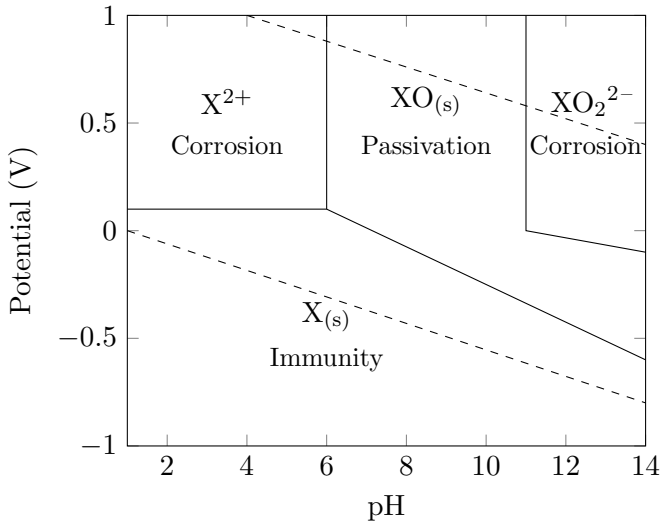

Figure 1.1: Eh-pH diagram for element X.

motor vehicles and defence, with total combined losses estimated to be around $90 billion [4]. In the same report it was stated that within the United States alone a total of $121 billion is spent yearly on combatting corrosion.

Corrosion can occur in many different forms, often depending on the conditions that a material is exposed to. For example, in environments where aggressive ions such as Cl^- or $S_2O_3{}^{3-}$ are present, we can frequently observe a form of corrosion known as pitting. This type of corrosion is of particular importance in this study as it involves the breakdown of a thin, protective oxide-layer known as the passive film, the details of which will be discussed later on in the text. A metal's stability in any given environment is dependent on a number of factors, most notably the pH and oxidising power. These effects can be displayed in Eh-pH diagrams (often referred to as Pourbaix diagrams), where the various phases within the aqueous electrochemical system are mapped out according to thermodynamics. An example of a Eh-pH diagram for a given element, X, is used in Figure 1.1. In water, the metal X can react to form an oxide:

$$X + H_2O \rightarrow XO + 2\,H^+ + 2\,e^- \tag{1.1}$$

In this case, the passive film will be stable between pH 6 and 11, with the oxide layer consisting of XO. However, outside of this range the oxide may dissolve by one of two ways, depending on the pH:

$$XO + 2H^+ \rightarrow X^{2+} + H_2O \tag{1.2}$$

$$XO + H_2O \rightarrow XO_2{}^{2-} + 2H^+ \tag{1.3}$$

Pourbaix showed that there are three possibilities for a metal in an electrochemical solution:

1. Immunity: When the potential and pH are such that the metal will not undergo corrosion or passivation; it is stable in the metallic form.

2. Corrosion: According to thermodynamics, within these ranges, the metal is most stable in an ionic and soluble form; the material is readily corroded.

3. Passivation: In this region an oxide or hydroxide film will form at the surface of the metal, preventing direct attack of the metal from the environment. The passive film may slowly dissolve upon contact with the electrolyte in which case passivity results in a slowing of the dissolution kinetics.

The area between the two dashed lines on the diagram indicates the stability region of water. Above the upper dashed line, i.e. highly oxidising conditions, water is oxidised to oxygen:

$$6H_2O \rightarrow O_{2(g)} + 4H_3O^+ + 4e^- \tag{1.4}$$

Below the bottom dashed line, i.e. highly reducing conditions, water is reduced to hydrogen:

$$2H_2O + 2e^- \rightarrow H_{2(g)} + 2OH^- \tag{1.5}$$

1.1.2 Stainless steel

Stainless steels are defined as a steel alloy with a minimum chromium content of 10.5 % and maximum of 1.2 % carbon, by mass. Stainless steels are renown for their corrosion resistance, owing to their high chromium content, where the higher the level of chromium, the higher the resistance to corrosion [6–11]. By adding small amounts of molybdenum, resistance to corrosion increases further due to its beneficial influences on pitting corrosion [12–14]. Due to their high corrosion resistance, stainless steels are ideal for a variety of applications where the material requires both strength and resistance to corrosion. Stainless steel is commonly used in architecture, both as a structural component and for aesthetic purposes. It was commonly used during the art-deco period in the early-mid 20^{th} century. Many skyscrapers built in the 1920's, such as the Chrysler building in New York City, were styled using stainless steel. This is just one example of stainless steels being used in modern society, but you can find it almost everywhere, from aircraft to cutlery and from nuclear power plants to art and design. It is a vital material in today's world.

There are generally considered to be five classes of stainless steel:

1. Austenitic: Alloys within this group of stainless steels have an austenitic microstructure, meaning that they possess an FCC crystal structure. The term austenitic comes from

Figure 1.2: The many uses of stainless steels: Surgical tools (left), architecture (middle) and motor vehicle parts (right).

austenite, a gamma-phase allotrope of iron (γ-Fe) with an FCC structure. Achieved by alloying with nickel, and manganese with nitrogen, they keep their austenitic structure at all temperatures until its melting point. As a result, they are not affected by heat treatment. Due to the austenitic structure, these materials are non-magnetic. Within the group there are two sub groups, commonly referred to as the 200 and 300 series. The 200 series contain chromium and manganese (and nitrogen), and because of this additional nitrogen content we observe up to 50 % more strength in comparison to the 300 series. The 300 series contain chromium and substitute manganese for nickel.

2. Ferritic: These stainless steels possess a ferrite microstructure, meaning that they have a BCC crystal structure. They contain 10.5–27 % chromium and have small or zero amounts of nickel. Exactly like austenitic stainless steels, they manage to maintain their microstructure at all temperatures until melting, so once again, they cannot be hardened by heat treatment. These stainless steels are magnetic. In the case of ferritic stainless steels there are four sub-categories, groups 1–4, depending on the amounts of certain elements and the subsequent properties.

3. Martensitic: This group of stainless steels gets its name from German metallurgist Adolf Martens and unlike austenitic and ferritic stainless steels they are able to undergo heat treatment in order to better provide the ideal properties required for the material. Martensitic stainless steels are formed via rapid cooling of austenite which ensures that the carbon does not have time to diffuse out of the crystal structure, resulting in a highly strained body-centred tetragonal. The quenching of the alloy causes a large number of dislocations which are key in strengthening the material. These metallic alloys have a range of possible

elemental compositions. They offer a wide range of potential properties due to their ability to be heat-treated. Again, they can be sub-divided into four sub-categories.

4. Duplex: Stainless steels in this category have a mixed microstructure containing two phases — austenitic and ferritic. They typically have high amounts of chromium, 19–32 %, molybdenum, 5 %, and low amounts of nickel, in comparison to austenitic stainless steels. As a result, these stainless steels are much stronger and have a higher resistance to chloride stress cracking corrosion and chloride related pitting corrosion. Duplex stainless steels are generally cheap to produce and therefore provide a very cost-effective performance when compared with austenitic or ferritic options. Their main downsides when compared with the main two categories are that they are not as easily welded and that the temperature range in which they can operate is not as wide.

5. Precipitation hardened: Similar to austenitic stainless steels with regard to their corrosion resistance, these steels can be hardened in order to make them stronger.

Due to their significance to this work, I feel that it is worth spending some extra time discussing 304 and 316 stainless steels in a little more depth. As previously mentioned, 304 stainless steel comes from the austenitic family and is the most commonly used stainless steel, in part due to its ability to be easily shaped and high resistance to corrosion. This alloy is typically used in many household appliances, as well as in architecture. It contains iron, chromium (18–20 wt.%) and nickel (8–10.5 wt.%). There are three types of this stainless steel, 304, 304L and 304H; they possess the same amounts of nickel and chromium, with the same corrosion resistance and ease of fabrication. The difference comes down to the small amounts of carbon (0.04–0.1 wt.%) that is added, which can influence certain properties. The stainless steel is known to be very versatile in different conditions, however, it struggles when met with a warm, chloride-rich environment. 304 is capable of withstanding chloride concentrations up 400 $mg{\cdot}l^{-1}$ at room temperature, however, this falls to just 150 $mg{\cdot}l^{-1}$ at 60 °C [15].

Once conditions have become too extreme for 304 stainless steel to be viable, 316 stainless steel is often used. It is the second most common type of stainless steel employed. It alloys iron, chromium (16–18 wt.%), nickel (10–12 wt.%) and molybdenum (2–3 wt.%), with the latter helping to provide much increased resistance to pitting corrosion. Due to this added strength, it will be used in more extreme environments, such as pharmaceutical equipment, waste water treatments, and marine equipment.

1.1.3 Passivation

Passivation, a term first coined by Schöbein in 1836, is the formation of an ultra-thin and non-porous oxide layer at the surface of a metallic material, that isolates the substrate from its environment. Passivation occurs when the bare metal is exposed to an oxidising environment, with this phenomena playing a vital role in the development of our metal-based society. Typically, these films do not exceed a few nanometres in thickness and are therefore transparent [8, 16, 17]. The oxides are either thermodynamically stable or dissolve at a negligible rate. For a metal to be thermodynamically stable in solution or air it must be a noble metal, such that its oxidation potential is more anodic than the reduction potential of species present in the local environment. For non-noble metals the reverse is observed, where oxide formation is driven due the oxidation potential being more cathodic. This results in the environment either favouring dissolution of the oxidised material or the formation of a three-dimensional thin oxide film. Uhlig gave two definitions for passivity [18]:

1. "A metal is passive if it substantially resists corrosion in a given environment as a result of marked anodic polarisation."

2. "A metal is passive if it substantially resists corrosion in a given environment despite a marked thermodynamic tendency to react."

The transfer of electrons through the film plays a key role in the passivation process, without it the film would not be able to form. Typically, many passive films are semiconductors, although they can exist as both conductors and insulators [19, 20]. However, it has been shown in the literature that passive films do not always behave as semiconductors, with this being due to their extremely low thickness, amorphous structure and high doping levels. This has an effect on the band-structure and whether it can truly form with such a small layer and large amounts of deficiencies [21].

Over the course of time, the passive film will begin to fail. Fortunately for us, these oxide layers are known to be self-healing when broken down at a local level [22, 23]. However, the self-healing process can be readily disturbed by aggressive anions such as chlorides and thiosulfates which can then cause local pitting corrosion. In these areas the rate of corrosion will be significantly increased compared to the rest of the material. A model developed by Marcus et al. [24], looking at the thinning of passive films states that if chloride is present in the electrolyte solution then it will compete with hydroxide anions for adsorption sites at the surface . Subsequently, if the chloride is adsorbed to the oxide then the surface complexes become less tightly bound to the oxide matrix, resulting in a lower activation energy for their transfer to the

electrolyte solution. The end result is an enhanced rate at which de-passivation occurs due to local thinning of the passive layer. Equally, the chloride ions may directly enter the film which can lead to localised breakdown. The stability of a film also comes down to the redox processes ongoing within the system. If the environmental conditions are such that a redox reaction is favoured, and the redox species is soluble, then there is likelihood of de-passivation occurring. The most common examples of this are the reduction of Fe_2O_3 to Fe^{2+} or Fe, and oxidation of Cr_2O_3 to $CrO_4{}^{2-}$ [25, 26].

The investigation of the structure and composition of passive films has been ongoing for many years now, with a wide range of analytical techniques being involved. Techniques such as X-ray photoelectron spectroscopy (XPS), time-of-flight secondary ion mass spectrometry (ToF-SIMS), and Auger electron spectroscopy (AES) have been vital in providing information on the composition and thickness of the oxide layers [27–30]. A key idea is that the film is not rigid, but fluid, such that species migrate within the structure; therefore, the thickness and chemical composition will change over time, and will be determined by many external factors [31–33]. When trying to determine the structure of the passive film, it is important that we consider the thickness of the film being analysed; X-ray diffraction is a useful tool, providing that the film is substantially thick, but when looking at films that are typically less than 10 nm in thickness, it can be difficult to use such a technique. This problem, especially when coupled with issues regarding changing conditions under which the film was formed electrochemically, has led the way to the use of sophisticated in-situ techniques such as scanning tunnelling microscopy (STM) and synchrotron techniques, such as EXAFS and grazing-incidence X-ray diffraction (GIXD) [34–40].

1.2 Oxidation and passivation of constituent metals

1.2.1 Iron

1.2.1.1 Oxidation of iron

It is generally agreed that at high temperatures, oxidation of iron results in a three-layer film consisting of magnetite (Fe_3O_4), hematite (Fe_2O_3) and wüstite (FeO), as discussed in depth in the review by Chen and Yuen [41]. Whilst extensively studied, the products formed during oxidation of iron below 570 °C are debated, in particular regarding the presence of FeO. Work by Grosvenor et al. [42], who investigated high oxygen exposures at room temperature, suggests that oxide films formed on iron contain a bilayer structure of Fe_3O_4 and γ-Fe_2O_3, with no detectable FeO. Similar reports have been made elsewhere [43, 44]. Several other studies have indicated that FeO is present in small amounts at room temperature, especially after exposures

less than 1000 L (where 1 L= 1.33×10^{-6} torr·s) [45–48]. Depending on the method used for growing the oxide, you may also find FeOOH or even FeO_x [45,46], with Lin et al. [46] suggesting that the latter forms during the very early stages of oxidation (0–50 L), on top of which Fe_3O_4 nucleates. Ultimately, the composition and thickness of iron oxide films are highly dependent on numerous factors such as temperature, pressure, humidity and environment.

1.2.1.2 Passivation of iron

When describing the passive film formed on iron, two models are commonly used. The first model describes the system with a single oxide layer consisting of Fe_2O_3 [49–52], whereas the second model uses an oxide bi-layer consisting of an inner layer of Fe_3O_4 and an outer layer of Fe_2O_3 [53–56]. Work by Nagayama et al. [55] found that the outermost part of the film had a defect structure of the general formula $Fe_x^{6+} \cdot Fe_{2-2x}^{3+} \cdot O_3$. The passive film thickness is found to be dependent on the potential and can range from 1–5 nm [55, 57].

1.2.2 Chromium

1.2.2.1 Oxidation of chromium

There are several known oxides of chromium (CrO, CrO_2, CrO_3), but by far the most common and most thermodynamically stable is Cr_2O_3. Allen et al. [58] performed an investigation into the initial oxidation (1–10^6 L) of chromium at 327 °C (600 K) and found that, whilst consisting of only Cr_2O_3, the bare metal reacts instantaneously with oxygen (< 1 L) producing an oxide film of around 0.4 nm, after which the growth rapidly slows down, following a logarithmic scale such that after one year of exposure to the gas it would reach a thickness of 2 nm. Studies have shown that the characteristics of oxide growth vary with temperature, as at 25 °C it was found that the Cr_2O_3 grows with constant stoichiometry and reaches a limiting thickness of 0.9 nm [59]. Sakisaka et al. [60] stated that the oxidation of chromium at RT can be broken down in to four stages:

1. 0–2 L - Dissociative chemisorption of oxygen at the surface.
2. 2–6 L - Surface reconstruction and oxygen incorporation.
3. 6–15 L - Rapid oxidation resulting in the growth of the Cr_2O_3 film.
4. >15 L - Slow thickening of film.

1.2.2.2 Passivation of chromium

In the literature, there are also two models that are used for describing the passivation of chromium in various electrolytes such as H_2SO_4, NaOH and H_2O. The first approach utilises a single layer consisting of an oxy-hydroxide, CrOOH [61–64] whereas the second approach uses a bi-layer consisting of an inner oxide layer of Cr_2O_3 and an outer hydroxide layer of $Cr(OH)_3$ [65, 66]. Naturally, the composition of the passive film will depend on the electrolyte and the potential at which it is formed, with the thickness of the film increasing with increased potential [64]. Work by Maurice et al. [66] concluded that the presence of Cr_2O_3 is dependent on passivation time and that longer passivation favours dehydration. The same work also showed that in the transpassive region Cr^{6+} is observed.

1.2.3 Nickel

1.2.3.1 Oxidation of nickel

There are two oxides of nickel, NiO and Ni_2O_3, with the former being the more dominant of the two. Evans et al. [67] characterised NiO after a 100 L exposure at room temperature, on polycrystalline and single crystal surfaces, and found that the oxide film of 1.8 nm was not completely stoichiometric NiO, but instead was characterised with two distinct O 1s peaks, suggesting that the second is due to Ni_2O_3. Norton et al. [68] came to a similar conclusion, attributing the Ni_2O_3 to a defect oxide (created by oxidising at 200 °C or damage from Ar^+), or $Ni(OH)_2$ in the presence of water.

1.2.3.2 Passivation of nickel

Unlike the cases with chromium and iron, there is only one reported model for describing the passivation of nickel in various electrolytes — a bi-layer model [69–74]. In both acidic and alkaline media the composition consists of an inner oxide layer of NiO and an outer hydroxide layer of $Ni(OH)_2$. Sato and Kudo [75] showed that in a borate buffer solution in the transpassive region, a high-valent nickel oxide, Ni_2O_3 is present. Once more it is concluded that the thickness of the passive film is dependent on the potential, with values varying from 0.4–3 nm [69, 75–78].

1.2.4 Molybdenum

1.2.4.1 Oxidation of molybdenum

In its oxide form, molybdenum is most commonly found as MoO_2 or MoO_3, however several papers suggest the existence of intermediate oxides such as MoO and Mo_2O_3 [79, 80].

1.2.4.2 Passivation of molybdenum

The passivation of molybdenum was investigated by Nobuyoshi et al. [81] who studied the nature of the film in different electrolytes using modulation spectroscopy and identified that the passive film consists mainly of MoO_2. Other authors found that depending on the conditions MoO_2 could be further oxidised to MoO_3 [82–84]. Badaway et al. [85] found that in alkaline conditions (1 M, NaOH) the passive film began to dissolve, possibly due to the formation of ${MoO_4}^{2-}$, which is soluble in basic solutions [86]. Work by Lu and Clayton [80] found that when in the transpassive range, the passive film consisted of trivalent, tetravalent, pentavalent and hexavalent species.

1.3 Oxidation and passivation of stainless steels

1.3.1 Oxidation of stainless steels

As a result of stainless steels' versatility they are exposed to many different environments and as a result they undergo oxidation in a wide range of conditions [31, 87–101]. For this work only oxidation carried out in air and in pure oxygen at RT–250 °C is of interest, so shall be the main focus of this section of the literature review.

If we first consider oxidation of stainless steel in air, we see that the oxide formed at the surface is a mixture of Fe^{2+}, Fe^{3+} and Cr^{3+} oxides [31, 87–89]. When nickel is present in the alloy it is typically not found in an oxidised form within the layer, although it is often found enriched underneath the oxide in what is known as the modified alloy region [31, 87–89]. Molybdenum is found in small amounts, notably in its +4 and +6 oxidation states, on the same order of magnitude as that of its bulk amount, when it is present in alloys such as 316 [88, 89]. The presence of hydroxides is not typical when the composition of oxide films formed in air is reported. A summary of data from the literature is shown in Table 1.1.

The composition and general behaviour of oxide films formed on stainless steel after exposure to oxygen is not too dissimilar to those formed in air; however, exposure with pure oxygen often allows for more control of the experimental conditions which can in turn help us to better understand the mechanisms that govern their growth. Ma et al. [90] recently carried out an in-situ XPS based experiment which provided a fascinating insight into the stepwise growth of the oxide on a FeCrNi(100) sample. In this paper, it was suggested that for the very initial stages of oxide growth there are two different regimes. Firstly, from 0–10 L we observe that oxygen uptake is at its fastest, with the rate of reaction decreasing with increased temperature, which suggests a nucleation of the surface oxide that is limited by the adsorption of oxygen.

Bulk composition (at%)	Conditions	Oxide composition (at%)	Thickness (nm)	Reference
Fe–18Cr–12Ni(100)	Exposure to air (3 h)	Fe–27Cr	1.8	[31]
	Exposure to air (20 h)	Fe–21Cr	2.0	
Fe–20Cr–12Ni–1.6Mo*	Exposure to air (5–10 min)	Fe–39Cr–6Mo	2.0	[88]
Fe–20Cr–12Ni–1.6Mo	Exposure to air	Fe–41Cr–4.1Mo	2.2	[89]

Table 1.1: Composition of oxides formed on austenitic stainless steels after exposure to air at room temperature. *It should be noted that where a crystallographic orientation is not given, the sample is assumed to be polycrystalline in nature.

The stainless steel sample saturates at this point when oxidised at room temperature; however, at elevated temperatures oxygen uptake is continued which suggests that now we are observing a growth regime that is governed by atomic displacement and mobility. In the nucleation phase, Cr^{3+} was preferentially formed over Fe^{3+}, after which the formation of Fe^{3+} oxide is promoted. This observation that Fe^{3+} is preferentially formed at higher exposures has been reported elsewhere [100], and is explained by Lince et al. [93], who states that during the initial oxidation chromium oxide production is favoured due to its high thermodynamic stability when compared with iron based oxides. Then, once a significant oxide layer has formed, the kinetics of the oxide film formation become all the more important, as the growth of the oxide is diffusion controlled. Due to iron's higher mobility within the oxide, it will diffuse more readily to the surface where it can undergo oxidation. Similar reasoning has been used to explain the absence of nickel in the oxide film as its diffusion coefficient is very low. There is no evidence to suggest the presence of well defined layers in the oxide film, despite the prevalence of layer models being used to describe the system [88,89,101,102]; however, it is unlikely that the oxide is completely homogeneous [90,93,98–100]. The presence of mixed oxides, such as $FeCr_2O_4$, cannot be excluded [93]. Very little data has been generated for controlled oxidation of molybdenum containing stainless steels; however, Lynch et al. [101] showed that a 100 L exposure at RT resulted in a three-fold enrichment of molybdenum in the oxide film when compared to its bulk amount. A select summary of data found in the literature can be found in Table 1.2.

When analysing oxide and passive films formed on stainless steel we must not just consider its composition, but also its structure. Recent work, led by the Marcus group, has begun to

Bulk composition (at%)	O_2 Exposure (L)	Temperature (°C)	Oxide composition (at%)	Thickness (nm)	Reference
Fe–18Cr–13Ni(100)	6	250	Fe–59Cr	1.7	[90]
	35		Fe–34Cr	2.2	
	100		Fe–22Cr	2.1	
Fe–17Cr*	1000	50	-	1.3	[99]
Fe–17Cr	10	327	Fe–45Cr	1.0	[100]
	30		Fe–29Cr	2.2	
	100		Fe–17Cr	3.5	
Fe–20Cr–12Ni–1.6Mo	100	25	Fe–23Cr–5Mo	1.2	[101]

Table 1.2: Composition of oxides formed on austenitic stainless steels after exposure to oxygen. *It should be noted that where a crystallographic orientation is not given, the sample is assumed to be polycrystalline in nature.

investigate how the nanostructure of the oxide layer affects the passive film and its corrosion properties [17, 90–92, 103]. In this work that looks at chromium enrichment in stainless steels at the nanoscale, it is suggested that the enrichment is in fact not homogenous within the oxide layer. The mechanism of initial oxidation, known as pre-passivation, has been found to produce enrichment heterogeneities at the origin of localised corrosion sites [17, 103]. This work has led to a series of papers, highly relevant to this work, being published by Ma et al. [90–92], addressing the initial stages of oxidation of the surface under controlled conditions. The first paper that focuses on the structure of the clean surface of a FeCrNi(100) sample, as prepared under ultra-high vacuum, and the subsequent modifications that are induced during the initial oxidation (0–1L) at 250 °C [92]. The paper notes that the clean surface itself is not heterogeneous and that at the step edges there is different structure present that can be attributed to two-dimensional chromium-nitride species that occur as a result of the co-segregation during the annealing process [90]. It is hypothesised by the author that this edge structure is present in order to reduce the surface energy, whilst vacancy lines aid reducing stress. Upon oxidation it was found that Cr^{3+} preferentially formed at these step edges with metallic chromium pumped from the terraces towards the step-edge, generating an inhomogeneity of the surface in doing so. Initial high reactivity at the step-edges is to be expected due to the lower coordination number of edge atoms. The second STM paper by Ma et al. [91] investigating the oxidation takes it further into the development of a three-dimensional oxide. Where chromium was found to be depleted, oxide islands rich in Fe^{2+} and Fe^{3+} formed. This work, displaying how local heterogeneities in

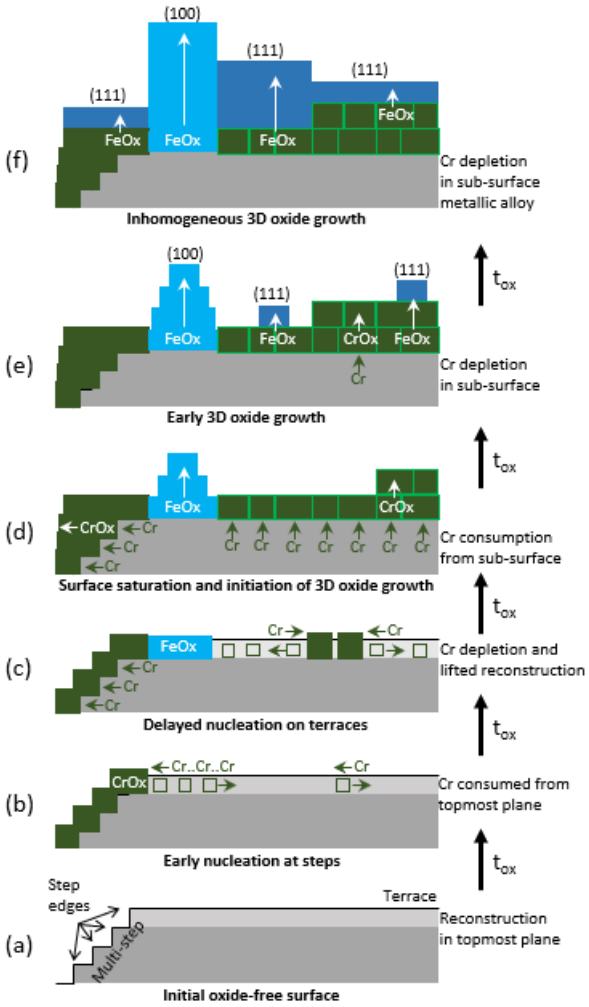

Figure 1.3: Oxide growth mechanism on a FeCrNi(100) stainless steel proposed by Ma et al. [91].

the oxide film can form even on carefully prepared surfaces in controlled environments, is neatly summarised in Figure 1.3.

1.3.2 Passivation of stainless steels

It is testament to the complexity of the passive film formed on austenitic stainless steels that after being the focus of intense investigation over a number years they are still not completely understood. Much like we saw with simple oxidation, passive films are formed in and exposed to a wide range of conditions [17, 30, 31, 35, 37, 88, 89, 102–110]. To better understand the nature of these films, many different analytical techniques have been used, such as XPS [12, 30, 37, 88, 89, 102, 111–114], STM [17, 31, 35, 104] and ToF-SIMS [30, 107, 108], amongst others [105, 106].

If we first consider the passive film formed in acidic environments, it is commonly observed that the protective layer is enriched with Cr^{3+} oxide and hydroxide, which is owed to iron's relatively high dissolution rate when in acidic environments [7, 8, 12, 17, 80]. It was found by

Maurice et al. [17] that this enrichment of chromium is more enhanced with further passivation and ageing. When entering the transpassive domain, this enrichment is reduced as Cr^{6+} oxides form that are readily dissolved in acidic media. Oxidised iron is typically found in the outer portion of the film, in part due to its higher rate of diffusion. As oxidised chromium is more enriched at the oxide-alloy interface, it has led to several studies employing a bi-layer model to describe the structure of the film [17, 89, 101, 102]. In FeCrNi based alloys, oxidised nickel is seldom found in the passive layer, but instead the metal is found enriched below the film in the modified alloy region [8, 89, 101, 102]. Work by Ryan et al. [35, 104] has suggested that the long range order FeCr passive films decreases when the amount of chromium is increased, which was confirmed after transmission electron microscopy (TEM) was used to show that crystalline structures were formed with 5 % chromium content, after which the passive film became amorphous when increased to 24 %. Anodic polarisation of a Fe–18–13Ni surface in H_2SO_4, used to age the film, was found to induce crystallisation in the film [31]. When molybdenum was included in the alloy, ageing under anodic polarisation did not result in the formation of a crystalline oxide, with Maurice et al. [17] suggesting that molybdenum, concentrated in the outer part of the film, stabilises the amorphous iron-rich oxide. Similar studies of passive films were made elsewhere [37]. In acidic environments, the passive film typically has a thickness of 1–3 nm [17, 30, 88, 89].

In strongly alkaline conditions, a significant Fe^{3+} overlayer forms on the passive film [109, 110, 115]. This observation is explained by knowing that iron in its +2 and +3 oxidation states is much less soluble at high pH values, contrary to what is seen in acidic conditions. As a result of this, we can produce passive films that are much thicker when working in basic media. This has been evidenced by Schmutz and Landolt [109] who analysed the films formed on two different austenitic stainless steel samples, one of which contained molybdenum, and in both cases upon increasing the potential in the passive range, those films formed in acid experienced a loss of mass (indicating dissolution), whilst those formed in NaOH gained mass (indicating film growth). Similar observations were obtained by Strehblow et al. [110, 115]. A graph showing the relation between passive film thickness, potential and pH is shown in Figure 1.4.

The literature shows that the nature of the passive film is complex and is highly dependent on the environment in which it is in, as well as the sample itself. A summary of the data can be found in Table 1.3.

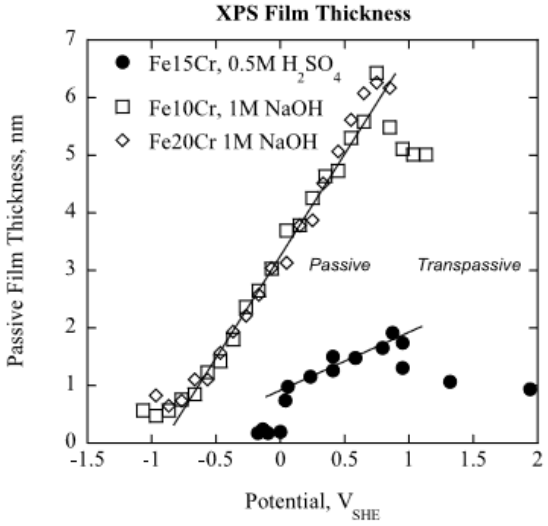

Figure 1.4: Passive film thickness in different media and potential [116].

Bulk composition (at%)	Conditions	Oxide composition (at%)	Thickness (nm)	Reference
Fe–18Cr–13Ni*	100 L O_2 then 0.05 H_2SO_4 + 30 mins at E_{pass}	Fe–72Cr	1.6	[102]
Fe–17Cr–14.5Ni–2.3Mo(100)	0.05 M H_2SO_4 + 2 hours at E_{pass}	Fe–67Cr–3.6Mo	1.9	[17]
	0.05 M H_2SO_4 + 20 hours at E_{pass}	Fe–72Cr–4.5Mo	1.8	
Fe–20Cr–12Ni–1.6Mo	100 L O_2 then 0.05 H_2SO_4 + 30 mins at E_{pass}	Fe–57Cr–15Mo	2.1	[101]
Fe–20Cr	10 minutes in NaOH at 0.5 V (vs SHE)	-	4.8	[76]

Table 1.3: Composition and thickness of passive films formed on stainless steels. *It should be noted that where a crystallographic orientation is not given, the sample is assumed to be polycrystalline in nature.

1.3.3 What role does molybdenum play in the passive film?

As has already been alluded to in the text, molybdenum can play a vital role in fighting against corrosion of stainless steels, with it being present in the passive film as Mo^{4+} and Mo^{6+}. Remaining at a concentration of just a few atomic percent, it is not thought to contribute to an increase in the thickness of the protective layer [14, 17], although Sugimoto et al. [117] state that the thickness of the film will increase with increased molybdenum content. The exact role that this small amount of molybdenum plays in preventing passive film breakdown and the initiation of localized corrosion by pitting is still not truly known. There are various hypotheses surrounding this phenomenon, but generally focus on one of two main arguments. Firstly, there is the notion that molybdenum prevents the breakdown of the passive film in the first place; and secondly, it has recently been suggested that rather molybdenum is involved in the reparation of the film after its initial breakdown.

Early work by Horvath and Uhlig [118] suggested that by adding small amounts of molybdenum it increases oxygen affinity for the stainless steel and subsequently decreases the tendency for chloride ions to adsorb to the surface and initiate passive film breakdown. Later work by Hashimoto et al. [14] came to a slightly different conclusion, stating that the presence of molybdenum resulted in the formation of stable oxy-hydroxides at active sites, evidenced by significant molybdenum enrichments whilst in the active region. It is unanimously agreed that chromium is a vital player in the fight against corrosion in stainless steels, as previously stated in this text, and it was Yang et al. [119] that proposed that molybdenum works together with the chromium to prevent the breakdown of the film. In this paper XPS and electrochemical analysis were used to show that in the early stages of passive film formation, Cr_2O_3 is preferentially formed and blocks propagation of localised corrosion; however, Cr^{3+} ions may hydrolyse which increases pH and enhances the rate of corrosion. If molybdenum is present, then a molybdenum oxide is formed and retards the process. Other works have suggested that molybdenum and chromium work in tandem [14, 120]. Olefjord [8] also cites synergistic properties between the chromium and molybdenum (as well as perhaps nickel), suggesting that it is in fact metallic enrichment of molybdenum at the metal/oxide interface that reduces active dissolution of the film by enhancing the bonding strength of surface atoms. This work also tentatively alludes to improved repassivation with molybdenum enrichment. Recent work, carried out by Lee [121] shows that in 0.05 M H_2SO_4 without chloride, increasing the amount of molybdenum in Fe–18Cr–xMo alloys, where x ranges from 0–6, had zero effect on the anodic polarisation curves. However, in chloride containing solutions of 0.05 M H_2SO_4 an increased molybdenum content resulted in the extension of the passive region and at the same time decreasing the critical current density for

passivation, with both factors indicating that higher molybdenum content promotes quicker formation of the passive film in chloride containing environments as well as being more stable. This observation was in agreement with previous work [117]. In Lee's paper, it was also remarked that molybdenum aids faster repassivation by reducing the peak current density transients. A paper by Maurice et al. [17] supports the point of view that molybdenum is involved in the reparation of the film and uses STM images to show that after transient dissolution takes place, local nanostructures, possibly molybdenum containing, form in the depressions left behind and help to heal the breakdown. These nanostructures were not found to form on non molybdenum containing stainless steels.

All in all, the mechanism behind the enhancement of corrosion protection due to the presence of molybdenum in stainless steels is still poorly understood. It is very likely that there is not just one sole effect or mechanism but rather many interconnected ones that all come together to aid the improvement of passivity in chloride containing environments.

1.4 Concluding statement

As seen above, the oxidation and subsequent passivation of stainless steels and their constituent elements is, despite having already been studied extensively, not completely understood. It is felt that by looking at the fundamentals of oxidation reactions on model austenitic stainless steel alloys one can better understand the core principles that govern the properties and performance of the passive film. This knowledge can then be used to potentially enhance said properties, with the end result of improving corrosion resistance, which in turn will lead to a range of benefits relating to the economy, the environment and to the health and safety of the global population.

CHAPTER 2

Analytical techniques

2.1 X-ray photoelectron spectroscopy

X-ray photoelectron spectroscopy (XPS), also known as electron spectroscopy for chemical analysis (ESCA), is an analytical technique based on the phenomenon that is the photoelectric effect. This discovery, made by Heinrich Hertz [122] and later explained by Albert Einstein [123], showed how electrons are emitted from a material upon its interaction with incident light. Shortly following Einstein's landmark publication, Innes showed that it was possible to record broad bands of electrons as a function of their velocity [124]. However, it was in the mid-1950's, some 40 years later, that the technique truly began to develop, when Kai Siegbahn recorded the first high resolution ESCA spectrum [125]. Despite this, it was not until 1967 when Siegbahn published a comprehensive explanation of the technique that it become widely acknowledged as an important analytical tool [126]. For his work on ESCA, Siegbahn went on to win the physics Nobel prize in 1981. A powerful surface sensitive technique, ESCA, or XPS as it is now more commonly referred to, provides information on the chemical states of the surface atoms and relative compositions of said surfaces as well as information on the valence band structure. XPS has helped shaped modern surface science and has been at the heart of many great discoveries within the various branches of science.

An electron's binding energy, E_b, is characteristic of the atom that it is emitted from. When an incoming photon, with energy corresponding to that of an X-ray, hits a sample, it causes the ejection of a core photoelectron with kinetic energy, E_k. Provided that we know the energy of the incoming photon, $h\nu$, that causes the excitation, and the work-function of the sample, Φ_s,

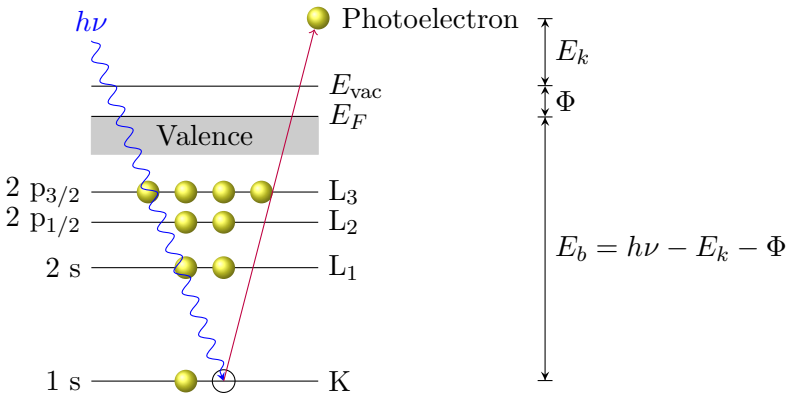

Figure 2.1: Schematic diagram showing the process of photoemission of a core electron.

we can calculate the binding energy of the emitted electron:

$$E_b = h\nu - E_k - \Phi_s \tag{2.1}$$

The inelastic mean free path, λ, is defined as the average distance an electron can go without altering its kinetic energy. This is the distance that an electron can travel before its energy decays to $1/e$ of its initial value. The probability of an electron being able to travel a distance, x, without losing energy decreases exponentially with distance:

$$p(x) = e^{-\frac{x}{\lambda}} \tag{2.2}$$

The value of λ is very small, typically around 1 nm for electrons with a kinetic energy of 10–1000 eV. Approximately 95% of the detected electrons come from the first 3 λ, showing that XPS is very much a surface sensitive technique. The value of λ is dependent on the electron energy and follows a typical curve (which varies slightly depending on the material), as shown in Figure 2.2.

2.1.1 XPS spectra

A typical XPS survey spectrum is shown in Figure 2.3. In most cases, intensity (counts per second, CPS) is plotted as a function of binding energy (electronvolts, eV), with the x-axis inverted.

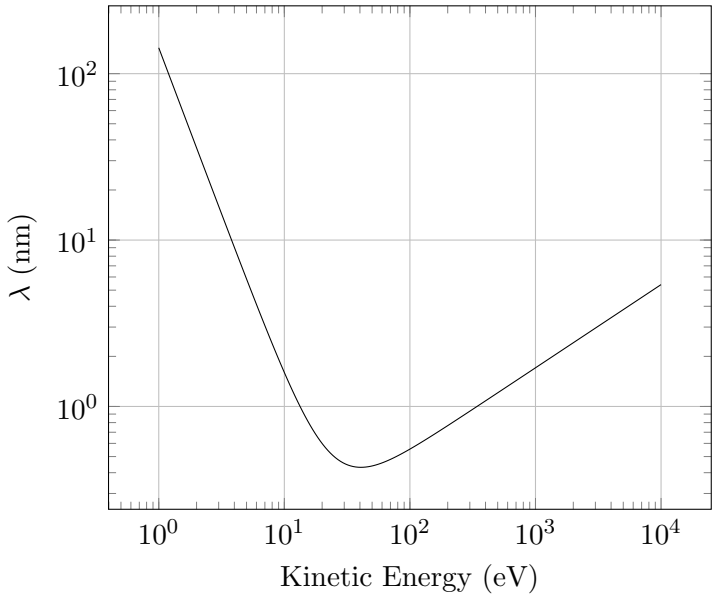

Figure 2.2: Variation in the inelastic mean free path as a function of kinetic energy.

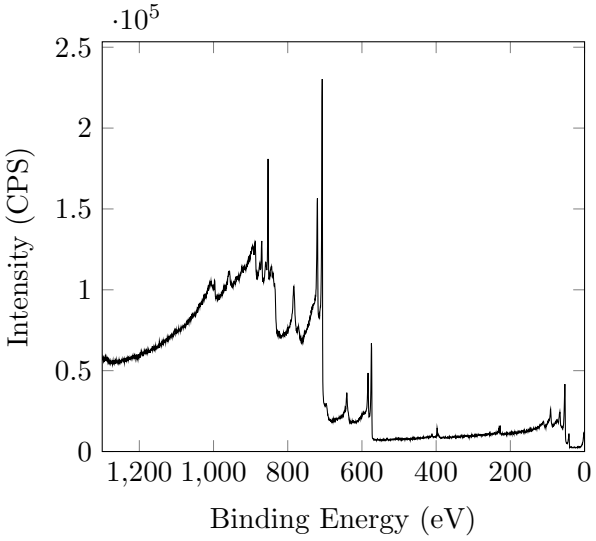

Figure 2.3: An XPS survey spectrum of FeCrNiMo.

An XPS spectrum has several notable features. The main peaks of concern are those that are a direct result of the photoemission of core electrons. It should be noted that binding energies are characteristic of the environment that the atoms are in. The electron of an oxidised atom will have a higher binding energy than a metallic atom, as there is an increased interaction between the nucleus and electrons, due to the positive charge of the oxidised atom. As well as spectral features observed due to the emission of core electrons, we also observe peaks caused by the emission of Auger electrons. The ejection of Auger electrons occurs when a core electron is emitted, resulting in the creation of a vacancy hole that an electron from a higher energy level falls in to, causing the release of energy, which can be transferred to another electron, which

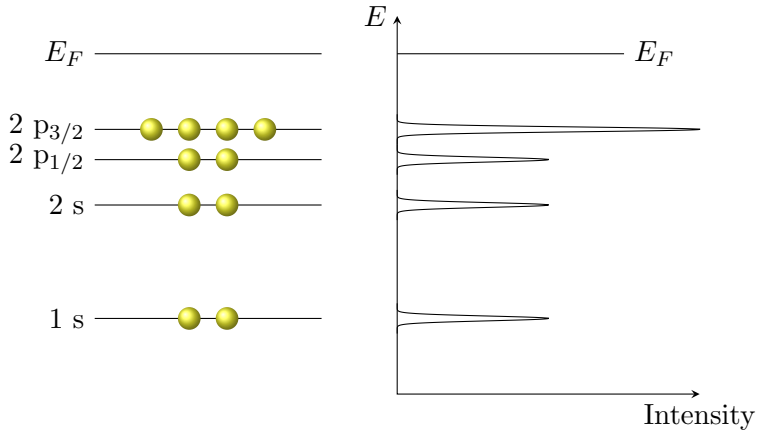

Figure 2.4: Spin-orbit coupling.

is subsequently ejected. The last thing to consider is the presence of shake-up satellite peaks; when an atom undergoes photoionization there is a finite possibility that it will be left in an excited state, and when this happens, the kinetic energy of the emitted photoelectrons is slightly reduced.

Spin-orbit coupling causes a splitting of electronic levels, with this being reflected in XPS spectra where doublet peaks are observed. Core levels can be defined using nl_j notation, where n corresponds to the principal quantum number, l is the orbital angular momentum quantum number, and $j = l + s$ (when $l > 0$). Here s is the spin angular momentum, taking values of $\pm\frac{1}{2}$. For all values of $l > 0$, we observe a doublet. The two peaks of the doublet have different intensities. These differences are mainly caused by the different degeneracies of each spin state (number of degenerate states= $2j + 1$). s-orbitals do not exhibit spin-orbit splitting as they possess no orbital momentum. However, with p-orbitals ($l = 1$) the ratio of the intensities for the two coupled peaks is 2:1, as there are 4 electron states ($2 \times \frac{3}{2} + 1 = 4$) in the $2p_{3/2}$ and 2 electron states ($2 \times \frac{1}{2} + 1 = 2$) in the $2p_{1/2}$, as shown in Figure 2.4. The same is observed for d-orbitals ($l = 2$) and f-orbitals ($l = 3$), with ratios of 3:2 ($d_{5/2}$:$d_{3/2}$) and 4:3 ($f_{7/2}$:$f_{5/2}$), respectively. One very important parameter to consider when thinking about intensity ratios is the photoionisation cross section, σ. Within the context of XPS, the photoionisation cross section relates to the probability of the electron being emitted from its electronic structure. This factor allows us to compare the relative intensities of different photoemission peaks. Using scattering theory, Scofield calculated all photoionisation cross-sections for Al K-α and Mg K-α radiation [127].

The intensity, dI_x, of a photoemission peak from an element, x, within a layer of thickness

dz, found at depth z, can be calculated using the following equation:

$$\mathrm{d}I_x = kFSN_x\sigma_x T_x \int_0^d \exp\left(-\frac{z}{\lambda_x \sin\theta}\right)\mathrm{d}z \tag{2.3}$$

where

k is a constant (dependent on the experimental equipment),

F is the photon flux,

S is area of analysed zone,

N_x is the density of atoms x,

σ_x is photoionization cross section of the electronic level of x,

T_x is the transfer function of the analyser (dependent on kinetic energy of the electrons), and

θ is the emission angle of electrons relative to the surface (take-off angle).

Geometry has a significant effect on the intensity, as the distance travelled, $z/\sin(\theta)$, in the material depends on the emission angle of the electrons and the depth, z, at which they are emitted. By choosing a grazing angle we increase surface sensitivity. This is just for the emission of electrons, as the angle at which the photons reach the surface is insignificant as the inelastic mean free path of a photon is significantly larger.

2.2 Time-of-flight secondary ion mass spectrometry

Time-of-flight secondary ion mass spectrometry (ToF-SIMS) is an analytical technique used to analyse the surface composition and distribution of elements within a solid or layer. The technique involves bombarding the surface with ions that cause the release of atoms and ions — an observation first made by J. J. Thomson at the beginning of the twentieth century [128]. As is the case with all UHV techniques, it was not until the enhancement of vacuum pump technology in the 1950s that the technique began to become what it is today, with Herzog and Viehböck [129] developing the first prototype experiments. Whilst many were involved with the development of secondary ion mass spectrometers, it is Benninghoven at the University of Münster who is accredited with the development of ToF-SIMS due to the introduction of static SIMS [130], where a low current density of primary ions is used allowing for analysis of the first few surface layers. The first commercial SIMS machines appeared during the 1960s. ToF-SIMS is regarded as one of, if not the most, sensitive techniques in surface science, with capabilities of measuring concentrations in the parts per billion.

Figure 2.5 shows a typical ToF-SIMS schematic diagram. Initially, the sample is bombarded by a focused, pulsed primary-ion beam at keV energies. Traditionally in SIMS, a liquid metal ion gun (LMIG) is used as a primary ion source, and there are generally three types to choose

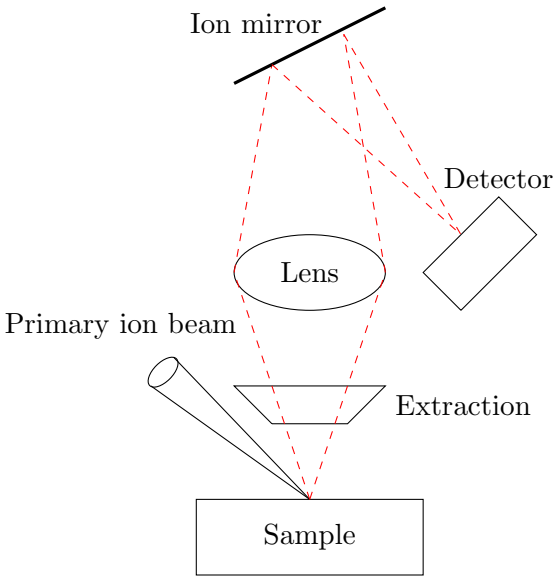

Figure 2.5: ToF-SIMS Schematic.

from — Ga, Au and Bi, the choice of which will depend on the desires of the user. Upon hitting the sample, the ion beam will transfer momentum to the surface atoms, resulting in the emission of secondary ions and ion clusters. The secondary ions produced are then extracted and focused towards an ion mirror, from which they are directed towards the detector. A time-of-flight (ToF) analyser will separate ions according to their velocity, and as the ToF is directly proportional to the square root of the weight, the time taken to arrive will be dependent on the ion's mass. As it is possible to measure the ToF to the nanosecond, the atomic mass of the incoming particle can be measured to within that of a thousandth of a proton, allowing for easy identification of species. An ion mirror, which minimises the spread of the kinetic energy of ions with the same mass to charge ratio, is used in order to extend the flight path, and therefore the flight time, allowing for a longer separation of the ions arriving at the detector, which increases the mass resolution. The end result is a mass spectrum spanning large amounts of atomic mass units plotted against the intensity, allowing the user to observe characteristic fragmentation patterns. Equally, the intensity of the signal from a given fragment can be followed as a function of time (or depth, providing that there is a known and constant sputtering rate), allowing the user to observe its distribution within the material that they are analysing. An example is given in Figure 2.6. Whilst SIMS is highly sensitive, it is not truly a quantitative technique as each material will have a unique ionisation probability and therefore requires comparisons with standards if it is to be treated as such.

SIMS is capable of operating in two modes — static, and dynamic. The latter uses a higher current and therefore has a faster sputtering rate, resulting in a higher ion count. This can

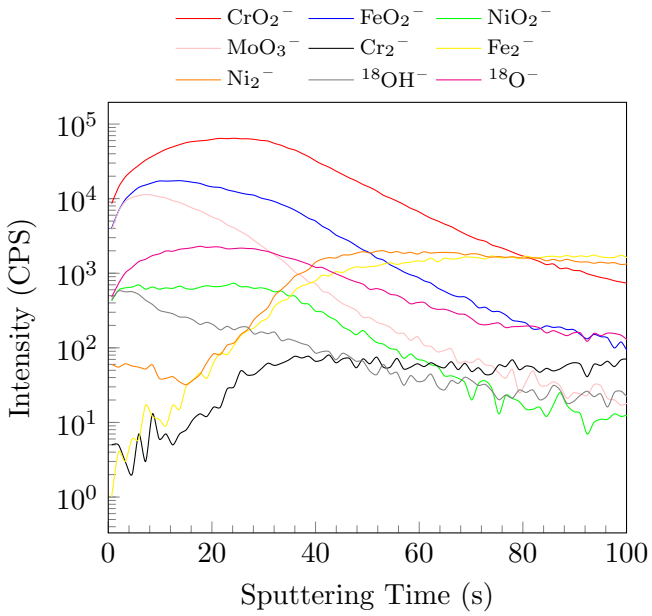

Figure 2.6: ToF-SIMS depth profile spectrum showing an oxide formed on a FeCrNiMo surface.

be useful when trying to identify trace elements, however, with the trade off that it causes degradation of the sample. Static SIMS meanwhile, has a lower current and is less destructive. It is typically used when wanting to look at just the first few monolayers.

When one wishes to probe deeper into the sample, surface etching is performed using ion sputtering (a combination of ToF-SIMS with sputtering). An element composition or molecular structure depth profile can be obtained from the spectrum information gained through alternating between sputtering and measurement. When carrying out surface etching, a sputter ion gun is used alongside the primary ion gun. In general, oxygen or caesium ions are used for depth profile analysis of inorganic materials while fullerene and argon gas cluster ions are used for organic materials.

2.3 Scanning tunnelling microscopy

Scanning tunnelling microscopy (STM) is an atomic imaging technique, frequently used in surface science, that utilises the phenomenon known as the quantum tunnelling effect to produce reconstructed images of surfaces with high lateral (< 1 Å) and vertical resolution (1 pm). The system was first developed by Gerd Binning and Henrich Rohrer at IBM in 1981 [131]; the invention would later win them the 1986 Nobel Prize in physics. The system consists of an atomically sharp tip that is rasted over a surface at a close distance (approximately 1 nm) with an applied potential bias, allowing electrons to tunnel through and produce a current which can be used to reconstruct an image of the surface. STM can be performed under a wide

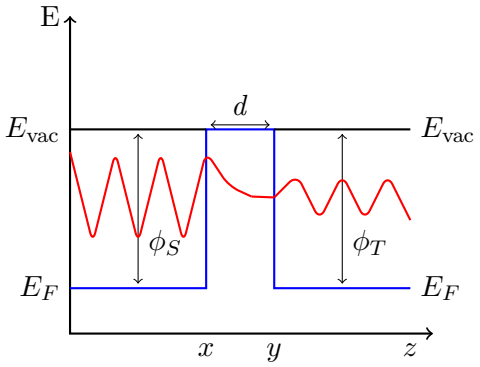

Figure 2.7: One-dimensional rectangular barrier showing the quantum tunnelling effect.

range of conditions, from ultra-high vacuum to liquids, and 0–1000 K. Since its inception, STM has helped researchers in a broad-range of fields to better understand what is going on at the nanoscale.

Quantum mechanics tells us that an electron can behave as both a particle and as a wave. If we consider the electron as a particle, using the classical model, it cannot tunnel through a barrier. However, if we consider the electron as a wave, using a quantum mechanics model, the electron can tunnel through the barrier. Electrons exist in specific energy levels, $\psi_n(z)$, and in a macroscopic material a band of electrons forms. The energy of these energy levels can be determined using the Schrödinger equation. These electrons are happy to sit in low energy states, and if an electron is to be ejected into free space, then an energy corresponding to that of the work function, ϕ, must be applied. However, as stated previously, those electrons could just pass straight through the energy barrier. An evanescent wave exists such that it extends out of a material and can be transmitted. The tunnel effect is detailed in Figure 2.7 using a simplified one-dimensional rectangular barrier. If the tip and sample are sufficiently close and under a potential bias, V, then there is an overlap of the wave-functions and it is therefore possible that an electron can exist within or on the other side of the barrier. The probability that an electron at position x can be found at another point, y, separated by a distance, d, is proportional to the square of the wave function:

$$P \propto |\psi_n(z)|^2 e^{-2\kappa d} \tag{2.4}$$

where

$$\kappa = \frac{\sqrt{2m\phi}}{\hbar} \tag{2.5}$$

At this point, we only have a model that gives the probability of an electron tunnelling. However, it would be much more convenient if we had an expression for the tunnelling current. In order to achieve this, the total sum of all the states of both sample and tip must be taken,

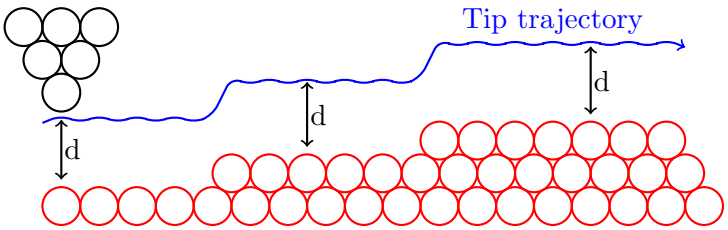

(a) Constant current

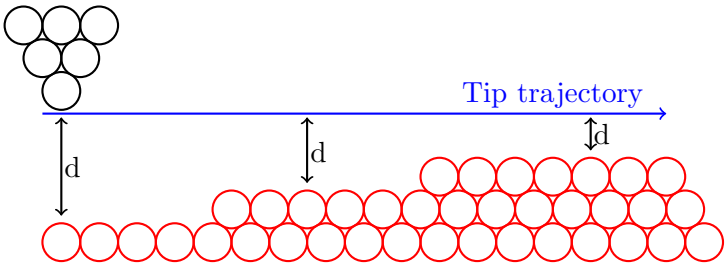

(b) Constant height

Figure 2.8: STM Modes

whilst bearing in mind that electrons can tunnel both ways. This very complicated problem was simplified in 1983 when the Tersoff and Hamman model was developed [132]. They replaced the unknown electronic structure of the tip with a model system, making several assumptions in doing so:

i Wave-function of outermost atom is that of an s-orbital.

ii Experiment is done at 0 K.

iii Very small applied potential bias → rectangular barrier.

iv Work function of tip and sample is identical.

Whilst these assumptions are not perfect, the Tersoff-Hamman model is the most widely used model today and can provide us with an equation for the tunnelling current that can be used to produce constructed images of the surface morphology:

$$I \propto V e^{-2\kappa d} \tag{2.6}$$

A theory based on more realistic wave-functions was developed by John Bardeen [133].

2.3.1 Operating modes of STM

There are three main operating modes when it comes to STM —- spectroscopy, constant height (Figure 2.8a) and constant current (Figure 2.8b). The latter of the three is a quick and simple method where the tip is kept at a constant distance from the surface and the current is

varied. It is a technique that can be employed provided that the surface is very flat; otherwise, there is a high risk of the tip crashing into the surface. The constant current operating mode uses a feedback loop as well as adjustment of the proportional and integral gains to analyse the roughness of the surface. The piezoelectric crystal adjusts so that the current is kept constant and maps the topographical features of the surface. Spectroscopy is used to probe the local changes in electronic structure, allowing for chemical analysis to be carried out on the surface. This is done by varying the applied potential bias and observing how the tunnelling current changes.

2.4 Low energy electron diffraction

Low energy electron diffraction (LEED) is a surface technique used in determining the surface periodicity of single crystal materials. The technique is built on the observations made by De Broglie [134], who first proposed that particles behave as waves, and Davisson and Germer [135] who three years later in 1927 observed how the angular dependence of the intensity of backscattered electrons showed diffraction patterns. For his work in electron diffraction, Davisson went on to win the 1937 physics Nobel prize. The technique was not initially used all too frequently due to the inadequacy of UHV systems at the time and trouble with monitoring the directions and intensities of the diffracted beams, however in the early 1960's UHV systems became more advanced and Germer himself pioneered a technique where the diffracted electrons could be accelerated, resulting in more clear diffraction patterns on the screen. LEED uses a collimated beam of low energy electrons, ranging from 20–200 eV, to bombard the surface of the single crystal allowing the user to observe the elastic backscattering of electrons creating a pattern as spots on a fluorescent screen. The electron waves will be scattered by the surface atoms which behave as point scatterers due to their high localised electron density. The De Broglie relationship states that the wavelength of an electron, λ, is inversely proportional to its momentum, p:

$$\lambda = \frac{h}{p} \tag{2.7}$$

now,

$$p = m_e v = \sqrt{2 m_e E_k} \tag{2.8}$$

where

m_e is the mass of an electron,

v is the velocity of an electron, and

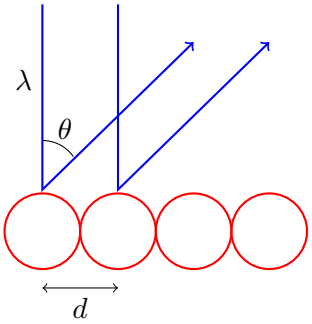

Figure 2.9: LEED.

E_k is the kinetic energy of an electron.

Therefore,

$$\lambda = \frac{h}{\sqrt{2m_e E_k}} \tag{2.9}$$

The wavelength of electrons between 20 and 200 eV is comparable to that of the distances between atoms, a key property in using diffraction to observe atomic structure. A simple one-dimensional model of atoms, separated by a distance, d, with the electron beam incident perpendicular the surface is modelled in Figure 2.9.

As θ can be measured, the distance between atoms can be calculated:

$$d = \frac{n\lambda}{\sin\theta} \tag{2.10}$$

where

n is an integer.

LEED is a surface sensitive technique as the electrons will only penetrate a few angstroms of the surface. As a result of its high sensitivity, LEED can detect changes as small as a hundredth of a structured monolayer adsorbed on the surface. The technique is most typically used in the identification of crystalline phases, the study of symmetry groups and the organisation of the surface.

CHAPTER 3

Experimental

This chapter aims to provide an overview of the general experimental details that have been used over the course of the study. The contents first focus on the equipment, in particular the analytical tools used. From here, an outline for the major experimental techniques is given, with a later focus on how the generated data are treated. In addition, the beginning of each results-based chapter will include a brief synopsis on the finer details that are pertinent to that particular section.

3.1 Equipment used

3.1.1 Platform for surface analysis and electrochemistry

The bulk of experiments that have been performed were carried out on an experimental platform consisting of a Scienta-Omicron UHV system with a directly attached Jacomex GP[Concept] glove box (Figure 3.1). The UHV system allowed for preparation of a clean surface (oxygen and carbon free), which could then subsequently be transferred to the surface analytical instruments attached. The UHV system has a base pressure of $< 1 \times 10^{-10}$ mbar, which is maintained by a series of turbo, ionic and Ti sublimation pumps, and consists of three chambers. The attached glovebox allowed for samples prepared under UHV conditions to undergo electrochemical treatments without exposure to the ambient air.

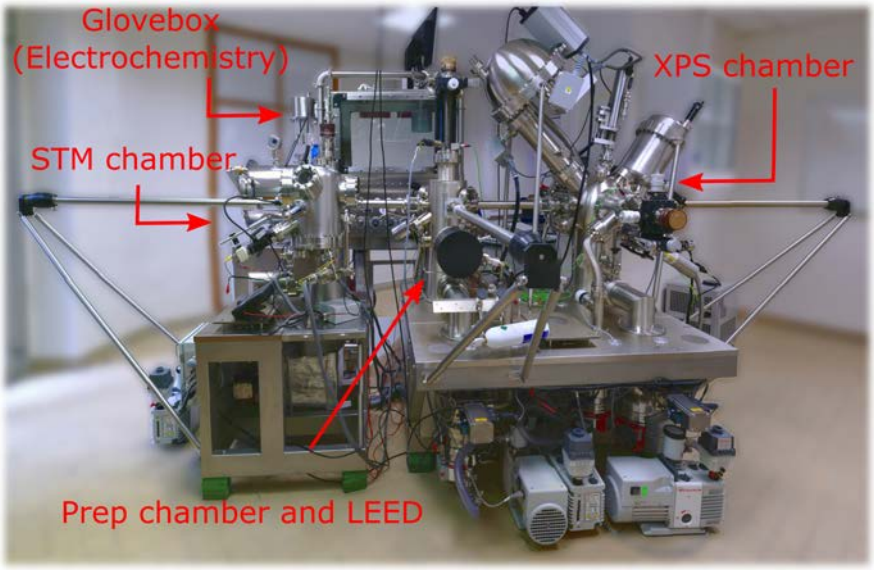

Figure 3.1: Platform for surface analysis and electrochemistry.

3.1.1.1 Preparation chamber

The preparation chamber is where the surface was prepared prior to experimental use. Attached to the chamber is an ISE 5 cold cathode ion sputter source, capable of operating between 0.3–5 keV, which is used to bombard the surface with argon ions that remove surface contaminants such as oxygen and carbon. If required, the sample can then be annealed up to 1400 °C via radiative backside heating of the sample. Annealing is typically performed in order to reorganise the surface structure.

This chamber also houses the LEED system, with measurements performed using a Scienta-Omicron SPECTALEED device (Figure 3.2), controlled by the supplied package. The device is capable of using the standard Ir/Th filament or a LaB_6 electron beam filament, depending on the requirements of the user, with the latter recommended for Auger work due to its higher emission current. A four-grid, gold coated molybdenum, system was used. The source energy range is 15 eV to 3.5 keV.

3.1.1.2 XPS analysis chamber

As the name would suggest, the XPS analysis chamber is where XPS measurements were carried out. The system utilises an Argus Spectrometer and Argus Detector, controlled using MATRIX software, all made by Scienta-Omicron. The spectrometer is a complete hemispherical electron spectrometer system, with a small spot lens that can also be used for imaging XPS (iXPS), as well as XPS. The Argus Spectrometer is based on a 124 mm mean radius electrostatic hemispherical dispersive energy analyser composed of two concentric hemispheres. The outer

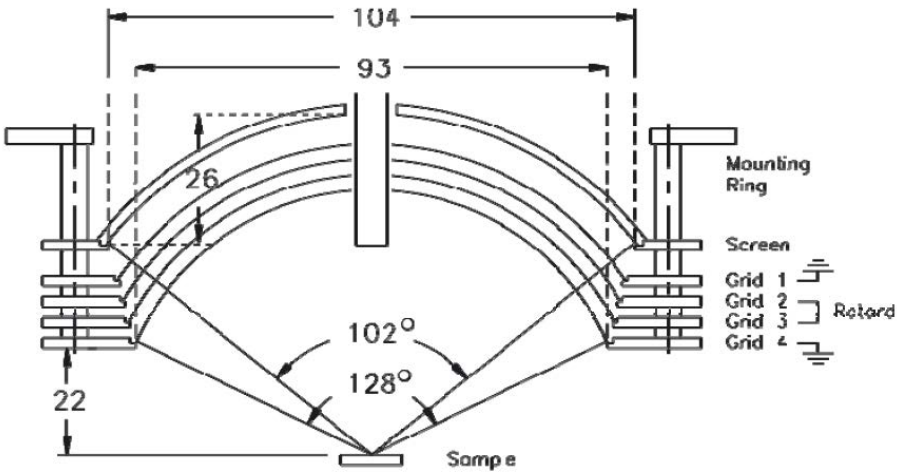

Figure 3.2: Scienta-Omicron SPECTALEED schematic.

146 mm and inner 102 mm radius hemispheres are biased negative and positive, respectively, with respect to the mean radius of the energy analyser. The system has 3 X-ray sources available — Mg Kα (1253.6 eV), Al Kα (1486.6 eV) and a monochromatised Al Kα (1486.6 eV), the latter being the one used for all measurements during the study. The use of a monochromatic X-ray source has several advantages, most notably improved resolution of spectra, which is attributed to the fact that the photon line width of monochromatised source (300 meV) is much smaller than that of standard XPS X-ray sources (700 meV). Additional benefits of using the monochromatic source include the removal of Bremsstrahlung background and satellite lines from the X-ray beam, which aids in increasing the signal to noise ratio. The main downside of monochromatic X-ray sources when compared to those that are polychromatic is the reduced intensity.

There are five main components of the Argus Spectrometer, which is shown in Figure 3.3:

1. A multi-element lens, with a 30 mm working distance from the sample, that collects the electrons from the sample and focuses them to the entrance of the hemispherical energy analyser. The lens may also accelerate or slow the electrons relative to the energy at which they have left the sample, as well as providing variable magnification and angular acceptance.

2. An in-lens deflector that scans the focal point of the lens across the sample.

3. An in-lens aperture that defines the area for sample analysis. The aperture can be mechanically selected from the apertures available. There are six apertures to choose from, depending on the needs of the user (i.e high resolution, high count rate or snapshot).

4. A hemispherical energy analyser, with 124 mm mean radius 180° double focusing geometry.

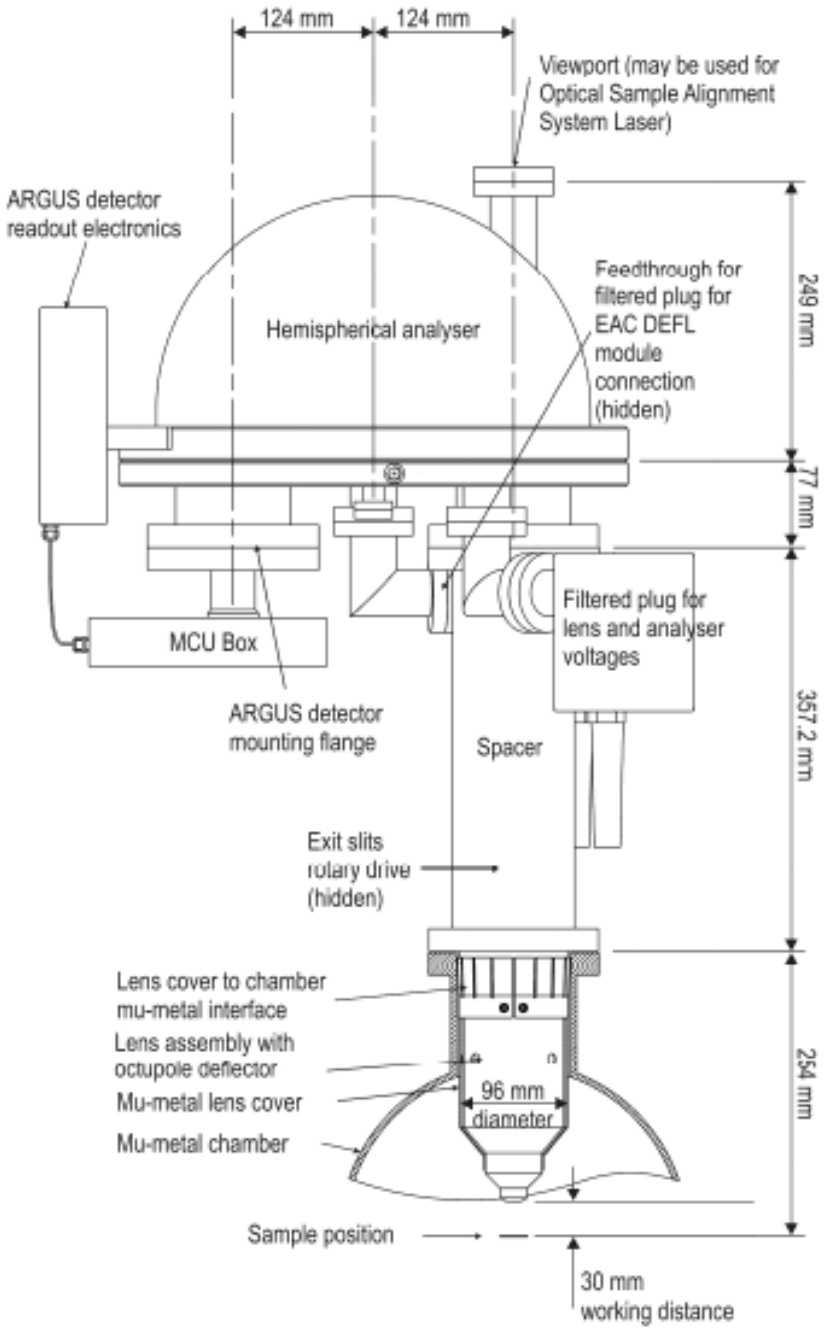

Figure 3.3: The Argus Spectrometer.

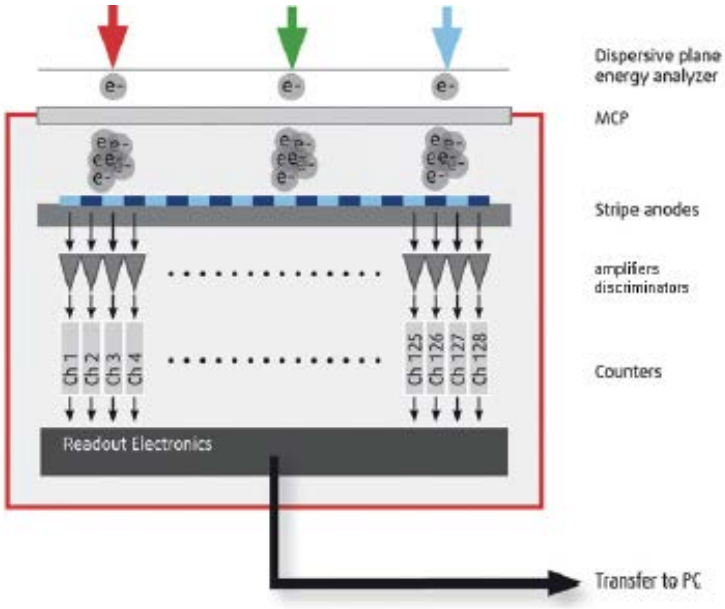

Figure 3.4: Scienta-Omicron Argus 128 detector.

5. A 128 channel detector, with micro-channel plate electron multipliers, a stripe anode detector and 128 discriminators.

When operating in constant analyser energy mode (CAE), the input lens is used to collect electrons from the sample and then focus them into the aperture at the entrance of the analyser whilst adjusting the kinetic energy such that it matches the pass energy of the analyser. The Argus Spectrometer uses a two lens system, with the electrons passing through the initial transfer lens and then onto the retard lens, before entering the analyser. The analysis area is defined as the region of the sample from where the electrons are emitted and transmitted through the analyser. The angular spread of these electrons that originate from the middle of the analysis area that pass through the lens is called the acceptance angle. An in-lens aperture is used to define the acceptance angle and analysis area. The range of lenses allow the analyser to analyse small areas with diameters of 60 μm and an acceptance angle of $\pm 1.1°$. In large area XPS, the instrument is capable of collecting and analysing electrons from an analysis area of more than 3 mm^2 with an acceptance angle of $\pm 9°$. The two apertures used during experiments were the Argus detector snapshot mode (used for measuring kinetic data) and an aperture designed for the best compromise between count rate and resolution (used for high resolution and survey spectra).

The Argus detector (Figure 3.4) consists of a chevron stack of micro channel plates (MCPs), placed across the exit plane of the analyser. These MCPs then produce a cloud of electrons for each electron. This cloud can then be collected by an anode, consisting of 128 separate strips,

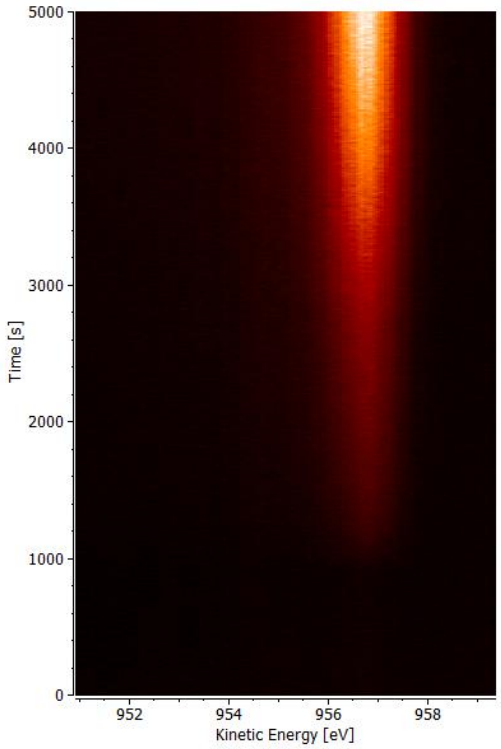

Figure 3.5: Snapshot measurement of the oxygen 1s region during oxidation.

and counted in one of the 128 in-vacuum counters. The high number of channels, complemented by the high spatial resolution, allows for recording of spectra with good resolution in an energy interval of 0.14 times the pass energy, keeping all voltages of the spectrometer fixed. This allows for continuous recording of spectra over time, previously referred to as a snapshot measurement, which is key when determining in-situ oxidation kinetics or monitoring elemental segregation. Spectra can be recorded every 10 seconds (a time that is a good compromise between speed of acquisition and signal to noise ratio), during which the sample can be exposed to oxygen or heated. An example of a snapshot measurement of the O 1s region during oxidation of a FeCrNiMo(100) sample is shown in Figure 3.5. The brighter the colour, the more intense the signal.

3.1.1.3 STM analysis chamber

STM measurements were carried out using a modified Scienta Omicron VTM XA (Figure 3.6), controlled by a Scienta Omicron MATRIX SPM control system. To minimise vibrations, the base plate is suspended by four soft springs, which are supported by four columns. In order to dampen any vibrations caused by the suspension system, a non-periodic eddy current dampening mechanism is used. This is achieved by surrounding the base plate by a ring of copper plates which come down between two magnets.

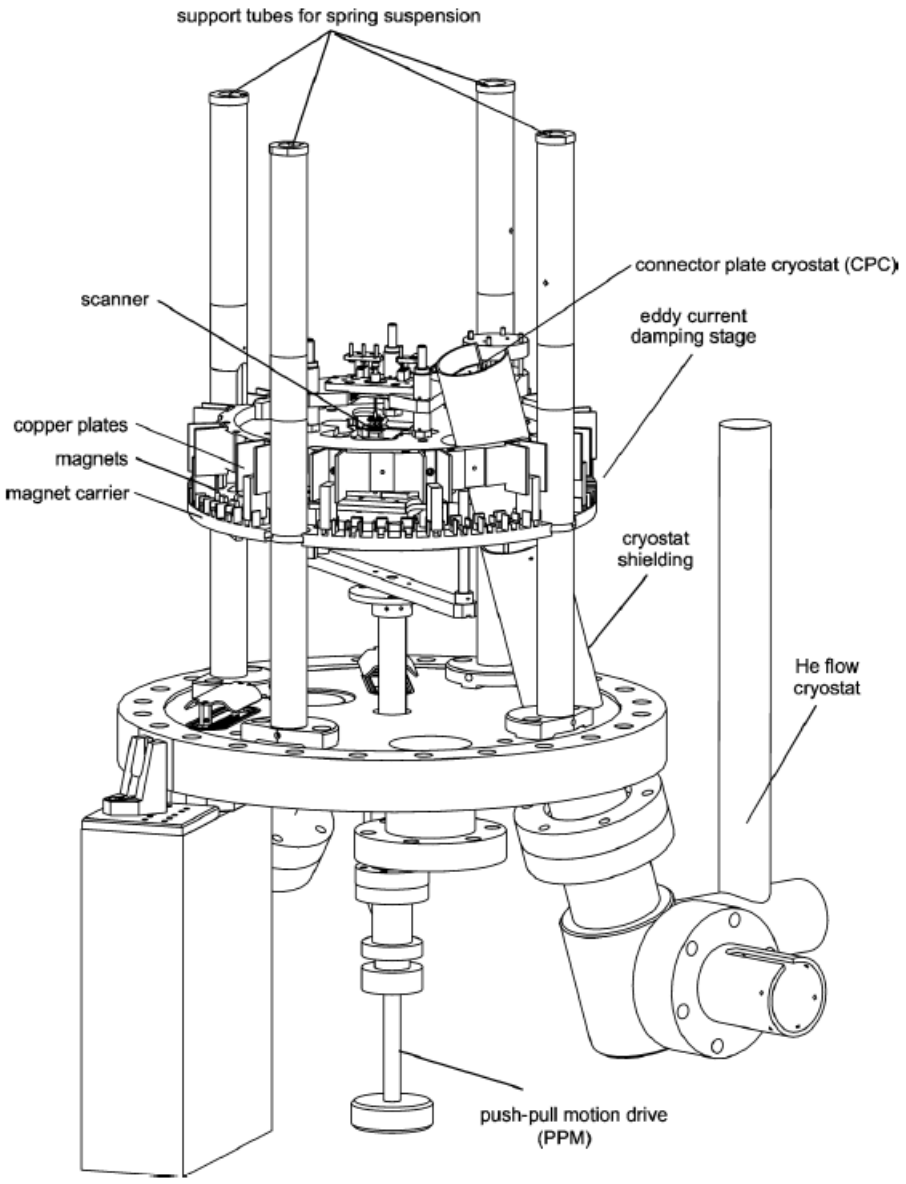

Figure 3.6: Side view of the VTM XA. Note that the system used in this work does not have the He flow cryostat, nor the cryostat shielding.

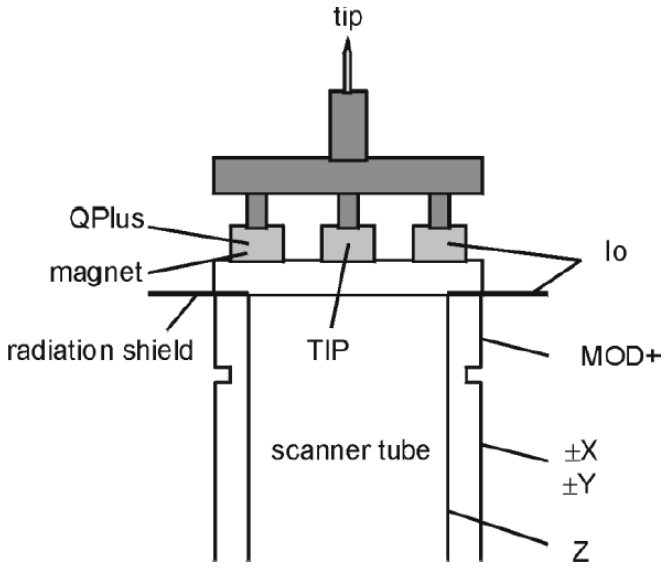

Figure 3.7: Piezoelectric scanner schematic.

The STM device uses a single tube scanner (Figure 3.7) with a maximum scanning range of 12 μm $\times$ 12 μm and travel in the Z-direction of up to 1.5 μm. The scanner's position is adjusted by a 3-axis linear piezo motor. Modifications made to the STM, such as gold plating of components to prevent corrosion, allows for the possibility of carrying out in-situ measurements where the surface is probed whilst being exposed to gases at pressures up to 1×10^{-6} mbar. The system is also capable of performing measurements at high temperatures, with operating conditions ranging from RT–700 °C. The VTM XA is not just limited to STM; the QPlus sensor allows the user to perform non-contact atomic force microscopy (NC-AFM). Tungsten tips were used throughout, with voltage pulses and high voltage scanning used for tip preparation.

3.1.1.4 Glove Box

Attached to the preparation chamber is the Jacomex GP[Concept] glove box, where electrochemical treatments were carried out. The inside of the glove box is filled with argon, with an operating pressure of approximately 250 Pa and with minimum levels of oxygen and water (0–10 ppm). In the presence of an aqueous electrolyte, an increase of the humidity and oxygen by approximately one order of magnitude was observed.

3.1.2 ToF-SIMS spectrometer

ToF-SIMS measurements were performed on a ToF-SIMS V spectrometer manufactured by IONTOF GmbH-Münster. The UHV system, shown in Figure 3.8, typically operates at 10^{-9} mbar, and consists of one preparation and one analysis chamber, coupled with an attached

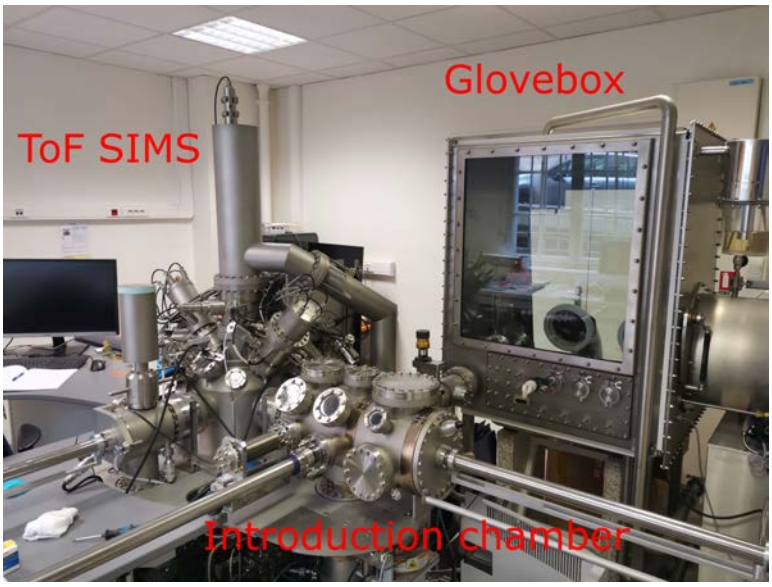

Figure 3.8: ToF-SIMS V spectrometer manufactured by IONTOF GmbH-Münster.

argon-filled glovebox. It is equipped with a pulsed Bi^+ primary ion gun, a Cs^+ sputtering ion gun, a flight tube, a highly accurate computer clock and a time-of-flight mass analyser. An Ar-filled and air-tight container was used to transfer the sample between the gloveboxes in order to avoid exposure to the ambient air.

3.2 Experimental procedure

3.2.1 Samples

The majority of the work was performed on the same 100-orientated single crystal with a bulk composition of Fe–18Cr–14Ni–1.3Mo (at%), which behaves as a good model for AISI 316L. The sample was previously synthesised and orientated at École des Mines de Saint-Étiene using spark machining and Laue X-ray diffraction. Other samples, such as a polycrystalline Fe–20Cr–12Ni–1.6Mo and a Fe–18Cr–13Ni (100) single crystal, were used for various references and collaborative work.

3.2.2 Preparation of clean surface

Prior to any treatment of the sample it was necessary to first prepare a clean surface, i.e. a flat, well organised surface, that is free of contaminants. This was achieved via cycles of sputtering and high temperature annealing in the preparation chamber of the UHV system. In order to first remove contaminants, the sample was subjected to Ar^+ sputtering (1–5 keV, P_{Ar}=6×10^{-6} mbar, 8–70 μA, 10 mins). The next stage, used to reorganise the surface, a

requirement due to the destructive nature of sputtering, involved annealing the sample (700 °C, 10 mins) via radiative heating of the backside. In some cases, particularly after sustained periods of electrochemistry, macroscopic defects would appear on the surface. Most commonly observed was a circular mark made by the O-ring, although small pits where infrequently observed. Due to this, it was necessary to mechanically polish the sample using progressively smoother polishing disks (6, 3, 1 and 0.25 μm) and corresponding diamond suspension. The sample was polished by moving in a circular motion over the polishing disk. Before progressing to a finer disk, the surface state was verified using an optical microscope. Once finished, a cleaning process, involving sonication in acetone followed by ethanol was carried out. This process, whilst much more efficient at removing macroscopic contamination than UHV sputtering and annealing cycles, created surface defects on the microscopic level. Therefore, after any mechanical polishing, multiple sputtering and annealing cycles were still required, typically starting at higher energies of argon ions (3–5 keV) which was then reduced (1 keV) to ensure that the surface is as defect free and as flat as possible. Removing the microscopic defects and re-preparing a flat, clean and well-organised surface was time-consuming, with the total time for the process often exceeding one week. Verification of the composition of the surface was routinely determined by XPS survey spectra, whilst the structural state was checked using LEED and STM.

3.2.3 Exposure to oxygen

Once a clean and well-organised surface had been achieved, the sample was then ready to be oxidised or have its surface structure analysed using STM or LEED. All controlled oxidations were carried out in the analysis chamber of the UHV system, where it is possible to control the temperature as well as the exact pressure and exposure time to gaseous oxygen (99.999% purity). Oxygen was introduced via a leak-valve connected to the chamber, with $P_{O_2} = 10^{-8}$ mbar. The exact exposure is calculated by plotting P_{O_2} vs time (s) and then finding the area under the curve. The exposure is then converted to units of langmuir (L), where 1 L corresponds to an exposure of 1×10^{-6} Torr for a period of one second. The Langmuir unit is derived from the knowledge that if every molecule stuck to the surface, i.e. a sticking coefficient of one, then an exposure of 1 L would result in the formation of about one monolayer. Controlled oxidations in the UHV system were carried out at room temperature (RT) and 250 °C. It was also possible to follow the reaction kinetics of the oxidation using the snapshot measuring mode.

As well as oxidation via controlled means in the UHV chamber, a native oxide was also formed for comparison. This is where the clean surface is exposed to the ambient air, or that of the glovebox, which immediately forms an oxide on the surface due to reactions with O_2 and

H_2O. Exposures to the glovebox environment were typically less than 10 minutes in duration.

3.2.4 XPS

3.2.4.1 Recording of XPS data

XPS survey spectra were recorded between −10 and 1300 eV at a pass energy of 50 eV and a step size of 0.5 eV. High resolution spectra were recorded for Fe 2p, Cr 2p, Mo 3d, Ni 2p, O 1s, N 1s, C 1s, S 2p and Cl 2p core levels as well as the Fermi level. The pass energy was 20 eV, coupled with a step size of 0.05 eV. Several iterations of each core level were made in order to maximise the signal to noise ratio. Both survey and high resolution spectra were recorded at take off angles of 45° and 90°.

XPS snapshot mode, which involves collecting electrons from a whole energy range at once, was used for the monitoring of oxidation kinetics and elemental segregation during annealing. By using the XPS snapshot measurement, one reduces the acquisition time as it eliminates lost time through stepping, settling and over-scanning. Spectra were recorded at a pass energy of 60 eV, with 128 points simultaneously recorded using all 128 available channels of the detector. Therefore, it is possible to record a spectrum for the O 1s peak, for example, every 10 s, with a reasonable signal to noise ratio. The intensity of the oxygen peak at a given time could be matched with the recorded exposure, allowing for a plot of O 1s intensity vs exposure to be made.

3.2.4.2 Treatment of XPS data

Theoretically, a photoelectron emission peak should be, at least in the first approximation, perfectly Lorentzian in shape, with possible asymmetrical characteristics present in metallic peaks. These asymmetries are caused by the photo-emitted electrons interacting with the free electrons of the metal. Asymmetries are not just limited to metallic components, as final-state effects can cause them to occur in non-conductive materials as well as metals. The probability of this decreases with increased energy, hence the asymmetry. However, the lens system, the kinetic energy analyser and the detector cause a Gaussian widening of the peaks. In fact, decomposition software, like Casa XPS [136], the one used in this work, has models of Gaussian, Lorentzian, symmetric and asymmetric function peaks; the art of a successful decomposition lies in the determining of the peak shape that is most suited to the sample, as well as to the XPS system used.

A key, and often neglected, aspect of XPS is the referencing of binding energies. This important step of the process is seldom given a lot of thought and can result in inaccurate

reporting of binding energies. It is commonly found in the literature that XPS binding energies are referenced relative to the peak that arises from adventitious carbon (AdC) contamination. This method involves recording the C 1s region and then setting aliphatic C-C/C-H bonds to an arbitrary binding energy, typically around 285 eV. The shift relative to this position can then be applied to all core levels. A review by Greczynski et al. [137] recently highlighted several issues with this method. The fundamental problems relate to a lack of standardisation, with no consensus when it comes to issues such as the nature of which carbon species is used for calibration, i.e is it aliphatic, graphitic or adsorbed hydrocarbon, and what binding energy to actually use as a reference point, with values ranging between 284 and 285.6 eV. The exact position of the AdC was found to vary significantly based on the sample, environment and exposure time [137, 138]. Fortunately, as the samples used in this work are conductive and in good electrical contact with the spectrometer, we can use the Fermi level as our reference for 0 eV on the binding energy scale, as this is, by definition, the cut-off point for the density of states (DOS). It is when the value of the Fermi-Dirac distribution is equal to one half. To determine if a shift is required, the Fermi level is recorded and the data graphed. The plotted data can then be fit using the Fermi-Dirac distribution, shown in equation (3.1). Equally, we can multiply by a linear function (see appendix) in order to better account for the slope, leading to a more accurate adjustment. From this fit we can determine the correction that must be applied such that the Fermi level is at 0 eV. This correction can then be made to all spectra in the set. An example is given in Figure 3.9.

$$f(E) = \frac{1}{1 + e^{\frac{E-E_F}{kT}}} \tag{3.1}$$

Several constraints were used when fitting the high resolution spectra (full width at half maximum (FWHM), binding energy (BE), peak area and line shape) in order to achieve a more accurate and consistent fit. Intensities of $2p_{3/2}$ and $2p_{1/2}$ for Fe, Cr and S, as well as $3d_{5/2}$ and $3d_{3/2}$ for Mo were fixed according to theoretical ratios, however, only the Ni $2p_{3/2}$ was treated due to the fact there is no overlap between that and the corresponding Ni $2p_{1/2}$ peak. When there is not a sufficient enough gap between spin-orbit peaks, both are fitted in order to fit a more accurate background. Metallic components were fitted with an asymmetric Lorentzian curve convoluted by a Gaussian curve, denoted LA (α, β, n) where α and β correspond to variables associated with the asymmetric Lorentzian curve and n takes an integer value (0–500) relating to the width of the Gaussian used in the convolution. For non-metallic peaks, which generally have a less asymmetric shape, a Lorentzian/Gaussian product formula, denoted

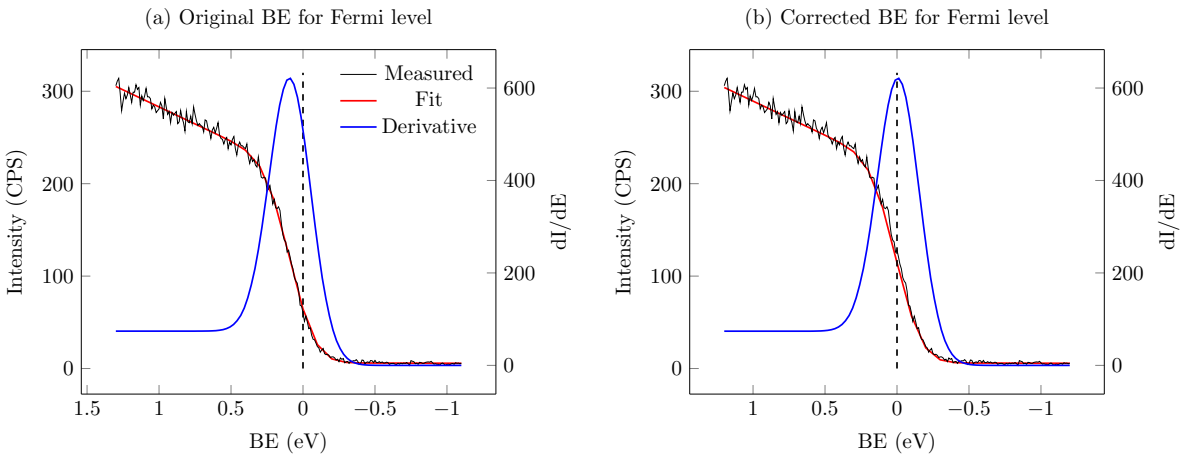

Figure 3.9: An example of how the Fermi level is used to correctly reference the binding energy for XPS spectra.

GL(m), where m refers to the percentage of Lorentzian character (GL(100) is pure Lorentzian and GL(0) is pure Gaussian), was used in most cases. Once a consistent set of parameters were established, achieved using an iterative method, they were applied to all spectra throughout in order to achieve a high level of consistency. Previous work carried out on similar systems was used as starting point and reference for the peak fitting process [90,102]. The fitting parameters[a] used for the XPS decomposition are shown in Table 3.1. Assignments of the four nitrogen peaks are justified in chapter 4. With regards to the satellite peaks, it should be noted that their contribution to the intensity was taken into account in the quantification results, as suggested by Brundle and Crist [139].

Similarly, another important parameter in the XPS spectrum decomposition is the determination of the continuous background. If the user wishes to produce reliable data this is a key step in doing so. There are several types of background that are available within Casa XPS, and the one that is best suited will depend on many different factors. For this work an adjustable Shirley background was used throughout. Essentially, a Shirley continuous background uses an iterative process to take account of the inelastic scattering of electrons. Casa XPS also allows the use of a manually adjustable Shirley background to correct slope errors due to low calculation iteration or multiple peaks for near binding energies. However, the general shape of the background was kept consistent for each region throughout the process.

[a] Refer to the appendix for Fe $2p_{1/2}$, Cr $2p_{1/2}$, S $2p_{1/2}$, and Mo $3d_{3/2}$ parameters.

Core level	State	Assignment	BE (± 0.1 eV)	FWHM (± 0.1 eV)	Line shape
S $2\,p_{3/2}$	S^{6+}	Sulphate	169.1	1.3	GL(30)
Mo $3\,d_{5/2}$	Mo^{0}	Metal	227.6	0.6	LA(1.2,6,20)
	Mo^{4+}	Oxide	228.9	1.4	LA(3,5,5)
	Mo^{4+}	(Oxy)hydroxide	230.1	1.7	GL(20)
	Mo^{6+}	Oxide	232.4	1.9	GL(50)
S 2s	S^{6+}	Sulphate	233.0	2.9	GL(70)
N 1s		$N_{chromium}$	396.6	1.1	GL(30)
		$N_{sub-surface}$	397.2	0.7	GL(30)
		$N_{interstitial}$	397.8	0.7	GL(30)
		$N_{minority}$	398.5–400.5	1.8–2.6	GL(30)
Cr $2\,p_{3/2}$	Cr^{0}	Metal	573.9	1.2	LA(0.85,5.3,19)
	Cr^{3+}	Oxide	576.6	2.0	LA(1.7,5.5,10)
	Cr^{3+}	Hydroxide	577.4	2.0	LA(1.7,5,20)
	Cr^{3+}	Satellite (ox)	588.5	3.5	GL(30)
	Cr^{3+}	Satellite (hyd)	589.6	5.4	GL(30)
Fe $2\,p_{3/2}$	Fe^{0}	Metal	706.9	0.7	LA(0.55,2.5,1)
	Fe^{2+}	Oxide	708.3	1.6	LA(1.5,3,5)
	Fe^{3+}	Oxide	710.3	3.1	LA(1.7,5,5)
	Fe^{3+}	Hydroxide	711.8	3.7	GL(30)
	Fe^{2+}	Satellite	712.8	3.8	LA(2.5,5,5)
	Fe^{3+}	Satellite	716.3	4.1	LA(1.4,13,5)
Ni $2\,p_{3/2}$	Ni^{0}	Metal	852.7	1	LA(1.2,3,5)
	Ni^{2+}	Oxide	855.1	2.0	GL(30)
	Ni^{0}	Satellite	859.0	4.5	GL(30)

Table 3.1: XPS peak fitting parameters obtained for reconstruction of spectra.

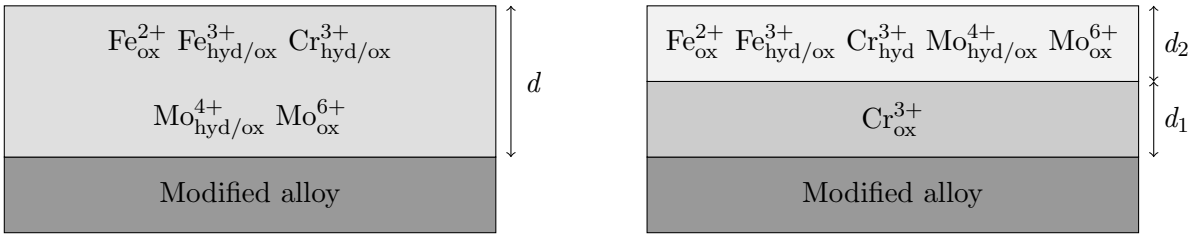

Figure 3.10: Single-layer (left) and bilayer (right) models of the oxide/passive films formed on FeCrNiMo stainless steel.

3.2.4.3 Thickness and composition calculation

Data from XPS can be used to calculate the thickness of an oxide film, as well as the corresponding composition. In order to do this, we must first select a model for the system, where it is assumed that the films are continuous, homogeneous and flat. For the purposes of this work investigating FeCrNiMo surfaces, two models will be used in the results based chapters — a single-layer model, and a bilayer model, both shown in Figure 3.10. The single-layer model assumes that oxide and hydroxide species (when present) are found in a single film with a homogeneous distribution, whereas the bilayer model assumes an outer exchange layer with the electrolyte and an inner barrier layer that is responsible for slowing down atomic transport and consists primarily of Cr_2O_3. The outer exchange layer consists of $Cr(OH)_3$, $Fe^{2+/3+}$ and $Mo^{4+/6+}$ species. The assignment of these species to their given layers is later justified in chapter 6 using the results obtained from ToF-SIMS measurements. The sole aim of this particular sub section is to explain the procedure and rational used to calculate the values for the thickness and composition of the oxide layers. Hydroxide species are not produced during the controlled oxidation under UHV conditions, so can be removed from consideration when calculating values for oxides generated in these conditions.

As the layers contain multiple different species it is necessary to make certain assumptions when calculating the thickness and composition. An important parameter in the calculation is the inelastic mean free path (λ), i.e the average distance an electron can travel through a material without losing energy. As the layers contain different compounds, the electrons will therefore have different λ values, as it is dependent on the material in which they are passing through, as well as the electron energy itself. It is therefore important to pick a value based on this fact. The difference in value between $\lambda^{Cr_2O_3}$ and $\lambda^{Fe_2O_3}$, the main oxides, is negligible ($\Delta\lambda < 1.5\%$), however there is a significant difference between $\lambda^{Cr_2O_3}$ and $\lambda^{Cr(OH)_3}$ ($\Delta\lambda \approx 12\%$). One can either use the value of the most common compound, in this case oxide, or one can estimate an average based on an approximate ratio of oxide:hydroxide. This is an issue that needs to

be considered for both the single-layer model and the outer layer of the bilayer model, as they have a mix of oxide and hydroxide. For the purposes of this thesis, an average value between $\lambda^{Cr_2O_3}$ and $\lambda^{Cr(OH)_3}$ was used for the single-layer model, when considering passive films formed in aqueous media. This value shall from now on be noted as λ^{CrO_x}. For the bilayer model, values for electrons passing through Cr_2O_3 are used for d_1 and CrO_x for d_2. There is obvious uncertainty in these assumptions and they are taken into account when calculating thickness values.

As the estimated thickness of the film is dependent on the calculated composition, we need to consider the variance in specific gravity ($g \cdot cm^{-3}$) for each compound. λ and specific gravity are related to one another so the same behaviour is observed. For the single-layer model (when looking at passive films formed in aqueous media) an average is used and the bilayer model uses the value corresponding to the oxide in the inner layer and an average of the oxide and hydroxide for the outer layer. With this knowledge, we can begin to construct a method for calculating the thickness of the oxide layer(s). It is first necessary to calculate a value for the molar density (N_x). For a layer of infinite thickness it is known that:

$$I_x = kFSN_x\sigma_x T_x \lambda_x \sin(\theta)$$

As the layer is not infinite we must take account of this.[b]

$$I_x = kFSN_x\sigma_x T_x \lambda_x \sin(\theta)\left[1 - \exp\left(-\frac{d}{\sin(\theta)\lambda_x}\right)\right]$$

In cases where we have multiple layers, as is such with the bilayer model, it is necessary to consider the fact that the electrons from the inner layer must pass through the outer layer. We must therefore multiply by an attenuation factor:

$$I_x = kFSN_x\sigma_x T_x \lambda_x \sin(\theta)\left[1 - \exp\left(-\frac{d_1}{\sin(\theta)\lambda_x^{d_1}}\right)\right]\exp\left(-\frac{d_2}{\sin(\theta)\lambda_x^{d_2}}\right)$$

We can define a normalised intensity[c] for a non-infinite single layer (remembering to consider attenuation factor if using bilayer model) as:

$$I_x^{'} = \frac{I_x}{\sigma_x T_x \lambda_x\left[1 - \exp\left(-\frac{d}{\sin(\theta)\lambda_x}\right)\right]}$$

therefore,

$$N_x = \frac{I_x^{'}}{kFS\sin(\theta)} \implies \frac{N_x}{N_x + N_y + N_z} = \frac{I_x^{'}}{I_x^{'} + I_y^{'} + I_z^{'}}$$

[b] As I_x is dependent on d, a value, d_{est}, is initially taken and subsequently adjusted until self-consistency is achieved.

[c] In practice area is typically used instead of intensity.

with

$$N_x + N_y + N_z = \frac{\rho_L}{\mathrm{m}} \therefore N_x = \frac{I_x^{'}}{I_x^{'} + I_y^{'} + I_z^{'}} \cdot \frac{\rho_L}{\mathrm{m}}$$

where

ρ_L is the layer density, and

m is the molecular weight of the layer.

For the single layer model, we can now calculate the thickness using the following calculation:

$$d = \lambda_{\mathrm{M}}^{\mathrm{CrO}_x} \sin(\theta) \ln\left(1 + \frac{\lambda_{\mathrm{M}}^{316\mathrm{L}} N_{\mathrm{M}}^{316\mathrm{L}} I_{\mathrm{M}}^{\mathrm{MOx}}}{\lambda_{\mathrm{M}}^{\mathrm{CrO}_x} N_{\mathrm{M}}^{\mathrm{MOx}} I_{\mathrm{M}}^{316\mathrm{L}}}\right)$$

The same method is used for calculating the thickness of the two layers of the bilayer model. Once again, for the inner layer, d_1, values relating to $\lambda^{\mathrm{Cr_2O_3}}$ values are used. For the outer layer, d_2, an average value of the hydroxide and oxide is again taken, provided that the former is present; adjusting the value to account for molybdenum oxide species is not worthwhile as it was found to have little influence on the results. The following calculations below are used to calculate d_1 and d_2, where M denotes the metal and MOx the corresponding metal oxide:

$$d_1 = \lambda_{\mathrm{M}}^{\mathrm{Cr_2O_3}} \sin(\theta) \ln\left(1 + \frac{\lambda_{\mathrm{M}}^{316\mathrm{L}} N_{\mathrm{M}}^{316\mathrm{L}} I_{\mathrm{M}}^{\mathrm{MOx}}}{\lambda_{\mathrm{M}}^{\mathrm{Cr_2O_3}} N_{\mathrm{M}}^{\mathrm{MOx}} I_{\mathrm{M}}^{316\mathrm{L}}}\right)$$

and

$$d_2 = \lambda_{\mathrm{M}}^{\mathrm{Cr(O)}_x} \sin(\theta) \ln\left[1 + \frac{\lambda_{\mathrm{M}}^{316\mathrm{L}} N_{\mathrm{M}}^{316\mathrm{L}} I_{\mathrm{M}}^{\mathrm{MOx}}}{\lambda_{\mathrm{M}}^{\mathrm{Cr(O)}_x} N_{\mathrm{M}}^{\mathrm{MOx}} I_{\mathrm{M}}^{316\mathrm{L}}} \exp\left(-\frac{d_1}{\lambda_{\mathrm{M}}^{\mathrm{Cr_2O_3}} \sin(\theta)}\right)\right]$$

We can use any metal that is present in the layer to calculate the thickness of said layer. Regardless of the metal chosen the same result should be obtained.

By altering the electron collection angle, θ, we should observe the same values for the composition and thickness, providing that the model is correct.

3.2.5 ToF-SIMS

3.2.5.1 Recording of ToF-SIMS data

Depth profiles were recorded with negative secondary ions. The Ion ToF spectrometer combined static SIMS and sputtering. A Bi^+ primary ion source was used for static SIMS operating in a HC-bunched mode (25 keV, 12 pA) over an area of 100×100 μm^2. Sputtering was carried out using a Cs^+ sputter beam (0.5 keV, 20 nA) over an area of 300×300 μm^2. Edge effects were avoided by performing static SIMS in the centre of the sputtered area.

3.2.5.2 Treatment of ToF-SIMS data

Before the depth profiles could be constructed, the data needed to be calibrated. This was achieved using the commercially available IonTof software. Fe_2^-, Cr_2^- and Ni_2^- ions were attributed to the metallic substrate, whilst $^{18}O^-$, $^{18}OH^-$, FeO_2^-, CrO_2^-, NiO_2^- and MoO_3^- were assigned to the oxide film. Metallic ions of the form M_2^- were selected for analysis over M^- for the simple reason that the former reduces the possibility that we observe a contribution to the "metallic signal" from an oxidised metal atom. Signal pertaining to M_2^- is most likely to come from a metal cluster found in the alloy, where as M^- could more feasibly come from an oxide species. MoO_3^- was selected over MoO_2^-, simply due to its higher intensity.

3.2.6 STM

3.2.6.1 Operating conditions

STM experiments were performed using tungsten tips that were prepared using high voltage pulses and high voltage scanning. Data acquisition was generally obtained in constant current mode with a potential bias between 0.1 and 2 V, with a scanning current of 0.1–4 nA. Spectroscopic measurements were attempted but with limited success due to the complex nature of the technique.

3.2.6.2 Treatment of STM data

SPIP software was used for data treatment and analysis. Terraces were levelled by correcting their slope and subtracting the differences in height. Image contrast was used in order to highlight particular areas of interest.

3.2.7 Electrochemistry

3.2.7.1 Electrochemical cell

The electrochemical cell (Figure 3.11) was made with the view of being compatible with a sample that could readily be transferred back to the UHV system without significant delay. The home-made cell can hold 350 μl of electrolyte and is made out of polychlorotrifluoroethylene, a fluorine based polymer, commonly known as Kel-F. The working electrode area of 16 mm^2 is defined by a Viton O-ring. The micro-cell was controlled by a Picostat potentiostat and Picoscan software sourced from Agilent Technologies. Two platinum wires were used as a pseudo reference electrode and counter electrode. The former had previously been calibrated as E/SHE = E/Pt +0.75 V by cathodic peaks of the polarisation curve obtained for copper in 0.1 M NaOH and was

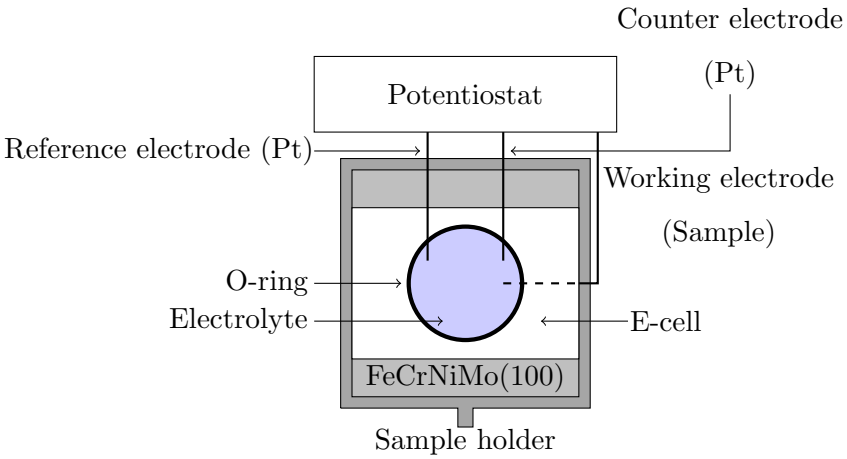

Figure 3.11: Schematic diagram of the electrochemical cell.

reported as being stable [140]. The cell was always cleaned prior to use, first in a 3:1 mixture of concentrated H_2SO_4 and H_2O_2, and secondly in concentrated HNO_3, before being rinsed off with pure water. After a certain period of time the electrodes were replaced due to degradation of the metal.

3.2.7.2 Electrochemical measurements

Various electrochemical measurements and treatments were implemented to analyse the corrosion properties of the material. A 0.05 M H_2SO_4 electrolyte was used throughout. For certain bits of analysis, NaCl was added to the electrolyte to observe what influence the presence of chloride ions had on passive film formation. An important parameter to consider in corrosion science is the open circuit potential (OCP), which can commonly be referred to as the corrosion potential. This property is exactly what it says it is — it is the potential generated in an open circuit. As no external load is added, when the electrode is placed in the electrolyte it will adopt the OCP. The sample was consistently placed in the electrolyte for 30 minutes in order to stabilise at the OCP before being analysed by XPS or ToF-SIMS. Anodic passivation was carried out by stepping the potential to the OCP + 0.2 V over a period of 30 minutes after having stabilised at the OCP. This value was chosen as it lies in the mid-range of the passive film, as suggested by the results obtained from linear sweep cyclic voltammetry experiments. These polarisation measurements were performed at a scan rate of 5 $mV{\cdot}s^{-1}$, from -1.2 to $+1.2$ V. The method of oxidation, followed by OCP, followed by anodic passivation in this controlled manner allows for direct comparison of the effect of the oxidation method on the properties of the passive film. Figure 3.12 shows the procedure as a schematic.

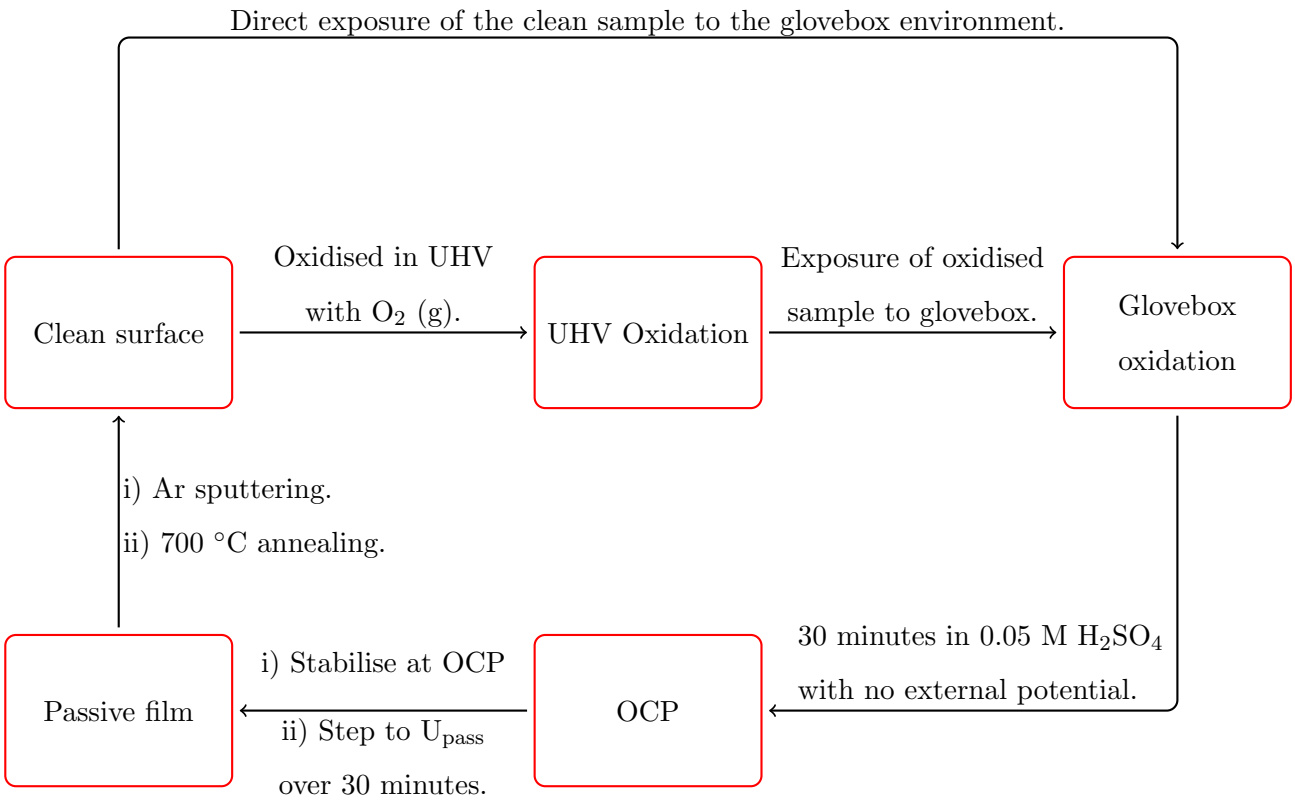

Figure 3.12: Schematic of experimental work used to compare the effect of oxidation method prior to passivation.

CHAPTER 4

An ever changing surface

If one is to properly understand the reactions that take place at the surface, it is imperative to first gain an understanding of the clean surface, that is to say, a surface free of contaminants, such as carbon and oxygen. The aim of this chapter is to shed light on characteristics of the pristine FeCrNiMo(100) prepared under UHV conditions and to highlight any points of interest that will govern the behaviour of the surface in later work.

4.1 Abstract

Surfaces are inherently complex, and the one of the FeCrNiMo(100) sample used in this study is in no way different. It was found that by annealing the sample to 700 °C under UHV, a necessary process that rearranges the single crystal surface after bombarding it with argon ions, chromium and nitrogen segregated to the surface, causing an enrichment of the pair relative to their bulk amounts. However, the quantity of the two that co-segregated during the annealing process was found to decrease with cumulative cycles of sputtering and annealing. This phenomenon causes significant changes in both the rate of oxidation and the composition of the oxide film that forms upon saturation with oxygen at room temperature. STM and LEED studies were performed to highlight key features of the oxide-free surface, notably the $(\sqrt{2} \times \sqrt{2})$R45° reconstruction, and the vacancy line-covered terrace structure.

4.2 Experimental overview

The entirety of this work was performed on the ultra-high vacuum platform for surface analysis and electrochemistry shown in chapter 3, where the experimental procedures are discussed in more detail. It should be noted that, when following the segregation of chromium and nitrogen during annealing using the XPS snapshot mode, it was only possible to follow one element at a time. The experiments were therefore carried out concurrently in order to be able to better relate the two, allowing for a comparison without having to worry about drastic surface modifications brought about by persistent sputtering.

In addition to levelling of the terraces in the STM images, filtering of noise was applied to the STM image of the bisecting vacancy lines in Figure 4.11 in order to improve the resolution of the image.

4.3 The chromium-nitrogen relationship

When the sample is first introduced to the UHV chamber from the outside, there is a layer of contamination and oxide present at the surface. This carbon and oxygen rich layer is a natural result of the sample's interaction with the ambient environment and is what we define as the native oxide. A survey spectrum of the native oxide, recorded at a take-off angle of 45°, is shown in Figure 4.1. The main signals observed are at 285 and 530 eV, which correspond to carbon and oxygen, respectively. Signals from the metallic components are attenuated by the carbon/oxide layer and therefore low in intensity. Sputtering with argon ions at an energy of 1 keV removes the carbon/oxide layer present at the surface and leaves just nickel (852 eV), iron (705 eV), chromium (575 eV), and molybdenum (230 eV) metallic components. Traces of residual argon may sometimes be found at 245 eV. After the sample has been bombarded by high energy argon cations, the surface is not flat and very much un-organised, which is not desirable when studying a single crystal. In order to reorganise the surface, high-temperature annealing is performed. This process provides sufficient energy to the atoms, which increases their mobility such that they can reorganise into a more well-structured system. Post-annealing, chromium is found to be significantly enriched at the surface when compared to the sputtered sample. We also observe the introduction of a peak at 400 eV (overlapping with the Mo 3p region), which can be attributed to nitrogen, an elemental impurity that is found in the bulk.

The dramatic change in composition at the surface is attributed to co-segregation of chromium and nitrogen, which has been previously investigated on similar samples [90–92, 100, 141]. The co-segregation of nitrogen and chromium was monitored using snapshot measurements, with the

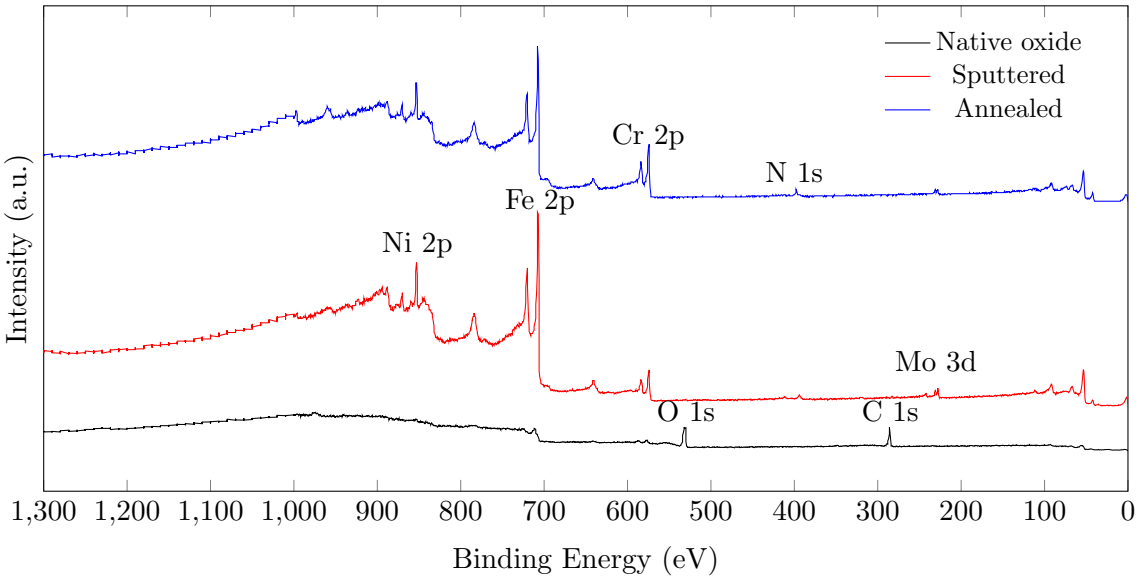

Figure 4.1: Survey spectra for the native oxide (black), sputtered surface (red) and annealed surface (blue) on the FeCrNiMo(100) sample.

data shown in Figure 4.2. Figures 4.2a and 4.2b show the change in Cr 2p and N 1s intensities as a function of time, respectively, whilst Figures 4.2c and 4.2d show the change in intensity of the chromium and nitrogen as a function of temperature, respectively. The intensity of the Cr 2p begins to increase at 300 °C, marked by the red dashed line in Figure 4.2c. From this point the Cr 2p intensity increases steadily until approximately 610 °C, marked by the dashed blue line. Beyond this temperature, the rate of chromium segregation appears to increase. These two phases are an indication of two different mechanisms for chromium segregation during annealing of the stainless steel sample. The intensity of the signal did not diminish during the cooling of the sample.

With regards to the increase in intensity of the nitrogen, we see no significant change in the intensity until a temperature of approximately 600 °C is reached. The beginning of this phase is indicated by the dashed blue line in Figure 4.2d, which is the point at which we see the second increase in the rate of chromium segregation, suggesting co-segregation of the elements, which has also been reported elsewhere on both ferritic and austenitic stainless steels [90–92, 100, 142]. Any apparent changes in nitrogen intensity below this temperature cannot really be considered due to the high level of noise, although no segregation of nitrogen was reported below this temperature on similar surfaces [90]. The rate of nitrogen segregation reaches its maximum value between 600 and 700 °C, which is the same range as that of the chromium, further reinforcing the evidence of co-segregation in this temperature range. It has been suggested in previous work that the chromium and nitrogen co-segregation results in the formation of chromium nitride

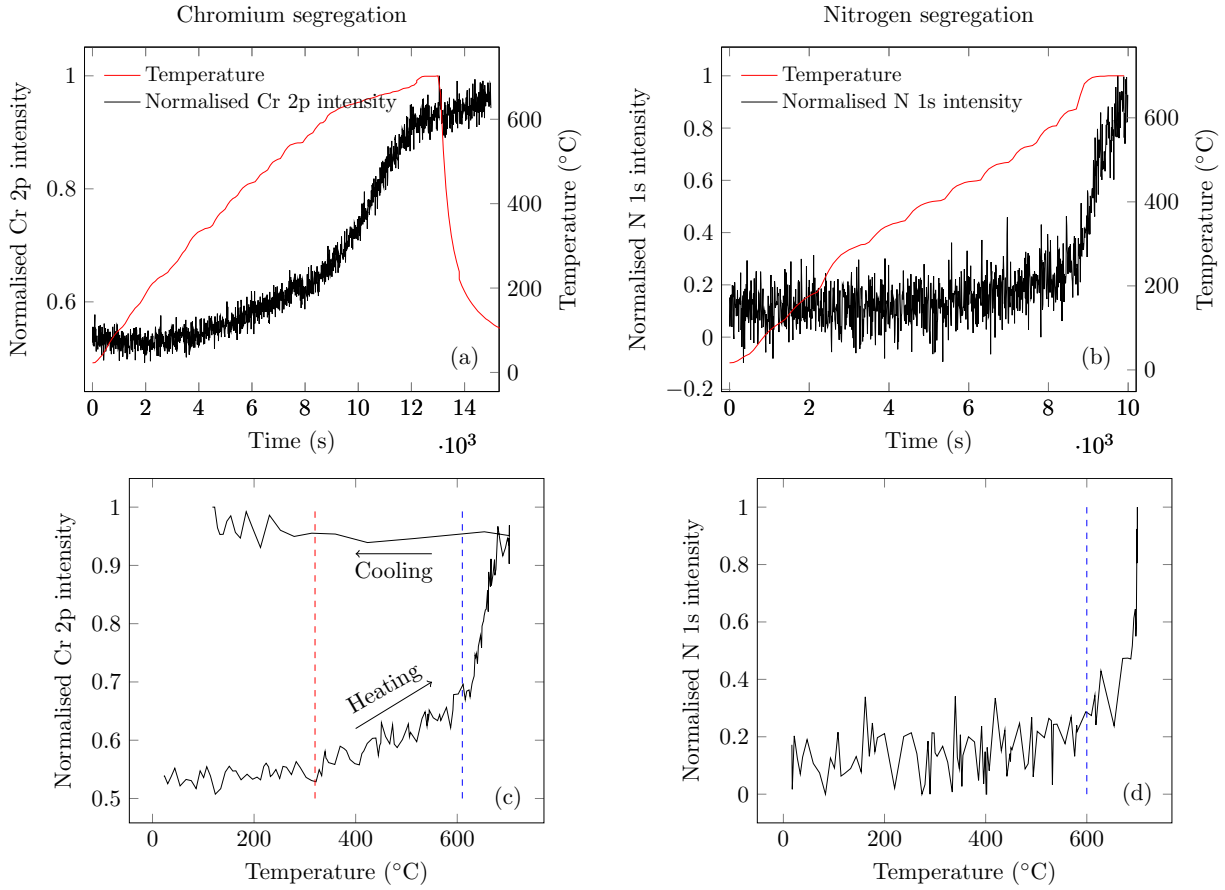

Figure 4.2: Real-time segregation of elements during the annealing process as measured using XPS snapshot measurements: (a) variation of normalised Cr 2p intensity, (b) variation of normalised N 1s intensity, (c) normalised Cr 2p intensity as a function of annealing temperature, (d) normalised N 1s intensity as a function of annealing temperature.

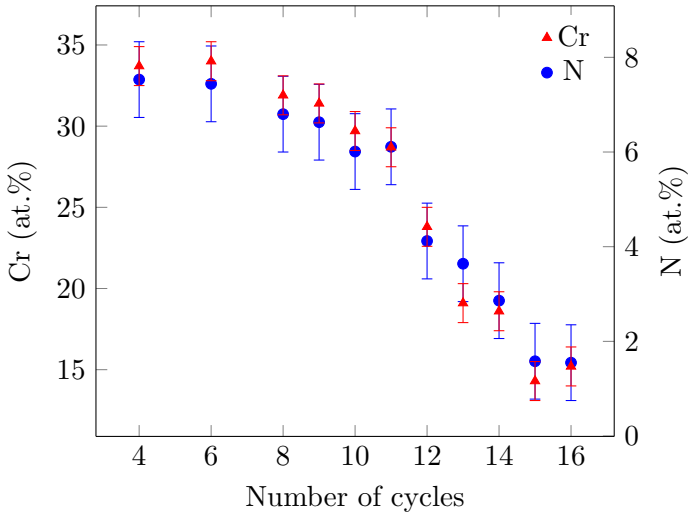

Figure 4.3: Diminution of chromium and nitrogen at the surface with increasing number of sputtering (at 1 keV) and annealing cycles (at 700 °C).

components that promote selective oxidation of chromium [90, 92, 141]. The time taken to reach 700 °C, as well as the time spent at this temperature, were found not to have an influence on the co-segregation of the elements. Whilst not shown in Figure 4.2d, cooling the sample was not found to result in a decrease of the N 1s signal when the experiment was repeated. The same observation during cooling was made on another stainless steel surface [90].

This is not where the changing composition ends; it was found that over the course of the investigation, cumulative cycles of sputtering (at 1 keV) and annealing (at 700 °C) lead to a reduction in the amount of chromium and nitrogen that segregated to the surface, as shown in Figure 4.3. Similar observations have been made where a metal element co-segregates with an impurity, such as sulphur [143, 144], nitrogen [143, 145] and phosphorus [143, 145], owed to depletion of the impurity in the near surface region with an increasing number of cycles. The relationship between the diminution of chromium and the diminution of nitrogen was found to be linear, as shown in Figure 4.4, further emphasising that the mechanism for the decrease of both elements may be linked.

When discussing the oxidation of 304 stainless steel and the relevance of nitrogen segregation on oxidation, Ma et al. [90, 142] assigned four components to the N 1s spectra when decomposing: 2D CrN structures formed at the extreme surface [90, 100, 141, 146], defined as surface CrN (396.6 eV); 3D CrN structures formed at the sub-surface [90, 100, 141, 147], defined as bulk CrN (397.2 eV); interstitial nitrogen (397.8 eV) [90, 100]; and minority nitrogen contributions (398.5–400.5 eV) [90]. The assignment of these peaks was based on the observations of their investigation (XPS and STM) [91, 92, 142] and other work found in the literature [100, 141, 146, 147]. The four

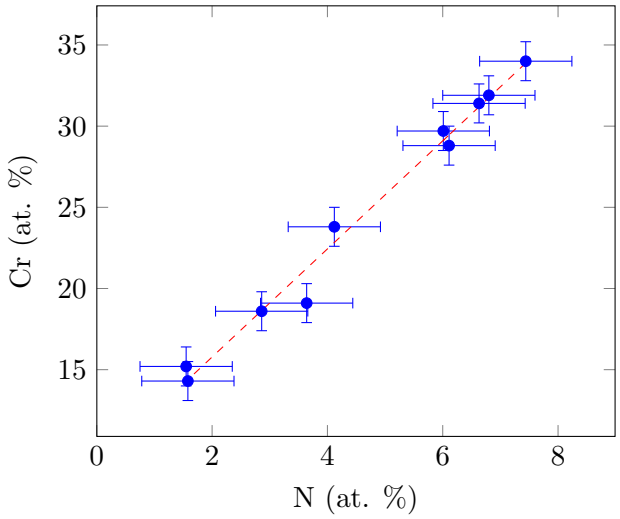

Figure 4.4: Relationship between chromium and nitrogen surface composition diminution during cycles of sputtering (1 keV) and annealing (700 °C).

components in the work where similarly applied when analysing the N 1s spectra, however, the assignment of some components has been re-evaluated. The reader is referred to the XPS decomposition parameters in chapter 3 for more details. Decomposition of the N 1s spectrum on a low chromium/nitrogen (LC) surface was attempted, however, the results should be taken with caution due to the high uncertainty owed to the overlapping Mo 3p region and low intensity. On the clean surface, the component at 397.2 eV, defined as "bulk Cr" by Ma et al. [90] is the most significant of the four, on both high chromium/nitrogen (HC) and LC surfaces. The clear difference when comparing N 1s spectra obtained on the two surfaces is the intensity, as seen in Figure 4.5a. Looking at the Cr 2p spectra at the same stage in 4.5b, one observes a similar marked decrease in intensity. The metallic chromium peak obtained on both HC and LC surfaces can be fitted with the same parameters, with no obvious change in the shape. Given the significant decrease in the amount of nitrogen that segregates, if the segregated nitrogen was present as CrN then one would expect this to be reflected in the Cr 2p spectra, which is not the case. This result therefore suggests that, whilst the segregation of chromium and nitrogen are inherently linked during annealing, it may not systematically result in the production of chromium nitride species at the surface. There is one other difference on which we can pass comment in the Cr 2p spectra; the shape of the background, marked by the black box in Figure 4.5a, is noticeably flatter in the case of the LC surface, whereas the one of the HC surface displays a more downward trajectory. It has been reported by Tougaard [44, 148] that changes in the background can indicate structural alterations at the surface. Given the reported [90, 92, 100, 141, 142, 146, 147] importance of CrN structures when it comes to oxide nucleation on

stainless steels, we can infer from our XPS results that by decreasing the amount of chromium and nitrogen segregation we are altering the structure of the surface. We can not say much more than this, as Tougaard typically suggests examining the background over a much larger binding energy range (50 eV) than is possible here in order to ensure that the changes are not related to other spectral features. With oxidation, we observe changes in N 1s spectra, with a decrease in the relative amount of "bulk CrN" and an augmentation of the peak at 396.6 eV, which was previously defined as surface CrN. The growth of this peak is accompanied with the presence of a corresponding peak that we can relate to chromium-nitrogen interactions in the Cr 2p spectra. Further explanation of the evolution of the N 1s spectra with ongoing oxygen exposure is attempted in chapter 5. To avoid any confusion, the component up until now associated with bulk nitride will from now on be referred to as sub-surface nitrogen. This distinction is made as for two reasons; firstly, we cannot know for sure if this component is a nitride; and secondly, sub-surface gives a more accurate description of the components location than "bulk." The nitrogen-containing chromium species that increase in relative intensity during the oxidation, previously referred to as surface chromium nitride (CrN) in previous work [90, 102], will be referred to as nitrogen-containing chromium species, or Cr(N) for short. The latter clarification relates to the fact that whilst we observe interaction of chromium and nitrogen at the surface, evidenced by changes in both the Cr 2p and N 1s spectra, there is not enough significant evidence that these species are pure chromium nitride and in fact could be complex chromium oxynitrides.

This decrease in chromium and nitrogen at the surface had a profound effect on the initial rate of oxidation at room temperature, as shown in Figure 4.6a, which shows the change in the intensity of the O 1s region as a function of oxygen exposure. We first note that the high chromium content surface (HC), with 32% chromium and 7% nitrogen (calculated composition from survey spectra is Fe–32Cr–8Ni–2Mo–7N (at%)), displays a very sharp initial rate of reaction until an exposure of approximately 10 L, after which it quickly tails off before saturating at around 25 L. This curve is similar to the one observed on the FeCrNi(100) sample, which also had a rapid initial rate of reaction before saturating at 10 L [90]. In contrast, a further eight sputtering (at 1 keV) and annealing (at 700 °C) cycles later, bringing the total to 16, we have a significantly reduced amount of chromium at the surface (LC), with 15% chromium and 2% nitrogen (calculated composition from survey spectra is Fe–15Cr–14Ni–2Mo–2N). The result is a significantly reduced initial rate of reaction and a much more steady climb to the saturation point, which, at around 80 L, is more than triple the amount of the previous saturation point when the HC surface was exposed to oxygen. Figure 4.6b may be considered as showing the rate of oxidation as a function of oxygen exposure. The blue line describes the rate of oxidation

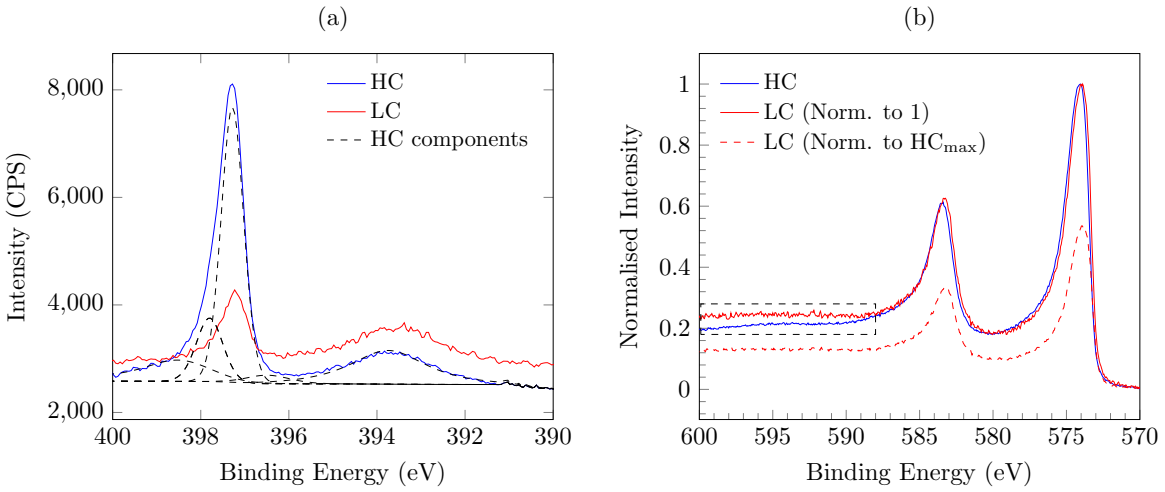

Figure 4.5: (a) N 1s spectra for the surfaces with a high chromium and nitrogen content (red) and low chromium and nitrogen content (blue). (b) Cr 2p spectra for the surfaces with a high chromium and nitrogen content (blue) and low chromium and nitrogen content (red). The black box indicates the difference in the background. The maximum intensity of each curve have been normalised to 1 to allow for better comparison of the shape.

for the surface that was initially high in chromium and nitrogen, and from that we observe a maximum rate of oxidation after an exposure of 5 L, after which there is a sharp decrease. After an exposure of 20 L the rate of change in the O 1s intensity falls to almost zero. Conversely, the red line in the same figure corresponds to the rate of oxidation for the surface that was initially low in metallic chromium and nitrogen, and shows a significantly lower, but more steady rate of oxidation. After an exposure of 5 L the rate of change in the O 1s intensity is approximately 3.5 times lower than the corresponding rate for the HC surface after the same exposure. Beyond 11 L, the rate of oxidation for the LC surface overtakes that of the HC surface.

As well as different kinetics, we also have an oxide film that significantly differs in composition. Figure 4.7 shows the high resolution XPS data recorded for the (a) Fe 2p (b) Cr 2p and (c) Mo 3d regions after 8 (left) and 16 (right) cycles, followed by RT oxidation. Table 4.1 gives the relative intensities of the components of the spectra. If we first compare the iron spectra, we can see that the two are rather comparable with similar ratios of metal to oxide. The oxide formed after 8 cycles, where the initial clean surface was high in chromium (HC), has a metal/oxide ratio of 0.92 ($\pm$0.08). Equally, in the case where the initial clean surface started with lower amounts of metallic chromium (LC), and therefore higher amounts of metallic iron, the metal/oxide ratio is slightly lower at 0.75 ($\pm$0.06). The intensity of the Fe 2p regions are comparable, with the total area of the Fe 2p region after 16 cycles (LC) 1.2 times greater than that of the 8 cycles

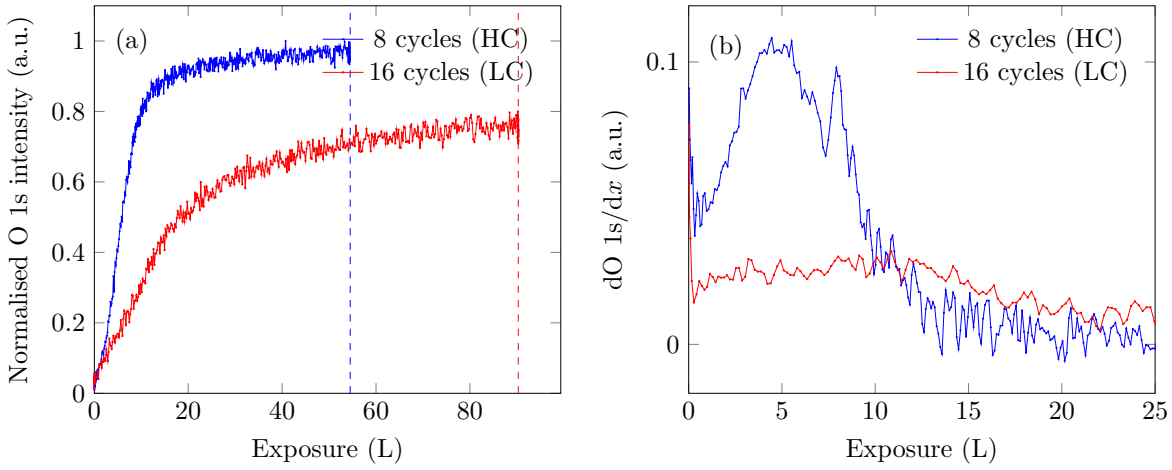

Figure 4.6: The effect of chromium and nitrogen surface amounts on the rate of oxidation using ultra-low pressures of oxygen at room temperature: (a) O 1s intensity as a function of oxygen exposure; (b) rate of change in O 1s intensity as a function of oxygen exposure (dO 1s/dx refers to the change in the intensity of the O 1s signal as a function of oxygen exposure).

(HC) spectrum, indicating a larger quantity of iron, providing that we assume that the oxides have the same structure. Next, we can compare the Cr 2p spectra shown in Figure 4.7b, where the differences are more notable. We first note that after 16 cycles of sputtering and annealing there is significantly less oxidised chromium (57% of total) compared to the oxide formed after 8 cycles (72% of total). The relative amounts of nitrogen-containing chromium species (Cr(N)) detected are similar, with a slightly increased amount found in the oxide formed on the HC surface. However, the second key difference to note is the Cr 2p's much smaller intensity in the case of the LC oxide. Comparing the areas of the two regions we see that the area of the HC oxide is 1.85 times greater than that of the LC oxide. The similar relative amounts of Cr(N), despite the much smaller total amount of chromium, further emphasises the link between the two. Then, very interestingly, in particular for corrosion scientists, is how all this affects the oxidation behaviour of molybdenum. The XPS spectra in Figure 4.7c clearly show that the molybdenum is more oxidised in the case where we have a more chromium enriched oxide. With reference to the values in Table 4.1, we see that in the HC oxide, metallic molybdenum makes up 49% of the analysed Mo 3d region, which is 18% less (67%) than in the LC oxide (the same difference as metallic chromium (18% vs 36%)). If we compare the two identified states of molybdenum, 4+ and 6+, we can see that there is a negligible difference in the relative amounts of Mo^{6+}. Instead, the relative amount of Mo^{4+} is much higher when we start with a surface enriched in chromium. The increased intensities of both molybdenum and iron after we start with a surface with a lower chromium concentration can perhaps just simply be attributed to the fact that the

chromium is replaced at the surface by more iron and molybdenum.

What is of more interest, is the behaviour of the elements themselves during oxidation. Why does less chromium at the clean surface result in a lower percentage being oxidised? And why does this affect the behaviour of molybdenum? The answer to the first question may relate to the ease at which metallic chromium can be activated to form Cr_2O_3. As previously discussed when reviewing the literature in chapter 1, nitrogen-containing chromium structures, found at the step edges of terraces, behave as a nucleation site for chromium oxidation on stainless steels [91, 92]. It is thought that the step edge localisation arises in order to relieve stress at the origin of the self-organisation of the vacancy lines. It is therefore possible that due to the significantly less chromium and segregation that occurs when we form the LC clean surface we have less of the active chromium-nitrogen compounds that form at the step edges and acts as a nucleation point for the formation of Cr_2O_3. This goes some way to explaining the reduced rate of reaction, as we have less Cr(N) —the site at which rapid oxidation takes place during the initial stages of the reaction [90–92]. This reduced rate of chromium oxidation may then in turn have an influence on how much of the metallic state is converted into oxide. Again referring to work by Ma et al. [90], it was shown that once the oxide formed on FeCrNi(100) is sufficiently thick, the rate of chromium oxidation quickly reduces (this is also corroborated later on in this work), with oxidation of iron becoming the dominant mechanism for growth of the layer. This part of the mechanism is explained by chromium's relatively poor atomic mobility through the oxide layer (assuming that for further oxidation it must migrate through the oxide lattice) and also how that metallic chromium will already be depleted due to formation of Cr_2O_3. Therefore, the retardation of the formation of chromium oxide during the early stages of oxidation results in a thicker, more iron-rich layer forming that prevents limits the amount of metallic chromium that can be oxidised. This hypothesis would suggest that the LC oxide would have a more homogeneous distribution of the oxidised elements when compared to that of the HC oxide, where one would expect more of an enrichment of Cr_2O_3 at the alloy-oxide interface. This could be investigated further using ToF-SIMS experiments.

The increased reactivity of metallic molybdenum is more difficult to explain, in part due to its low atomic percentage making it hard to identify when probing the surface with STM. The differences that arise in the oxidation behaviour of molybdenum may relate to the modified structure of the surface that is associated with the varying amounts of chromium present after annealing. Equally, the issue may be more complex and be related to synergistic properties between chromium and molybdenum. In order to better understand this issue, STM would be a very powerful technique. Unfortunately, over the time period in which this work was carried out,

Cycles	Relative intensity (±2%)								
	Fe	Fe^{2+}	Fe^{3+}	Cr	Cr^{3+}	Cr(N)	Mo	Mo^{4+}	Mo^{6+}
8 (HC)	48	7	45	18	72	10	49	35	16
16 (LC)	43	10	47	36	57	7	67	19	14

Table 4.1: Relative intensities for each component of Fe, Cr, and Mo for the oxide formed at saturation, for surfaces having previously undergone 8 and 16 cycles of sputtering and annealing.

several issues with the apparatus were encountered, resulting in limited use of the technique. Hopefully, future work will be able to elucidate further understanding on this interesting topic, as it has both relevance from a fundamental and corrosion science point of view, the latter due to the beneficial role that molybdenum plays in the passivity of stainless steels.

Table 4.2 shows the calculated composition of the oxide film and modified alloy region, as well as the estimated thickness of the former. These values were calculated using the single-layer model that is described in chapter 3. There is no dramatic difference in the calculated thickness of the oxide films, with 1.3 and 1.5 nm estimated for the LC and HC oxides, respectively. These values are similar to those reported on like surfaces that have been oxidised at RT [6, 14, 31, 88, 89, 102, 149, 150]. The calculated composition further demonstrates how the HC oxide is much more chromium rich at the point of saturation, with 40% of the relative concentration attributed to Cr_2O_3, which is more than double the relative concentration of the LC oxide (18%). The lack of chromium in the oxide film formed after 16 cycles is solely compensated by an increase in the relative amount of oxidised iron present, with no noted increase in the relative amount of oxidised molybdenum found in the film, despite the increased relative amount of oxidation that molybdenum undergoes. Nickel remains unoxidised in both cases. Nickel is found to increase its share of the overall relative concentration in the modified alloy region (when compared to the starting clean surface composition) in both cases. Equally, in both cases the amount of chromium in the modified alloy decreases as it is consumed during oxidation, with the effect much more exaggerated on the surface where we started with a high chromium content (HC=32% to 11%, LC=15% to 9%).

Some control of the surface composition could be kept, albeit at the expense of some time. It was found that by mechanically polishing the sample, or performing many(!) cycles sputtering at 5 keV, the composition would revert back to the high chromium content. This is consistent with the idea that the nitrogen that segregates along with chromium comes from the sub-surface and becomes depleted by diffusion. The multiple cycles lead to a depletion of nitrogen in this

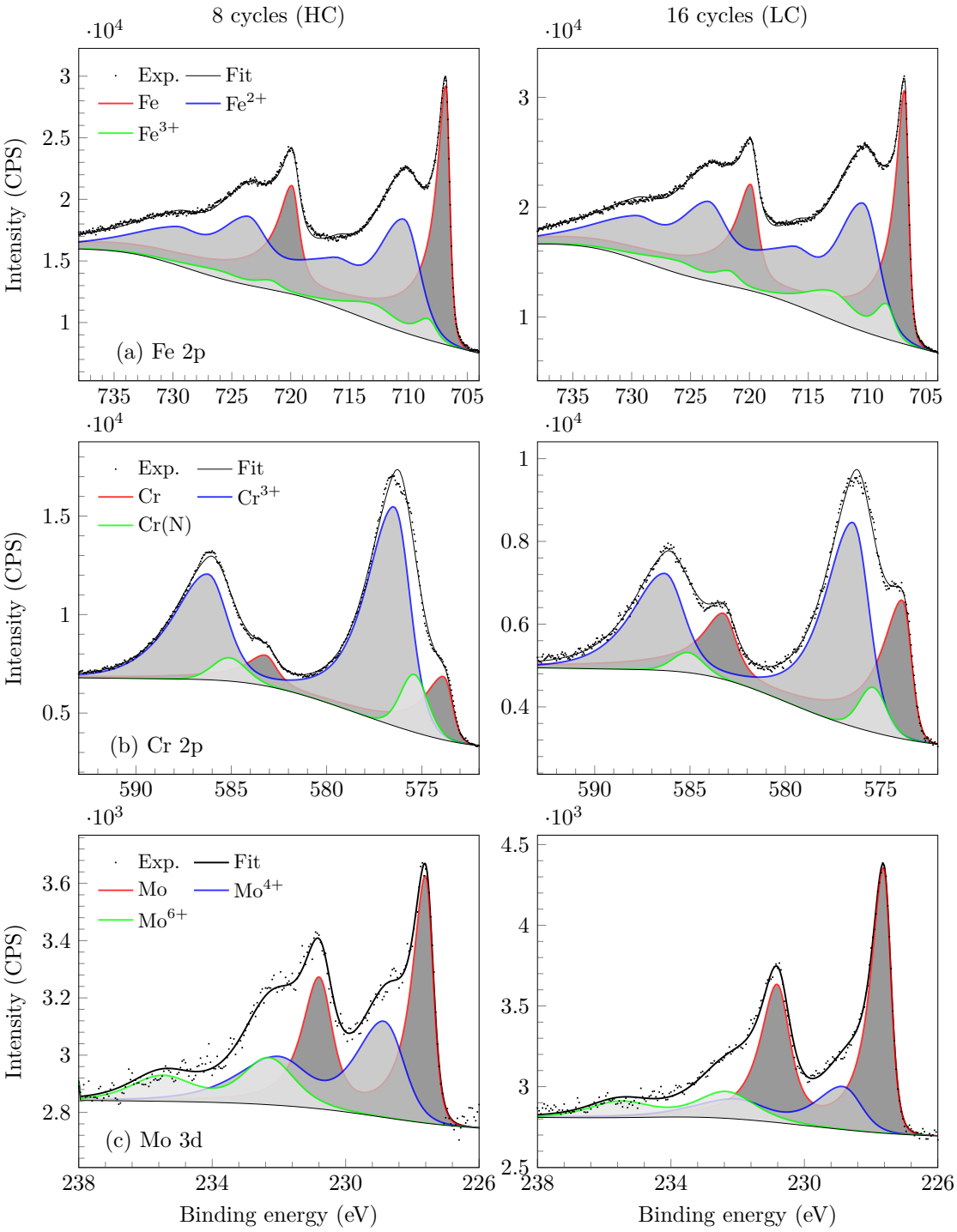

Figure 4.7: Comparison of (a) Fe 2p, (b) Cr 2p and (c) Mo 3d high resolution XPS spectra after 8 cycles (HC) and 54.5 L oxidation (left) and 16 cycles (LC) and 90.3 L oxidation (right).

Cycles	Thickness (nm) (±0.1)	Relative concentration (±2%)						
		Oxide layer			Modified alloy			
		Fe	Cr	Mo	Fe	Cr	Ni	Mo
8 (HC)	1.5	59	40	1	76	11	12	1
16 (LC)	1.3	81	18	1	72	9	17	2

Table 4.2: Thickness and composition of the oxide formed at saturation, for surfaces having previously undergone 8 and 16 cycles of sputtering and annealing.

region, however, it is still present deeper within the bulk. Similar observations were made by Burton et al [143]. By mechanically polishing the sample and/or sputtering in a more aggressive manner, i.e. at high energies, we remove the nitrogen depleted region as well as the top surface and gain access to the nitrogen rich region below from which segregated nitrogen can reach the surface.

This piece of work serves to highlight the importance of surface preparation and how seemingly small changes can have significant consequences. In order to achieve consistency and better understand later results it was decided that at the start of each experimental block we would, where possible, endeavour to start with a consistent surface composition and structure. A surface with a high chromium content was preferred as it is the natural reset point and is similar to the composition of the FeCrNi(100) sample previously analysed by Ma et al. [90].

4.4 Surface reconstruction

4.4.1 LEED

Figure 4.8a displays a typical LEED pattern, obtained using an electron energy of 120 eV, of the well organised and contaminant-free FeCrNiMo(100) sample. In this particular case, the surface was high in metallic chromium. The surface structure was found to have a $(\sqrt{2}\times\sqrt{2})$R45° reconstruction, which is indicated by the red square.

Figure 4.8b is a recorded LEED image of the same surface at 120 eV, but with a change in the position and angle of observation. This image has a doubled diffraction pattern, with no noticeable loss in the contrast of the image. This type of phenomenon typically suggests that the surface possesses a vicinal structure, observed locally in the present case. Figure 4.9 shows another LEED image of the FeCrNiMo, taken at an electron energy of 120 eV, but when the surface had a low metallic chromium (12.5%) and nitrogen (1%) content. It is shown that we still

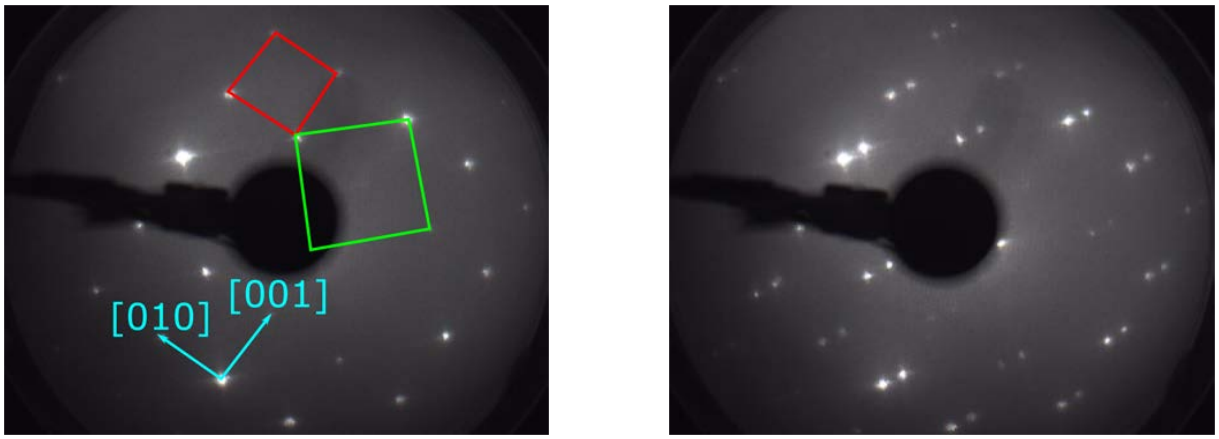

Figure 4.8: LEED pattern obtained using an electron energy of 120 eV of the sputtered and annealed FeCrNiMo(100), with a high metallic chromium content at the surface, showing: (a) $(\sqrt{2} \times \sqrt{2})$R45° reconstruction (marked by the red square) alongside the unreconstructed 1×1 structure (marked by the green square); (b) double diffraction pattern observed after changing the observing angle.

have the same $(\sqrt{2} \times \sqrt{2})$R45° reconstruction, although there is a clear rotation of the surface orientation. Whilst not investigated during the course of this investigation, this phenomenon was previously reported in the thesis of Li Ma [151] during her work on a FeCrNi(100) sample. In this work it was found that for the FeCrNi(100) sample, the angle of orientation relative to the horizontal axis decreased with an increased number of sputtering and annealing cycle. It should be noted that the FeCrNi(100) surface did not suffer from the dramatic changes in composition at the surface with the increased number of sputtering and annealing cycles, so it is unlikely that the differences in metallic chromium are the main reason for this change in orientation. One possible explanation given by Ma is that the top atomic plane is not in good agreement with the bulk lattice below due to screw dislocations. Given that the two samples were produced by the same team and using the same method, it is possible that the rotation may be related to the manufacturing process that causes the bulk orientation to not be in good agreement with the surface due to the production of defects that may result in screw dislocations.

4.4.2 STM

Figure 4.10a shows a typical STM image of the surface structure found present on the FeCrNiMo(100) sample when the surface possessed a high chromium (31%) and nitrogen (7%) content. The 100×100 nm image shows characteristic terraces, of nominal (100) orientation, where the width of the terraces ranges from 15–40 nm. The height of the steps is approximately 0.40 nm, which corresponds to around two atomic planes, as seen in the height profile across the

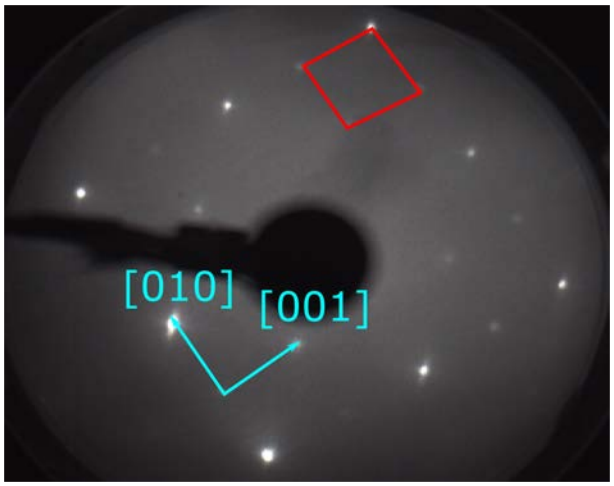

Figure 4.9: LEED diagram obtained using an electron energy of 120 eV of the sputtered and annealed FeCrNiMo(100), with a low metallic chromium content at the surface, showing a ($\sqrt{2}\times\sqrt{2}$)R45° reconstruction (marked by the red square).

terrace seen in Figure 4.10c, made after slop correction. These steps result in a misorientation of the surface of 0.9 ±0.1° with respect to the (100) plane. As shown in Figure 4.10c, there is no clear evidence on this surface of monoatomic multi-steps (but rather multi-atomic steps) between the terraces, such as the ones that were reported on the similar FeCrNi(100) surface, although this may be attributed to the poorer quality of resolution when the two are compared. When looking at step edge we observe bright spots (circled in Figure 4.10a) that are absent on the terrace structures. Whilst there is a small chance that this may be a different structure, it is in all likelihood from traces of contamination. Due to the previously mentioned difficulties with the STM equipment, it was not possible to probe the step edge structure with a high enough resolution to remark on any differences when the surface became depleted in chromium and nitrogen at the surface (LC). However, Figure 4.10b gives perhaps more clear evidence of a differing composition and/or structure at the step edge, with areas that differ in contrast to the rest of the terrace highlighted in blue. We also see more bright spots that dot the step edge. On the terraces themselves we can observe periodic lines along both the [010] and [001] directions. These lines are better highlighted in Figure 4.10b, where the distance between lines ranges from 2.6 to 5.1 nm, with the height profile suggesting that they are depressive in nature. This notable feature was ever present on the oxide-free surface, whether the amount of chromium was high or low. The lines are also apparent on the similar FeCrNi(100) surface [91, 92], although more periodic in nature and with fewer perpendicular lines. This difference could perhaps be explained by the slightly larger terraces present on this FeCrNiMo(100) surface, with the additional vacancy lines, along as well as across the terrace, present in order to reduce stress at

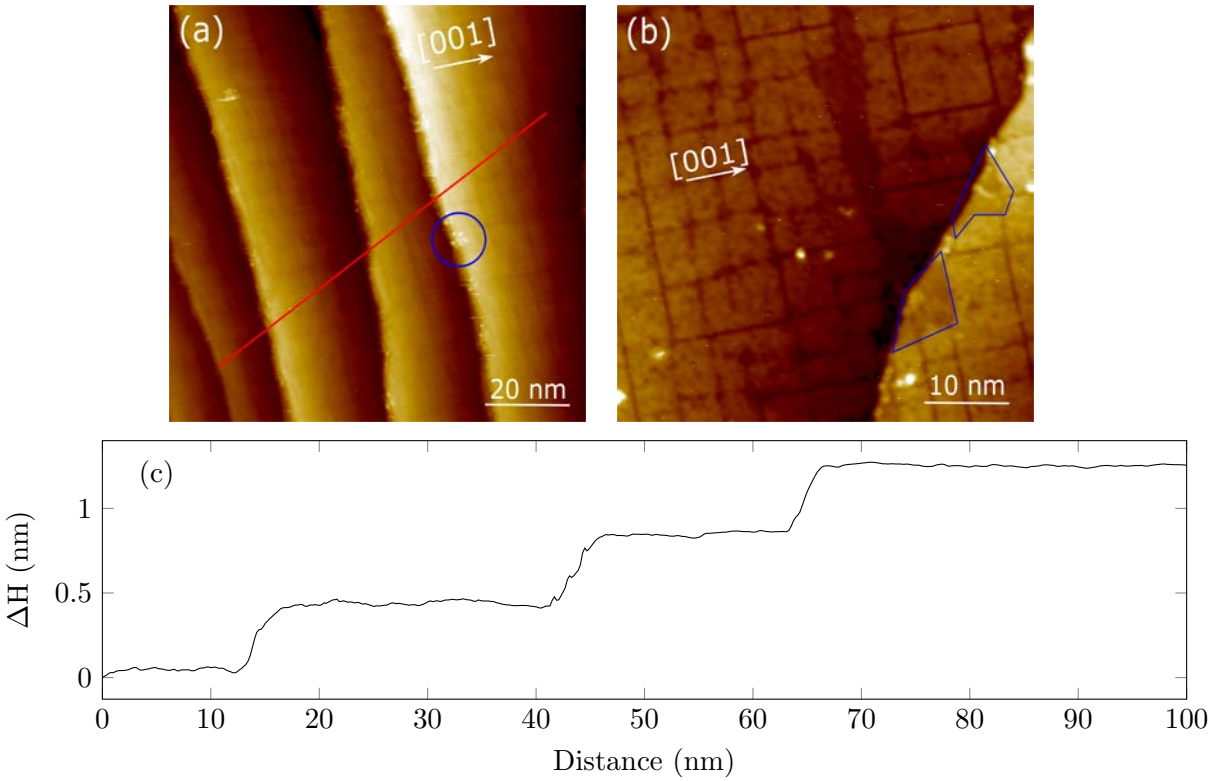

Figure 4.10: The structure of the terraces and steps formed on the FeCrNiMo(100) surface: (a) Terrace structure (100×100 nm, I=0.2 nA, V=0.7 V); (b) Perpendicular vacancy lines on the terraces (50×50 nm, I=0.2 nA, V=-0.1 V); (c) Height variation across the terraces along the red line in (a).

the surface.

Figure 4.11a shows an atomic resolution image of the FeCrNiMo(100) surface, featuring two bisecting vacancy lines. At the point where the two lines bisect, one remarks that the line going in the nominative [010] direction terminates, whereas the vacancy line that is directed along the [001] direction continues to propagate. Figure 4.11b is a depth profile bridging the vacancy line and confirms its depressive nature, with a depth of approximately 70 pm. This is somewhat deeper than the value of 50 pm that was reported on the FeCrNi(100) sample by Ma et al. [92], although the accuracy of this measurement may be limited by the sharpness of the tip. Whilst regarding the surface at such a small scale, one can observe that we have a variation in the brightness of atoms which is owed to the chemical contrast between iron, chromium, nickel and molybdenum, as suggested by the literature [152–154]. This contrast between different elements is a result of differing electronic structures [153]. We can see in the same figure that there are obvious height differences across the surface owed to the presence of different sized atoms. From this data alone, we can not specifically identify which atom is which with any certainty. Scanning tunnelling spectroscopy was attempted on a few occasions, but

with little to no success, due to a combination of unfavourable STM conditions and the complex nature of the technique. Further work using this technique could be of great value, in particular if the intention is to discover where molybdenum is found on the surface. Density functional theory (DFT) could be used in conjunction with this technique to aid in the interpretation of the observed chemical contrast [155]. The width of the depressions, determined once more from Figure 4.11b, is around 0.50 nm, which corresponds to 2–3 missing atoms. In certain areas, one can make out electronic density found inside the vacancy line, evidenced by the bright spots found inside the channel. Figure 4.11c is a height profile along the vacancy line, and from that we can observe that the electron density is, in this case, periodic, with a periodicity of 0.39 (±0.01 nm), which corresponds to approximately two missing atoms between the electron density. The periodic nature of the electronic density was not always present within the vacancy lines, with some possessing less electron density and with more of a random distribution. As confirmed by the LEED image back in Figure 4.8, this topmost plane is a reconstructed and denoted $(\sqrt{2} \times \sqrt{2})$R45° relative to the underlying unreconstructed (1×1) structure. A lattice parameter of 0.36 ±0.01 nm was determined, in line with literature reports [92, 156, 157]. Figure 4.12 shows a birds-eye view of the $(\sqrt{2} \times \sqrt{2})$R45° reconstructed surface (yellow square), present with a vacancy line, in which we see the underlying (1×1) non-reconstructed structure (green square).

4.5 Conclusion

Chromium and nitrogen were found to co-segregate to the surface during annealing of the FeCrNiMo(100) sample, a process necessary to obtain a well-ordered surface. Chromium appeared to segregate using two different mechanisms. The amounts of chromium and nitrogen that were found to segregate from the bulk to the surface, displacing metallic iron and nickel, were found to diminish over time with an increasing number of sputtering and annealing cycles. This change in the composition at the surface had significant consequences when it came to the rate of oxidation, with a maximum rate of three and a half times faster on the surface that had a higher starting amount of metallic chromium and nitrogen. This also lead to dramatic changes in the composition of the oxide formed at the saturation point after oxidation at room temperature, with a higher initial chromium content promoting an oxide that was richer in Cr_2O_3 and was accompanied with a larger proportion of metallic molybdenum being oxidised.

LEED and STM characterisation of the oxide-free surface showed that the topmost layer consists of a $(\sqrt{2} \times \sqrt{2})$R45° reconstruction with vacancy lines propagated along both the [010] and [001] directions. These perpendicular lines, that were sometimes found to have periodic

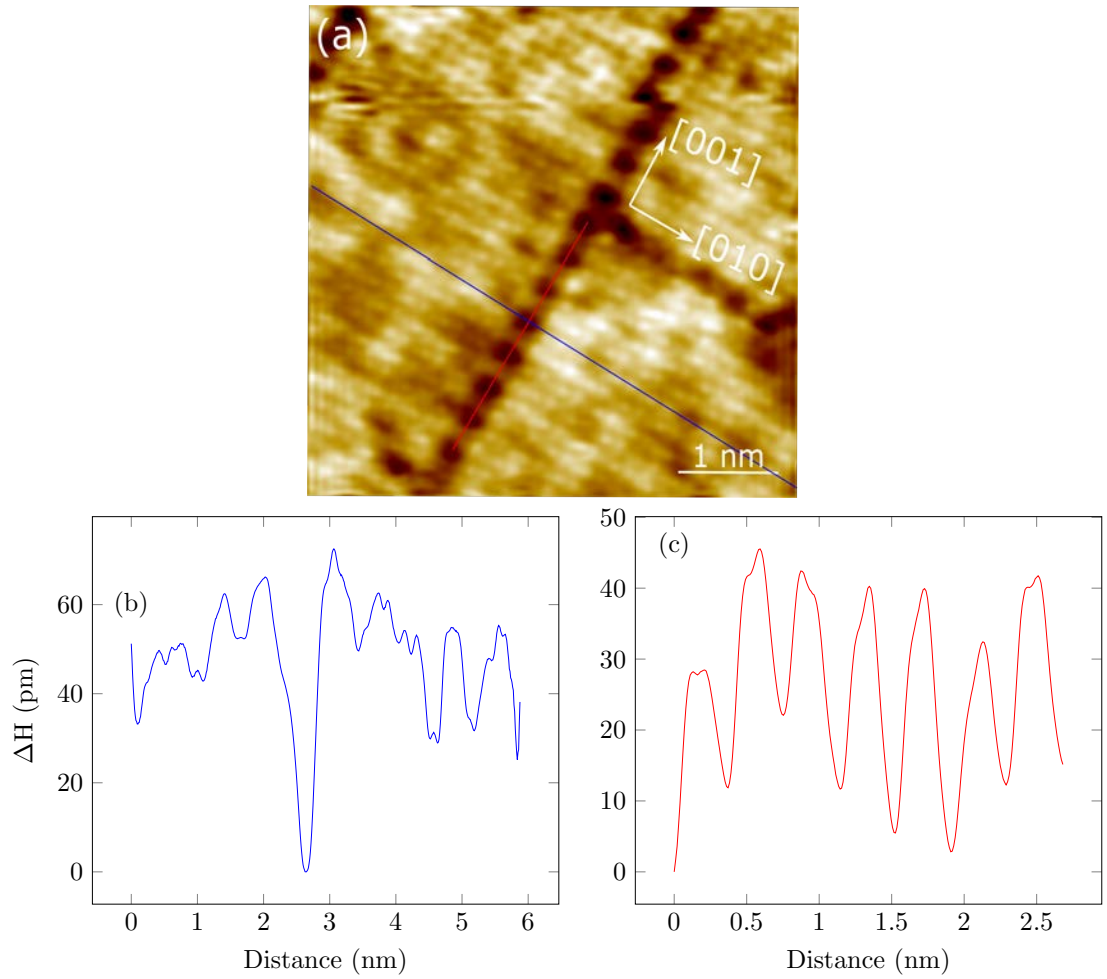

Figure 4.11: (a) Atomic resolution of the bisecting vacancy lines (5×5 nm, I=4.0 nA, V=0.01 V); (b) height profile across the vacancy line, recorded along the blue line in (a); (c) height profile inside vacancy line, recorded along the red line in (a).

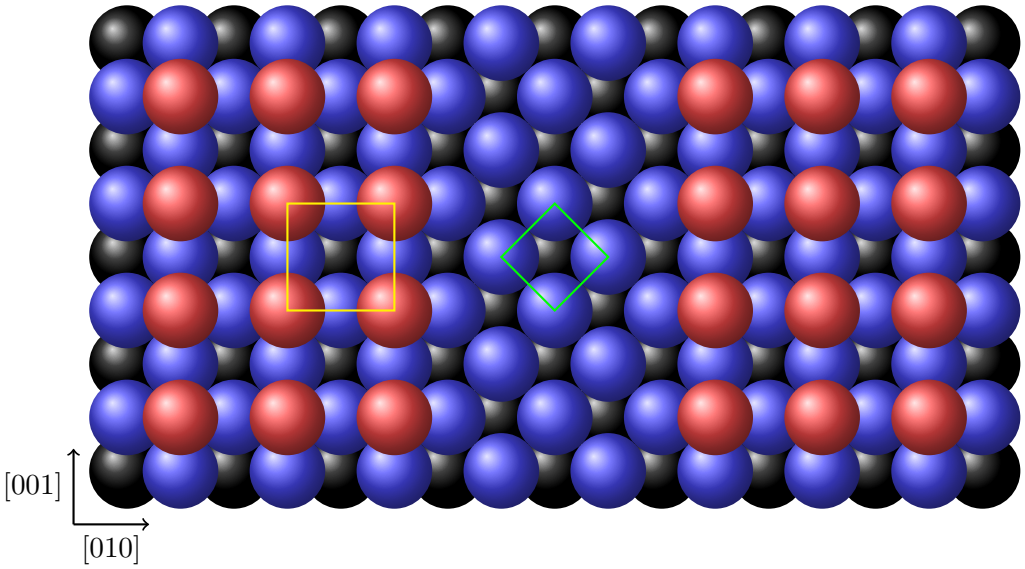

Figure 4.12: Structure of the reconstructed surface and of that found in the vacancy line, as seen from above. The green square serves to highlight the unreconstructed (1×1) structure present within the vacancy lines, whereas the yellow square denotes the reconstructed $(\sqrt{2} \times \sqrt{2})$R45° surface. The spheres depict Fe, Cr, Ni and Mo atoms indifferently.

electron density within them, were perhaps present in order to reduce the stress associated with the large terraces that exist on the surface. The steps that separated the terraces did not shown any signs of having an atomic multi-step structure, but rather multi-atomic steps. There were, however, some possible differences, with regards to the composition and structure, with images showing differences in the contrast and organisation of the surface at the edge of the steps.

CHAPTER 5

Oxide nucleation and growth mechanisms

This paper is based on the work that has been published in Applied Surface Science: B. Lynch, F. Wiame, V. Maurice, P. Marcus, "XPS study of oxide nucleation and growth mechanisms on a model FeCrNiMo stainless steel surface," *Applied Surface Science* (2021) 151681 [158]. https://doi.org/10.1016/j.apsusc.2021.151681.

The detailed mechanisms for oxide growth on molybdenum-containing stainless steels are not very well understood. In this chapter, the focus of the work is the study of nucleation and stepwise growth of the oxide layer that forms on a clean FeCrNiMo(100) surface during a controlled oxidation.

5.1 Abstract

High resolution X-ray photoelectron spectroscopy analysis has been used to investigate, in-situ, the mechanisms for oxide nucleation and growth on a FeCrNiMo single crystal alloy. Ultra-high vacuum conditions provided the ideal environment in which an oxide-free surface could be oxidised in a controlled manner, using extremely low pressures and step-wise exposures of oxygen. High resolution XPS spectra were used to follow the evolution of the key elements at step-wise intervals, allowing for detailed insights into the nucleation and growth mechanisms. Angular XPS analysis provided further information on the in-depth distribution and stratification of the oxide film.

Exposure (L)	RT		250 °C	
	45°	90°	45°	90°
0	✓		✓	
1	✓		✓	
3	✓		✓	
6	✓	✓	✓	✓
10	✓	✓	✓	✓
15	✓	✓	✓	✓
25	✓	✓	✓	✓
35			✓	✓
50			✓	✓
75			✓	✓
100			✓	✓

Table 5.1: List of oxygen exposures during step-wise oxidation of FeCrNiMo(100) at both RT and 250 °C and take-off angles recorded.

5.2 Experimental overview

The entirety of this work was performed on the ultra-high vacuum platform for surface analysis and electrochemistry shown in chapter 3, where the experimental procedures are discussed in more detail. Prior to oxidation, the sample was prepared using the previously discussed cycles of sputtering and annealing. Oxidation reactions were performed at pressures on the order of 10^{-8} mbar and in a step-wise and cumulative manner. The exact exposures, performed at both room temperature (RT) and 250 °C, are shown in Table 5.1.

5.3 Initial oxidation

A selection of high resolution XPS spectra recorded at 250 °C between 0–100 L are shown in Figure 5.1. Figure 5.1a shows Fe 2p spectra fitted with three components, metallic Fe, and oxidised Fe^{2+} and Fe^{3+}. Similarly, in Figure 5.1b, where the Cr 2p spectra are shown, we also identify three components which are assigned as metallic Cr and Cr^{3+}, present as both an oxide and the nitrogen-containing chromium species discussed in the previous chapter. With regards to the Mo 3d spectra shown in Figure 5.1c, we have metallic Mo, and oxidised Mo^{4+} and Mo^{6+}. Nickel was not found in an oxidised form at any point in the process, which can be expected

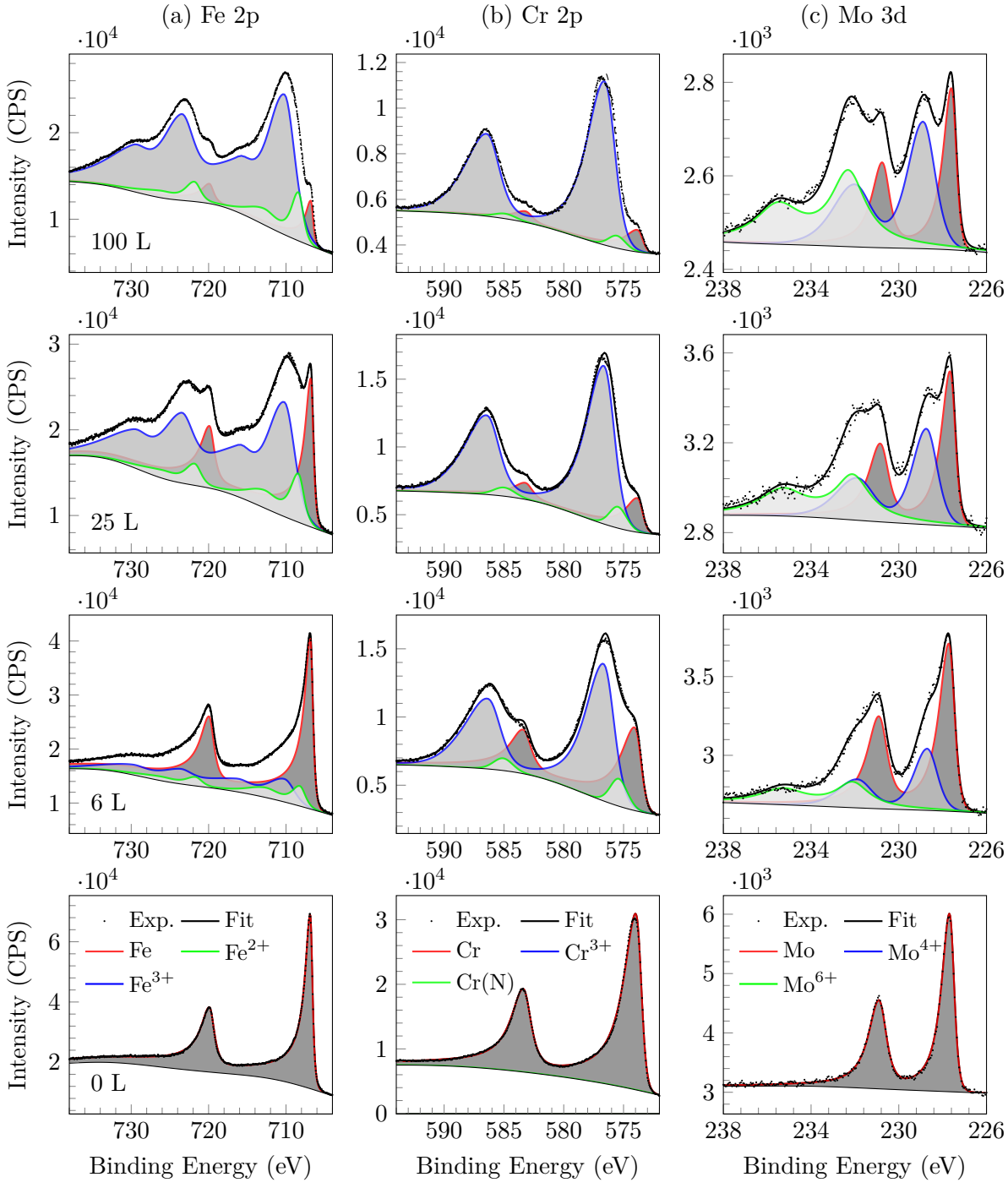

Figure 5.1: High resolution XPS spectra of (a) iron, (b) chromium and (c) molybdenum recorded after oxygen exposures of 0, 6, 25 and 100 L at 250 °C.

given its high enthalpy of formation relative to those of iron, chromium and molybdenum [159]. Ni 2p spectra, recorded after oxidation at 250 °C, can be found in the appendix. Peak fitting analysis of exposures 0–3 L was not performed as the uncertainty in the process was too large when compared with the small changes in the peak shape. Instead, a method of normalising and comparing the experimental curves obtained was applied, allowing us to observe the changes without direct assignment. In order to do this, the binding energy of all individual spectra were referenced to the Fermi level and a constant background associated with the flat, low intensity part of the spectra was subtracted. The maximum intensity was then normalised to one. If we first consider exposures made at RT, after 1 L of oxygen there is no apparent change in the shape of the iron (Figure 5.2a), chromium (Figure 5.2b) or molybdenum (Figure 5.2c) spectra. At 1 L, there is an increase in the intensity of the O 1s signal, indicating that oxygen is interacting with the surface. This change can be attributed to a mixture of adsorption and the beginnings of oxide nucleation at levels that are undetectable in the metallic spectra. The O 1s spectra for during the first 3 L of oxygen exposure can be found in the appendix. It is after we increase the exposure to 3 L that we observe the first changes in the iron and chromium spectra, with molybdenum remaining unchanged. At this stage it is impossible to relate these changes to particular chemical species with any great certainty. With regards to iron, it is highly likely that we are observing the nucleation of Fe^{2+} and Fe^{3+} oxides, such as FeO and Fe_2O_3, the two most common iron based oxides formed on stainless steels [7, 87]. However, the formation of mixed valence and non-stoichiometric oxides cannot be ruled out at such an early stage of the oxide growth process. Lin et al. [46] have previously suggested that under exposures of 50 L on polycrystalline iron surfaces the nucleating oxide of iron is FeO_x ($x = 0.67$–1) which becomes Fe_3O_4 after further exposure to oxygen. Ma et al. [90] have recently reported a ratio of 1.4 of Fe^{3+}/Fe^{2+} after an exposure of 3 L at RT on a FeCrNi(100) surface. Analysis of the chromium at such an early stage is even more difficult, owed to the complex nature of the chromium-nitrogen species, which form as a result of chromium and nitrogen co-segregation, the mechanisms of which were discussed in the previous chapter. XPS spectra of the N 1s region for the first three langmuirs at both RT and 250 °C are shown in Figure 5.3. Four main components have been assigned in the decomposition of each spectrum, as well as the presence of structures relating to Mo $3p_{3/2}$, which needed to be considered during the peak fitting process. Combing the results in chapter 3 with references to previous work [90–92, 100, 146, 160, 161] we can give tentative assignments of the N 1s components. N_{Cr} is noted as nitrogen-containing chromium species (corresponding with the Cr(N) observed in the Cr 2p spectra); N_i as interstitial nitrogen; N_s as sub-surface nitrogen; and N_m as minority contributions (such as N–O interactions). Figure

5.4a plots the evolution of the nitrogen components as a function of oxygen exposure at RT and from that we can see that on the clean surface, sub-surface nitrogen is by far the most common component, making up 67% of the total. However, upon the introduction of oxygen, a decrease of this peak is observed in conjunction with a rise in the relative amounts of Cr(N) and minority nitrogen, indicating that there is a change in the structure of the surface as a result of early oxidation. At RT, the change is initially slow before accelerating between 3 and 6 L, with no significant changes observed after 15 L — the point at which the uptake of oxygen is significantly reduced, as evidenced in Figure 5.5 which shows the O 1s intensity as a function of oxygen exposure. Once we have reached saturation of the surface, the sub-surface nitrogen component is now the smallest contributor to the N 1s peak, now making up 16%, which is more than four times less than on the clean surface. The increasing amounts of Cr(N) is reflected in the Cr 2p spectra, which adds to the uncertainty when fitting of the chromium components at less than 3 L. Therefore, we can only say that the changes in the chromium peaks at RT at these low exposures are due to the increasing presence of both chromium oxide (most likely Cr_2O_3) and Cr(N). At room temperature, there is no obvious change in the molybdenum spectrum during the initial stages of oxidation of the stainless steel sample.

At 250 °C, the rate of change of the spectra between 0–3 L is accelerated when compared to what was observed at RT, as shown in Figure 5.2, indicating a faster rate of reaction. This is also evidenced in Figure 5.5 where we have a higher relative intensity at 250 °C (0.29) than at RT (0.17) in the O 1s spectra after an exposure of 3 L. This result is contrary to the kinetic data shown in recent work on a FeCrNi(100) sample [90], where it was shown that the initial rate of reaction was quicker at room temperature owed to oxide growth being limited by oxygen adsorption. After an exposure of 1 L at 250 °C, there is clear evidence of changes in the shape of both the iron and chromium species, with molybdenum still remaining unchanged (Figure 5.2). The observed changes can once again be attributed to a mixture of oxide growth, and in the case of the chromium, a change in the surface structure and the small augmentation of the amount of Cr(N) present, the precise mechanisms of which are still to be determined and require further investigation. It is after an exposure of 3 L that we see more significant changes to the spectra. We should first comment on the nitrogen spectra in Figure 5.3, where the change in the amount of sub-surface nitrogen to Cr(N), minority and interstitial nitrogen is much quicker at this temperature than at RT. In Figure 5.4b, we can see that after 3 L Cr(N) makes up approximately 11% of the total nitrogen area, compared to around 4% at room temperature. This rapid onset of nitrogen-containing chromium species may go some way to explain the difference in reactivity, with such species being proposed as the nucleation site for

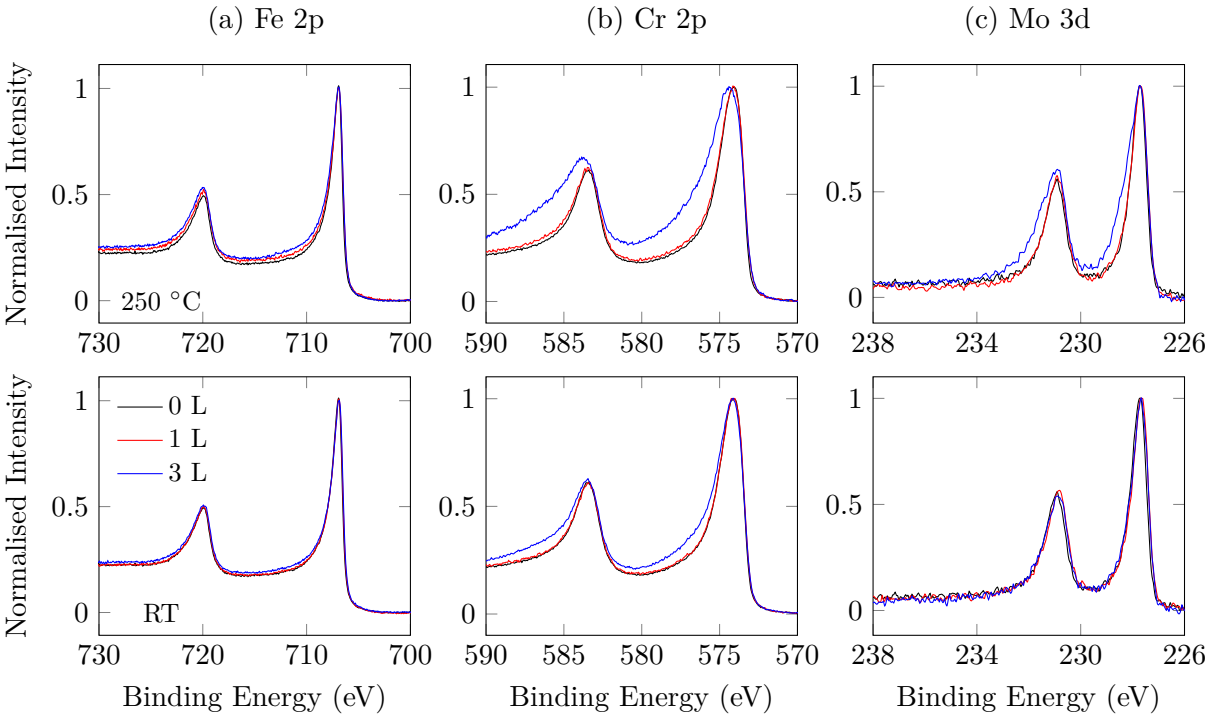

Figure 5.2: Comparison of peak shapes for (a) Fe 2p, (b) Cr 2p and (c) Mo 3d during the first 3 L of oxygen exposure at RT (top) and 250 °C (bottom).

Cr_2O_3 [91, 92]. As a result, significant changes are observed in the chromium spectrum. We notice further change in the shape of the iron spectrum at binding energies associated with that of iron oxide, after an exposure of 3 L, which indicates further nucleation of iron-based oxides. It is at this point, after chromium and iron oxidation have already begun, that we see the first notable changes in the molybdenum spectrum in Figure 5.2c, with an asymmetric broadening of Mo 3d peaks at higher binding energies relative to the metallic component at 227.6 eV, indicating that oxide formation has begun. The approximate position would indicate that it is a Mo^{4+} oxide; we would expect Mo^{6+} species to influence the shape of the curve at higher binding energies relative to that of what we observe.

5.4 Evolution of the elements

At exposures greater than 3 L, we can have more confidence in the assignment of changes in the XPS spectra. Figure 5.6 shows the evolution of the relative intensities of (a) iron, (b) chromium and (c) molybdenum as a function of the oxygen exposure. We shall first consider the evolution of the elements at room temperature. As discussed above, Cr^{3+} is owed to the presence of Cr_2O_3, although mixed oxide species cannot be discounted. At no point in the process, at both RT and at 250 °C, is chromium found in its +6 oxidation state. If it were present, we would

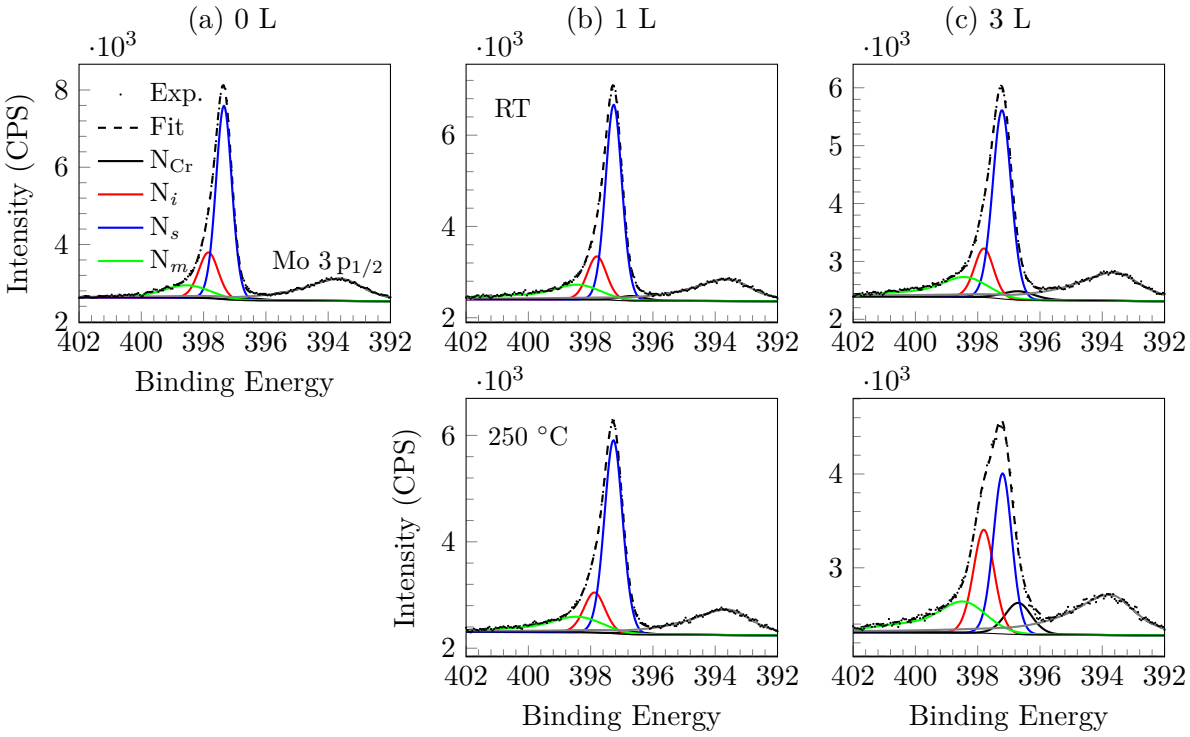

Figure 5.3: High resolution XPS spectra of the N 1s region during the first 3 L of oxygen exposure at both RT (top) and 250 °C (bottom), showing the four identified components, N_{Cr} (nitrogen-containing chromium species), N_i (interstitial nitrogen), N_s (sub-surface nitrogen) and N_m (minority nitrogen).

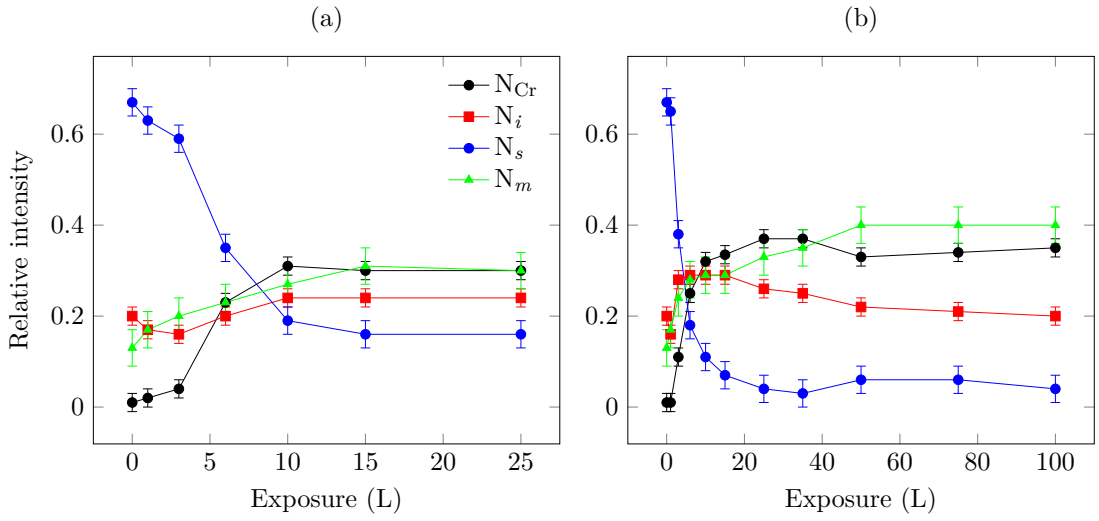

Figure 5.4: Evolution of relative nitrogen component intensities as a function of oxygen exposure at (a) RT and (b) 250 °C.

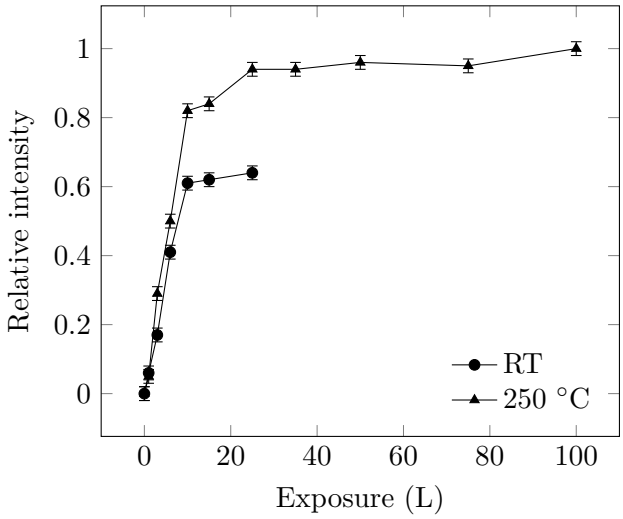

Figure 5.5: Relative intensity of O 1s signal plotted as a function of oxygen exposure at both RT and 250 °C. The O 1s intensities were normalised to the area of the O 1s peak after an exposure of 100 L at 250 °C.

expect a peak at around 580 eV. The growth of Cr_2O_3 stops, or at least significantly slows at 10 L, as beyond this point we observe no significant changes in the spectra. Equally, the amount of Cr(N) at the surface reaches it maximum relative intensity between 6 and 10 L before levelling off. As Cr(N) is present at the outermost surface of the oxide-free alloy, on top of which the oxide will grow, and is considered as a nucleation site [91,92], one's immediate thought may be to expect a decrease in the relative amount of Cr(N) detected. We can consider a few possibilities as to why this is not the case. Firstly, it may be due to the morphology of the oxide, with it being previously shown that the surface is not a completely homogeneous oxide layer but rather islands of oxide [91], suggesting that we will still have large areas of the surface with Cr(N) at the outermost surface. Secondly, rearrangement of the surface may continue beyond the early phase, resulting in steady state production of Cr(N) at the surface, which then stops as the surface becomes saturated with oxygen. Figure 5.6b shows that upon saturation with oxygen, metallic chromium represents 25–30% of the overall intensity associated with chromium. Iron is less readily oxidised than chromium at RT, with approximately 70% of the intensity of the iron spectrum being attributed to its elemental form. Fe^{3+} is found to be more common than Fe^{2+} at exposures beyond 6 L. In the case of molybdenum, two oxidation states are observed, those of Mo^{4+} and Mo^{6+}, with the former being found in a larger amount beyond exposures of 10 L. The most two common oxides associated with these oxidation states are MoO_2 and MoO_3. At saturation metallic molybdenum makes up around 52% of the total intensity.

Figure 5.6 shows that at 250 °C, we observe significantly more oxidation of the metallic

components. Once more, chromium is only found in one of three states — metallic Cr^0, oxidised Cr^{3+} and Cr(N). The oxide to metal ratio has an initial rapid increase during the first 15 L, before a significant reduction of the rate of oxidation. The Cr(N) signal is at its maximum relative intensity between 6 and 25 L before it begins to decrease due to attenuation of the signal caused by growth of the oxide on top, indicating that the Cr(N) species are mainly present close to the oxide-alloy interface. A steady-state supply production of Cr(N) that is converted into chromium oxide cannot be ruled out, however this is unlikely due to the relatively small amounts of nitrogen that segregated towards the surface. As previously stated, the signal associated with N_s decreases much faster at 250 °C than at RT, with this factor being used to explain the enhanced reactivity towards oxygen during the nucleation period. We do, however, observe a similar trend in the evolution of the nitrogen species for both temperatures (Figure 5.4). In the two cases we observe a significant decrease of N_s with increased relative intensity of N(Cr), N_i and N_m. N(Cr), which is attributed to Cr(N) and forms at the oxide-alloy interface, decreases after 25 L owed to attenuation of the signal, with this behaviour also reflected in Figure 5.6b. Similar to what we saw at RT, Fe^{2+} is primarily formed during the initial stages of oxidation (0–10 L). Beyond these exposures at 250 °C, the relative amount of Fe^{3+} increases continuously, with the rate of its formation decreasing steadily after 15 L. This corresponds with a decrease in the relative amount of metallic iron, whilst that of Fe^{2+} remains stable. It is possible that the higher temperature promotes further oxidation of Fe^{2+} to Fe^{3+}, although, for this to be the case there is the requirement of Fe^{2+} being continuously formed from the metallic iron supply in the modified alloy region beneath the oxide film. Equally, it is possible that beyond this early nucleation period in which Fe^{2+} forms, metallic iron is directly converted to Fe^{3+}. Regardless of the mechanism, it is clear that oxidation at 250 °C allows for increased diffusion of the iron through the oxide, resulting in an increase in the amount of oxide species present upon oxygen saturation. The two oxides of molybdenum behave differently to those of iron. In this case, the relative intensity of both Mo^{4+} and Mo^{6+} shown in Figure 5.6c increases steadily, with the ratio of the former to the latter always between values of 1–1.3 at exposures of 6–100 L. The ratio decreases slightly as the oxygen exposure increases, however, not as significantly as seen in the case of iron. Given that at an exposure of 3 L at 250 °C we attribute changes in the molybdenum spectrum to Mo^{4+} with no Mo^{6+} character, it could be suggested that in the case of molybdenum the metal is first converted into Mo^{4+} which is then further oxidised at higher exposures of oxygen. For all three elements we observe a decrease in the intensity associated with the metal which is owed to attenuation of the signal by the growth of the oxide.

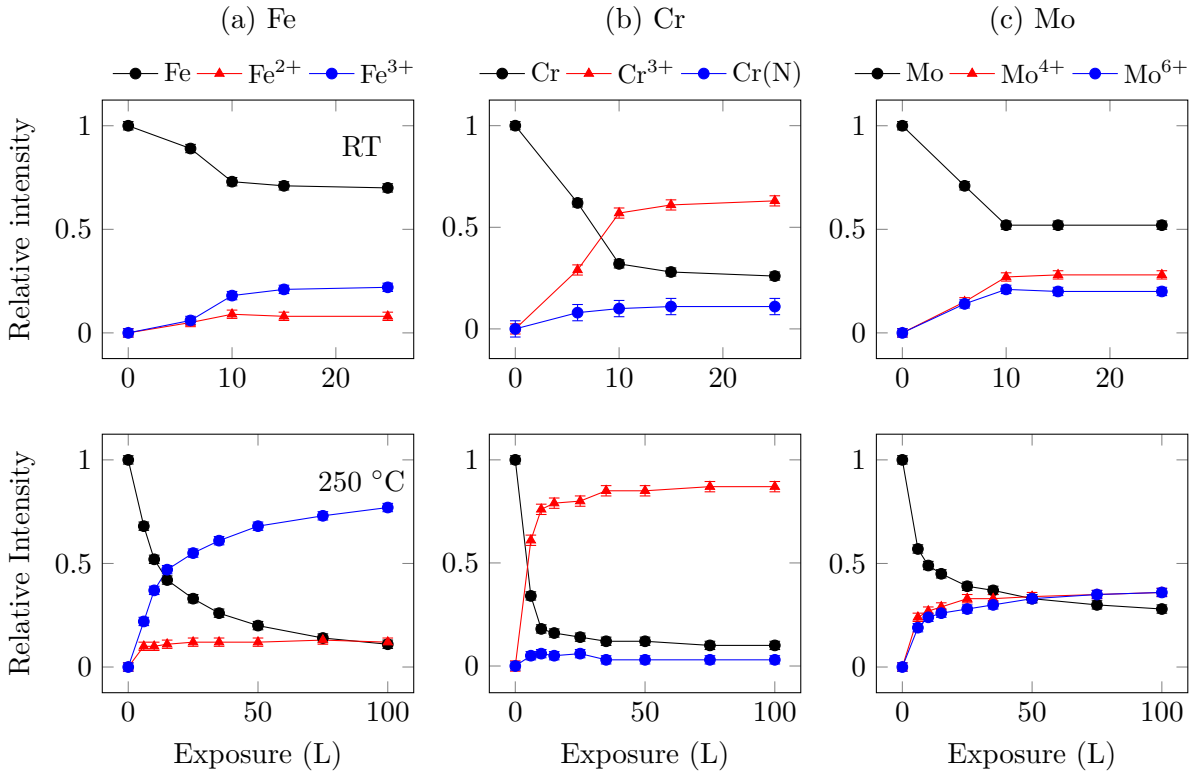

Figure 5.6: Evolution of (a) iron, (b) chromium and (c) molybdenum at RT (top) between 0–25 L, and 250 °C (bottom) between 0–100 L oxygen exposure at a 45° take-off angle.

5.5 Composition of the oxide layer

Previous work has shown that there are no defined layers formed within the oxide layer on austenitic stainless steels [90, 93, 99, 100]; however, layered models have frequently been used in order to describe the system in more depth with regards to their thickness, stratification and composition [31, 90, 101, 158, 162]. It is important to note that the following work does not account for the heterogeneities, both morphological and chemical, of the surface which have been shown to form [91, 102]. These heterogeneities may lead to differences in the calculated and actual thickness of the film which in turn has an influence on the calculated composition. The simplified model, described in detail in chapter 3, assumes a homogeneous distribution of the species within the oxide film, and provides a good approximation of the composition, stratification and thickness of the oxide, which allows us to better understand the growth of the film. Figure 5.7 shows the variation of the composition of both the oxide film and the modified alloy underneath as a function of the oxygen exposure at both RT and 250 °C. At ambient temperature (Figure 5.7a), the oxide is found to be enriched in Cr^{3+}, with it making up approximately 48% of the film after an exposure of 6 L. At the same time the amounts of Fe^{2+} and Fe^{3+} are equal, each making up around 16%. Cr(N), assigned to the oxide layer, is at its

maximum percentage in terms of contribution to the overall composition of the film formed on top of the modified alloy after an exposure of 6 L. Oxidised molybdenum never goes above a few percent of the film's composition, indicating that at no point is it enriched. Between 6 and 15 L Fe^{3+} growth becomes more dominant and increases its overall percentage of the composition. At no point during the oxidation process is molybdenum found to be significantly enriched within the oxide film. At the saturation point we have an oxide film with the composition Fe–50Cr–2Mo, with a calculated thickness of 0.8 nm. Comparatively, when the oxide formed at 250 °C is of an approximate thickness of 0.7 nm (after an exposure of 6 L), the composition is calculated to be Fe–48Cr–2Mo, which is almost identical to the composition of the oxide of 0.8 nm thickness formed at RT. The composition of the modified alloy at RT, displayed in Figure 5.7b, is found to be initially rich in chromium as a result of the annealing process carried out to prepare the clean surface prior to oxidation. This metal is quickly consumed during the early stages of oxide formation and at 10 L the chromium contribution to the modified alloy has reduced from 31% on the clean surface to just 14%, which is much closer to that of the bulk amount. As the intensity of the metallic chromium diminishes, that of the iron increases, reaching a peak contribution of 76%. Concurrently, we begin to see the modified alloy become enriched in metallic nickel, which is owed to the fact that iron and chromium from the alloy are being transported through the oxide film and oxidising. At the saturation point, the modified alloy has the a composition of Fe–12Cr–10Ni–2Mo.

Similar behavioural patterns can be seen during the first 6 L of oxygen exposure at 250 °C in Figure 5.7c, with chromium oxide making up 45% of the oxide film. Whereas at RT we saw equal amounts of Fe^{2+} and Fe^{3+} at this exposure, the evolution is different at the higher temperature, now with significantly more Fe^{3+}. The relative amount of Cr(N) peaks at low exposures of oxygen before reducing to negligible amounts. Beyond an exposure of 6 L, the formation of Fe^{3+} oxide becomes dominant, aided by the increased mobility of metallic iron through the oxide lattice. The relative amount of Fe^{2+} remains stable as the oxygen exposure increases. Once again, no enrichment of molybdenum is observed. After a 100 L exposure at 250 °C, the composition of the oxide film was Fe–19Cr–1Mo. The thickness of the film was calculated as 2.1 nm (±0.1 nm), which is similar to values reported on comparable surfaces [90, 101, 158]. The calculated composition suggests that oxidised molybdenum is not enriched within the film. With regards to the composition of the modified alloy at 250 °C in Figure 5.7d, we essentially see a continuation of the trends exhibited at room temperature where we have the initial decrease in the relative amount of chromium in conjunction with an enrichment of iron and nickel. Beyond 6 L, when growth of iron oxide begins to dominate and metallic iron is consumed, the lack of

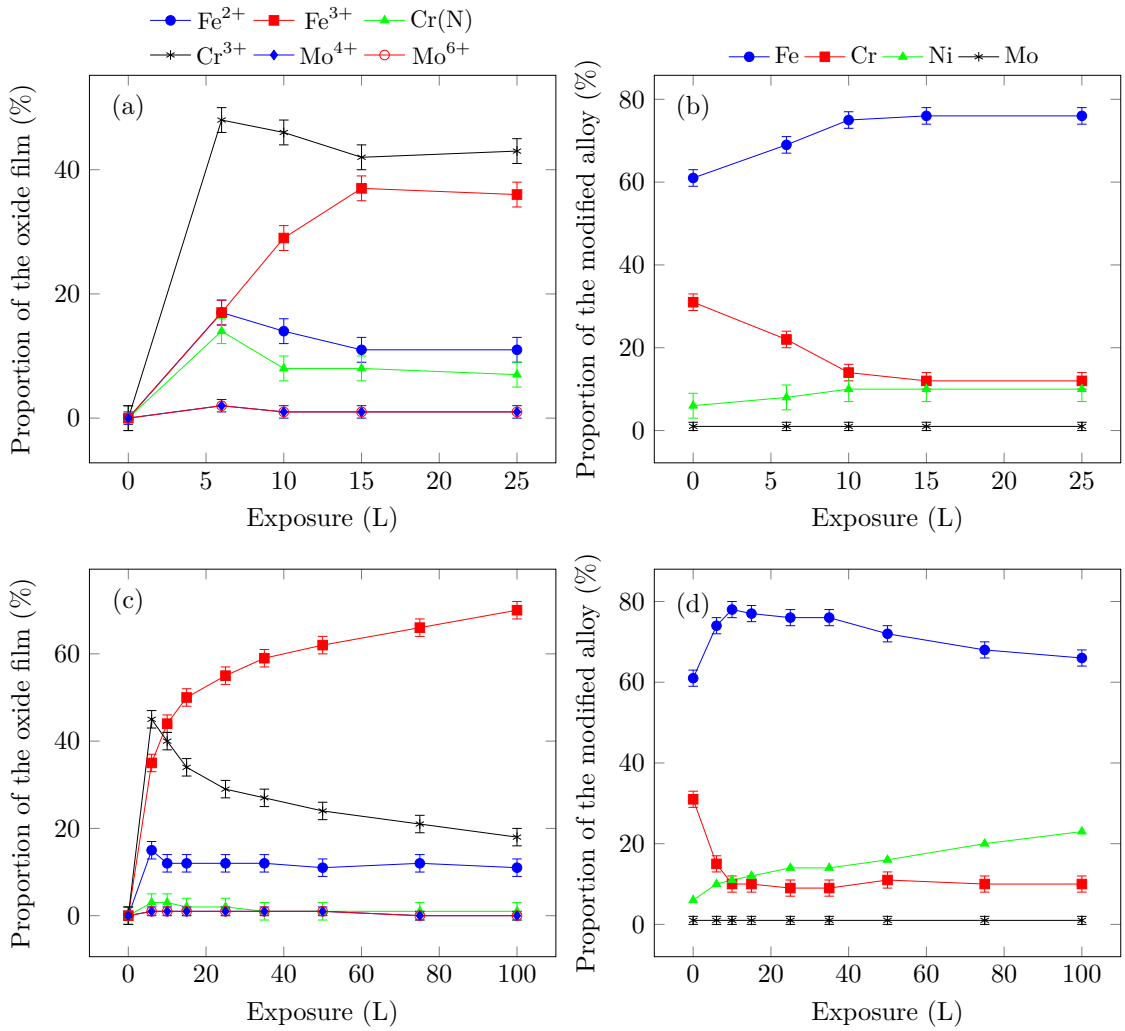

Figure 5.7: Composition of the (a) oxide at RT, (b) modified alloy at RT, (c) oxide at 250 °C, and (d) modified alloy at 250 °C, as a function of oxygen exposure.

nickel oxide formed results in a significant enrichment of the metal underneath the oxide film. After a 100 L exposure at 250 °C, the composition of the modified alloy was Fe–10Cr–23Ni–1Mo, indicating that further oxidation of 316 stainless steel samples increases the amount of metallic nickel enriched in the modified alloy region.

Angular analysis of the high resolution spectra, carried out at photoelectron take-off angles of 45° and 90°, was performed to verify the in-depth distribution of the elements within the oxide film. Figure 5.8 shows composition of the oxide film as a function of oxygen exposure at 250 °C, at both take-off angles. If the oxides were completely homogeneous, we would expect the same results regardless of the angle, however, here this is not the case, indicating that the in-depth distribution of the oxidised species is somewhat heterogeneous. This suggests that the model used to estimate the thickness and composition of the film is imperfect, however, the differences in the results are not significant enough that the model is not a good approximation.

By decreasing the take-off angle we become more surface sensitive and therefore would expect species found closer to the surface to have a higher relative intensity than at larger angles. The opposite can be said in that we would expect to see a decrease in the relative intensity for species found closer to the alloy-oxide interface. From the data in Figure 5.8, we can see that Fe^{2+} is more enriched closer to alloy-oxide interface, as evidenced by the fact that we have a consistently stronger intensity when probing deeper into the surface. This can be combined with what was shown earlier where it was suggested that Fe^{2+} is formed early on in the oxidation process before growth of the oxide film is dominated by Fe^{3+}. This claim is further backed up when we see that Fe^{3+} is more enriched in the outer part of the oxide film. Chromium oxide is also found more enriched closer to oxide-alloy interface, once more evidenced by the fact that we have a decreased relative intensity when using a more surface sensitive angle. Again referring back to earlier in the text, this is perhaps not too surprising seeing as it was shown that chromium oxide growth dominates the initial stages of oxidation. The data relating to distribution of Cr(N) suggests that it too is found enriched at the alloy-oxide interface, as we would expect based on previously shown data, although given the relatively small amounts present beyond 15 L the uncertainty using this method is significant. The two angles were not enough to suggest that molybdenum is found enriched at any part of the oxide film, although we were able to compare the relative ratios of Mo^{4+} to Mo^{6+} at the two angles and it showed that the two oxides are equally distributed within the film. These angular measurements suggest that oxide growth proceeds via outward cation diffusion, which is in line with reports made by Wang et al. [163] when investigating oxide growth on a FeCrNi alloy.

Based on all these observations and previous work on other model stainless steel samples, it is possible to propose a mechanism for the very initial stages of oxidation of FeCrNiMo stainless steels, the first reported of its kind. Upon introduction of oxygen, the clean and well-organised surface enriched in chromium and nitrogen as a result of elemental segregation caused during the annealing process, is modified due to the formation of nitrogen-containing chromium species that behave as nucleation sites for growth of chromium oxide, most likely Cr_2O_3. During this initial nucleation phase, we also observe growth of iron oxide, with iron found in both the +2 and +3 oxidation state. The results suggest that the oxidation of molybdenum is delayed until after the process has already begun on iron and chromium. Once the oxide film becomes sufficiently thick, the growth of the oxide film is increased thanks to augmentation of the amount of Fe^{3+} oxide which may be directly oxidised from the metal or via further oxidation of Fe^{2+}. Once an oxide thickness of approximately 0.8 nm is reached, which in this case corresponds to an exposure between 10–15 L, transport of iron through the oxide film is no longer feasible in the

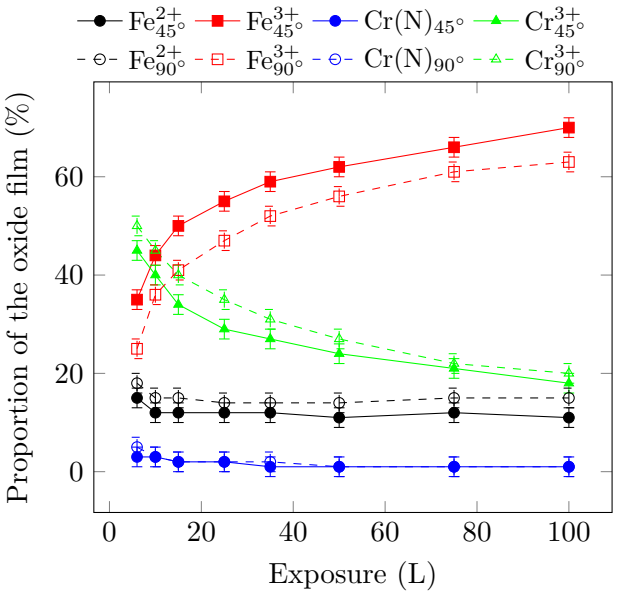

Figure 5.8: Composition of oxide film at 250 °C as a function of oxygen exposure at 45° and 90° photoelectron take-angles.

given conditions and the surface saturates. At 250 °C, the initial oxide growth follows a similar regime; however, the higher temperature allows for increased mobility of the atoms through the oxide film which results in further oxidation of the sample, which at this point can mainly be attributed to oxidation of iron. As the thickness of the oxide increases even at these elevated temperatures atom transport through the oxide lattice becomes difficult and the rate of oxide growth falls dramatically.

5.6 Conclusion

XPS high resolution, angular and in situ analysis has been used to provide unprecedented insight into the mechanism for very first stages of oxide growth on an FeCrNiMo austenitic stainless steel. The initial stages of oxidation result in rearrangement of the surface and the formation of Cr(N) species that behave as nucleation sites for growth of Cr_2O_3. Iron oxides, present as both Fe^{2+} and Fe^{3+}, are found to nucleate at the same time as as those of chromium. Initial oxidation of molybdenum was found to occur after these two elements had already begun to oxidise. At no point was nickel found in an oxidised form within the oxide film, however, metallic nickel became more enriched within the modified alloy region as the oxide grew thicker. The initial stages of oxidation follow standard thermodynamic principles, however it is once the oxide film becomes significantly thick that kinetic parameters become the presiding factor with the iron cation's increased mobility through the film resulting in the main contributor to

continued oxidation being Fe^{3+} oxide. Oxidation at 250 °C was found to result in a faster rate of oxidation which is attributed to the enhanced rate of surface reorganisation and production of Cr(N) that behaves as a nucleation site of oxidation of chromium.

Angular analysis was used in determining the in-depth distribution of the oxidised species within the oxide film. It was shown that Cr^{3+} and Fe^{2+} are found enriched closer to the modified alloy-oxide interface with Fe^{3+} found predominantly at the outer portion of the film. Oxidised molybdenum was found as both Mo^{4+} and Mo^{6+}, with neither found to be enriched or depleted at a given depth within the film.

RT oxidation resulted in surface saturation after a total oxygen exposure of between 10 and 15 L, with the composition of the oxide determined as Fe–50Cr–2Mo. At this stage the thickness was found to be approximately 0.8 nm. The rate of oxidation at 250 °C significantly reduced between 15 and 25 L, with the oxide thickness determined as approximately 2.1 nm after an exposure of 100 L. The composition of the oxide at this stage was Fe–19Cr–1Mo.

The present work, focusing on the growth of the oxide on austenitic stainless steel, helps to build on the fundamental knowledge relating to how the oxidation mechanism prior to passivation can later influence the properties of the passive film formed on austenitic stainless steels.

CHAPTER 6

The role of pre-oxidation on passive film behaviour

This chapter uses results that have been published in Applied Surface Science: B. Lynch, S. Neupane F. Wiame, A. Seyeux, V. Maurice, P. Marcus, "An XPS and ToF-SIMS study of the passive film formed on a model FeCrNiMo stainless steel surface in aqueous media after thermal pre-oxidation at ultra-low oxygen pressure" *Applied Surface Science* (2021) 149435 [101]. https://doi.org/10.1016/j.apsusc.2021.149435.

6.1 Abstract

A combined XPS, ToF-SIMS and electrochemical approach was used to investigate how pre-oxidation carried out at 250 °C in controlled UHV conditions affects the corrosion behaviour, as well as the composition, thickness and stratification of the film in acidic environments when compared with a sample on which a native oxide was directly formed. A clean FeCrNiMo (100)-oriented surface, prepared under ultra-high vacuum (UHV), was exposed to ultra-low pressures of oxygen at 250 °C, forming a thin oxide film, rich in iron and chromium, as well as containing molybdenum. For comparison, a native oxide was formed on the same sample and subjected to the same electrochemical treatments. The Ar-filled glovebox, which is directly attached to the UHV system, allowed for electrochemical alterations to be carried out without exposure to ambient air. Voltametric experiments indicate that pre-oxidising at ultra-low pressures (ULP) of oxygen beneficially influences the corrosion behaviour, notably suppressing the activation peak prior to entering the passive region, aiding in protection against active dissolution during anodic passivation. ULP pre-oxidation at high temperature was found to cause significantly more

molybdenum enrichment when the sample was held at open circuit potential. Depth profile experiments provided evidence of a bilayer structure of the oxide film, with Cr_2O_3 enriched at the metal substrate-oxide interface, with oxidised iron and molybdenum found more readily in the outer region of the film, alongside any hydroxide species. The controlled pre-oxidation promoted enhanced dehydroxylation in the passive region resulting in a thicker inner barrier layer.

6.2 Experimental overview

For this section of work, both the platforms for surface analysis and electrochemistry and ToF-SIMS equipment shown in chapter 3 were used. More experimental details discussing the general procedures and techniques can be found in detail in the section 3.2.7. Transfer between the two UHV systems was performed without direct exposure to the air, with an argon-filled vessel being used to transport the sample between the two. The native oxide was formed after a five minute exposure of the clean sample, prepared under UHV conditions, to the glovebox environment. Levels of H_2O and O_2 in the glovebox were typically around 10 and 130 ppm, respectively. Longer exposures have not been shown to have any effect on the composition of the oxide [102]. The surface composition prior to formation of the native oxide, as determined by survey spectra, was Fe–28Cr–11Ni–1Mo–8N. The clean sample was also pre-oxidised in the UHV chamber at 250 °C in order to observe how the pre-passivation method altered the behaviour of the passive film formed in a 0.05 M H_2SO_4 electrolyte. Unfortunately, the surface composition prior oxidation in the ultra-low pressure (ULP) oxygen was comparatively low in chromium and nitrogen, with the composition calculated as Fe–14Cr–7Ni–2Mo–2N. As a result, an exposure of 750 L was required to produce a sufficiently thick oxide. This difference in starting surface composition is considered when interpreting the results.

6.3 Characterisation of the native oxide

6.3.1 XPS analysis

The native oxide, which can sometimes be referred to as the as-received passive film, was formed after exposure of the clean surface to the glove box environment for a period of five minutes. After the exposure, and subsequent oxidation of the surface, the now oxidised model stainless steel sample was placed back in the UHV chamber and analysed by XPS analysis. It is assumed that the surface is saturated with oxygen, which is not an unrealistic assumption, with it reported that exposure beyond five minutes did not result in any further change in the

composition of the oxide formed on a stainless steel surface [102]. This supposition allows for the comparison of the oxides formed at saturation after having undergone a controlled oxidation in pure oxygen at room temperature and equally after having been exposed to an environment with a significantly higher pressure of oxygen and traces of water. The high resolution XPS spectra of the native oxide, recorded at a take-off angle of 45°, are shown in Figure 6.1. The evolution of the relative intensities for the four elements are summarised at the end of the chapter in Table 6.1. If we first consider the differences in the behaviour of iron, we see that in the native oxide film a larger proportion of the metallic species has been converted to an oxidised form (57% oxidised) than on the ultra-low pressure (ULP) oxide formed at RT (30% oxidised) in chapter 5. Additionally, on the native oxide, we see the presence of a peak found at 711.8 eV, which is attributed to iron oxy-hydroxide (FeOOH), with similar binding energies reported for this species in the literature on similar surfaces [6, 101, 164–167]. This oxy-hydroxide was not observed in the ULP oxide due to the lack of water present in the UHV system. In both cases, Fe^{3+} is the more commonly found oxidised state, although the ratio of Fe^{3+} to Fe^{2+} is much higher in the case of the native oxide, owed to the further oxidation of the sample. The behaviour of chromium is similar in both cases, with comparable relative amounts of metal, 26 and 20% for the ULP and native oxides, respectively, present after saturation. Chromium-nitrogen species are once more found within the native oxide film (5%), albeit in a slightly reduced relative amount when compared to the ULP oxide (11%). This difference may be reflected by the smaller amount of segregated nitrogen on the clean surface prior to forming the native oxide. No chromium hydroxide formed in either case. The relative amounts of metallic (51%) and oxidised molybdenum (49%) are strikingly similar to the ULP oxide, with any differences well within the margin associated with the uncertainty. Interestingly, on the native oxide sample we observe for the first time the presence of oxidised nickel, albeit in a limited quantity, contributing 13% of the total relative amount present. Given the position of the binding energy, this species is most likely $Ni(OH)_2$ [69, 168, 169] that has formed due to the presence of water during the formation of the oxide.

The composition of the native oxide is Fe–37Cr–1Ni–1Mo, with a reported thickness of 1.5 nm, which is markedly thicker and more rich in oxidised iron than the oxide formed at saturation in the controlled UHV conditions, which boasted a composition of Fe–50Cr–2Mo and a thickness of 0.8 nm. There were no dramatic differences in the composition of the underlying modified alloy, which on the native oxide was found to be Fe–11Cr–14Ni–1Mo.

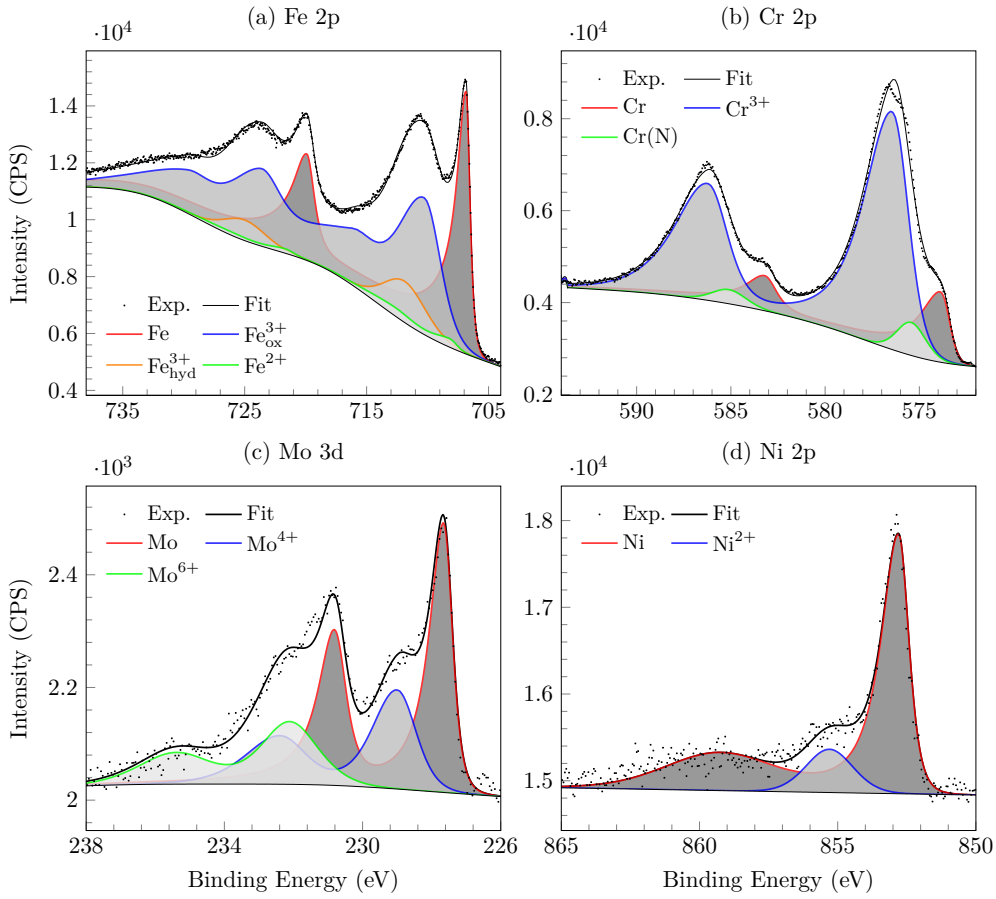

Figure 6.1: High resolution XPS spectra of (a) Fe 2p, (b) Cr 2p, (c) Mo 3d and (d) Ni $2p_{3/2}$ regions for the native oxide formed after the clean FeCrNiMo(100) sample was exposed to the glovebox environment, recorded at a take-off angle of 45°.

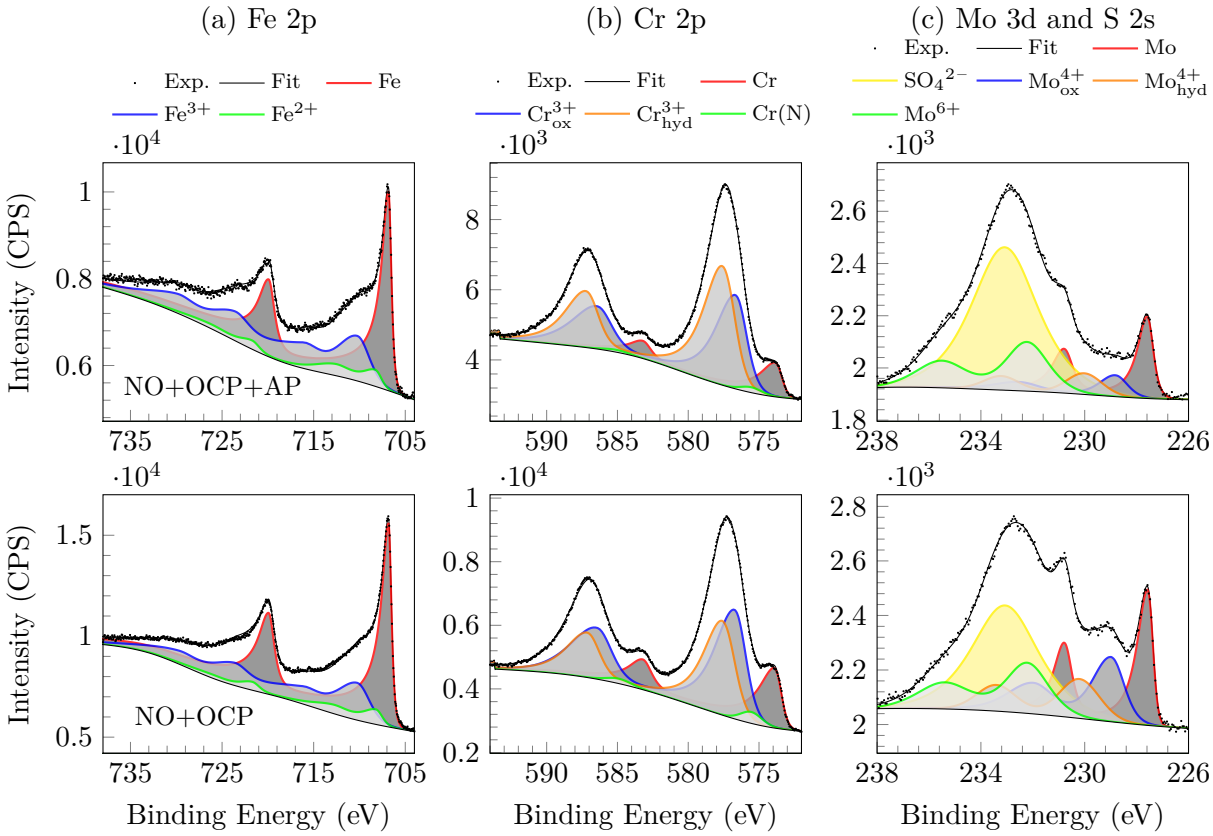

Figure 6.2: High resolution XPS spectra of (a) Fe 2p, (b) Cr 2p and (c) Mo 3d and S 2s regions for the native oxide + OCP (bottom) and native oxide + OCP + anodic passivation (top) formed on an FeCrNiMo(100) sample, recorded at a take-off angle of 45°.

6.4 Electrochemical passivation of the native oxide

The protocol for forming the passive film is well-described in the third chapter of this thesis. After formation and characterisation of the native oxide, the sample then underwent its first electrochemical treatment where it was held at the OCP for 30 minutes in 0.5 M H_2SO_4. After the oxide film formed at OCP had been characterised, the sample was then anodically passivated. The XPS spectra for the Fe 2p, Cr 2p and Mo 3d after the sample had undergone these treatments are shown in Figure 6.2. The nickel spectra are not shown, as any Ni^{2+} was found to have dissolved in the solution, leaving only the metallic peak. The reader is once more reminded that the relative intensities for the four elements can be found in Table 6.1 at the end of the chapter.

If we now consider the evolution of iron after the first exposure to the acidic solution, where it is simply held at the OCP, the primary thing to note is the increase in the relative amount of metallic iron present. This is owed to the preferential dissolution of Fe^{3+} in the acidic solution. This is in good agreement with other reports found within the literature [89, 102, 170]. Equally,

we no longer observe any of the FeOOH that was found present in the native oxide. At the same time we also observe a rise in the relative amount of Fe^{2+} present. This may be due to the fact that, if on the native oxide Fe^{2+} forms early on and close to the oxide-alloy interface, similar to what we saw during the step-wise growth of the oxide formed in UHV conditions, then it is shielded from dissolution by the Fe^{3+} layers that form on top. After the second treatment where we form the electrochemical passive film, oxide growth is now driven as the more oxidising conditions counteract the preferential dissolution of Fe^{3+} in the oxide layer. Subsequently, we observe a reduction in the relative amount of metallic iron when compared to the film formed at OCP (66% at OCP versus 59% on the passive film). The relative amounts of Fe^{2+} remain the same, in both cases the value is reported at approximately 7% of the total. The production of Fe^{3+} may be due to the direct result of oxidation of metallic iron or equally via further oxidation of Fe^{2+} which is being produced in a steady state manner.

After being held at OCP, the relative amount of metallic chromium remains the same at 20–22%, with the main change being the hydroxylation of chromium oxide, forming $Cr(OH)_3$. This observation is shared by multiple reports in the literature [17, 88, 89, 102]. The presence of Cr(N) species can still be noted, albeit in a slightly reduced amount (3%); however, after electrochemical treatment, fitting of the N 1s spectra became more difficult. As a result, the calculation for the amount of Cr(N) comes with a large uncertainty. Anodically passivating the surface results in further oxidation of metallic chromium, which now represents 13% of the total. Further hydroxylation (34 to 46%) of chromium oxide is observed which is contrary to what is often noted, where anodic passivation typically promotes dehydroxylation [17, 31, 88, 89, 162].

Analysis of the molybdenum spectra was complex owed to the presence of the overlapping S 2s region and the presence of sulphate anions ($SO_4{}^{2-}$). The area, A, of the sulphur 2s peak was fixed according to the corresponding area of the sulphur 2p region, as

$$A_{2s} \approx A_{2p} \frac{\sigma_{2s} \cdot T_{2s} \cdot \lambda_{2s\cdot}}{\sigma_{2p} \cdot T_{2p} \cdot \lambda_{2p\cdot}},$$

where the values for the photoionisation cross section, σ, the transmission of the analyser, T, and the inelastic mean free path, λ are known. Even with this calculation, which allows for a good approximation of the S 2s contribution to the spectra, the wide FWHM (2.9 eV) and often large relative amount in the region (60–78%) means that analysis of the molybdenum will have a much larger uncertainty than that of the iron and chromium. The potential ambiguity is fortunately somewhat reduced by the decomposition of the molybdenum spectra carried out in the early chapters of this thesis. Characterisation of the clean surface and oxides meant that the positions, FWHM, and line-shapes of the metallic Mo, and the Mo^{4+} and Mo^{6+} oxide peaks were already well defined before the added complexity of the overlapping S 2s region. So therefore, whilst

the large sulphur contribution will increase the uncertainty of the molybdenum decomposition, steps can and have been taken in order to reduce it. Even with the Mo, Mo^{4+}, Mo^{6+} and $SO_4{}^{2-}$ components fitted, the envelope was not a good match for the experimental data, with clear indication of an additional peak at 230.1 eV, which was only found to be present after exposure to the electrolyte. Given that in the S 2p region we only see spectral peaks that would seemingly correspond to strongly overlapping $2\,p_{3/2}$ and $2\,p_{1/2}$ $SO_4{}^{2-}$ components (see Figure 6.3), it is difficult to attribute it to a secondary sulphur species based on the information obtained from S 2p spectra. In addition, the sulphur 2s region has not been extensively characterised in the literature, with researchers typically preferring to analyse the 2p region when possible. A search of the literature where molybdenum is found in a passive film formed in a H_2SO_4 electrolyte, typically shows a single (or sometimes zero) S 2s peak(s) being assigned to $SO_4{}^{2-}$ anions at 233 eV (the same as in this work), albeit with an often lower relative intensity than in our case [88, 89, 162, 171, 172]. The significant intensity of the overlapping S 2s peak in our work may be a quirk of the home-made electrochemical cell set-up or inconsistencies with the rinsing of the sample. Work performed on an analogous FeCrNiMo polycrystal sample, by a different user, but who used the same cell, equally yielded high relative amounts of intensity related to sulphur, which indicates that the issue may be related to the UHV-compatible cell. With all this information taken into consideration, the most logical way to proceed is to assign this additional peak to an oxidised form of molybdenum. Molybdenum oxyhydroxide has been frequently shown to form in passive films [164, 171, 172]; however, the reporting of its binding energy is wide-ranging, from 229.5–231.1 eV [164, 171–174]. Whilst admittedly, there is no real need for a direct assignment, only that we attribute it to molybdenum in the passive film; given the lack of evidence for a secondary sulphur species in the S 2p region and no literature references, the component at 230.1 eV was assigned as molybdenum oxyhydroxide, with the corresponding Mo $3\,d_{3/2}$ component at 233.3 eV.

With that being said, we can now look at the evolution of the molybdenum spectra after electrochemical treatments. After being held at OCP for 30 minutes, we observe that the molybdenum is further oxidised, with the relative amount of metallic molybdenum reducing from 51% to 31%. This is contrary to the behaviour of iron and chromium who maintained and increased the relative amounts of metal found at the surface, respectively. Molybdenum in both its +4 and +6 oxidation states are found in equal amounts at around 25% of the total molybdenum concentration. The hydroxide species previously discussed contributes the least amount to the total concentration of the four species present. Upon anodic passivation of the surface, further oxidation of Mo^{4+} is promoted, with its share of the relative amount decreasing

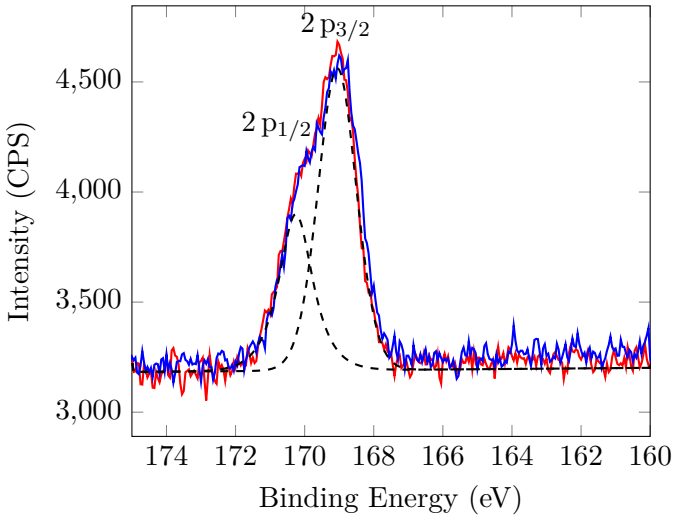

Figure 6.3: Sulphur 2p region when the unknown peak at 233.1 eV in the Mo 3d region is at its maximum (red) and minimum (blue) intensity.

to just 12%. In turn we see an increased share for Mo^{6+}, that now contributes 40% of the total molybdenum concentration. The relative amount of metal present remained the same, within the margin of error. The amount of hydroxide decreased slightly.

The thickness and composition model, described in chapter 3 and used for the step-wise oxidation reactions in chapter 4, can be applied to the electrochemically formed passive films as well as the native oxide. The simple model, taking into consideration the hydroxylated species, is shown as a reminder in Figure 6.4. As already discussed, the composition of the native oxide was determined as Fe–37Cr–1Ni–1Mo, with a thickness of 1.5 nm. Once the surface had been exposed to the electrolyte for the first time and held at OCP, the thickness of the oxide layer was found to decrease to 1.2 nm. This small change can be attributed to the dissolution of oxidised iron in the acidic medium. The composition, determined as Fe–57Cr–4Mo, reflects this observation, with clear evidence of chromium enrichment in the oxide layer. Molybdenum may also be seen as enriched within the oxide film, although one should be cautious with this result due to the high relative uncertainty. Anodically passivating the surface drives further oxidation, resulting in a thickening of the oxide layer to 1.5 nm. Despite iron being oxidised at a rate greater than that of its dissolution, chromium becomes further enriched within the oxide film. The reported composition is now Fe–67Cr–3Mo. Nickel became increasingly more enriched in the modified alloy region.

The thicknesses and compositions obtained from the single layer model are summarised at the end of the chapter in Table 6.2.

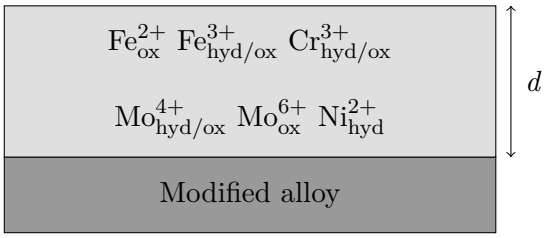

Figure 6.4: Single layer model for describing the passive film.

6.5 Corrosion behaviour

We can use voltammetry experiments to observe the corrosion behaviour within a range of conditions. Figure 6.5 compares two polarisation curves obtained on the FeCrNiMo(100) surface — one after pre-oxidation using ULP oxygen at 250 °C in the UHV (blue) and the second after being directly transferred to the Ar-filled glovebox at room temperature, forming the traditional native oxide that has previously been discussed (red). The two oxidised surfaces show the same corrosion potential, where $U_{corr} = -0.80 \pm 0.01$ V/Pt. This is expected for the same sample that is fully covered by surface oxide. The cathodic branches of the polarisation curves have a similar shape; however, the ULP pre-oxidised sample has a lower current density, indicating a slightly decreased proton reduction activity in the electrolyte. Similar behaviour in the cathodic branches has previously been reported [102].

The anodic branch shows that the current density of the ULP prepared surface is comparatively lower at the active-passive transition than that of the native oxide covered surface prior to passivation and with clear suppression of the active peak. Similar observations have previously been made when comparing native oxide covered and room temperature pre-oxidised ULP surfaces on polycrystalline 316L samples [101]. We can therefore deduce that the ULP pre-oxidised sample, prepared at 250 °C and exposed to an acidic electrolyte, is fully protected against active dissolution, much like the ULP pre-oxidised samples prepared at room temperature, whilst the native oxide covered samples, formed in air or an Ar-filled glovebox, remain only partially protected.

If one compares the densities of anodic charge transferred in the potential range of the active-passive transition, defined as U_{corr} to $U_{corr} + 0.20$ V, we obtain values of 0.265 and 0.458 mC·cm^{-2} for the ULP pre-oxidised and native oxide covered samples, respectively. From the charge transfer difference (0.193 mC·cm^{-2}), if one then assumes that the charge is completely associated with metal dissolution and that all elements dissolve as $M \rightarrow M^{2+} + 2\,e^-$, then we can estimate the amount of metal that was additionally lost by transient active dissolution in the case of the native oxide. By taking into account that the thickness of the (100) plane for

the *fcc* structure of the alloy is 0.18 nm, and that the atomic density is 1.55×10^{15} at·cm^{-2}, we arrive at a value of 0.07 nm, not taking account the stoichiometry of dissolution, which corresponds to less than one monolayer (0.38 ML) of additionally consumed metal. In the case of the polycrystalline sample [101], the charge transfer difference at the active-passive transition was reported as 0.38 mC·cm^{-2}, twice the amount of the present case, which yields a value of 0.76 ML of additionally consumed metal for the native oxide-covered sample, assuming a (100) orientation for the calculation. Therefore, we can say that the presence of ULP and native oxide films provides protection and pre-passivation at OCP on both FeCrNiMo single and 316L poly crystalline samples. However, it is evident that ULP pre-oxidation treatment, whether performed at moderate (250 °C) or room temperature, promotes an enhanced protectiveness against active dissolution owed to more efficient blocking of the residual transient active dissolution upon anodic passivation.

In the passive domain we observe a slightly higher current density for the ULP pre-oxidised surface although the difference between it and that of the native oxide is within the range of reproducibility. It should be noted that entrance into the transpassive region is met with an activation peak in the case of the native oxide, which is not the case for the ULP oxide. No other significant changes in behaviour can be noted in the passive region.

In the following, we will focus the discussion on the surface composition and stratification of the ULP oxidised sample, thermally pre-oxidized at 250 °C, and how this may relate to the differences in the corrosion behaviour when compared with the native oxide.

6.6 Electrochemical passivation of a ULP surface

6.6.1 XPS analysis

The relative intensities that will be made reference to are shown in Table 6.1 at the end of the chapter. Once more we will start with the evolution of the specific elements, beginning with the ULP oxide formed at 250 °C and following the progression all the way to the film formed when we are in the passive region. The Fe 2p spectra are shown in Figure 6.6a. After the low chromium clean surface was exposed to 750 L of gaseous O_2 in the UHV chamber, the same three species identified in the previous chapters, metallic Fe, Fe^{2+} and Fe^{3+}, were once more found to be present. The relative amounts of each were determined as 65%, 9% and 26%, respectively. The still high amounts of metallic iron further demonstrate the slowing kinetics of oxidation that are exhibited when the amount of chromium and nitrogen at the surface are diminished. Upon exposure to the glovebox that contains residual oxygen and water, we see further oxidation of

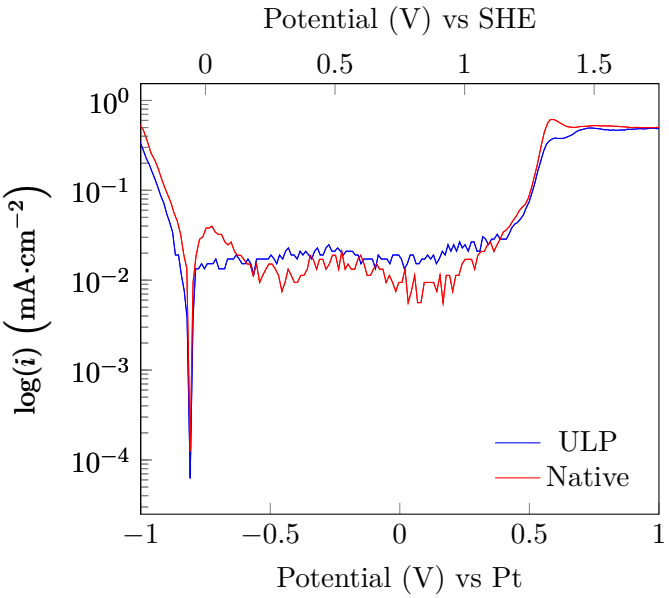

Figure 6.5: Polarisation curves of a Fe–17Cr–14.5Ni–2.3Mo (100)-oriented model stainless steel surface prepared oxide-free in UHV and subsequently pre-oxidised by exposure to ultra-low pressures of oxygen (ULP, blue) or via exposure to the glovebox environment (Native, red).

iron. Metallic iron now makes up only 33% of the total relative iron concentration. Comparing this with the native oxide, we see that a larger percentage of the metallic iron has been oxidised. Also given the fact that the initial clean surface was richer in the ferrum metal, we can already hypothesise that the oxide formed at this stage will be more enriched in the iron compared to the native oxide. The extra oxidised Fe is found as Fe^{3+}, with the relative amounts of Fe^{2+} and FeOOH having similar values to the ones observed on the native oxide. Exposure of the ULP-based oxide to the acidic electrolyte leads to similar and unsurprising results when considering what has already been seen when investigating the native oxide, with preferential dissolution of iron oxide. The relative amount of the metal present was now determined as 65%, which is almost identical to when the native oxide was exposed to the same electrolyte for the same duration. The ratio of Fe^{3+}/Fe^{2+} is higher in the case of the ULP-based film after exposure to the electrolyte, however this result should be taken with caution given the low amounts of Fe^{2+} compared to the potential error associated with the results. The FeOOH species was no longer found present. Once more, we see that stepping the potential into the passive range promotes re-oxidation of the metal, with the more oxidising conditions counteracting the dissolution of the oxide. Whereas before, after leaving the sample to rest at OCP, we saw almost exactly the same relative amounts when comparing the ULP+GB oxide and the native oxide, we now have 16% more of the metallic iron being oxidised in the case of the ULP-based oxide after passivating the surface. This may suggest that pre-oxidising the surface allows for increased atomic mobility

of iron through the oxide layer when in the passive region. The further oxidation results in a higher relative amount of Fe^{3+} when compared to the passive film formed on the native oxide.

The Cr 2p spectra are shown in Figure 6.6b. Now looking at the evolution of chromium, the first thing to note is the lack of Cr(N) that forms throughout. The amount formed was too insignificant to be included in the results when considering the uncertainty. Clearly this is a direct result of next to no segregation of the chromium and nitrogen during the preparation of the surface. Therefore, until we expose to the electrolyte, we only have to consider metallic chromium and chromium oxide, Cr_2O_3. After the pre-oxidation at 250 °C, the relative amounts of metallic and oxidised chromium were 46% and 54%, respectively. The ratio of metal to oxide is significantly higher than what was seen after just 100 L of exposure at the same temperature in chapter 5, where we observed 26% Cr and 63% Cr_2O_3 (and 11% Cr(N)). Once more this result further emphasises the differences in the reactivity of the sample with changing initial surface composition. Exposure to the glove-box environment promotes further oxidation of the metal, with the oxide increasing its share of the total concentration to 74%. As we still observe no significant amounts of Cr(N), this means that the relative amount of metallic chromium stands at 26%. This is 7% more than what was observed on the native oxide. Exposure to the H_2SO_4 electrolyte brings about the introduction of chromium hydroxide, which was also the case after the native oxide was exposed to the solution. The relative amount of hydroxide is much higher (54%) than what was noted after the native oxide (34%) was exposed to the same conditions. Instead, we have a relatively low amount of Cr_2O_3 (25%), which is less than was formed when the native oxide (42%) was subjected to the 0.05 M H_2SO_4 medium. Anodically passivating the surface results in the expected dehydroxylation of $Cr(OH)_3$ in favour of forming more Cr_2O_3. At the same time, we also report further oxidation of the metal, which now only makes up 8% of the relative chromium concentration at the surface. This is much lower than the case of the native oxide-based passive film, which suggests that ULP pre-oxidation allows for a larger relative percentage of the chromium to be oxidised, which will benefit passive film performance.

The Mo 3d spectra are shown in Figure 6.6c. Prior to exposure to the electrolyte we must only concern ourselves with the three well-defined states, Mo, Mo^{4+} (MoO_2) and Mo^{6+} (MoO_3). The relative molybdenum concentration at the surface of these three species with regards to the ULP oxide is 65%, 11% and 24%, respectively. This is further evidence that lower chromium content at the surface on a pristine sample slows the oxidation kinetics of all elements involved in the process. As we have seen with iron and chromium, exposure to the glovebox causes further oxidation of the metallic molybdenum. Almost double the relative amount of Mo^{6+} was found to be present in the oxide formed after exposure of the ULP-prepared sample was exposed to

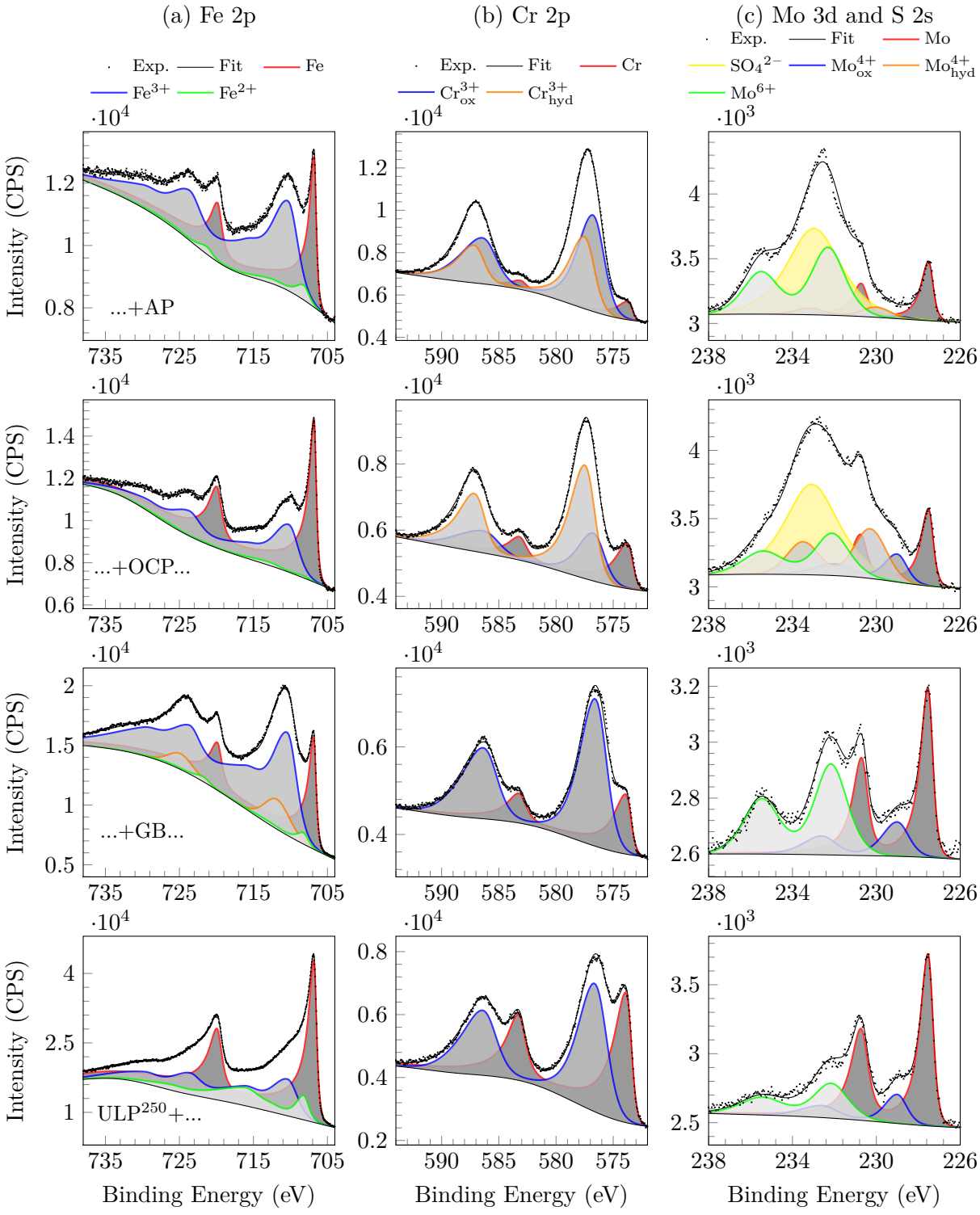

Figure 6.6: High resolution XPS spectra of (a) Fe 2p, (b) Cr 2p and (c) Mo 3d and S 2s regions for the ULP prepared oxide at 250 °C and subsequent treatments formed on an FeCrNiMo(100) sample, recorded at a take-off angle of 45°.

the glovebox than in the native oxide. This corresponds with less relative amounts of metallic Mo and Mo^{4+}. After exposure to the electrolyte, we once more observe the overlapping sulphur contribution to the spectra, further complicating analysis of the molybdenum-based species. Upon being held at OCP for thirty minutes in the electrolyte, molybdenum is further oxidised, with the relative amount of metal going from 42% in the ULP+GB oxide to 25%. Whilst we do see a decrease in the relative concentration of Mo^{6+} to 29%, this does not necessarily indicate a loss of the actual concentration as the total area of the component remains almost the same as the value in the ULP+GB oxide. The species that we defined as MoOOH is found in a significant relative amount (32%), much more than what was observed in the case where the native oxide was exposed to the electrolyte (18%). This follows the same behaviour of the chromium where hydroxylation of the film was more significant after the stainless steel sample had been pre-oxidised in UHV conditions. Re-entry into the electrolyte followed by anodic passivation produces marked dehydroxylation and further oxidation of the molybdenum species found present in the oxide film. Mo^{4+} is nearly undetectable in the film, with Mo^{6+} now making up an impressive 67% of the total molybdenum surface concentration. This value is 27% more than what was observed for the native oxide-based passive film. This remarkable enrichment there results in a less significant contribution from both Mo and Mo^{4+}. Whilst these results are interesting, we must keep in mind the high uncertainty related with the decomposition of the molybdenum spectra after exposure to the sulphur-based electrolyte.

Nickel was only found oxidised in small amounts after exposure to the glovebox environment, forming $Ni(OH)_2$ in similar relative amounts to what was observed on the native oxide in Figure 6.1. After the sample had undergone electrochemical treatments no more oxidised nickel was observed.

Oxidising in 750 L pure gaseous oxygen at 250 °C in UHV conditions produced a 0.8 nm thick oxide with a Fe–19Cr–1Mo composition. This iron-rich oxide reflects the lack of chromium present on the clean surface prior to oxidation. In chapter 5, where the stepwise oxide growth was investigated at 250 °C, an oxide layer of 0.7 nm was produced after an exposure of just 6 L of O_2 gas and was markedly more enriched in Cr_2O_3 (45%). Exposure of the ULP oxide to the glovebox environment resulted in further oxidation and subsequent growth of the layer to an approximate thickness of 1.6 nm, which is comparable with the native oxide (1.5 nm). However, the calculated composition, Fe–18Cr–1Ni–2Mo, was still found to be significantly affected by the low chromium content at the surface — the native oxide was almost twice as rich in oxidised chromium (37%). Exposure to the electrolyte without applying an external potential produces a thinner (1.2 nm) oxide with a composition of Fe–53Cr–8Mo. This result shows

marked enrichment of molybdenum in the oxide film when compared with what was shown on the native oxide-based film at the same stage and may explain the beneficial properties that were observed in the corrosion behaviour prior to passivation. The amount of chromium is now almost exactly the same, suggesting that the relationship between starting chromium concentration at the surface and the passive film composition when formed in acidic media is minimal. Polarising anodically the sample results in considerable growth of the oxide to 1.9 nm, some 27% thicker than what was produced on the native oxide passive film. Molybdenum enrichment was reduced to 4%, giving an overall composition of Fe–57Cr–4Mo. Once more nickel was found to become increasingly more enriched in the underlying modified alloy region. Chromium was depleted in the same region on the ULP-based oxides.

The thicknesses and compositions for the ULP pre-oxidised surface and the oxide films formed after the aforementioned treatments can be found in Table 6.2.

6.6.2 ToF-SIMS analysis

ToF-SIMS analysis was used to probe the depth distribution of the oxide film and underlying modified alloy. Figure 6.7 shows the ToF-SIMS negative ion depth profiles for the ULP^{250} oxide formed on FeCrNiMo(100) after it was exposed to the glovebox (ULP+GB), then held at OCP in 0.05 M H_2SO_4 (OCP), and then anodically passivated (AP). Depth profile analysis of the ULP oxide was not possible as in order to transport the sample to the ToF-SIMS platform it is necessary to go via the glovebox, which further oxidises the sample before analysis is possible. Along with the oxide film itself, we can also define a region corresponding to the modified alloy; it is widely reported that we observe an enrichment of metallic nickel in austenitic and duplex stainless steels in the region between the metallic substrate and the oxide film [8, 17, 89, 120]. The position of the modified alloy-oxide interface will be defined by the maximum intensity of Ni_2^- ions and is indicated by a dashed line. Estimations made using ToF-SIMS, taking into account the interface roughness, suggest that the thickness of this modified alloy region is of the same magnitude as that of the oxide film.

Looking at the ToF-SIMS depth profile of the oxide formed after the ULP pre-oxidised sample was exposed to the glovebox, the maximum intensity attributed to CrO_2^- ions is at 34 s, whilst the maximum of the FeO_2^- and MoO_3^- ions is at 14 s and 8 s, respectively. It should be noted that these times are taken using the median value from a small range, typically no greater than ± 3 s (depending on the shape of the curve), in which the intensity is at its highest point. This result indicates an inhomogeneous distribution of chromium oxide in the film, with an enrichment close to the metal substrate-oxide interface, as previously reported for native

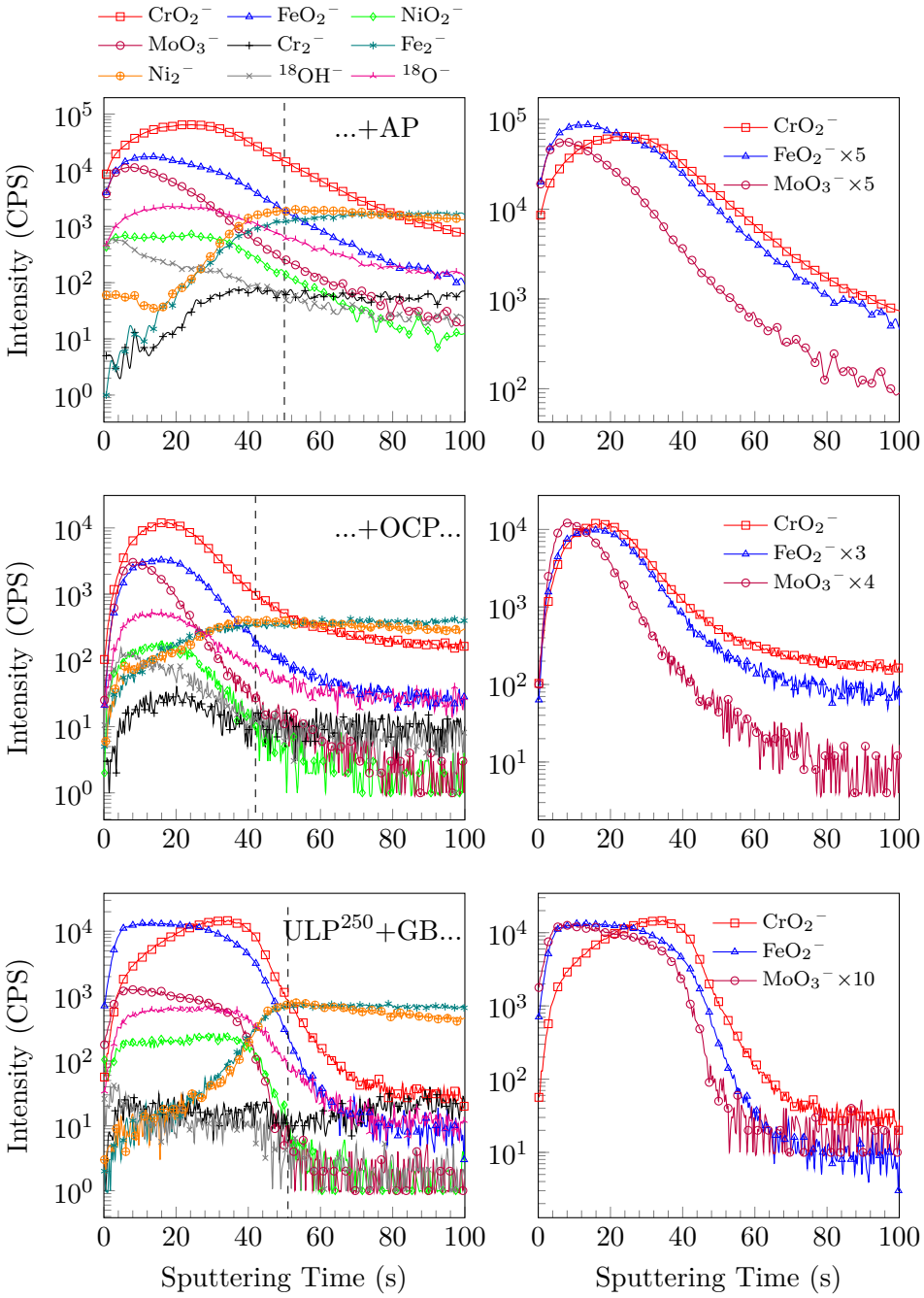

Figure 6.7: ToF-SIMS negative ion depth profiles for the ULP^{250} oxide formed on FeCrNiMo(100) after it was exposed to the glovebox (ULP+GB), then held at OCP in 0.05 M H_2SO_4 (OCP), and then anodically passivated (AP): (left) CrO_2^-, FeO_2^-, NiO_2^-, MoO_2^-, Cr_2^-, Fe_2^-, Ni_2^-, $^{18}OH^-$ and $^{18}O^-$ secondary ions, (right) Only CrO_2^-, FeO_2^- and MoO_3^- secondary ions. The dashed line indicates the position of the oxide-modified alloy interface, determined by the maximum of the Ni_2^- profile.

oxides formed on 316L SS in air [88, 89, 107]. Whilst we observe maxima for the Fe and Mo oxide ions at 8–14 s, the shape of the curves suggest a more homogeneous distribution within the layer with a more pronounced presence of molybdenum oxides in the outer part of the film, which has also been the case for other films formed on 316L stainless steels in air [88, 89, 107]. The depth profile shows the presence of NiO_2^- ions throughout the oxide layer, suggesting that there is in fact a nickel oxide distributed in the film, however, it is only present in a very small quantity as indicated by the XPS data. This can be explained by acknowledging that ToF-SIMS is highly sensitive to trace amounts which can be below the detection limit of XPS. Comparing the distribution of $^{18}OH^-$ and $^{18}O^-$, we can see that the former peaks very early at 4 s and then rapidly declines, whilst the latter is more homogeneously distributed, with its maximum at 26 s. At this stage XPS suggests that the only hydroxide present is that of iron, which is evidence of the early formation of the well-reported bilayer structure of the passive films formed on stainless steel, with an inner oxide barrier layer and an outer exchange layer [17, 88, 89, 161, 175]. Using the previously mentioned definition for the modified alloy, where the metallic nickel intensity is at its maximum, we can state that it begins at the 51 s mark. The curve then slowly decreases, suggesting an enrichment of nickel underneath the oxide film, which is confirmed by surface composition analysis presented in Table 6.2.

Moving on to the depth profile after the oxidised sample was first exposed to the 0.05 M H_2SO_4 electrolyte and held at OCP, the first thing to note is the clear shift to a lower sputtering time (relative to the other ions) of the maximum intensity of CrO_2^-, now at 17 s, whilst the maxima for FeO_2^- and MoO_3^- are at 14 s and 9 s, respectively. As already evidenced by XPS, at this stage there is a large amount of chromium hydroxide present, which has previously been shown to be in the outer layer of the oxide film [88, 89, 102]. The result is a broader curve for the CrO_2^- ions, indicating a more homogeneous distribution of chromium within the now thinner passive film. MoO_3^- ions also exhibit a shift to a lower sputtering time relative to that of the iron ions, partly due to the formation of molybdenum hydroxide near the outermost surface, and partly due to the loss of iron oxide via dissolution in the acidic medium. At this stage, according to the XPS data, we witness the presence of a molybdenum based hydroxide, which will be present in the extreme outer portion of the film. The distribution of oxidised molybdenum is much sharper, which one would expect if we, in fact, have the high hydroxide content (in the outer region of the film) that was observed in the XPS data. Once more, we see the same behaviour when comparing $^{18}OH^-$ and $^{18}O^-$, with an early peak and subsequent decline for the hydroxide, whilst oxide ions peak slightly later but with a shallower decline, confirming the bilayer structure of the passive film. In this case, the modified alloy region is shown to begin

after 42 s, which is a reduction in time compared to the ULP+GB oxide, indicating a likely reduction in the thickness of the oxide, providing that we assume a close to constant sputtering yield. This is not surprising as XPS data showed that there is a significant loss of iron oxide caused by its preferential dissolution in acidic media. This effect has been noted on an array of stainless steel surfaces whether oxidised in air or using a controlled pre-oxidation [88,89,101,102].

Moving on to the final stage after the sample had been stepped to the anodic passivation potential for 30 minutes, we note a shift to an increased sputtering time for the maximum of the curve (26 s) corresponding to that of CrO_2^- ions. This is due to the dehydroxylation of the chromium into Cr_2O_3, which is present in the inner part of the oxide film. The sputtering time corresponding to the maximum intensity of both the FeO_2^- and MoO_3^- ions remains similar to what was seen after OCP, with maxima of 13 s and 8 s, respectively. The distribution of MoO_3^- ions is now broader compared to what was observed in the depth profile after entry into the electrolyte and being held at OCP. This coincides with the significant oxidation in favour of Mo^{6+} production that was noted in the XPS analysis. The position of the modified alloy is shifted to a higher sputtering time, now beginning after 50 s, indicating a possible significant growth in the oxide film when compared to the previous stage, in agreement with XPS thickness estimations. Similar observations have previously been made when investigating room temperature oxidation in air and ultra-low pressures of oxygen [88, 89, 101, 102].

6.7 A bilayer model

The ToF-SIMS data indicate that Cr_2O_3 is enriched at the alloy-oxide interface, whilst the other species are more prevalent at the outer surface. A frequently used model to describe passive films formed on stainless steels is the bilayer model shown in Figure 6.8. This simplified model, described in detail in the experimental chapter of this thesis, consists of two-layers, an inner barrier Cr_2O_3 layer and an outer hydroxide layer rich in oxidised iron. Whilst evidently the passive film does not possess a sharp and defined interface as the model suggests, but rather localised enrichments coupled with gradual changes in the concentration of various species, the bilayer model can nonetheless aid in bettering our understanding of the system by separating components contributions to the film and allowing a more in-depth analysis.

The thicknesses and compositions of the outer oxide layer of all the oxide films formed, calculated using the bilayer model, are shown in Table 6.3. The bilayer model was not applied to the ULP oxide prepared at high temperature, partly as the oxide itself is very thin (as suggested by the single layer model), but also due to a lack of ToF-SIMS analysis on this sample. Although admittedly, if we assume the same growth model as we saw in chapter 5, we

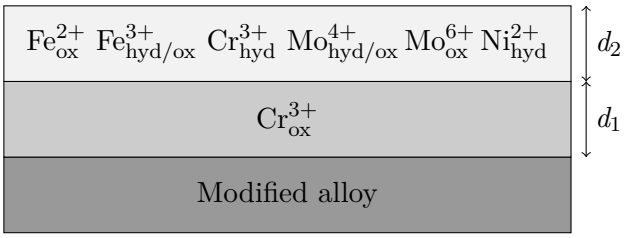

Figure 6.8: Bilayer model of the oxide/passive films formed on FeCrNiMo stainless steel.

can most likely assume a similar chromium enrichment at the alloy-oxide interface upon which Fe^{3+} oxide forms, much like what is described by the bilayer model and is in agreement with results obtained on FeCrNi(100) surfaces [91]. If we first start by comparing the native oxide and the oxide that is formed after the ULP pre-oxidised sample is exposed to the glovebox, we see that the result is rather unsurprising; the outer oxide layer is composed almost entirely of iron oxide, with small amounts of nickel and molybdenum. With regards to the thickness of the respective inner and outer layers, once more the results should come as no surprise given what we have observed in the above text thus far; in the native oxide, an initial high chromium content at the surface results in a more Cr_2O_3 rich oxide, promoting a relatively thicker inner layer. Conversely, the surface prior to ULP oxide formation possesses less chromium and we therefore observe a more iron oxide-rich oxide, leading to a relatively thicker outer layer. The bilayer model is more interesting after exposure to the electrolyte where we form hydroxide species. As previously stated, exposure to the acidic electrolyte results in dissolution of iron oxide, which causes enhanced chromium and molybdenum enrichment in the film. The relative enhancement of the amount of the molybdenum found in the outer layer is markedly higher where the surface was initially pre-oxidised in the UHV system. The value of 10% of the outer layer composition is close to five times to that of the bulk, and is also almost double the amount that was formed in native oxide-based film. At the same stage, we note that due to the ULP based oxide being more readily hydroxylated (see Table 6.1) that the outer layer is thicker and with less oxidised iron. At this stage the inner layer is very thin in both cases due to the small amounts of Cr_2O_3. The thicker, more chromium rich outer layer, found present after ULP pre-oxidation, may provide more protection against active dissolution in the acidic medium due to its higher stability. This combined with the high increased molybdenum content, a known combatant against corrosion of stainless steels, may explain its enhanced performance prior to passivation. After stepping to the passivation potential, we observe significant thickening of the inner layer in the case where the film was initially pre-oxidised in ULP oxygen, with the calculated value increasing three-fold from 0.3 to 0.9 nm. This is attributed to the noted dehydroxylation that occurred on the sample. The native oxide-based passive film was not as readily dehydroxylated and as a result sees no

noticeable thickening of the inner layer but rather a more chromium hydroxide enriched outer layer. The thicker inner barrier that affects atomic transport may be beneficial to the passive film performance.

It is perhaps, at this stage, worth commenting on the models themselves. If one compares the total thicknesses calculated using both models, one can see that the bilayer model always produces a thickness value slightly higher than the single layer model, albeit if the uncertainty of the models is taken into consideration the reported differences are perfectly acceptable. Whilst neither model is truly correct, as the oxide layer is neither completely homogeneous in its distribution, nor does it have defined layers, both can be used to better understand the system. Also when considering the values derived after the exposure to the glovebox and electrolyte, we must note that the model does not account for residual carbon and sulphur that may sit on the surface attenuating signal from the oxide layer. One final comment should be made on the bilayer model itself; in chapter 5 it was noted that Fe^{2+} was formed during the initial stages of the oxidation process, on top of which Fe^{3+} preferentially formed, as suggested by the angular analysis that was carried out during the following stepwise oxidation. Traditional bilayer models reported in the literature for passive films formed on stainless steels place Fe^{2+} in the outer layer, but if one assumes that the oxidation model remains similar to what is reported in this work, then perhaps a more accurate representation of this system would be to include it in the inner layer. Doing so does not really alter the results too dramatically given the relatively low concentration of Fe^{2+} based species, however, it is still worth considering. A third model, with Fe^{2+} considered as part of the inner layer, was applied to the results found in this chapter. The table documenting the findings can be found in the appendix.

6.8 Adding Cl^- to the electrolyte

Chloride ions are well known for their destructive behaviour when it comes to passive film breakdown. Small amounts of chloride anions were added to the electrolyte (0.05 M NaCl) when forming the passive film. The starting surface composition was again low in chromium, prior to being pre-oxidised at 250 °C, allowing for a good comparison with the passive film formed without the presence of Cl^-. With regards to the behaviour of iron, the addition of chloride ions resulted in less metallic iron being oxidised, with 51% of the relative intensity remaining unoxidised compared to 41% where Cl^- was not added. The amounts of Fe^{2+} and Fe^{3+} where found in the expected magnitudes. Chromium behaviour was near identical, with any differences within the reported margin of error. 36% of molybdenum found at the surface was found present in the metallic form, a value higher than before the ULP pre-oxidised surface without chloride

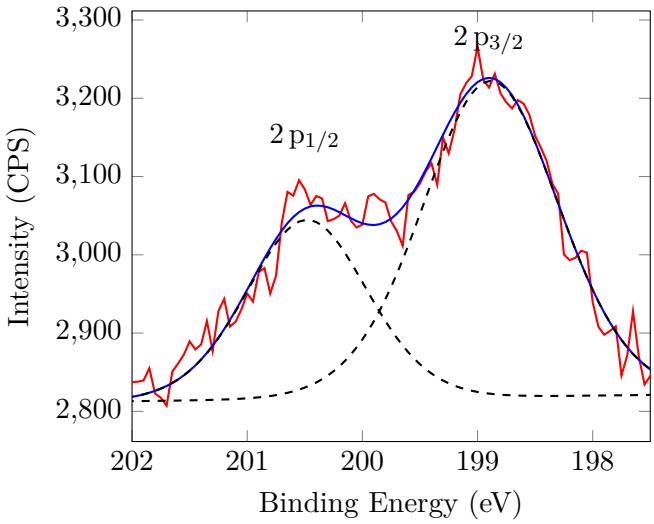

Figure 6.9: High resolution spectrum of the Cl 2p region after the FeCrNiMo(100) sample was pre-oxidised at 250 °C, before being passivated in 0.05 M H_2SO_4 + 0.05 M NaCl.

ions and the native oxide. The same Mo^{6+} enrichment that was previously observed was not seen when chloride ions were present in solution, with the ratio of all four species more akin to what was observed on the native oxide-based passive film. The composition of the oxide film using the single layer model was determined as Fe–61Cr–3Mo, with a thickness of 1.7 nm. Both these results are remarkably similar to what was seen when the passive film was formed in the absence of chloride ions. Analysis using the bilayer method showed no differences of note, with equally similar results. High resolution spectra of the chlorine 2p region was recorded after exposure to the electrolyte, shown in Figure 6.9. The spectrum appears to show one environment, with the two spin-orbit split peaks at 198.9 and 200.5 eV attributed to Cl^- [176]. No other chlorine species were detected. Chloride ions made up approximately 1% of the surface concentration, as determined from the survey spectrum. ToF-SIMS analysis was performed to see whether chloride ions had penetrated into the passive film, with the depth profile shown in Figure 6.10. From that we can see that the chloride ions have a very narrow distribution with the maximum intensity at a sputtering time between 4-6 seconds, which is significantly before we reach the maximum intensities of either of the other three species that are found in the passive film. The intensity then quickly drops. This result suggests that at these concentrations, the majority of chloride ions sit at the extreme surface and are not incorporated in the oxide structure. The efficient blocking of chloride ions into the oxide layer is to be compared with non ULP pre-oxidised surfaces.

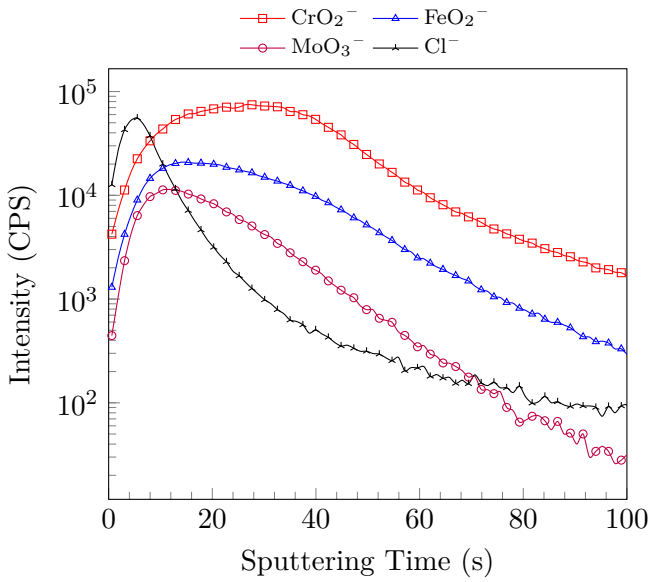

Figure 6.10: ToF-SIMS depth profile after the FeCrNiMo(100) sample was pre-oxidised at 250 °C, before being passivated in 0.05 M H_2SO_4 + 0.05 M NaCl.

6.9 Conclusion

ULP pre-oxidation at 250 °C was found to benefit the corrosion properties of the passive film formed on an FeCrNiMo(100) surface in acidic conditions, aiding in protecting against active dissolution during anodic passivation. Molybdenum enrichment of the film was significantly enhanced after the pre-oxidation in UHV conditions when compared to native oxide-based passive films at the open circuit potential. In the passive region, the two pre-passivation techniques resulted in passive films that exhibited similar corrosion behaviours, despite differences in the chemical make-up. ToF-SIMS showed evidence of Cr_2O_3 enrichment at the substrate-oxide interface, with oxidised molybdenum and iron more readily found in the outer parts of the film along with any hydroxide species that readily formed after encountering the electrolyte. ULP pre-oxidation at 250 °C produced an oxide film in the passive region that was markedly rich in Mo^{6+} and with a thick inner Cr_2O_3 layer, produced due to favourable dehydroxylation upon anodically passivating the surface. Dehydroxylation upon anodic passivation was not as pronounced in the case where the clean stainless steel had been initially oxidised in the glovebox. The native oxide-based oxide films were typically more enriched in oxidised chromium which can be attributed to the different surface composition prior to oxidation that is brought about by multiple cycles of sputtering and annealing. The addition of chloride ions (0.05 M) to the electrolyte solution was found to have limited effect on the thickness and composition of the passive film formed after anodic polarisation of the ULP pre-oxidised sample. Chloride ions

were not found to entering the oxide film, but only present at the outermost surface. Holding the sample at OCP lead to a decrease in the thickness of the film owed to preferential dissolution of oxidised iron. Conversely, anodic passivation in the same medium promotes oxide film growth due to more oxidising conditions which counteract the active dissolution. Nickel and iron hydroxide were found present after exposure to the glovebox, however both were readily dissolved in acidic electrolyte. Metallic nickel was found to become enriched in the modified alloy region underneath the oxide.

Treatment	Relative intensity (%)													
	Fe	Fe^{2+}	Fe^{3+}_{ox}	Fe^{3+}_{hyd}	Cr	Cr^{3+}_{ox}	Cr^{3+}_{hyd}	Cr(N)	Mo	Mo^{4+}_{ox}	Mo^{4+}_{hyd}	Mo^{6+}	Ni	Ni^{2+}
Native Oxide (NO)	43	3	47	7	20	75	0	5	51	28	0	21	87	13
NO + OCP	66	7	27	0	22	42	34	3	31	25	18	26	100	0
NO + OCP + AP	58	8	34	0	13	40	46	1	33	12	14	41	100	0
ULP^{RT}	70	8	22	0	26	63	0	11	52	28	20	0	100	0
ULP^{250}	65	9	26	0	46	54	0	0	65	11	0	24	100	0
ULP^{250} + GB	32	3	55	10	26	74	0	0	42	13	0	45	92	8
ULP^{250} + GB + OCP	65	3	32	0	21	25	54	0	25	13	32	29	100	0
ULP^{250} + GB + OCP + AP	43	5	52	0	8	54	38	0	25	1	7	67	100	0
ULP^{250} + GB + OCP + AP^{NaCl}	51	6	43	0	11	53	36	0	31	24	6	40	100	0

Table 6.1: Relative intensities (±2%) of Fe, Cr, Ni and Mo on the FeCrNiMo(100) sample after different surface preparations. It should be noted upon the introduction of the electrolyte the uncertainty with regards to the relative amounts of molybdenum can vary by up to 8% when estimating the error based on fit-adjustment.

Treatment	Oxide comp. (%)				Modified alloy comp. (%)				Thickness (nm)
	Fe	Cr	Ni	Mo	Fe	Cr	Ni	Mo	
Native Oxide (NO)	61	37	1	1	74	11	14	1	1.5
NO+OCP	39	57	0	4	73	12	14	1	1.2
NO+OCP+AP	30	67	0	3	66	12	21	1	1.5
ULP^{RT}	48	50	0	2	76	12	10	2	0.8
ULP^{250}	80	19	0	1	80	7	12	1	0.8
ULP^{250}+GB	79	18	1	2	74	9	16	1	1.6
ULP^{250}+GB+OCP	39	53	0	8	71	11	17	1	1.2
ULP^{250}+GB+OCP+AP	39	57	0	4	66	9	24	1	1.9
ULP^{250}+GB+OCP+Ap^{NaCl}	37	61	0	3	68	10	21	1	1.7

Table 6.2: Thickness (±0.1 nm) and composition of oxide layer and modified alloy (±1%) using the single-layer model as calculated from XPS data.

Treatment	Outer oxide composition (%)				Thickness (nm)	
	Fe	Cr	Ni	Mo	Outer layer (±0.1)	Inner layer (±0.1)
Native Oxide (NO)	96	0	1	3	1	0.7
NO+OCP	56	38	0	6	0.9	0.5
NO+OCP+AP	43	52	0	5	1.1	0.6
ULP^{250}+GB	96	0	1	3	1.3	0.5
ULP^{250}+GB+OCP	47	43	0	10	1.1	0.3
ULP^{250}+GB+OCP+AP	57	37	0	6	1.2	0.9
ULP^{250}+GB+OCP+AP^{NaCl}	57	39	0	4	1.1	0.8

Table 6.3: Thickness and composition (±1%) of the outer oxide layer using the bilayer model as calculated from XPS data. As Cr_2O_3 is the only species found in the inner layer, as per the model, it makes up 100% of its composition.

Conclusions and perspectives

This work has focused on trying to better understand the mechanisms of oxidation at both RT and 250 °C of a FeCrNiMo(100) surface and how this may influence the passivation in acidic media. The investigation employed a combined surface science and electrochemistry approach, using techniques such as XPS, STM, LEED, ToF SIMS and voltammetry. The body of work can be split into three main sections. The first results-based chapter focuses on characterisation of the clean surface prior to oxidation, highlighting the importance of surface preparation and chromium and nitrogen segregation on the composition of the oxide. STM and LEED were used to identify key features of the oxide-free surface. From here, the work focuses on the initial oxidation, highlighting both the oxide nucleation and growth at RT and 250 °C. Angular measurements gave an indication of the in-depth distribution of the oxidised species. The influence of oxidation at ultra-low pressures (ULP) of oxygen, in a controlled manner, at 250 °C, on the performance of a passive film formed in 0.05 M H_2SO_4 was then studied and compared with the passive film formed in the same conditions after a native oxide formed. Pre-oxidising the surface in controlled conditions proved beneficial to passive film performance at the active-passive transition. This was attributed to enhanced molybdenum enrichment. ToF SIMS gave further indication of the in-depth distribution of the passive films, highlighting the well-known bilayer structure.

An ever changing surface

Chromium and nitrogen were found to co-segregate to the surface during annealing of the FeCrNiMo(100) sample, a process necessary for a well-ordered surface. Chromium was found to segregate using two different mechanisms. The amounts of chromium and nitrogen that

segregated from the bulk to the surface, displacing metallic iron and nickel, were found to diminish over time with an increasing number of sputtering and annealing cycles. This change in the composition at the surface had significant consequences when it came to the rate of oxidation, with a maximum rate three and a half times faster on the surface that had a higher starting amount of metallic chromium and nitrogen. This also lead to dramatic changes in the composition of the oxide formed at the point of oxygen saturation, with a higher initial chromium content promoting an oxide that was richer in Cr_2O_3 and resulted in a larger proportion of metallic molybdenum being oxidised.

LEED and STM characterisation of the oxide-free surface showed that the topmost layer consists of a $(\sqrt{2} \times \sqrt{2})$R45° reconstruction with vacancy lines propagated along both the [010] and [001] directions. These perpendicular lines, that were sometimes found to have periodic electron density within them, were perhaps present in order to reduce the stress associated with the large terraces that exist on the surface. The steps that separated the terraces did not show any signs of having a atomic multi-step structure, but rather multi-atomic steps, however possibly differences of the composition and structure were observed at the edge of the steps.

The role of chromium and nitrogen segregation as a result of annealing is clearly a vital and complex component in the oxidation mechanism for not only the FeCrNiMo(100) sample investigated in this work, but stainless steels in general. Further investigation of the role of chromium and nitrogen contents present at the surface prior to oxygen exposure may be of interest from a corrosion perspective given how it influences the composition of the oxide formed in air. Better control of the surface composition may lead to beneficial performances of stainless steels. STM would be an important tool in any further work, allowing the investigator to probe the surface structure and highlight the key differences that arise from different surface quantities of chromium and nitrogen. Equally, ToF-SIMS may give an indication to how the change in amounts of chromium at the surface alters the in-depth distribution of the oxidised species.

Oxide nucleation and growth mechanisms

XPS high resolution, angular and in situ analysis were used to provide unprecedented insight into the mechanism for very first stages of oxide growth on an FeCrNiMo austenitic stainless steel. The initial stages of oxidation result in rearrangement of the surface and the formation of nitrogen-containing species that behave as nucleation sites for growth of Cr_2O_3. Iron oxides, present as both Fe^{2+} and Fe^{3+}, are found to nucleate at the same time as as those of chromium. Initial oxidation of molybdenum was found to occur after these two elements had already begun to oxidise. At no point was nickel found in an oxidised form within the oxide film, however,

metallic nickel became more enriched within the modified alloy region as the oxide grew thicker. The initial stages of oxidation follow standard thermodynamic principles, however it is once the oxide film becomes significantly thick that kinetic parameters become the presiding factor with the iron cation's increased mobility through the film resulting in the main contributor to continued oxidation being Fe^{3+} oxide. Oxidation at 250 °C was found to result in a faster rate of oxidation which is attributed to the enhanced rate of surface reorganisation and production of chromium-nitrogen species that behave as nucleation sites for the oxidation of chromium.

Angular analysis was used in determining the in-depth distribution of the oxidised species within the oxide film. It was shown that Cr^{3+} and Fe^{2+} are found enriched closer to the modified alloy-oxide interface with Fe^{3+} found predominantly at the outer portion of the film. Oxidised molybdenum was found as both Mo^{4+} and Mo^{6+}, with neither found to be enriched or depleted at a given depth within the film.

RT oxidation resulted in surface saturation after a total oxygen exposure of between 10 and 15 L, with the composition of the oxide determined as Fe–50Cr–2Mo. At this stage the thickness was found to be approximately 0.8 nm. The rate of oxidation at 250 °C significantly reduced between 15 and 25 L, with the oxide thickness determined as approximately 2.1 nm after an exposure of 100 L. The composition of the oxide at this stage was Fe–19Cr–1Mo.

This section of work further highlighted the importance of the role that chromium and nitrogen species play in the oxidation of the sample, in particular during the nucleation phase. Understanding the mechanism for oxide growth helps to build on the fundamental knowledge relating to how the oxidation mechanism prior to passivation can later influence the properties of the passive film formed on austenitic stainless steels. This is necessary to comprehend if we are to relate heterogeneities formed during oxidation to corrosion related phenomena.

The role of pre-oxidation on passive film behaviour

ULP pre-oxidation at 250 °C was found to benefit the corrosion properties of the passive film formed on an FeCrNiMo(100) surface in acidic conditions, aiding in protecting against active dissolution during anodic passivation. Molybdenum enrichment of the film was significantly enhanced after the pre-oxidation in UHV conditions when compared to native oxide-based passive films at the open circuit potential. In the passive region, the two pre-passivation techniques resulted in passive films that exhibited similar corrosion behaviours, despite differences in the chemical make-up. ToF-SIMS showed evidence of Cr_2O_3 enrichment at the substrate-oxide interface, with oxidised molybdenum and iron more readily found in the outer parts of the film along with any hydroxide species that readily formed after encountering the electrolyte. ULP

pre-oxidation at 250 °C produced an oxide film in the passive region that was markedly rich in Mo^{6+} and with a thick inner Cr_2O_3 layer, produced due to favourable dehydroxylation upon anodically passivating the surface. Dehydroxylation upon anodic passivation was not as pronounced in the case where the clean stainless steel had been initially oxidised in the glovebox. The native oxide-based oxide films were typically more enriched in oxidised chromium which can be attributed to the different surface composition prior to oxidation, which arose from multiple cycles of sputtering and annealing. Holding the sample at OCP lead to a decrease in the thickness of the film owed to preferential dissolution of oxidised iron. Conversely, anodic passivation in the same medium promotes oxide film growth due to more oxidising conditions which counteract the active dissolution. Nickel and iron hydroxide were found present after exposure to the glovebox, however both were readily dissolved in acidic electrolyte. Metallic nickel was found to become enriched in the modified alloy region underneath the oxide. The addition of chloride ions (0.05 M) to the electrolyte solution was found to have limited effect on the thickness and composition of the passive film formed after anodic polarisation of the ULP pre-oxidised sample. Chloride ions were not found to entering the oxide film, but only present at the outermost surface.

The final chapter of this work served to highlight the beneficial properties induced by pre-oxidising the clean FeCrNiMo(100) sample at high temperature in ultra-low pressures of oxygen, notably by suppressing the activation peak prior to passivation. It was thought that this was achieved by promoting molybdenum enrichment within the passive film. The beneficial effect of pre-oxidising in controlled UHV conditions has now been demonstrated on several stainless steel surfaces where passive films have been formed in H_2SO_4. From here it may be of interest to test a wider range of conditions, as well as starting to consider the feasibility of scaling up the process, such that it could be applied to larger and more industrially relevant samples.

Closing statement

Despite the difficult couple of years that we have all gone through, this thesis has ultimately provided positive results and hopefully contributed in some way, however small, to better understanding what goes on around us. Whilst it is clearly important to answer questions when carrying out research, it is equally as important to ask them. I feel that this piece of work has provided enough questions that can become the basis of future work, notably with regards to how surface preparation influences the amounts of chromium and nitrogen at the surface, and how this alters passive film properties. As well as this, we have further demonstrated the benefit of pre-oxidising in controlled conditions on the behaviour of the passive film. This technique of

improving corrosion resistance should be investigated further and comes with its own set of new and exciting challenges.

I would to take one last opportunity to thank all those who have contributed in any way to the making of this thesis, from its conception all the way through to its end. I am eternally grateful to all those who have supported me and my work over the past three years.

Appendix

Equation A1 shows the Fermi-Dirac distribution multiplied by a linear function in order to better account for the slope, leading to a more accurate adjustment.

$$\frac{h(1+a(x-E_F))}{2}+\frac{h}{\sqrt{2\pi}\cdot a\cdot e^{-\frac{(x-E_F)^2}{2w^2}}}+\frac{h(1+a(x-E_F))\cdot erf\left(\frac{x-E_F}{\frac{\sqrt{2}}{w}}\right)}{2}+h_0 \tag{A1}$$

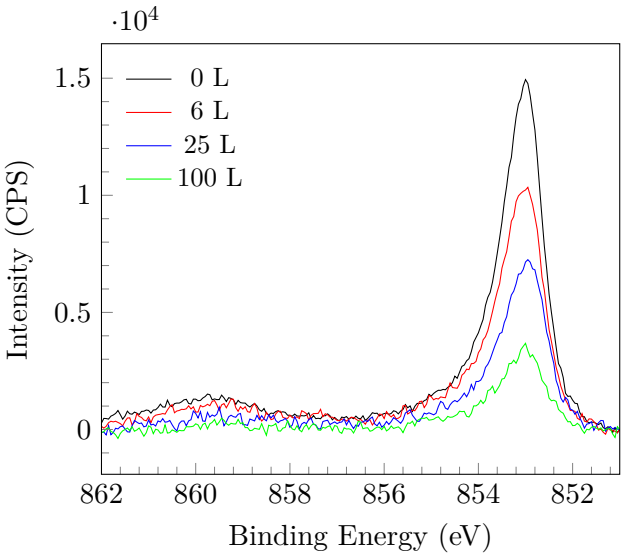

Figure A1: High resolution Ni $2\,p_{3/2}$ spectra recorded after oxygen exposures of 0, 6, 25 and 100 L at 250 °C. At no stage was the element found in an oxidised form.

Core level	State	Assignment	BE (± 0.1 eV)	FWHM (± 0.1 eV)	Line shape
S 2 $p_{1/2}$	S^{6+}	Sulphate	170.3	1.3	GL(30)
Mo 3 $d_{3/2}$	Mo^{0}	Metal	230.8	0.8	LA(1.2,2,20)
	Mo^{4+}	Oxide	232.1	1.4	LA(3,5,5)
	Mo^{4+}	(Oxy)hydroxide	233.3	1.7	GL(30)
	Mo^{6+}	Oxide	235.4	1.9	GL(50)
Cr 2 $p_{1/2}$	Cr^{0}	Metal	583.3	1.5	LA(0.80,2,10)
	Cr^{3+}	Oxide	586.3	2.5	LA(2,5,5)
	Cr^{3+}	Hydroxide	587.1	2.2	LA(1.7,5,10)
	Cr^{3+}	Cr(N)	585.0	2	GL(30)
Fe 2 $p_{1/2}$	Fe^{0}	Metal	720.0	1.4	LA(0.6,1.9,5)
	Fe^{2+}	Oxide	721.8	1.9	LA(1.5,4,5)
	Fe^{3+}	Oxide	723.6	3.6	LA(1.7,5,5)
	Fe^{3+}	Hydroxide	725.0	4.0	GL(30)
	Fe^{2+}	Satellite	726.2	4.0	LA(1.7,5,5)
	Fe^{3+}	Satellite	729.8	4.0	LA(1.5,6,5)

Table A1: XPS fitting parameters for Fe 2 $p_{1/2}$, Cr 2 $p_{1/2}$, S 2 $p_{1/2}$, and Mo 3 $d_{3/2}$ regions.

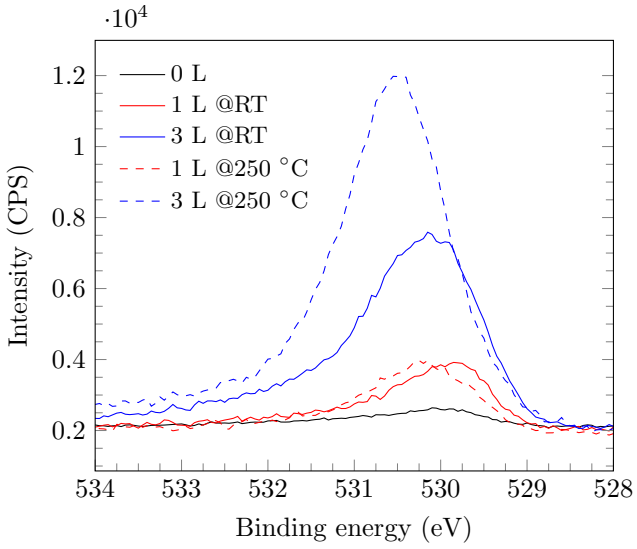

Figure A2: High resolution O 1s spectra recorded after oxygen exposures of 0, 1 and 3 L at RT and 250 °C.

Treatment	Outer composition. (%)						Thickness (nm)	
	Outer layer				Inner layer		Outer layer (±0.1)	Inner layer (±0.1)
	Fe	Cr	Ni	Mo	Fe	Cr		
Native Oxide (NO)	95	0	2	3	9	91	0.9	0.7
NO+OCP	44	49	0	6	26	74	0.9	0.5
NO+OCP+AP	38	56	0	5	16	84	1	0.8
ULP^{250}+GB	96	0	1	3	18	82	1.2	0.5
ULP^{250}+GB+OCP	45	45	0	10	15	85	1.1	0.3
ULP^{250}+GB+OCP+AP	56	38	0	6	9	91	1.1	1.0

Table A2: Thickness and composition (±1%) of the outer and inner oxide layers using the bilayer model, whilst considering Fe^{2+} as part of the inner layer, as calculated from XPS data.

Résumé étendu de thèse

Chapitre 1 : État de l'art

Introduction générale

La corrosion est, selon l'Union internationale de chimie pure et appliquée (IUPAC) [1], « une réaction d'interface irréversible d'un matériau avec son environnement qui entraîne la consommation du matériau ou la dissolution dans le matériau d'un composant de l'environnement. » Cela conduit fondamentalement à la destruction lente du matériau, ce qui peut entraîner une perte des propriétés fonctionnelles ainsi que d'esthétique. Le processus, qui découle de la réaction du matériau avec son environnement local, est un enjeu majeur dans une variété de domaines, en particulier lorsque les matériaux métalliques et alliages jouent un rôle important dans la structure et la stabilité des composants utilisés. La corrosion peut se produire sous de nombreuses formes différentes, souvent en fonction des conditions auxquelles un matériau est exposé. Par exemple, dans des environnements où des ions agressifs tels que Cl^- ou ${S_2O_3}^{3-}$ sont présents, on peut fréquemment observer une forme de corrosion localisée appelée corrosion par piqûres. Ce type de corrosion est particulièrement important dans cette étude car il implique la rupture d'une fine couche d'oxyde protectrice, formée en surface et connue sous le nom de film passif.

Les aciers inoxydables sont définis comme un alliage d'acier avec une teneur en chrome minimale de 10,5 % et maximale de 1,2 % de carbone, en masse. Les aciers inoxydables sont réputés pour leur résistance à la corrosion, du fait de leur forte teneur en chrome, où plus la teneur en chrome est élevée, plus la résistance à la corrosion est élevée [6–11]. En ajoutant de petites quantités de molybdène, la résistance à la corrosion augmente encore en raison de ses influences bénéfiques sur la corrosion par piqûres [12–14]. En raison de leur importance pour ce travail, je

pense qu'il vaut la peine de passer un peu plus de temps à discuter des aciers inoxydables 304 et 316 de manière un peu plus approfondie. Comme mentionné précédemment, l'acier inoxydable 304 provient de la famille austénitique et est l'acier inoxydable le plus couramment utilisé, en partie en raison de sa capacité à être facilement mis en forme et à sa haute résistance à la corrosion. Cet alliage est généralement utilisé dans de nombreux appareils électroménagers, ainsi qu'en architecture. Il contient du fer, du chrome (18–20 wt.%) et du nickel (8–10,5 wt.%). Il existe trois types de cet acier inoxydable, 304, 304L et 304H ; ils possèdent les mêmes quantités de nickel et de chrome, avec la même résistance à la corrosion et la même facilité de fabrication. La différence se résume aux petites quantités de carbone (0,04–0,1 wt.%) ajoutées, qui peuvent influencer certaines propriétés. L'acier inoxydable 304 est connu pour être très polyvalent dans différentes conditions, cependant, il ne résiste pas à un environnement chaud riche en chlorure. Il résiste à des concentrations de chlorure jusqu'à 400 $mg{\cdot}l^{-1}$ à température ambiante, cependant, cela tombe à seulement 150 $mg{\cdot}l^{-1}$ à 60 °C [15]. Une fois que les conditions sont devenues trop sévères pour que l'acier inoxydable 304 soit viable, l'acier inoxydable 316 est souvent utilisé. C'est le deuxième type d'acier inoxydable austénitique le plus couramment utilisé. Il allie fer, chrome (16–18 wt.%), nickel (10–12 wt.%) et molybdène (2–3 wt.%), ce dernier contribuant à augmenter la résistance à la corrosion par piqûres. En raison de cette résistance supplémentaire, il sera utilisé dans des environnements plus extrêmes, tels que les équipements pharmaceutiques, les traitements des eaux usées et les équipements marins.

La passivation, un terme inventé pour la première fois par Schöbein en 1836, est la formation d'une couche d'oxyde ultra-mince et non poreuse à la surface d'un matériau métallique, qui isole le substrat de son environnement. La passivation se produit lorsque le métal nu est exposé à un environnement oxydant, ce phénomène jouant un rôle essentiel dans le développement de notre société où les métaux et alliages sont très largement utilisés. Typiquement, ces films n'excèdent pas quelques nanomètres d'épaisseur et sont donc transparents [8, 16, 17]. Les oxydes sont soit thermodynamiquement stables, soit se dissolvent à une vitesse négligeable. Pour qu'un métal soit thermodynamiquement stable en solution ou dans l'air, il doit être un métal noble, de sorte que son potentiel d'oxydation soit plus anodique que celui des espèces présentes dans l'environnement local. Pour les métaux non nobles, l'inverse est observé, où la formation d'oxyde est entraînée. En raison du potentiel d'oxydation plus cathodique, il y a dissolution du matériau à l'état oxydé ou formation d'un film d'oxyde mince tridimensionnel. Au fil du temps, le film passif peut rompre localement. Heureusement pour nous, ces couches d'oxyde sont connues pour s'auto-réparer [22, 23]. Cependant, le processus d'auto-guérison peut être facilement perturbé par des anions agressifs tels que les chlorures et les thiosulfates qui peuvent alors provoquer une

Composition du volume (at%)	Conditions	Composition du film d'oxyde (at%)	Epaisseur (nm)	Référence
Fe–18Cr–12Ni(100)	Exposition à l'air (3 h)	Fe–27Cr	1.8	[31]
	Exposition à l'air (20 h)	Fe–21Cr	2.0	
Fe–20Cr–12Ni–1.6Mo*	Exposition à l'air (5–10 min)	Fe–39Cr–6Mo	2.0	[88]
Fe–20Cr–12Ni–1.6Mo	Exposition à l'air	Fe–41Cr–4.1Mo	2.2	[89]

Tableau F1: Composition des oxydes formés sur les aciers inoxydables austénitiques après exposition à l'air à température ambiante. *Il convient de noter que lorsqu'une orientation cristallographique n'est pas donnée, l'échantillon est supposé être de nature polycristalline.

corrosion localisée par piqûres. Dans ces zones, la vitesse de corrosion sera considérablement augmentée par rapport au reste du matériau qui reste protégé.

L'oxydation des aciers inoxydables

En raison de leur polyvalence, les aciers inoxydables peuvent être exposés à de nombreux environnements différents et, par conséquent, subire une oxydation dans un large éventail de conditions. [31, 87–101]. Dans ce travail, seule l'oxydation réalisée à l'air ou à l'oxygène pur à RT–250 °C sera considérée. Elle fait donc l'objet principal de cette section de la revue de la bibliographique.

Si l'on considère d'abord l'oxydation de l'acier inoxydable à l'air, on constate que l'oxyde formé en surface est un mélange de Fe^{2+}, Fe^{3+} et Cr 3+ oxydes [31, 87–89]. Lorsque le nickel est présent dans l'alliage, il ne se trouve généralement pas sous une forme oxydée dans la couche, bien qu'il se trouve souvent enrichi sous l'oxyde dans ce que l'on appelle la région de l'alliage modifié [31, 87–89]. Le molybdène se trouve en faible quantité, notamment dans ses états d'oxydation +4 et +6, du même ordre de grandeur que sa concentration en volume, lorsqu'il est présent dans des alliages tels que le 316 [88, 89]. La présence d'hydroxydes n'est pas typique lorsque la composition des films d'oxyde formés dans l'air est rapportée. Un résumé des données de la littérature est présenté dans le Tableau F1.

La composition et le comportement général des films d'oxyde formés sur l'acier inoxydable après exposition à l'oxygène ne sont pas trop différents de ceux formés dans l'air ; cependant, l'exposition à l'oxygène pur permet souvent de mieux contrôler les conditions expérimentales, ce

Composition du volume (at%)	O_2 Exposition (L)	Temperature (°C)	Composition d'oxyde (at%)	Epaisseur (nm)	Référence
Fe–18Cr–13Ni(100)	6	250	Fe–59Cr	1.7	[90]
	35		Fe–34Cr	2.2	
	100		Fe–22Cr	2.1	
Fe–17Cr*	1000	50	-	1.3	[99]
Fe–17Cr	10	327	Fe–45Cr	1.0	[100]
	30		Fe–29Cr	2.2	
	100		Fe–17Cr	3.5	
Fe–20Cr–12Ni–1.6Mo	100	25	Fe–23Cr–5Mo	1.2	[101]

Tableau F2: Composition des oxydes formés sur les aciers inoxydables austénitiques après exposition à l'oxygène. *Il convient de noter que lorsqu'une orientation cristallographique n'est pas donnée, l'échantillon est supposé être de nature polycristalline.

qui peut à son tour nous aider à mieux comprendre les mécanismes qui régissent leur croissance. Un résumé sélectionné des données trouvées dans la littérature peut être trouvé dans le Tableau F2.

Lors de l'analyse des films d'oxyde et passifs formés sur l'acier inoxydable, il ne faut pas seulement considérer sa composition, mais aussi sa structure. Des travaux récents, lancés par le groupe Marcus, ont commencé à étudier comment la nanostructure de la couche d'oxyde affecte les propriétés anticorrosion du film passif [17, 90–92, 103]. D'après ce travail qui s'intéresse à l'enrichissement en chrome des aciers inoxydables à l'échelle nanométrique, l'enrichissement n'est en fait pas homogène au sein de la couche d'oxyde. Le mécanisme d'oxydation initiale, appelé pré-passivation, s'avère produire des hétérogénéités d'enrichissement créant des points faibles propices à la rupture localisée de la passivité [17, 103].

Passivation des aciers inoxydable

Si l'on considère d'abord le film passif formé en milieu acide, il est communément observé que la couche protectrice est enrichie en Cr^{3+} oxyde et hydroxyde, du fait de la vitesse de dissolution relativement élevée du fer oxydé en milieu acide. [7,8,12,17,80]. Il a été trouvé par Maurice et al. que cet enrichissement en chrome est davantage amélioré avec une passivation et un vieillissement supplémentaires [17]. En entrant dans le domaine transpassif, cet enrichissement est réduit car des oxydes Cr^{6+} se forment qui sont facilement dissous dans les milieux acides. Le fer oxydé se trouve généralement dans la partie externe du film, en partie en raison de sa vitesse de diffusion

plus élevée. Le chrome oxydé étant plus enrichi à l'interface oxyde-alliage, il a conduit à plusieurs études utilisant un modèle bicouche pour décrire la structure du film [17, 89, 101, 102]. Dans les alliages à base de FeCrNi, le nickel oxydé est rarement trouvé dans la couche passive, mais le nickel métallique est enrichi sous le film dans la région d'alliage modifié [8, 89, 101, 102]. Selon les travaux de Ryan et al. [35, 104] ; les films passifs formés sur les binaires FeCr ont un ordre à longue distance qui dimune lorsque la quantité de chrome augmente, en accord avec la microscopie électronique en transmission (MET) qui a montré que les structures cristallines sont formées avec 5 % teneur en chrome dans l'alliage, après quoi le film passif devient amorphe lorsque la teneur passe à 24 %. La polarisation anodique d'une surface Fe–Cr18–13Ni dans H_2SO_4, utilisée pour vieillir le film, induit une cristallisation dans le film [31]. Lorsque le molybdène est présent dans l'alliage, le vieillissement sous polarisation anodique n'entraine pas la formation d'un oxyde cristallin, Maurice et al. suggérant que le molybdène, concentré dans la partie externe du film, stabilise l'oxyde amorphe riche en fer [17]. Des études similaires de films passifs ont été faites ailleurs [37]. Dans les environnements acides, le film passif a généralement une épaisseur de 1 à 3 nm [17, 30, 88, 89].

Dans des conditions fortement alcalines, une importante couche de Fe^{3+} se forme sur le film passif [109, 110, 115]. Cette observation s'explique par le fait que le fer dans ses états d'oxydation +2 et +3 est beaucoup moins soluble à pH élevé, contrairement à ce qui est observé en conditions acides. De ce fait, des films passifs beaucoup plus épais sont formés dans des solutions basiques. Ceci a été mis en évidence par Schmutz et Landolt [109] qui ont analysé les films formés sur deux échantillons d'acier inoxydable austénitique différents, dont l'un contenait du molybdène. Dans les deux cas en augmentant le potentiel dans la région passive, les films formés dans l'acide ont subi une perte de masse (indiquant une dissolution), tandis que ceux formés dans NaOH ont gagné de la masse (indiquant une croissance du film). Des observations similaires ont été obtenues par Strehblow et al. [110, 115].

La littérature montre que la nature du film passif est complexe et dépend fortement de l'environnement dans lequel il se trouve, ainsi que de l'échantillon lui-même. Un résumé des données se trouve dans le Tableau F3.

Chapitre 2 : Techniques d'analyse

Spectroscopie de photoélectrons X

La spectroscopie de photoélectrons X (XPS — *X-ray photoelectron spectroscopy*), également connue sous le nom de spectroscopie électronique pour analyse chimique (ESCA — *electron*

Composition du volume (at%)	Conditions	Composition d'oxyde (at%)	Epaisseur (nm)	Référence
Fe–18Cr–13Ni*	100 L O_2 puis 0.05 H_2SO_4 + 30 mins à E_{pass}	Fe–72Cr	1.6	[102]
Fe–17Cr–14.5Ni–2.3Mo(100)	0.05 M H_2SO_4 + 2 hours à E_{pass}	Fe–67Cr–3.6Mo	1.9	[17]
	0.05 M H_2SO_4 + 20 heures à E_{pass}	Fe–72Cr–4.5Mo	1.8	
Fe–20Cr–12Ni–1.6Mo	100 L O_2 puis 0.05 H_2SO_4 + 30 mins à E_{pass}	Fe–57Cr–15Mo	2.1	[101]
Fe–20Cr	10 mins dans NaOH à 0.5 V (vs SHE)	-	4.8	[76]

Tableau F3: Composition et épaisseur des films passifs formés sur les aciers inoxydables. *Il convient de noter que lorsqu'une orientation cristallographique n'est pas donnée, l'échantillon est supposé être de nature polycristalline.

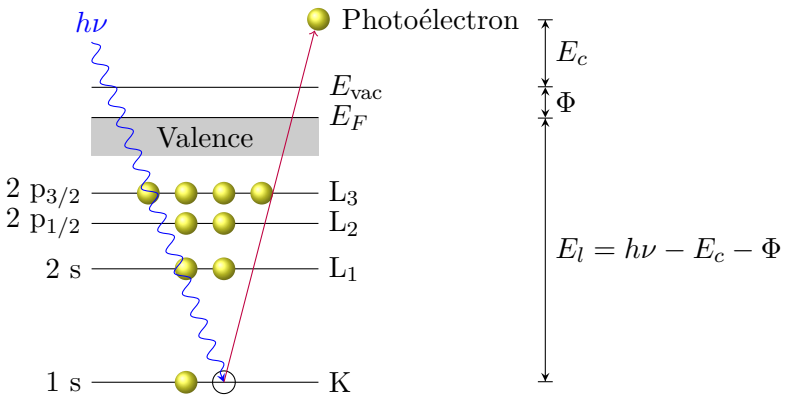

Figure F1: Diagramme schématique montrant le processus de photoémission d'un électron de cœur.

spectroscopy for chemical analysis), est une technique analytique basée sur le phénomène qu'est l'effet photoélectrique.

L'énergie de liaison d'un électron, E_l, est caractéristique de l'atome d'où il est émis (Figure F1). Lorsqu'un photon entrant, avec une énergie correspondant à celle d'un rayon X, frappe un échantillon, il provoque l'éjection d'un photoélectron de cœur avec une énergie cinétique, E_c. À condition de connaître l'énergie du photon entrant, $h\nu$, qui provoque l'excitation, et le travail de sortie de l'échantillon, Φ_s, nous pouvons calculer l'énergie de liaison de l'électron émis :

$$E_l = h\nu - E_c - \Phi_s \tag{F1}$$

Le libre parcours moyen inélastique, λ, est défini comme la distance moyenne qu'un électron peut parcourir sans altérer son énergie cinétique. C'est la distance qu'un électron peut parcourir avant que son énergie ne décroisse à $1/e$ de sa valeur initiale. La probabilité qu'un électron puisse parcourir une distance, x, sans perdre d'énergie décroît de façon exponentielle avec la distance :

$$p(x) = e^{-\frac{x}{\lambda}} \tag{F2}$$

La valeur de λ est très petite, typiquement autour de 1 nm pour les électrons avec une énergie cinétique de 10–1000 eV. Environ 95% des électrons détectés proviennent des premiers 3 λ, ce qui montre que l'XPS est une technique très sensible à la surface. La valeur de λ dépend de l'énergie des électrons et suit une courbe typique (qui varie légèrement selon le matériau), comme le montre la Figure F2.

Un spectre XPS a plusieurs caractéristiques notables. Les principaux pics d'intérêt sont ceux qui sont le résultat direct de la photoémission des électrons. Il convient de noter que les énergies de liaison sont caractéristiques de l'environnement dans lequel se trouvent les atomes. L'électron d'un atome oxydé aura une énergie de liaison plus élevée qu'un atome métallique, car il y a

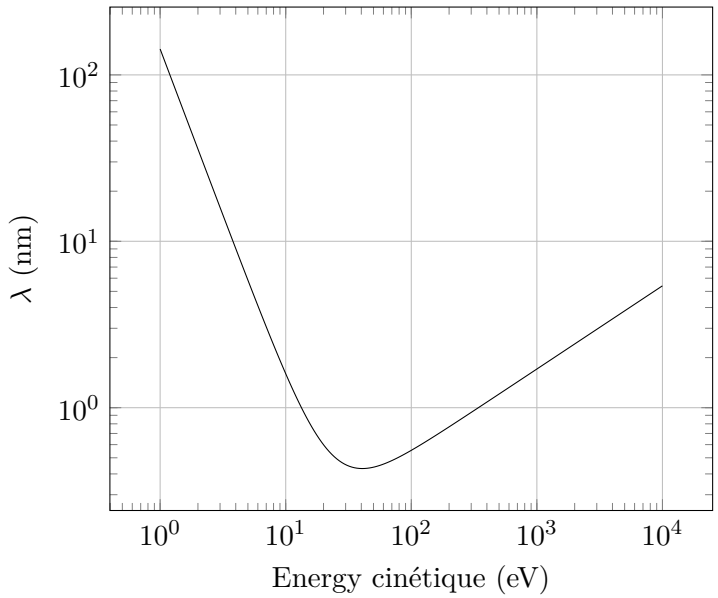

Figure F2: Variation du libre parcours moyen inélastique en fonction de l'énergie cinétique.

une interaction accrue entre le noyau et les électrons, en raison de la charge positive de l'atome oxydé.

Spectrométrie de masse des ions secondaires à temps-de-vol

La spectrométrie de masse des ions secondaires à temps-de-vol (ToF-SIMS — *time-of-flight secondary ion mass spectrometry*) est une technique analytique utilisée pour analyser la composition de surface et la distribution des éléments dans un solide ou une couche. La technique consiste à bombarder la surface avec des ions qui provoquent la libération d'atomes et d'ions.

La Figure F3 montre un diagramme schématique du principe du ToF-SIMS. Initialement, l'échantillon est bombardé par un faisceau d'ions primaires focalisé et pulsé à des énergies de l'ordre du keV. Traditionnellement en SIMS (*secondary ion mass spectrometry*), un canon à ions métal liquide est utilisé comme source d'ions primaires, et il y en a de trois types — Ga, Au et Bi, dont le choix dépendra des besoins de l'utilisateur. En frappant l'échantillon, le faisceau d'ions transférera une quantité de mouvement aux atomes de surface, entraînant l'émission d'ions secondaires et d'aggrégats ionisés. Les ions secondaires produits sont ensuite extraits et focalisés vers un miroir d'ions, d'où ils sont dirigés vers le détecteur. Un analyseur de temps de vol (ToF — *time-of-flight*) séparera les ions en fonction de leur vitesse, et comme le ToF est directement proportionnel à la racine carrée du poids, le temps nécessaire pour arriver dépendra de la masse de l'ion. Comme il est possible de mesurer le ToF à la nanoseconde, la masse atomique de la particule entrante peut être mesurée au millième de proton près, ce qui permet une identification facile des espèces. Un miroir ionique, qui minimise la propagation de l'énergie

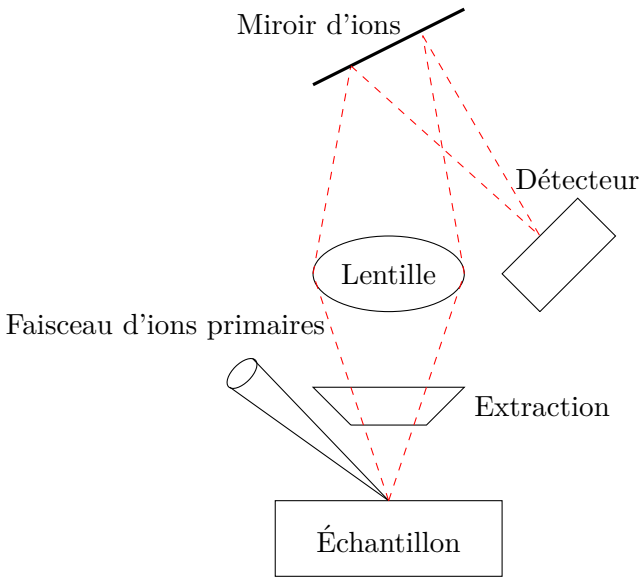

Figure F3: Diagramme schématique de ToF-SIMS.

cinétique des ions de même rapport masse/charge, est utilisé afin d'allonger la trajectoire de vol, et donc le temps de vol, permettant une séparation accrue des ions arrivant au détecteur, ce qui augmente la résolution en masse. Le résultat final est un spectre de masse couvrant de grandes gammes d'unités de masse atomique et dont l'intensité permet à l'utilisateur d'observer des fragments caractéristiques des espèces en surface. De même, l'intensité du signal d'un fragment donné peut être suivie en fonction du temps de décapage de la surface par un second faisceau d'ions primaires (ou de la profondeur, à condition d'avoir une vitesse de pulvérisation connue et constante), permettant à l'utilisateur d'observer sa répartition au sein du matériau qu'il analyse. Bien que le SIMS soit très sensible, ce n'est pas vraiment une technique quantitative car chaque matériau aura une probabilité d'ionisation unique et nécessite donc des comparaisons avec des matrices identiques ou similaires s'il doit être traité comme tel.

Microscopie à effet tunnel

La microscopie à effet tunnel (STM — *scanning tunnelling microscopy*) est une technique d'imagerie atomique, fréquemment utilisée en science des surfaces, qui utilise le phénomène connu sous le nom d'effet tunnel quantique pour produire des images reconstruites de surfaces avec une résolution latérale (< 1 Å) et verticale (1 pm) élévée. Le système se compose d'une pointe sonde qui balaye la surface à une distance proche (environ 1 nm) avec une polarisation appliquée, qui permet aux électrons de passer à travers la barrière de potential par effet tunnel pour produire un courant qui peut être utilisé pour reconstruire une image de la surface. La microscopie peut être réalisée dans une large gamme de conditions, du vide ultra poussé au

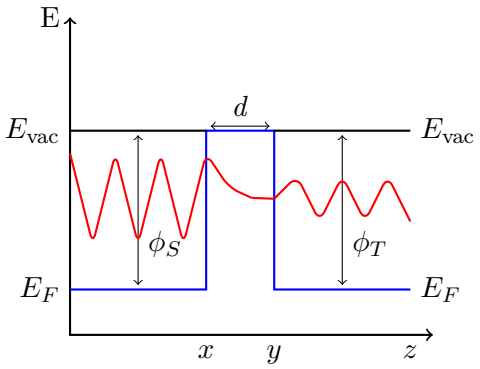

Figure F4: Barrière rectangulaire unidimensionnelle montrant l'effet tunnel quantique.

milleu liquide et à des temperatures de 0–1000 K.

La mécanique quantique nous dit qu'un électron peut se comporter à la fois comme une particule et comme une onde. Si nous considérons l'électron comme une particule, en utilisant le modèle classique, il ne peut pas traverser une barrière de potentiel. Cependant, si nous considérons l'électron comme une onde, en utilisant un modèle de mécanique quantique, l'électron peut passer à travers la barrière. Les électrons existent à des niveaux d'énergie spécifiques, $\psi_n(z)$, et dans un matériau macroscopique une bande d'électrons se forme. L'énergie de ces niveaux électroniques peut être déterminée à l'aide de l'équation de Schrödinger. Les électrons sont heureux de rester dans des états de faible énergie, et si l'électron doit être éjecté dans l'espace libre, alors une énergie correspondant à celle du travail de sortie, ϕ, doit être appliqué. Cependant, comme indiqué précédemment, ces électrons peuvent passer directement à travers la barrière d'énergie car une onde évanescente existe qui s'étend hors d'un matériau et peut être détectée à très courte distance. L'effet tunnel est détaillé dans Figure F4 en utilisant une barrière rectangulaire unidimensionnelle simplifiée. Si la pointe et l'échantillon sont suffisamment proches et sous un potentiel de polarisation, V, alors il y a un chevauchement des fonctions d'onde et il est donc possible qu'un électron puisse exister à l'intérieur ou de l'autre côté de la barrière. La probabilité qu'un électron à la position x puisse être trouvé à un autre point, y, séparé par une distance, d, est proportionnelle au carré de la fonction d'onde :

$$P \propto |\psi_n(z)|^2 e^{-2\kappa d} \tag{F3}$$

ou

$$\kappa = \frac{\sqrt{2m\phi}}{\hbar} \tag{F4}$$

Le STM fonctionne généralement dans l'un des deux modes, courant constant (Figure F5a) et hauteur constante (Figure F5b).

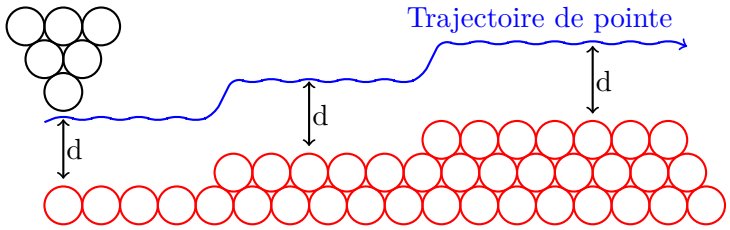

(a) Courant constant

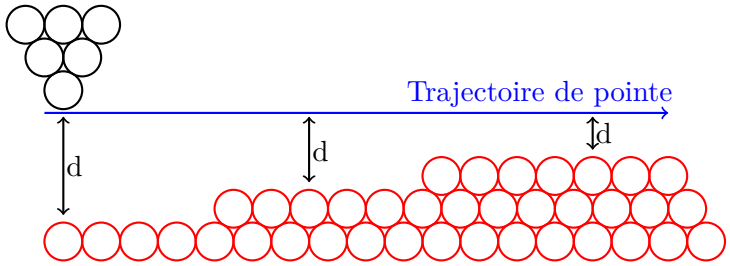

(b) Hauteur constante

Figure F5: Modes de fonctionemment STM

Diffraction d'électrons lents

La diffraction d'électrons lents (LEED — *low energy electron diffraction*) est une technique de surface utilisée pour déterminer la périodicité de surface des matériaux monocristallins et leur structure. Le LEED utilise un faisceau collimaté d'électrons de faible énergie, allant de 20–200 eV, pour bombarder la surface du monocristal permettant à l'utilisateur d'observer la rétrodiffusion élastique des électrons créant un motif dans l'espace réciproque et intercepté sous forme de taches sur un écran fluorescent. Les ondes électroniques seront diffusées par les atomes de surface qui se comportent comme des diffuseurs ponctuels du fait de leur forte densité électronique localisée.

Chapitre 3 : Conditions expérimentales

Equipement utilisé

La plupart des expériences ont été réalisées sur une plate-forme expérimentale constituée d'un système UHV Scienta-Omicron avec une boîte à gants Jacomex GP[Concept] directement attachée. Le système UHV a permis de préparer une surface propre (sans oxygène et sans carbone), pour ensuite être transférée aux instruments d'analyse de surface attachés. Le système UHV a une pression de base de $< 1 \times 10^{-10}$ mbar, qui est maintenue par une série de pompes turbo, ioniques et de sublimation Ti, et se compose de trois chambres. La boîte à gants attenante permettait aux échantillons préparés dans des conditions UHV de subir des traitements électrochimiques sans exposition à l'air ambiant.

La chambre de préparation est l'endroit où la surface a été préparée avant l'utilisation expérimentale. Attachée à la chambre se trouve une source de pulvérisation d'ions à cathode froide ISE 5, capable de fonctionner entre 0,3 et 5 keV, qui est utilisée pour bombarder la surface avec des ions argon qui éliminent les contaminants de surface tels que l'oxygène et le carbone. Si nécessaire, l'échantillon peut ensuite être recuit jusqu'à 1400 °C, via un chauffage radiatif par l'arrière de l'échantillon. Le recuit est généralement effectué afin de réorganiser la structure de surface. Cette chambre abrite également le système LEED, avec des mesures effectuées à l'aide d'un appareil Scienta-Omicron SPECTALEED.

Comme son nom l'indique, la chambre d'analyse XPS est l'endroit où les mesures XPS ont été effectuées. Le système utilise un spectromètre Argus et un détecteur Argus, contrôlés à l'aide du logiciel MATRIX, tous fabriqués par Scienta-Omicron. Le système dispose de trois sources de rayons X disponibles — Mg Kα (1253,6 eV), Al Kα (1486,6 eV) et un Al Kα monochromatisé (1486,6 eV), cette dernière étant celle utilisée pour toutes les mesures au cours de l'étude.

Les mesures STM ont été effectuées à l'aide d'un Scienta Omicron VTM XA modifié, contrôlé par un système de contrôle Scienta Omicron MATRIX SPM. La position du scanner est ajustée par un moteur piézo linéaire à 3 axes. Les modifications apportées au STM, telles que le plaquage d'or des composants pour empêcher la corrosion, permettent d'effectuer des mesures in situ où la surface est sondée tout en étant exposée à des gaz à des pressions allant jusqu'à 1 $\times 10^{-6}$ mbar. Le système est également capable d'effectuer des mesures à haute température, avec des conditions de fonctionnement allant de RT–700 °C. Des pointes en tungstène ont été utilisées, avec des impulsions de tension et un balayage à haute tension utilisés pour la préparation des pointes.

Accolée à la chambre de préparation se trouve la boîte à gants Jacomex GP[Concept], où ont été effectués les traitements électrochimiques. L'intérieur de la boîte à gants est rempli d'argon, avec une pression de fonctionnement d'environ 250 Pa et avec des niveaux minimum d'oxygène et d'eau (0–10 ppm). En présence d'un électrolyte aqueux, une augmentation de l'humidité et de l'oxygène d'environ un ordre de grandeur a été observée.

Les mesures ToF SIMS ont été effectuées sur un spectromètre ToF SIMS V fabriqué par IONTOF GmbH-Münster. Le système UHV fonctionne généralement à 10^{-9} mbar, et se compose d'une chambre de préparation et d'une chambre d'analyse, la première couplée à une boîte à gants sous atmosphère d'argon. La chambre d'analyse est équipée d'un canon à ions primaires Bi^+ pulsé, d'un canon à ions de pulvérisation Cs^+, d'un tube de vol, d'une horloge informatique de haute précision et d'un analyseur de masse à temps de vol. Un récipient rempli d'Ar et étanche à l'air a été utilisé pour transférer l'échantillon entre les boîtes à gants des deux plateformes d'analyse afin d'éviter l'exposition à l'air ambiant.

Procédure éxperimentale

La majorité du travail a été réalisée sur le même monocristal orienté 100 avec une composition en masse de Fe–18Cr–14Ni–1,3Mo (at%), qui est un bon modèle pour la nuance d'acier inoxydable AISI 316L. L'échantillon a été préalablement synthétisé et orienté à l'Ecole des Mines de Saint-Etiene en utilisant l'usinage par étincelles et la diffraction des rayons X de Laue. D'autres échantillons, tels qu'un polycristal Fe–20Cr–12Ni–1.6Mo et un monocristal Fe–18Cr–13Ni (100), ont été utilisés pour diverses références et travaux collaboratifs.

Avant tout traitement de l'échantillon, il était nécessaire de préparer d'abord une surface propre, c'est-à-dire une surface plane, bien organisée, exempte de contaminants. Ceci a été réalisé via des cycles de pulvérisation ionique et de recuit à haute température dans la chambre de préparation du système UHV. Afin d'éliminer d'abord les contaminants, l'échantillon a été soumis à une pulvérisation Ar^+ (1–5 keV, P_{Ar}=6×10^{-6} mbar, 8–70 μA, 10 min). L'étape suivante, utilisée pour réorganiser la surface, une nécessité due à la nature destructive de la pulvérisation ionique, impliquait le recuit de l'échantillon (700 °C, 10 min) via un chauffage radiatif de la face arrière. La vérification de la composition de la surface était systématiquement réalisée par analyse XPS, tandis que l'état structural était vérifié par LEED et STM.

Une fois qu'une surface propre et bien organisée était obtenue, l'échantillon était alors prêt à être oxydé ou étudié par STM ou LEED. Toutes les oxydations contrôlées ont été réalisées dans la chambre d'analyse du système UHV, où il est possible de contrôler la température ainsi que la pression exacte et le temps d'exposition à l'oxygène gazeux (pureté 99,999%). L'oxygène a été introduit via une vanne de fuite connectée à la chambre à une pression $P_{O_2} = 10^{-8}$ mbar. L'exposition exacte est calculée en traçant P_{O_2} en fonction du temps (s), puis en calculant l'aire sous la courbe. L'exposition est ensuite convertie en unités de langmuir (L), où 1 L correspond à une exposition de 1×10^{-6} Torr pendant une période d'une seconde. L'unité de Langmuir est dérivée de la connaissance que si chaque molécule collait à la surface, c'est-à-dire un coefficient de collage de un, alors une exposition de 1 L entraînerait la formation d'environ une monocouche. Des oxydations contrôlées dans le système UHV ont été réalisées à température ambiante (RT) et à 250 °C. Il a également été possible de suivre la cinétique de réaction de l'oxydation en exposant l'échantillon directement dans la chambre XPS et utilisant le mode de mesure Snapshot. En plus de l'oxydation via des moyens contrôlés dans la chambre UHV, un oxyde natif a également été formé à des fins de comparaison. Pour cela, la surface propre est exposée à l'air ambiant, ou à l'atmosphère de la boîte à gants. Un film d'oxyde se forme alors sur la surface en raison des réactions avec O_2 et H_2O. Les expositions à l'environnement de la boîte à gants duraient généralement moins de 10 minutes.

La cellule électrochimique a été conçue dans le but d'être compatible avec un échantillon qui pourrait facilement être transféré dans le système UHV sans délai significatif. La cellule faite maison peut contenir 350 μl d'électrolyte et est faite en polychlorotrifluoroéthylène, un polymère à base de fluor, communément appelé Kel-F. La zone de travail de l'électrode de 16 mm^2 est définie par un joint torique en Viton. Cette micro-cellule était contrôlée par un potentiostat Picostat et un logiciel Picoscan provenant d'Agilent Technologies. Deux fils de platine ont été utilisés comme électrode de référence et contre-électrode. L'électrode de référence, préalablement calibre comme E/SHE = E/Pt +0.75 V au moyen de la courbe de polarisation obtenue pour le cuivre dans 0.1 M NaOH, est rapporté comme étant stable [140]. La cellule a toujours été nettoyée avant utilisation, d'abord dans un mélange 3 à 1 de H_2SO_4 concentré et H_2O_2, et d'autre part dans du HNO_3 concentré, avant d'être rincée à l'eau pure. Après un certain temps, les électrodes ont été remplacées en raison de la dégradation du métal. Diverses mesures et traitements électrochimiques ont été mis en œuvre pour analyser les propriétés de corrosion du matériau. Un électrolyte 0,05 M H_2SO_4 a été utilisé dans tout les cas. Pour certaines analyses, du NaCl a été ajouté à l'électrolyte pour observer l'influence de la présence d'ions chlorure sur la formation d'un film passif. Un paramètre important à prendre en compte dans l'étude de la corrosion est le potentiel de circuit ouvert (OCP — *open circuit potential*), communément appelé potentiel de corrosion. Ce paramètre est exactement ce qu'il dit — c'est le potentiel adopté par l'interface dans un circuit ouvert par équilibrage des courants des réactions cathodiques et anodiques. Comme aucune polarisation externe n'est appliquée, lorsque l'électrode est placée dans l'électrolyte, elle adopte une valuer OCP qui évolue en fonction de la stabilisation ou de la dégradation de l'interface. L'échantillon a été systématiquement placé dans l'électrolyte pendant 30 minutes afin de se stabiliser à l'OCP avant d'être analysé par XPS ou ToF SIMS. La passivation anodique a été réalisée par saut de potentiel à l'OCP + 0,2 V et maintien sur une période de 30 minutes après stabilisation à l'OCP. Cette valeur du potentiel de passivation a été choisie car elle se situe dans le milieu du domaine passif, tel que déterminé par voltamétrie. Les mesures de polarisation linéaire ont été effectuées à une vitesse de balayage de 5 $mV{\cdot}s^{-1}$, de -1.2 à $+1,2$ V. Le protocole adopté de pré-oxydation controlée suivie d'immersion à OCP puis de passivation anodique permet une comparaison directe de l'effet de la méthode de pré-oxydation sur les propriétés du film passif. La Figure F6 montre le protocole sous forme de schéma.

Chapitre 4 : Une surface en constante évolution

Le recuit de l'échantillon FeCrNiMo(100), nécessaire à la réorganisation de la surface, a entraîné la ségrégation du chrome et de l'azote à la surface. Nous avons pu suivre la ségrégation

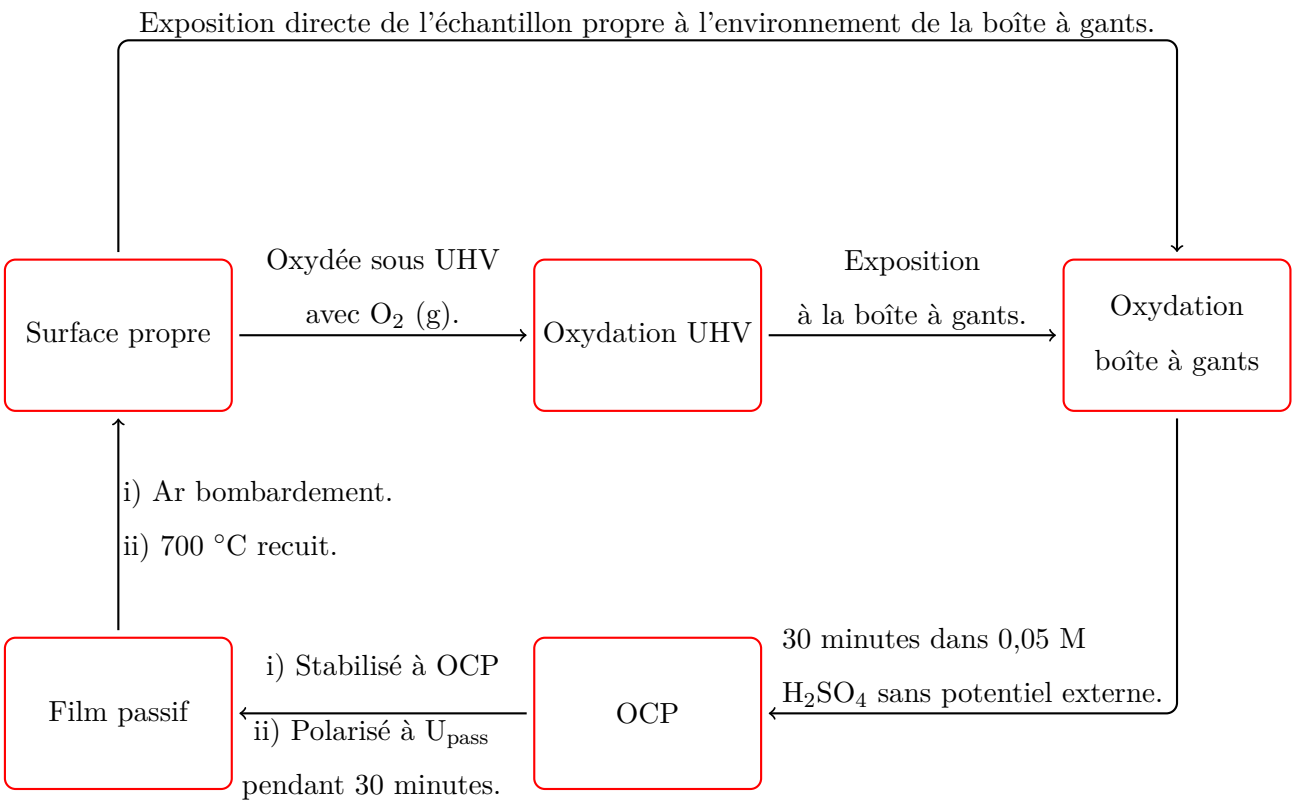

Figure F6: Schéma du protocole expérimental utilisé pour comparer l'effet de la méthode d'oxydation avant la passivation.

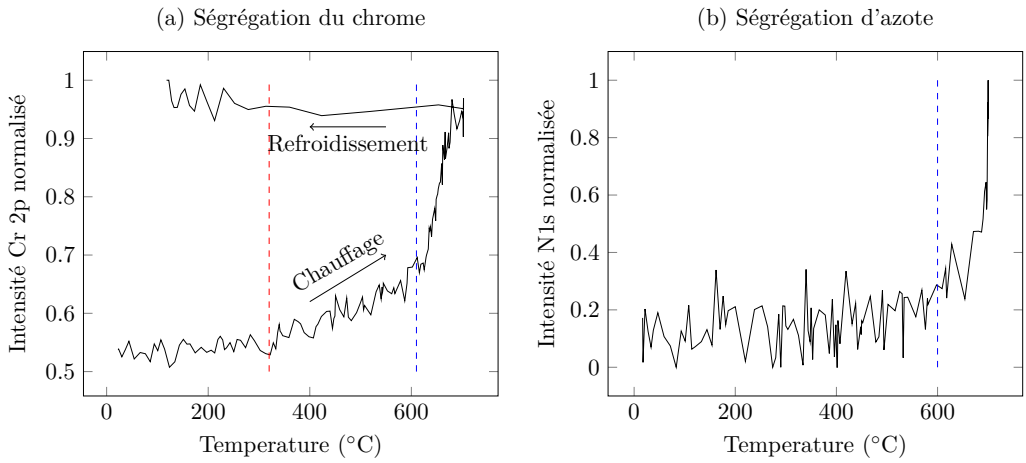

Figure F7: (a) Intensité Cr 2p normalisée en fonction de la température de recuit, (d) Intensité N 1s normalisée en fonction de la température de recuit.

de chaque élément à l'aide de mesures XPS en mode snapshot, comme le montre la Figure F7. L'intensité du Cr 2p commence à augmenter à 300 °C, température marquée par la ligne pointillée rouge sur la Figure F7a. À partir de cette température, l'intensité de Cr 2p augmente régulièrement jusqu'à environ 610 °C, température marquée par la ligne pointillée bleue. Au-delà de 610 °C, le taux de ségrégation du chrome semble augmenter. Ces deux phases indiquent deux mécanismes différents de ségrégation du chrome pendant le recuit de l'échantillon d'acier inoxydable. L'intensité du signal ne diminue pas pendant le refroidissement de l'échantillon. En ce qui concerne l'augmentation de l'intensité de l'azote, nous ne voyons aucun changement significatif de l'intensité jusqu'à ce qu'une température d'environ 600 °C soit atteinte. Le début de cette phase est indiqué par la ligne pointillée bleue sur la Figure F7b, et correspond à la deuxième augmentation du taux de ségrégation du chrome, suggérant une co-ségrégation des éléments. Le taux de ségrégation de l'azote atteint sa valeur maximale entre 600 et 700 °C, dans le même intervalle que celui du chrome, confirmant la co-ségrégation dans cette plage de température. Il a été suggéré dans des travaux antérieurs que la co-ségrégation du chrome et de l'azote entraîne la formation de composants de nitrure de chrome qui favoriseraient l'oxydation sélective du chrome [90, 92, 141].

Cependant, ce n'est pas là que se termine l'évolution de la composition. Il a été constaté au cours de notre etude que les cycles cumulatifs de pulvérisation (à 1 keV) et de recuit (à 700 °C) conduisent à une diminution de la quantité de chrome et d'azote ségrégés à la surface, comme le montre la Figure F8a. La relation entre la diminution du chrome et la diminution de l'azote s'est avérée linéaire, comme le montre la Figure F8b, soulignant en outre que les mécanismes de diminution de la ségrégation des deux éléments sont liés.

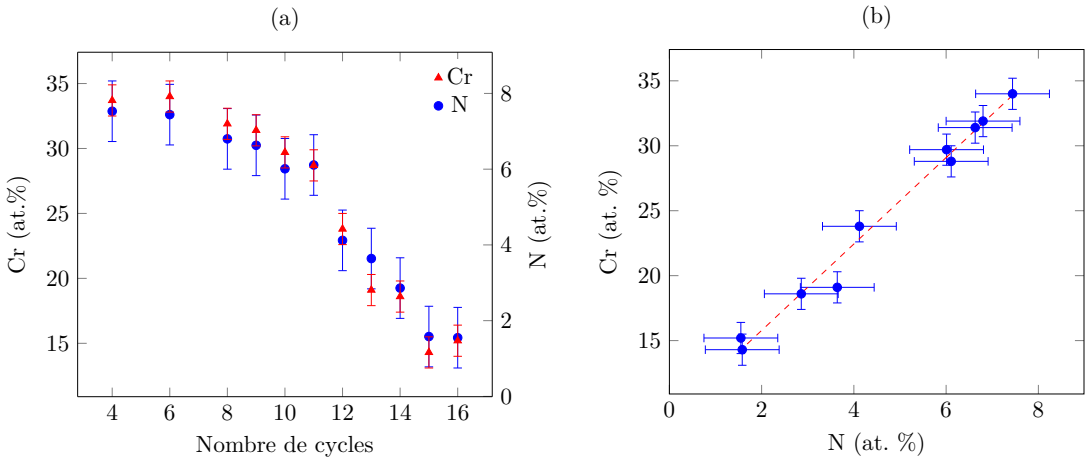

Figure F8: (a)Diminution du chrome et de l'azote en surface avec l'augmentation du nombre de cycles de pulvérisation (à 1 keV) et de recuit (à 700 °C) ; (b) relation entre la diminution du chrome et la diminution de l'azote.

Cette diminution du chrome et de l'azote ségrégés à la surface a un effet marqué sur la vitesse d'oxydation à température ambiante, comme l'illustre la Figure F9a qui montre l'évolution de l'intensité de la région O 1s en fonction de l'exposition à l'oxygène. On note tout d'abord que la surface à haute teneur en chrome (HC — *high chromium*), avec 31,9% de chrome et 6,8% d'azote (la composition calculée à partir des spectres complets est Fe–31,9Cr–7,7Ni–1,7Mo–6,8N (at %)), affiche une vitesse de réaction initiale très rapide jusqu'à une exposition d'environ 10 L, après quoi elle diminue rapidement avant de saturer à environ 25 L. En revanche, après huit autres cycles de pulvérisation (à 1 keV) et de recuit (à 700 °C) plus tard, portant le total à 16, nous avons une quantité considérablement réduite de chrome et d'azote à la surface (LC — *low chromium*), avec 15,2% de chrome et 1,6% d'azote (la composition calculée à partir des spectres complets est Fe–15,2Cr–14,4Ni–2.1Mo–1.6N). Le résultat est une vitesse de réaction initiale considérablement réduite et une montée beaucoup plus régulière jusqu'au point de saturation, qui, à environ 80 L, est plus du triple du point de saturation lorsque la surface HC était exposée à l'oxygène.

Le Tableau F4 rapporte la composition calculée du film d'oxyde et de la région d'alliage modifié, ainsi que l'épaisseur estimée du film d'oxyde. Ces valeurs ont été calculées à l'aide du modèle d'une seule couche d'oxyde de composition homogène. Il n'y a pas de différence très marquée dans l'épaisseur calculée des films d'oxyde, avec, respectivement, 1,3 et 1,5 nm estimés pour les oxydes LC et HC. Ces valeurs sont similaires à celles rapportées sur des surfaces similaires oxydées à RT [6, 14, 31, 88, 89, 102, 149, 150]. La composition calculée montre en outre que l'oxyde HC est beaucoup plus riche en chrome au point de saturation, avec 40% de la

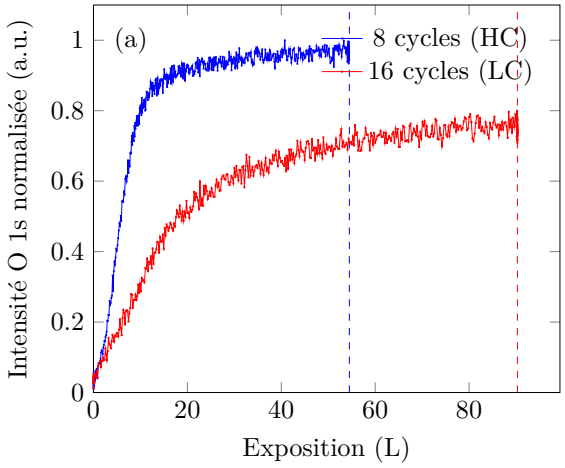

Figure F9: Evolution de l'intensité du spectre O 1s en fonction de l'exposition à l'oxygène.

Cycles	Epaisseur (nm) (±0.1)	Concentration relative (±2%)						
		Couche d'oxyde			Alliage modifié			
		Fe	Cr	Mo	Fe	Cr	Ni	Mo
8 (HC)	1.5	59	40	1	76	11	12	1
16 (LC)	1.3	81	18	1	72	9	17	2

Tableau F4: Epaisseur et composition de l'oxyde formé à saturation, pour des surfaces ayant préalablement subi 8 et 16 cycles de pulvérisation ionique et de recuit.

concentration relative attribuée à Cr_2O_3, ce qui est plus du double de la concentration relative de l'oxyde LC (18 %). Le manque de chrome dans le film d'oxyde formé après 16 cycles est uniquement compensé par une augmentation de la quantité relative de fer oxydé présent, sans augmentation notable de la quantité relative de molybdène oxydé présent dans le film. Le nickel reste non oxydé dans les deux cas. Le nickel augmente sa part de la concentration relative globale dans la région de l'alliage modifié (par rapport à la composition de surface propre de départ) dans les deux cas. De même, dans les deux cas la quantité de chrome dans l'alliage modifié diminue au fur et à mesure qu'il est consommé lors de l'oxydation, avec un effet beaucoup plus marqué sur la surface où l'on est parti avec une teneur en chrome élevée (HC=32% à 11%, LC =15% à 9%).

Heureusement, un certain contrôle de la composition initiale de la surface a pu être reproduit, bien qu'au prix d'un certain temps. Il a été constaté qu'en polissant mécaniquement l'échantillon ou en effectuant de nombreux (!) cycles de pulvérisation ionique à 5 keV, la composition revenait à la teneur élevée en chrome. Ceci est cohérent avec l'idée que l'azote qui ségrège avec le chrome provient de la région sous-surfacique et s'épuise par diffusion. Les cycles multiples conduisent à

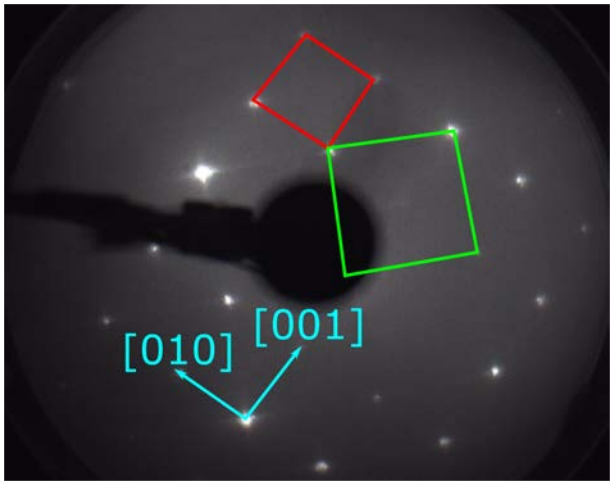

Figure F10: Diagramme LEED (120 eV) du FeCrNiMo(100), pulvérisé et recuit, avec une teneur élevée en chrome métallique à la surface, montrant une $(\sqrt{2} \times \sqrt{2})$R45° reconstruction (marquée par le carré rouge), à côté de la structure 1×1 non reconstruite (marquée par le carré vert).

l'épuisement de l'azote dans cette région, cependant, il est toujours présent plus profondément dans le volume de l'échantillon. En polissant mécaniquement l'échantillon et/ou en pulvérisant de manière plus agressive, c'est-à-dire à haute énergie, nous supprimons la région appauvrie par ségrégation ainsi que la surface supérieure et accédons à la région non appauvrie en dessous à partir de laquelle azote et chrome peuvent atteindre la surface.

Reconstruction de surface

La Figure F10 présente un diagramme LEED typique, obtenue à une énergie électronique de 120 eV, de l'échantillon FeCrNiMo(100) bien organisé et sans contaminant. Dans ce cas particulier, la surface était riche en chrome métallique. La surface est reconstruite selon une surstructure $(\sqrt{2} \times \sqrt{2})$R45°, indiquée par le carré rouge.

La Figure F11a montre une image STM typique de la structure de surface présente sur l'échantillon FeCrNiMo(100). L'image 100×100 nm montre des terrasses caractéristiques, d'orientation nominale (100), de largeur de 15–40 nm. La hauteur des marches est d'environ 0,40 nm, ce qui correspond à environ deux plans atomiques. La Figure F11b montre plus clairement une composition et/ou une structure différente au bord de la marche, avec des zones délimitées en bleu qui diffèrent du reste de la terrasse. Sur les terrasses elles-mêmes, nous pouvons observer des lignes périodiques suivant les deux directions [010] et [001]. Ces lignes sont mieux mises en évidence sur la Figure F11b, où la distance entre les lignes varie de 2,6 à 5,1 nm, le profil de hauteur suggérant qu'elles sont en creux.

La Figure F11c montre une image à résolution atomique de la surface FeCrNiMo(100), com-

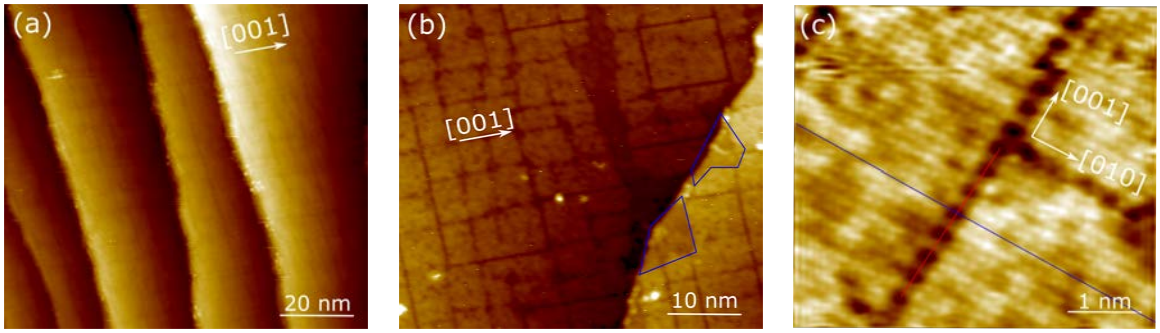

Figure F11: Images STM de la surface FeCrNiMo : (a) Structure en terrasse ; (b) Structure en bord de terrasse ; (c) image à résolution atomique des lignes de lacunes sur les terrasses.

portant deux lignes de lacunes bissectrices. Au point où les deux lignes se coupent, on remarque que la ligne selon la direction indiquée [010] se termine, tandis que la ligne selon la direction indiquée [001] continue de se propager. La largeur des dépressions est d'environ 0,50 nm, ce qui correspond à 2 à 3 rangées atomiques manquantes. Dans certaines zones, on peut distinguer la densité électronique trouvée à l'intérieur de la ligne de lacunes, mise en évidence par les points lumineux présents à l'intérieur du canal. La nature périodique de la densité électronique n'est pas toujours présente dans les lignes de lacunes, certaines possédant une densité électronique inférieure et une distribution plus aléatoire.

Chapitre 5 : Germination et croissance des oxydes

Ce chapitre traite de la germination et de la croissance des oxydes sur un échantillon de FeCrNiMo (100) à RT et 250 °C. Des expositions à l'oxygène ont été effectuées par étapes successives entre 0 et 100 L, avec des spectres XPS enregistrés pour chaque exposition.

Oxydation initiale

L'analyse par reconstruction des spectres XPS n'a pas été effectuée pour des expositions de 0–3 L car l'incertitude dans le processus était trop grande par rapport aux petits changements dans la forme du pic. Au lieu de cela, une méthode de normalisation et de comparaison des courbes expérimentales obtenues a été appliquée. Si nous considérons d'abord les expositions faites à la température ambiante, après 1 L d'oxygène, il n'y a aucun changement apparent dans la forme des spectres du fer (Figure F12a), du chrome (Figure F12b) ou du molybdène (Figure F12c). À 1 L, il y a une augmentation de l'intensité du signal O 1s, indiquant que l'oxygène interagit avec la surface. Ce changement peut être attribué à un mélange d'adsoprtion et de formation de germes d'oxydes à des niveaux indétectables dans les spectres métalliques. C'est après avoir

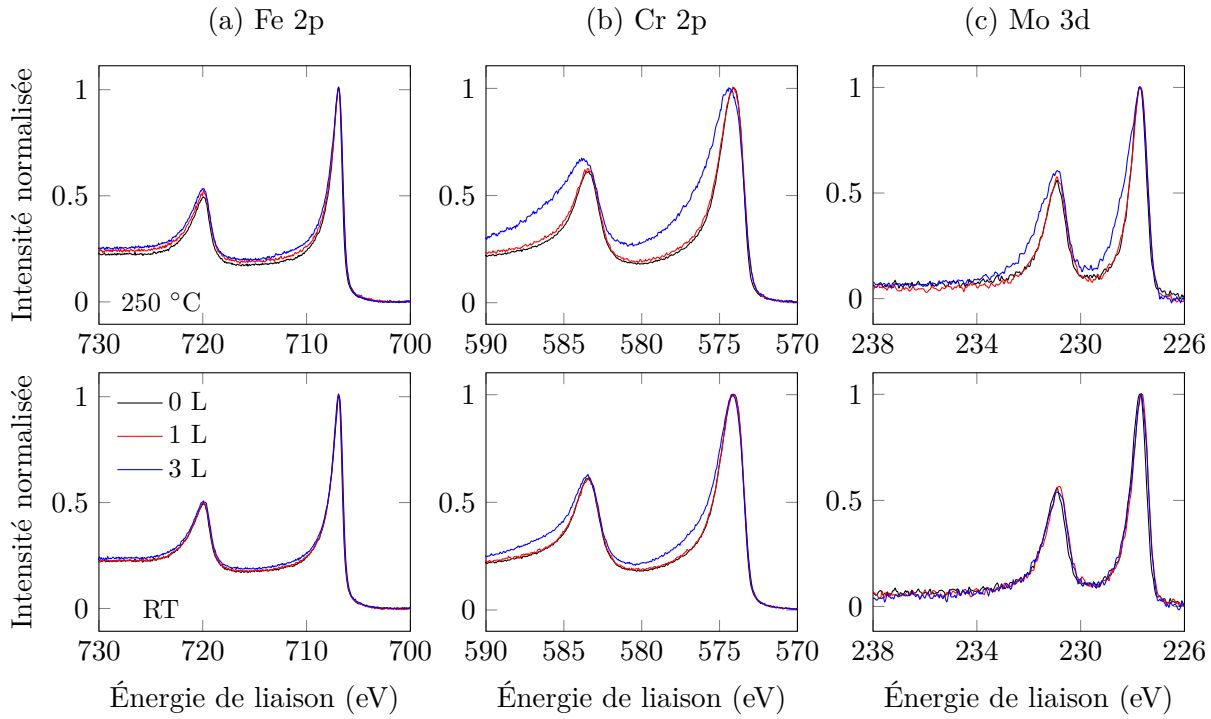

Figure F12: Comparaison des formes de pic pour les spectres de (a) Fe 2p, (b) Cr 2p et (c) Mo 3d pendant les premiers 3 L d'exposition à l'oxygène à RT (en haut) et 250 °C (en bas).

augmenté l'exposition à 3 L que l'on observe les premiers changements dans les spectres du fer et du chrome, le molybdène restant inchangé. À ce stade, il est impossible de relier ces changements à des espèces chimiques particulières avec une plus grande certitude. Concernant le fer, il est fort probable que l'on observe la nucléation des oxydes Fe^{2+} et Fe^{3+}, tels que FeO et Fe_2O_3. Nous pouvons seulement dire que les changements dans les pics de chrome à RT à ces faibles expositions sont dus à la présence croissante d'oxyde de chrome (très probablement Cr_2O_3) et de Cr(N) de surface. A température ambiante, il n'y a pas de changement évident dans le spectre du molybdène pendant les étapes initiales d'oxydation de l'échantillon d'acier inoxydable.

À 250 °C, le changement des spectres entre 0–3 L est plus rapide que celui observé à RT, comme le montre la Figure F12, indiquant une vitesse plus rapide de réaction. Après 1 L à 250 °C, les premiers changements apparaissent dans la forme des pics de fer et de chrome, le molybdène restant inchangé (Figure F12). Les changements observés peuvent une fois de plus être attribués à la formation de germes d'oxydes, et dans le cas du chrome, à un changement de la structure de surface et à la faible augmentation de la quantité des espèces de chrome contenant de l'azote. C'est après une exposition de 3 L que l'on observe des changements plus importants. Nous devons d'abord commenter les spectres d'azote de la Figure F13, où la vitesse de changement de la quantité d'azote surface comparée à celles de l'azote de sous-surface, de l'azote minoritaire et de l'azote interstitiel est beaucoup plus rapide à cette température qu'à la

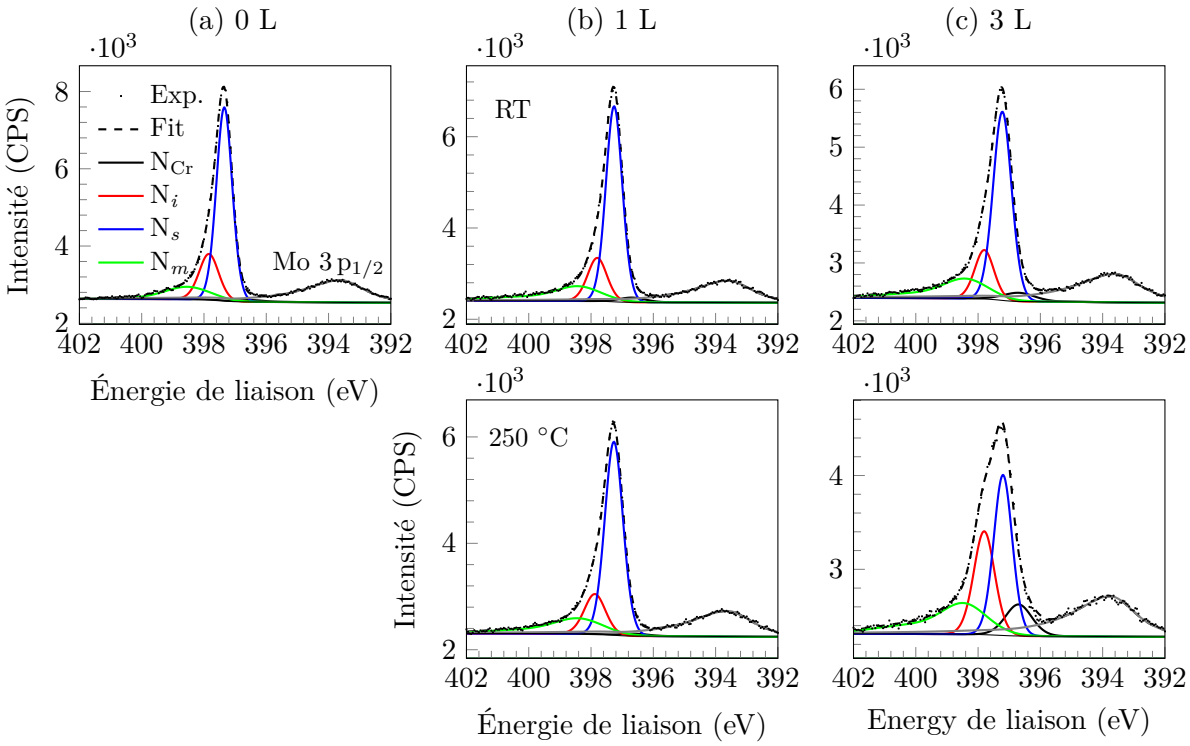

Figure F13: Spectres XPS haute résolution de la région N 1s pendant les premiers 3 L d'exposition à l'oxygène à RT (en haut) et 250 °C (en bas), montrant les quatre composants identifiés, N_{Cr} (espèces de chrome contenant de l'azote), N_i (azote interstitiel), N_s (azote de sous-surface) et N_m (azote minoritaire).

température ambiante. Cette apparition rapide de Cr(N) de surface peut expliquer en partie la différence de réactivité, le nitrure de chrome de surface étant proposé comme site de germination pour Cr_2O_3 [91,92]. C'est à ce stade, après le début de l'oxydation du chrome et du fer que l'on observe les premiers changements notables dans le spectre du molybdène sur la Figure F12c, avec un élargissement asymétrique des pics Mo 3d à des énergies de liaison plus élevées par rapport au métal à 227,6 eV, indiquant que la formation d'oxyde a commencé.

Évolution des éléments

La Figure F14 montre l'évolution des espèces formées en fonction de l'exposition à l'oxygène. Pour le fer, nous identifions trois espèces, Fe, Fe^{2+} et Fe^{3+}. Une oxydation à plus haute température favorise considérablement l'enrichissement en Fe^{3+} du film d'oxyde. Concernant le chrome, trois espèces sont également identifiées, Cr, Cr^{3+} et CrN. Une fois de plus, la température plus élevée entraîne la production d'une plus grande quantité d'oxyde, bien que l'effet soit moins important par rapport au fer. La quantité relative de Cr(N) est constante à partir d'environ 10 L. Mo, Mo^{4+} et Mo^{6+} sont identifiés dans les spectres du molydebnum, avec des quantités

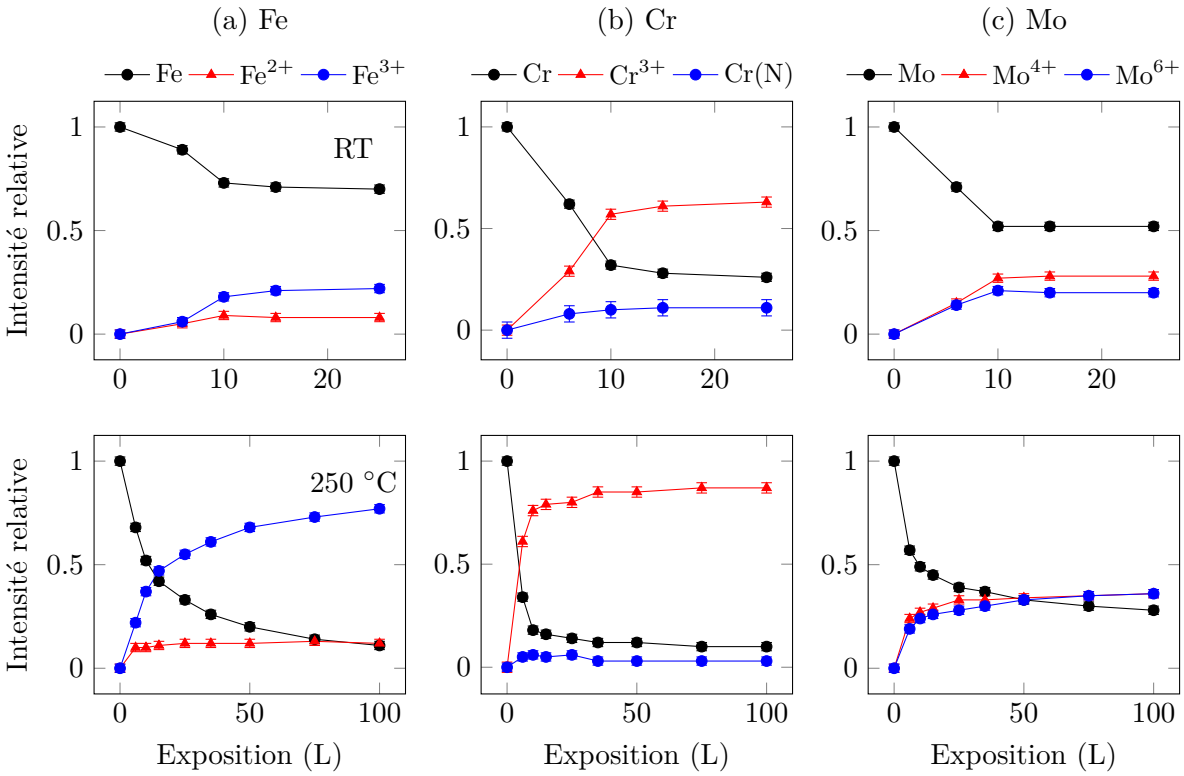

Figure F14: Évolution des espèces de (a) fer, (b) chrome et (c) molybdène à RT (en haut) entre 0–25 L, et 250 °C (en bas) entre 0–100 L d'exposition à l'oxygène.

approximativement égales de chaque espèce oxydée.

Composition de la couche d'oxyde

La Figure F15 montre la variation de la composition à la fois du film d'oxyde et de l'alliage modifié en dessous en fonction de l'exposition à l'oxygène à RT et 250 °C. A température ambiante (Figure F15a), l'oxyde est enrichi en Cr^{3+}, qui constitue environ 48% du film après une exposition de 6 L. Au même stade, les quantités de Fe^{2+} et Fe^{3+} sont égales, chacune représentant environ 16%. Cr(N), qui dans ce cas a été affecté à la couche d'oxyde, est à son pourcentage maximum en termes de contribution à la composition globale du film formé après une exposition de 6 L. Le molybdène oxydé ne dépasse jamais quelques pour cent de la composition du film, ce qui indique qu'à aucun moment il n'est enrichi. Entre 6 et 15 L, la croissance de Fe^{3+} prédomine, ce qui conduit à augmenter son pourcentage global de la composition. À aucun moment pendant le processus d'oxydation, le molybdène n'est significativement enrichi dans le film d'oxyde. Au point de saturation, nous avons un film d'oxyde de composition Fe–50Cr–2Mo, avec une épaisseur calculée de 0,8 nm. Comparativement, lorsque l'oxyde formé à 250 °C a une épaisseur approximative de 0,7 nm (après une exposition de 6 L), la composition est

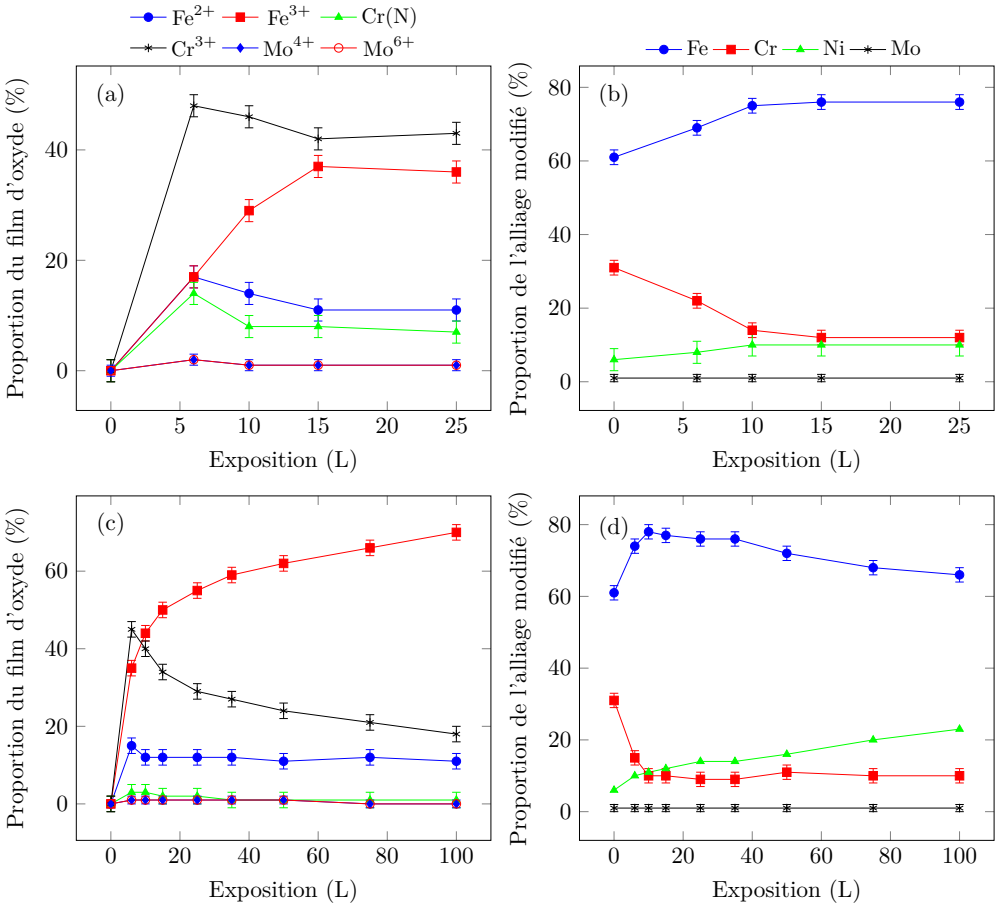

Figure F15: Composition de (a) l'oxyde à RT, (b) l'alliage modifié à RT, (c) l'oxyde à 250 °C, et (d) l'alliage modifié à 250 °C, en fonction de l'exposition à l'oxygène.

calculée comme étant Fe–48Cr–2Mo, ce qui est presque identique à la composition de l'oxyde de 0,8 nm d'épaisseur formé à RT. La composition de l'alliage modifié à température ambiante, représentée sur la Figure F15b, est initialement riche en chrome à la suite du processus de recuit effectué pour préparer la surface propre avant oxydation. Cet élément est rapidement consommé pendant les premiers stades de la formation d'oxyde et à 10 L, la contribution du chrome dans l'alliage modifié est passée de 31% sur la surface propre à seulement 14%, ce qui est beaucoup plus proche de celui de la quantité en volume. Au fur et à mesure que l'intensité du chrome métallique diminue, celle du fer augmente, atteignant un pic de contribution de 76%. Parallèlement, nous commençons à voir l'alliage modifié s'enrichir en nickel métallique, ce qui est dû au fait que le fer et le chrome de l'alliage sont oxydés préférentiellement. Au point de saturation, l'alliage modifié a une composition de Fe–12Cr–10Ni–2Mo.

Le comportement observé au cours des 6 premiers L d'exposition à l'oxygène à 250 °C est similaire (Figure F15c), conduisant à un film constitué à 45% d'oxyde de chrome. Alors qu'à RT nous avons vu des quantités égales de Fe^{2+} et Fe^{3+} à cette exposition, l'évolution est différente à

température plus élevée, avec formation de nettement plus de Fe^{3+}. Comme attendu, la quantité relative de Cr(N) culmine à de faibles expositions à l'oxygène avant de se réduire à des quantités négligeables. Au-delà d'une exposition de 6 L, la formation d'oxyde Fe^{3+} devient dominante, aidée par la mobilité accrue du fer à travers le réseau d'oxyde. La quantité relative de Fe^{2+} reste stable à mesure que l'exposition à l'oxygène augmente. Là encore, aucun enrichissement en molybdène n'est observé. Après une exposition de 100 L à 250 °C, la composition du film d'oxyde est Fe–19Cr–1Mo. L'épaisseur du film a été calculée comme étant de 2,1 nm (±0,1 nm). La composition calculée suggère que le molybdène oxydé n'est pas enrichi dans le film. En ce qui concerne la composition de l'alliage modifié à 250 °C (Figure F15d), nous voyons essentiellement une poursuite des tendances observées à température ambiante où nous avons la diminution initiale de la quantité relative de chrome associé à un enrichissement en fer et en nickel. Au-delà de 6 L, lorsque la croissance de l'oxyde de fer commence à dominer et que le fer métallique est consommé, l'absence de formation d'oxyde de nickel entraîne un enrichissement significatif de ect élément sous le film d'oxyde. Après une exposition de 100 L à 250 °C, la composition de l'alliage modifié était Fe–10Cr–23Ni–1Mo, indiquant qu'une oxydation supplémentaire augmente la quantité de nickel métallique enrichi dans la région de l'alliage modifié sur un échantillon modèle de l'acier inoxydable 316L.

L'analyse de la variation angulaire des spectres à haute résolution, enregistrés à des angles d'émission des photoélectrons de 45° et 90°, a été réalisée pour vérifier la distribution en profondeur des espèces au sein du film d'oxyde. Il s'est avéré que Cr_2O_3, Cr(N) and Fe^{2+} étaient plus enrichis à l'interface métal-oxyde, dans la partie interne du film au-dessus de laquelle Fe^{3+} se formait plus facilement. Les espèces Mo^{4+} et Mo^{6+} se répartissent de façon homogène au travers du film d'oxyde.

Sur la base de toutes ces observations et de travaux antérieurs sur d'autres échantillons modèles d'aciers inoxydables, il est possible de proposer un mécanisme pour les toutes premières étapes d'oxydation des aciers inoxydables FeCrNiMo, le premier rapporté du genre. Lors de l'introduction d'oxygène, la surface propre, bien organisée et enrichie en chrome et en azote à la suite de la co-ségrégation de ces éléments lors du processus de recuit, est modifiée en raison de la formation d'espèces de chrome contenant de l'azote qui se comportent comme des sites de germination de l'oxyde de chrome, probablement Cr_2O_3. Au cours de cette phase de germination, nous observons également la formation d'oxyde de fer, le fer se trouvant à la fois à l'état d'oxydation +2 et +3. Nos résultats suggèrent que l'oxydation du molybdène est retardée jusqu'à ce que le processus ait déjà commencé sur le fer et le chrome. Une fois que le film d'oxyde devient suffisamment épais, la croissance du film d'oxyde est augmentée, alimentée par

l'augmentation de la quantité d'oxyde Fe^{3+} qui peut être directement oxydé à partir du métal ou via une oxydation supplémentaire de Fe^{2+}. Une fois qu'une épaisseur d'oxyde d'environ 0,8 nm est atteinte, ce qui correspond dans ce cas à une exposition de 10–15 L, le transport du fer à travers le film d'oxyde n'est plus possible à température ambiante et la surface sature. A 250 °C, la croissance initiale de l'oxyde suit un régime similaire ; cependant, la température plus élevée permet une mobilité accrue des atomes à travers le film d'oxyde, ce qui entraîne une oxydation supplémentaire de l'échantillon, qui à ce stade peut principalement être attribuée à l'oxydation du fer. Au fur et à mesure que l'épaisseur de l'oxyde augmente, même à ces températures élevées, le transport des atomes à travers le réseau d'oxydes devient difficile et la vitesse de croissance de l'oxyde chute considérablement.

Chapitre 6 : Rôle de la pre-oxydation sur le comportement passif

Caractérisation de l'oxyde natif

L'oxyde natif a été obtenu dans notre cas par exposition de la surface propre à l'environnement de la boîte à gants pendant une période de cinq minutes. Après oxydation de la surface, l'échantillon a été re-transféré dans la chambre UHV pour analyse XPS. La composition de l'oxyde natif ainsi obtenu est Fe–37Cr–1Ni–1Mo, et son épaisseur 1,5 nm, ce qui est nettement plus épais et plus riche en fer oxydé que pour le film d'oxyde formé à saturation dans les conditions UHV (composition de Fe–50Cr–2Mo et épaisseur de 0.8 nm). Contrairement à l'oxyde préparé par UHV, des espèces hydroxydées telles que FeOOH et $Ni(OH)_2$ ont été observées. Il n'y avait pas de différences très marquées dans la composition de l'alliage modifié sous-jacent.

Passivation électrochimique de l'oxyde natif

Après formation et caractérisation de l'oxyde natif, l'échantillon a ensuite subi un premier traitement électrochimique où il a été maintenu à l'OCP pendant 30 minutes dans 0,5 M H_2SO_4. Après caractérisation du film d'oxyde formé à l'OCP, l'échantillon a ensuite été passivé anodiquement.

Si nous considérons l'évolution spectrale du fer après la première exposition à OCP dans la solution acide, la principale chose à noter est l'augmentation de la quantité relative de fer métallique. Ceci est dû à la dissolution préférentielle de Fe^{3+} dans la solution acide et est en bon accord avec d'autres rapports trouvés dans la littérature [89, 102, 170]. De même, nous n'observons plus aucun des FeOOH trouvés présents dans l'oxyde natif. Dans le même temps, nous observons également une augmentation de la quantité relative de Fe^{2+} présente. Cela peut

être dû au fait que, si pour l'oxyde natif Fe^{2+} se forme tôt et près de l'interface oxyde-alliage, en accord avec à ce que nous avons vu lors de la croissance par étapes de l'oxyde formé dans des conditions UHV, il est alors protégé de la dissolution par les couches Fe^{3+} qui se forment au dessus. Après la deuxième exposition à la solution et passivation anodique, la croissance de l'oxyde est maintenant générée car les conditions plus oxydantes appliquées contrecarrent la dissolution préférentielle de Fe^{3+}. On observe alors une diminution de la quantité relative de fer métallique par rapport au film formé à l'OCP (66% à l'OCP contre 59% sur le film passif). Les quantités relatives de Fe^{2+} restent les mêmes, dans les deux cas la valeur est environ 7% du total. La production de Fe^{3+} peut être le résultat direct de l'oxydation du fer métallique ou également via une oxydation supplémentaire de Fe^{2+} qui est produit de manière stable.

Après exposition à l'OCP, la quantité relative de chrome métallique reste la même à 20–22%, le principal changement étant l'hydroxylation de l'oxyde de chrome, formant $Cr(OH)_3$. Cette observation est partagée par plusieurs rapports dans la littérature [17, 88, 89, 102]. On peut encore noter la présence de CrN, bien qu'en quantité légèrement réduite. Cependant, après passivation anodique, les spectres N 1s sont devenus moins intenses et, par conséquent, le calcul de la quantité de Cr(N) comporte une grande incertitude. La passivation anodique de la surface entraîne une oxydation supplémentaire du chrome, qui ne représente désormais que 13% du total. Une hydroxylation supplémentaire de l'oxyde de chrome est observée, ce qui est contraire à ce qui est souvent noté, où la passivation anodique favorise généralement la dehydroxylation [17, 31, 88, 89, 162].

L'analyse des spectres du molybdène a été complexe en raison de la présence de la région S 2s chevauchante et de la présence d'anions sulfate ($SO_4{}^{2-}$). Nous pouvons néanmoins analyser l'évolution des spectres du molybdène après traitements électrochimiques. Après maintien à l'OCP pendant 30 minutes, nous observons que le molybdène est davantage oxydé, la quantité relative de molybdène métallique diminuant de 51% à 31%. Ceci est contraire au comportement du fer et du chrome qui respectivement augmente et maintient les quantités relatives de métal trouvées à la surface. Le molybdène dans ses états d'oxydation +4 et +6 est en quantité égale à environ 25% de la concentration totale de molybdène. L'espèce hydroxyde précédemment discutée contribue le moins à la concentration totale des quatre espèces présentes. Après passivation anodique de la surface, une oxydation supplémentaire de Mo^{4+} est favorisée, sa quantité relative diminuant à seulement 12%. En parallèle, nous constatons une augmentation de Mo^{6+}, qui contribue désormais à 40% de la concentration totale de molybdène. La quantité relative de métal présent est restée la même, dans la marge d'erreur. La quantité d'hydroxyde a légèrement diminué.

Le modèle de calcul d'épaisseur et de composition peut être appliqué aux films passifs formés électrochimiquement ainsi qu'à l'oxyde natif. Comme déjà discuté, la composition de l'oxyde natif a été déterminée comme Fe–47Cr–1Ni–1Mo, avec une épaisseur de 1,5 nm. Après exposition à l'électrolyte et maintien à l'OCP, l'épaisseur de la couche d'oxyde a diminué jusqu'à 1,2 nm. Ce petit changement peut être attribué à la dissolution du fer oxydé dans le milieu acide. La composition, déterminée comme Fe–57Cr–4Mo, reflète cette observation, montrant clairement l'enrichissement en chrome dans la couche d'oxyde. Le molybdène peut également être considéré comme enrichi dans le film d'oxyde, bien qu'il faille être prudent avec ce résultat en raison de l'incertitude relative plus élevée. La passivation anodique de la surface entraîne une oxydation supplémentaire, entraînant un épaississement de la couche d'oxyde à 1,5 nm. Bien que le fer soit oxydé à une vitesse supérieure à celle de sa dissolution, le chrome s'enrichit davantage à l'intérieur du film d'oxyde. La composition rapportée est maintenant Fe–67Cr–3Mo. Le nickel est devenu de plus en plus enrichi dans la région de l'alliage modifié.

Comportement à la corrosion

Des expériences de voltamétrie ont été realisé pour distinguer le comportement en corrosion en millieu H_2SO_4 après 30 minutes d'exposition à OCP. La Figure F16 compare deux courbes de polarisation obtenues sur la surface FeCrNiMo(100) — une après pré-oxydation en conditions ULP à 250 °C dans l'UHV (bleu) et l'autre après pré-oxydation dans la boîte à gants remplie d'Ar à température ambiante, pour former l'oxyde natif discuté ci-dessus (rouge). Les deux surfaces oxydées présentent le même potentiel de corrosion, $U_{corr}=-0.8 \pm 0.01$ V/Pt. Ceci est attendu pour le même échantillon entièrement recouvert d'oxyde de surface. Les branches cathodiques des courbes de polarisation présentent des formes similaires ; cependant, l'échantillon préoxydé ULP a une densité de courant plus faible, indiquant une activité de réduction de protons légèrement diminuée dans l'électrolyte. Un comportement similaire dans les branches cathodiques a déjà été rapporté [102].

La branche anodique montre que la densité de courant de la surface préparée ULP est comparativement plus faible lors de la transition active-passive que celle de la surface recouverte d'oxyde natif et avec une nette suppression du pic actif. Des observations similaires ont déjà été faites en comparant des surfaces recouvertes d'oxyde natif et préoxydées ULP à température ambiante sur des échantillons polycristallins 316L [101]. On peut donc en déduire que l'échantillon pré-oxydé ULP, préparé à 250 °C et exposé à un électrolyte acide, est totalement protégé contre la dissolution active, tout comme les échantillons pré-oxydés ULP préparés à température ambiante, tandis que les échantillons recouverts d'oxyde natif, formés à l'air ou dans une boîte

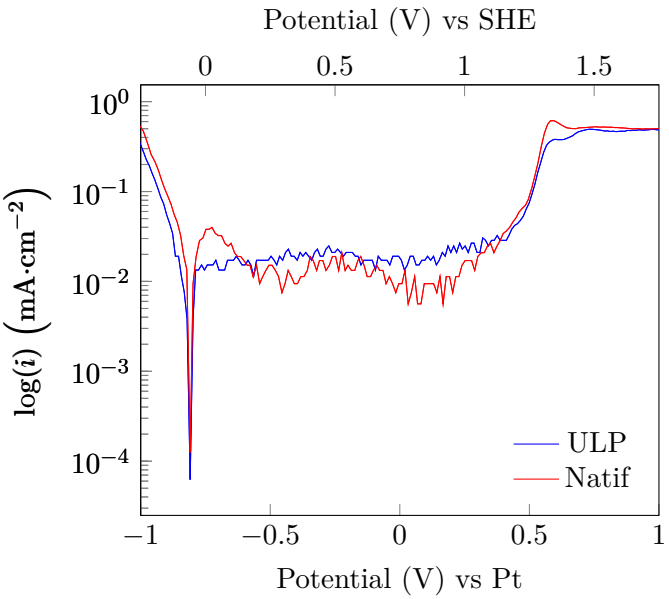

Figure F16: Courbes de polarisation d'un acier inoxydable Fe–17Cr–14,5Ni–2,3Mo (100) préparé sans oxyde sous UHV puis préoxydé par exposition à des pressions ultra-basses d'oxygène (ULP, bleu) ou par exposition à l'environnement de la boîte à gants (Natif, rouge).

à gants remplie d'Ar, ne restent que partiellement protégés.

Comparatif de films passifs

Le Tableau F5 montre les épaisseurs et les compositions calculées por les différents films d'oxyde étudiés dans ce travail. L'oxydation par exposition à 750 L d'oxygène gazeux pur à 250 °C dans des conditions UHV produit un oxyde de 0,8 nm d'épaisseur avec une composition Fe–19Cr–1Mo. Cet oxyde riche en fer reflète le manque de chrome présent sur la surface propre avant l'oxydation. Dans le chapitre 5, où la croissance de l'oxyde par étapes a été étudiée à 250 °C, nous avons montré qu'une couche d'oxyde de 0,7 nm est formée après une exposition de seulement 6 L à O_2 et est nettement plus enrichie en Cr_2O_3 (45%). L'exposition de la surface pré-oxydée ULP à l'environnement de la boîte à gants entraîne une oxydation supplémentaire et une croissance ultérieure de la couche jusqu'à une épaisseur approximative de 1,6 nm, ce qui est comparable à l'oxyde natif directement formé en boîte à gants (1,5 nm). Cependant, la composition calculée, Fe–18Cr–1Ni–2Mo, s'est avérée encore significativement affectée par la faible teneur initiaile en chrome à la surface — l'oxyde natif était presque deux fois plus riche en chrome oxydé (37%). L'exposition à l'électrolyte sans appliquer de polarisation externe produit un oxyde avec une composition de Fe–53Cr–8Mo. Ce résultat montre un enrichissement marqué du molybdène dans le film d'oxyde par rapport à celui observé dans le film obtenu à partir de l'oxyde base d'oxyde natif au même stade et qui peut expliquer les effets bénéfiques observés dans

Traitement	Comp. d'oxyde (%)				Comp. d'alliage modifée (%)				Épaisseur (nm)
	Fe	Cr	Ni	Mo	Fe	Cr	Ni	Mo	
Oxyde natif (ON)	61	37	1	1	74	11	14	1	1.5
ON+OCP	39	57	0	4	73	12	14	1	1.2
ON+OCP+AP	30	67	0	3	66	12	21	1	1.5
ULP^{250}	80	19	0	1	80	7	12	1	0.8
ULP^{250}+BG	79	18	1	2	74	9	16	1	1.6
ULP^{250}+BG+OCP	39	53	0	8	71	11	17	1	1.2
ULP^{250}+BG+OCP+AP	39	57	0	4	66	9	24	1	1.9

Tableau F5: Épaisseur (±0,1 nm) et composition de la couche d'oxyde et de l'alliage modifié (±1%) en utilisant le modèle monocouche tel que calculé à partir des données XPS.

le comportement à la corrosion lors de la transition active-passive. La quantité de chrome est maintenant presque exactement la même, ce qui suggère que la relation entre la concentration de chrome de départ à la surface et la composition du film passif lorsqu'il est formé dans un milieu acide est minime. La polarisation anodique de l'échantillon entraîne une croissance considérable de l'oxyde jusqu'à 1,9 nm, soit quelque 27% plus épais que ce qui a été produit sur le film passif produit à partir de l'oxyde natif. L'enrichissement en molybdène a été réduit à 4%, donnant une composition globale de Fe–57Cr–4Mo. Une fois de plus, nous trouvons que le nickel s'enrichissait de plus en plus dans la région sous-jacente de l'alliage modifié. Le chrome est plus appauvri dans la même région sous le film passif formé sur la surface pré-oxydée en conditions ULP.

Les résultats XPS ont été complétés par les données ToF SIMS qui permettent l'observation de la structure bicouche et confirment les observations liées à l'épaisseur mesurée par XPS.

Ajout de chlorure à l'électrolyte

L'ajout d'ions chlorure (0,05 M) à la solution acide H_2SO_4 a un effet limité sur le comportement observé dans la région passive, sans changement notable d'épaisseur et composition du film passif. Les résultats de ToF SIMS indiquent que les ions chlorure ne pénètrent pas dans la couche d'oxyde mais restent en extrême surface dans les conditions testées.

List of references

[1] A. D. McNaught, *Compendium of chemical terminology*, vol. 1669. Blackwell Science Oxford, 1997.

[2] P. A. Schweitzer, *Corrosion of polymers and elastomers*. CRC Press, 2006.

[3] E. J. Opila and N. S. Jacobson, "Oxidation and corrosion of ceramics," *Ceramics Science and Technology*, vol. 4, pp. 74–79, 2013.

[4] G. H. Koch, M. P. Brongers, N. G. Thompson, Y. P. Virmani, J. H. Payer, *et al.*, "Corrosion cost and preventive strategies in the United States," tech. rep., United States. Federal Highway Administration, 2002.

[5] P. A. Schweitzer *et al.*, *Fundamentals of Corrosion: Mechanisms, Causes, and Preventative Methods*. CRC press, 2009.

[6] A. Brooks, C. Clayton, K. Doss, and Y. Lu, "On the role of Cr in the passivity of stainless steel," *Journal of the Electrochemical Society*, vol. 133, no. 12, pp. 2459–2464, 1986.

[7] P. Marcus, *ed. Corrosion Mechanisms in Theory and Practice*. CRC press, 2011.

[8] I. Olefjord, "The passive state of stainless steels," *Materials Science and Engineering*, vol. 42, pp. 161–171, 1980.

[9] N. Sato, *Basics of corrosion chemistry*. Wiley Online Library, 2012.

[10] A. Padilha, "Decomposition of austenite in austenitic stainless steels," *ISIJ international*, vol. 42, no. 4, pp. 325–327, 2002.

[11] M. P. Ryan, D. E. Williams, R. J. Chater, B. M. Hutton, and D. S. McPhail, "Why stainless steel corrodes," *Nature*, vol. 415, no. 6873, p. 770, 2002.

[12] C. Clayton and Y. Lu, "A bipolar model of the passivity of stainless steel: the role of Mo addition," *Journal of the Electrochemical Society*, vol. 133, no. 12, pp. 2465–2473, 1986.

[13] M. W. Tan, E. Akiyama, A. Kawashima, K. Asami, and K. Hashimoto, "The effect of air exposure on the corrosion behavior of amorphous Fe-8Cr-Mo-13P-7C alloys in 1 M HCl," *Corrosion Science*, vol. 37, no. 8, pp. 1289–1301, 1995.

[14] K. Hashimoto, K. Asami, and K. Teramoto, "An X-ray photo-electron spectroscopic study on the role of molybdenum in increasing the corrosion resistance of ferritic stainless steels in HCl," *Corrosion Science*, vol. 19, no. 1, pp. 3–14, 1979.

[15] S. F. Wika *et al.*, "Pitting and crevice corrosion of stainless steel under offshore conditions," Master's thesis, Institutt for Materialteknologi, NTNU, Norway, 2012.

[16] N. Sato, T. Noda, and K. Kudo, "Thickness and structure of passive films on iron in acidic and basic solution," *Electrochimica Acta*, vol. 19, no. 8, pp. 471–475, 1974.

[17] V. Maurice, H. Peng, L. H. Klein, A. Seyeux, S. Zanna, and P. Marcus, "Effects of molybdenum on the composition and nanoscale morphology of passivated austenitic stainless steel surfaces," *Faraday Discussions*, vol. 180, pp. 151–170, 2015.

[18] H. H. Uhlig, "Passivity in metals and alloys," *Corrosion Science*, vol. 19, no. 11, pp. 777–791, 1979.

[19] R. Krishnakumar and Z. Szklarska-Smialowska, "Optical and Impedance Characteristics of Passive Films on Pure Aluminum," in *Materials Science Forum*, vol. 111, pp. 565–580, Trans Tech Publ, 1992.

[20] J. W. Schultze and M. Lohrengel, "Stability, reactivity and breakdown of passive films. Problems of recent and future research," *Electrochimica Acta*, vol. 45, no. 15-16, pp. 2499–2513, 2000.

[21] M. H. Dean and U. Stimming, "Capacity of semiconductor electrodes with multiple bulk electronic states Part I. Model and calculations for discrete states," *Journal of Electroanalytical Chemistry and Interfacial Electrochemistry*, vol. 228, no. 1–2, pp. 135–151, 1987.

[22] P. Schmuki, "From Bacon to barriers: a review on the passivity of metals and alloys," *Journal of Solid State Electrochemistry*, vol. 6, no. 3, pp. 145–164, 2002.

[23] D. D. Macdonald, "Passivity–the key to our metals-based civilization," *Pure and Applied Chemistry*, vol. 71, no. 6, pp. 951–978, 1999.

[24] P. Marcus, V. Maurice, and H. H. Strehblow, "Localized corrosion (pitting): A model of passivity breakdown including the role of the oxide layer nanostructure," *Corrosion Science*, vol. 50, no. 9, pp. 2698–2704, 2008.

[25] P. Schmuki, S. Virtanen, A. J. Davenport, and C. M. Vitus, "In Situ X-Ray Absorption Near-Edge Spectroscopic Study of the Cathodic Reduction of Artificial Iron Oxide Passive Films," *Journal of the Electrochemical Society*, vol. 143, no. 2, pp. 574–582, 1996.

[26] P. Schmuki, S. Virtanen, A. J. Davenport, and C. M. Vitus, "Transpassive dissolution of Cr and sputter-deposited Cr oxides studied by in situ X-ray near-edge spectroscopy," *Journal of the Electrochemical Society*, vol. 143, no. 12, pp. 3997–4005, 1996.

[27] M. Graham, "The application of surface techniques in understanding corrosion phenomena and mechanisms," *Corrosion Science*, vol. 37, no. 9, pp. 1377–1397, 1995.

[28] N. Ramasubramanian, N. Preocanin, and R. Davidson, "Analysis of passive films on stainless steel by cyclic voltammetry and Auger spectroscopy," *Journal of the Electrochemical Society*, vol. 132, no. 4, pp. 793–798, 1985.

[29] R. Revie, B. Baker, and J. Bockris, "The passive film on iron: an application of auger electron spectroscopy," *Journal of the Electrochemical Society*, vol. 122, no. 11, pp. 1460–1466, 1975.

[30] A. Rossi, B. Elsener, G. Hähner, M. Textor, and N. Spencer, "XPS, AES and ToF-SIMS investigation of surface films and the role of inclusions on pitting corrosion in austenitic stainless steels," *Surface and Interface Analysis*, vol. 29, no. 7, pp. 460–467, 2000.

[31] V. Maurice, W. P. Yang, and P. Marcus, "X-Ray photoelectron spectroscopy and scanning tunneling microscopy study of passive films formed on (100) Fe-18Cr-13Ni single-crystal surfaces," *Journal of the Electrochemical Society*, vol. 145, no. 3, pp. 909–920, 1998.

[32] R. Kirchheim, B. Heine, H. Fischmeister, S. Hofmann, H. Knote, and U. Stolz, "The passivity of iron-chromium alloys," *Corrosion Science*, vol. 29, no. 7, pp. 899–917, 1989.

[33] W. Yang, D. Costa, and P. Marcus, "Resistance to Pitting and Chemical Composition of Passive Films of a Fe-17% Cr Alloy in Chloride-Containing Acid Solution," *Journal of the Electrochemical Society*, vol. 141, no. 10, pp. 2669–2676, 1994.

[34] M. F. Toney, A. J. Davenport, L. J. Oblonsky, M. P. Ryan, and C. M. Vitus, "Atomic structure of the passive oxide film formed on iron," *Physical Review Letters*, vol. 79, no. 21, p. 4282, 1997.

[35] M. Ryan, R. Newman, and G. Thompson, "An STM study of the passive film formed on iron in borate buffer solution," *Journal of the Electrochemical Society*, vol. 142, no. 10, pp. L177–L179, 1995.

[36] R. Cortes, M. Froment, A. Hugot-Le Goff, and S. Joiret, "Characterization of passive films on Ni and Ni alloys by ReflEXAFS and raman spectroscopy," *Corrosion Science*, vol. 31, pp. 121–127, 1990.

[37] V. Maurice, W. Yang, and P. Marcus, "XPS and STM Study of Passive Films Formed on Fe-22Cr (110) Single-Crystal Surfaces," *Journal of the Electrochemical Society*, vol. 143, no. 4, pp. 1182–1200, 1996.

[38] A. Machet, A. Galtayries, S. Zanna, L. Klein, V. Maurice, P. Jolivet, M. Foucault, P. Combrade, P. Scott, and P. Marcus, "XPS and STM study of the growth and structure of passive films in high temperature water on a nickel-base alloy," *Electrochimica Acta*, vol. 49, no. 22-23, pp. 3957–3964, 2004.

[39] C. Örnek, M. Långberg, J. Evertsson, G. Harlow, W. Linpé, L. Rullik, F. Carlà, R. Felici, E. Bettini, U. Kivisäkk, *et al.*, "In-situ synchrotron GIXRD study of passive film evolution on duplex stainless steel in corrosive environment," *Corrosion Science*, vol. 141, pp. 18–21, 2018.

[40] M. Sato and S. Fujimoto, "Structural analysis of passive films on stainless steel by synchrotron radiation," *Zairyo To Kankyo*, vol. 57, no. 6, pp. 250–257, 2008.

[41] R. Chen and W. Yeun, "Review of the high-temperature oxidation of iron and carbon steels in air or oxygen," *Oxidation of Metals*, vol. 59, no. 5-6, pp. 433–468, 2003.

[42] A. Grosvenor, B. Kobe, and N. McIntyre, "Examination of the oxidation of iron by oxygen using X-ray photoelectron spectroscopy and QUASESTM," *Surface Science*, vol. 565, no. 2-3, pp. 151–162, 2004.

[43] C. Brundle, T. Chuang, and K. Wandelt, "Core and valence level photoemission studies of iron oxide surfaces and the oxidation of iron," *Surface Science*, vol. 68, pp. 459–468, 1977.

[44] A. Grosvenor, B. Kobe, N. McIntyre, S. Tougaard, and W. Lennard, "Use of QUASES^{TM}/XPS measurements to determine the oxide composition and thickness on an iron substrate," *Surface and Interface Analysis*, vol. 36, no. 7, pp. 632–639, 2004.

[45] S. Roosendaal, B. Van Asselen, J. Elsenaar, A. Vredenberg, and F. Habraken, "The oxidation state of Fe (100) after initial oxidation in O_2," *Surface Science*, vol. 442, no. 3, pp. 329–337, 1999.

[46] T. C. Lin, G. Seshadri, and J. A. Kelber, "A consistent method for quantitative XPS peak analysis of thin oxide films on clean polycrystalline iron surfaces," *Applied Surface Science*, vol. 119, no. 1-2, pp. 83–92, 1997.

[47] B. Sinković, P. Johnson, N. Brookes, A. Clarke, and N. Smith, "Magnetic structure of oxidized Fe (001)," *Physical Review Letters*, vol. 65, no. 13, p. 1647, 1990.

[48] G. W. Simmons and D. J. Dwyer, "A LEED-AES study of the initial stages of oxidation of Fe (001)," *Surface Science*, vol. 48, no. 2, pp. 373–392, 1975.

[49] N. Sato, K. Kudo, and T. Noda, "Single layer of the passive film on Fe," *Corrosion Science*, vol. 10, no. 11, pp. 785–794, 1970.

[50] K. Ogura and K. Sato, "Cathodic dissolution of the passive film on iron—I. Kinetics and mechanism," *Electrochimica Acta*, vol. 25, no. 6, pp. 857–862, 1980.

[51] K. Ogura and T. Majima, "Formation and reduction of the passive film on iron in phosphate-borate buffer solution," *Electrochimica Acta*, vol. 23, no. 12, pp. 1361–1365, 1978.

[52] J. S. Kim, E. A. Cho, and H. S. Kwon, "Photoelectrochemical study on the passive film on Fe," *Corrosion Science*, vol. 43, no. 8, pp. 1403–1415, 2001.

[53] A. J. Davenport and M. Sansone, "High resolution in situ XANES investigation of the nature of the passive film on iron in a pH 8.4 borate buffer," *Journal of the Electrochemical Society*, vol. 142, no. 3, pp. 725–730, 1995.

[54] C. Foley, J. Kruger, and C. Bechtoldt, "Electron diffraction studies of active, passive, and transpassive oxide films formed on iron," *Journal of the Electrochemical Society*, vol. 114, no. 10, pp. 994–1001, 1967.

[55] M. Nagayama, "The anodic oxidation of iron in a neutral solution I. The nature and composition of the passive film," *Journal of the Electrochemical Society*, vol. 109, no. 9, pp. 781–790, 1962.

[56] M. Nagayama and M. Cohen, "The anodic oxidation of iron in a neutral solution II. Effect of ferrous ion and pH on the behavior of passive iron," *Journal of the Electrochemical Society*, vol. 110, no. 6, pp. 670–680, 1963.

[57] M. Büchler, P. Schmuki, and H. Böhni, "Formation and dissolution of the passive film on iron studied by a light reflectance technique," *Journal of the Electrochemical Society*, vol. 144, no. 7, pp. 2307–2312, 1997.

[58] G. C. Allen, P. M. Tucker, and R. K. Wild, "X-ray photoelectron/Auger electron spectroscopic study of the initial oxidation of chromium metal," *Journal of the Chemical Society*, vol. 74, pp. 1126–1140, 1978.

[59] V. Maurice, S. Cadot, and P. Marcus, "XPS, LEED and STM study of thin oxide films formed on Cr (110)," *Surface Science*, vol. 458, no. 1-3, pp. 195–215, 2000.

[60] Y. Sakisaka, H. Kato, and M. Onchi, "Oxygen chemisorption and initial oxidation of Cr (110)," *Surface Science*, vol. 120, no. 1, pp. 150–170, 1982.

[61] T. P. Moffat, H. Yang, F. R. F. Fan, and A. J. Bard, "Electron-transfer reactions on passive chromium," *Journal of the Electrochemical Society*, vol. 139, no. 11, pp. 3158–3167, 1992.

[62] T. Moffat and R. Latanision, "An electrochemical and X-Ray photoelectron spectroscopy study of the passive state of chromium," *Journal of the Electrochemical Society*, vol. 139, no. 7, pp. 1869–1879, 1992.

[63] M. Okuyama, M. Kawakami, and K. Ito, "Anodic dissolution of chromium in acidic sulphate solutions," *Electrochimica Acta*, vol. 30, no. 6, pp. 757–765, 1985.

[64] B. Stypula and J. Stoch, "The characterization of passive films on chromium electrodes by XPS," *Corrosion Science*, vol. 36, no. 12, pp. 2159–2167, 1994.

[65] G. Bouyssoux, M. Romand, H. Polaschegg, and J. Calow, "XPS and AES studies of anodic passive films grown on chromium electrodes in sulphuric acid baths," *Journal of Electron Spectroscopy and Related Phenomena*, vol. 11, no. 2, pp. 185–196, 1977.

[66] V. Maurice, W. Yang, and P. Marcus, "XPS and STM investigation of the passive film formed on Cr (110) single-crystal surfaces," *Journal of the Electrochemical Society*, vol. 141, no. 11, pp. 3016–3027, 1994.

[67] S. Evans, J. Pielasze, and J. M. Thomas, "Oxidation of nickel studied by UV and X-ray photoelectron spectroscopy," *Surface Science*, vol. 55, no. 2, pp. 644–662, 1976.

[68] P. Norton, R. Tapping, and J. Goodale, "A photoemission study of the interaction of Ni (100), (110) and (111) surfaces with oxygen," *Surface Science*, vol. 65, no. 1, pp. 13–36, 1977.

[69] T. Dickinson, A. F. Povey, and P. M. Sherwood, "Dissolution and passivation of nickel. An X-ray photoelectron spectroscopic study," *Journal of the Chemical Society*, vol. 73, pp. 327–343, 1977.

[70] N. Sato and G. Okamoto, "Anodic passivation of nickel in sulfuric acid solutions," *Journal of the Electrochemical Society*, vol. 110, no. 6, pp. 605–614, 1963.

[71] R. Hummel, R. Smith, and E. Verink Jr, "The passivation of nickel in aqueous solutions—I. The identification of insoluble corrosion products on nickel electrodes using optical and ESCA techniques," *Corrosion Science*, vol. 27, no. 8, pp. 803–813, 1987.

[72] P. Marcus and J. M. Herbelin, "The entry of chloride ions into passive films on nickel studied by spectroscopic (ESCA) and nuclear (^{36}Cl radiotracer) methods," *Corrosion Science*, vol. 34, no. 7, pp. 1123–1145, 1993.

[73] B. MacDougall, D. Mitchell, and M. Graham, "Changes in oxide films on nickel during long-term passivation," *Journal of the Electrochemical Society*, vol. 132, no. 12, p. 2895, 1985.

[74] P. Marcus, J. Oudar, and I. Olefjord, "Studies of the influence of sulphur on the passivation of nickel by Auger electron spectroscopy and electron spectroscopy for chemical analysis," *Materials Science and Engineering*, vol. 42, pp. 191–197, 1980.

[75] N. Sato and K. Kudo, "An ellipsometric study of anodic passivation of nickel in borate buffer solution," *Electrochimica Acta*, vol. 19, no. 8, pp. 461–470, 1974.

[76] H. W. Hoppe and H. H. Strehblow, "XPS and UPS examinations of the formation of passive layers on Ni in 1 M sodium hydroxide and 0.5 M sulphuric acid," *Surface and Interface Analysis*, vol. 14, no. 3, pp. 121–131, 1989.

[77] H. W. Hoppe and H. H. Strehblow, "XPS and UPS examinations of passive layers on Ni and Fe53Ni alloys," *Corrosion Science*, vol. 31, pp. 167–177, 1990.

[78] J. Scherer, B. Ocko, and O. Magnussen, "Structure, dissolution, and passivation of Ni (111) electrodes in sulfuric acid solution: an in situ STM, X-ray scattering, and electrochemical study," *Electrochimica Acta*, vol. 48, no. 9, pp. 1169–1191, 2003.

[79] N. McIntyre, D. Johnston, L. Coatsworth, R. Davidson, and J. Brown, "X-ray photoelectron spectroscopic studies of thin film oxides of cobalt and molybdenum," *Surface and Interface Analysis*, vol. 15, no. 4, pp. 265–272, 1990.

[80] Y. Lu and C. Clayton, "An XPS study of the passive and transpassive behavior of molybdenum in deaerated 0.1 M HCl," *Corrosion Science*, vol. 29, no. 8, pp. 927–937, 1989.

[81] K. Nobuyoshi and K. Sugimoto, "Modulation spectroscopic analysis of passivation and transpassivation films on molybdenum," *Journal of the Japan Institute of Metals*, vol. 44, no. 11, pp. 1312–1321, 1980.

[82] J. Johnson, C. Chi, C. Chen, and W. James, "The anodic dissolution of molybdenum," *Corrosion*, vol. 26, no. 8, pp. 338–342, 1970.

[83] J. Johnson, M. Lee, and W. James, "Electrochemical behavior of molybdenum in acid chloride solutions," *Corrosion*, vol. 26, no. 11, pp. 507–510, 1970.

[84] B. Brox, W. Yi-Hua, and I. Olefjord, "Electrochemical and Surface Analyses of Mo (100) Single Crystal Polarized in 0.5 M H_2SO_4," *Journal of the Electrochemical Society*, vol. 135, no. 9, p. 2184, 1988.

[85] W. Badawy, A. Gad-Allah, H. A. El-Rahman, and M. Abouromia, "Kinetics of the passivation of molybdenum in acids and alkali solutions as inferred from impedance and potential measurements," *Surface and Coatings Technology*, vol. 27, no. 2, pp. 187–196, 1986.

[86] W. Badawy and F. Al-Kharafi, "Corrosion and passivation behaviors of molybdenum in aqueous solutions of different pH," *Electrochimica Acta*, vol. 44, no. 4, pp. 693–702, 1998.

[87] G. Allen, J. Dyke, S. Harris, and A. Morris, "A surface study of the oxidation of type 304L stainless steel at 600 K in air," *Oxidation of Metals*, vol. 29, no. 5, pp. 391–408, 1988.

[88] Z. Wang, F. Di-Franco, A. Seyeux, S. Zanna, V. Maurice, and P. Marcus, "Passivation-induced physicochemical alterations of the native surface oxide film on 316L austenitic stainless steel," *Journal of the Electrochemical Society*, vol. 166, no. 11, pp. C3376–C3388, 2019.

[89] Z. Wang, E. M. Paschalidou, A. Seyeux, S. Zanna, V. Maurice, and P. Marcus, "Mechanisms of Cr and Mo enrichments in the passive oxide film on 316L austenitic stainless steel," *Frontiers in Materials*, vol. 6, p. 232, 2019.

[90] L. Ma, F. Wiame, V. Maurice, and P. Marcus, "New insight on early oxidation stages of austenitic stainless steel from in situ XPS analysis on single-crystalline Fe–18Cr–13Ni," *Corrosion Science*, vol. 140, pp. 205–216, 2018.

[91] L. Ma, F. Wiame, V. Maurice, and P. Marcus, "Origin of nanoscale heterogeneity in the surface oxide film protecting stainless steel against corrosion," *npj Materials Degradation*, vol. 3, no. 1, pp. 1–9, 2019.

[92] L. Ma, F. Wiame, V. Maurice, and P. Marcus, "Stainless steel surface structure and initial oxidation at nanometric and atomic scales," *Applied Surface Science*, vol. 494, pp. 8–12, 2019.

[93] J. R. Lince, S. V. Didziulis, D. K. Shuh, T. D. Durbin, and J. A. Yarmoff, "Interaction of O_2 with the $Fe_{0.84}Cr_{0.16}$ (001) surface studied by photoelectron spectroscopy," *Surface Science*, vol. 277, no. 1-2, pp. 43–63, 1992.

[94] A. Vesel, M. Mozetic, A. Drenik, N. Hauptman, and M. Balat-Pichelin, "High temperature oxidation of stainless steel AISI316L in air plasma," *Applied Surface Science*, vol. 255, no. 5, pp. 1759–1765, 2008.

[95] S. Lozano-Perez, D. W. Saxey, T. Yamada, and T. Terachi, "Atom-probe tomography characterization of the oxidation of stainless steel," *Scripta Materialia*, vol. 62, no. 11, pp. 855–858, 2010.

[96] D. Rodriguez and D. Chidambaram, "Oxidation of stainless steel 316 and Nitronic 50 in supercritical and ultrasupercritical water," *Applied Surface Science*, vol. 347, pp. 10–16, 2015.

[97] R. Wild, "High temperature oxidation of austenitic stainless steel in low oxygen pressure," *Corrosion Science*, vol. 17, no. 2, pp. 87–104, 1977.

[98] P. Jussila, H. Ali-Löytty, K. Lahtonen, M. Hirsimäki, and M. Valden, "Inhibition of initial surface oxidation by strongly bound hydroxyl species and Cr segregation: H_2O and O_2 adsorption on Fe–17Cr," *Surface Science*, vol. 603, no. 19, pp. 3005–3010, 2009.

[99] P. Jussila, K. Lahtonen, M. Lampimäki, M. Hirsimäki, and M. Valden, "Influence of minor alloying elements on the initial stages of oxidation of austenitic stainless steel materials," *Surface and Interface Analysis*, vol. 40, no. 8, pp. 1149–1156, 2008.

[100] H. Ali-Löytty, P. Jussila, M. Hirsimäki, and M. Valden, "Influence of CrN surface compound on the initial stages of high temperature oxidation of ferritic stainless steel," *Applied Surface Science*, vol. 257, no. 17, pp. 7783–7791, 2011.

[101] B. Lynch, Z. Wang, L. Ma, E. M. Paschalidou, F. Wiame, V. Maurice, and P. Marcus, "Passivation-Induced Cr and Mo Enrichments of 316L Stainless Steel Surfaces and Effects of Controlled Pre-Oxidation," *Journal of the Electrochemical Society*, vol. 167, no. 14, p. 141509, 2020.

[102] L. Ma, E.-M. Pascalidou, F. Wiame, S. Zanna, V. Maurice, and P. Marcus, "Passivation mechanisms and pre-oxidation effects on model surfaces of FeCrNi austenitic stainless steel," *Corrosion Science*, vol. 167, p. 108483, 2020.

[103] T. Massoud, V. Maurice, L. H. Klein, A. Seyeux, and P. Marcus, "Nanostructure and local properties of oxide layers grown on stainless steel in simulated pressurized water reactor environment," *Corrosion Science*, vol. 84, pp. 198–203, 2014.

[104] M. Ryan, R. Newman, and G. Thompson, "A scanning tunnelling microscopy study of structure and structural relaxation in passive oxide films on Fe-Cr alloys," *Philosophical Magazine B*, vol. 70, no. 2, pp. 241–251, 1994.

[105] J. J. Kim and Y. M. Young, "Study on the passive film of type 316 stainless steel," *International Journal of Electrochemical Science*, vol. 8, no. 10, pp. 11847–11859, 2013.

[106] K. M. Ismail, A. Jayaraman, T. Wood, and J. Earthman, "The influence of bacteria on the passive film stability of 304 stainless steel," *Electrochimica Acta*, vol. 44, no. 26, pp. 4685–4692, 1999.

[107] L. Wang, A. Seyeux, and P. Marcus, "Thermal stability of the passive film formed on 316L stainless steel surface studied by ToF-SIMS," *Corrosion Science*, vol. 165, p. 108395, 2020.

[108] D. Xia, Y. Sun, and H. Fan, "Characterization of passive film formed on 304 SS in simulated alkaline water chemistries containing sulfur at 300 °C," *Transactions of Tianjin University*, vol. 21, no. 6, pp. 554–561, 2015.

[109] P. Schmutz and D. Landolt, "In-situ microgravimetric studies of passive alloys: potential sweep and potential step experiments with Fe–25Cr and Fe–17Cr–33Mo in acid and alkaline solution," *Corrosion Science*, vol. 41, no. 11, pp. 2143–2163, 1999.

[110] H. W. Hoppe, S. Haupt, and H. H. Strehblow, "Combined surface analytical and electrochemical study of the formation of passive layers on Fe/Cr alloys in 1 M NaOH," *Surface and Interface Analysis*, vol. 21, no. 8, pp. 514–525, 1994.

[111] I. Olefjord, "Application of ESCA to oxide films formed on stainless steels at intermediate and high temperatures," *Metal Science*, vol. 9, no. 1, pp. 263–268, 1975.

[112] I. Olefjord, B. Brox, and U. Jelvestam, "Surface composition of stainless steels during anodic dissolution and passivation studied by ESCA," *Journal of the Electrochemical Society*, vol. 132, no. 12, p. 2854, 1985.

[113] I. Olefjord and L. Wegrelius, "Surface analysis of passive state," *Corrosion Science*, vol. 31, pp. 89–98, 1990.

[114] J. Castle and C. Clayton, "The use of in the X-ray photo-electron spectroscopy analyses of passive layers on stainless steel," *Corrosion Science*, vol. 17, no. 1, pp. 7–26, 1977.

[115] S. Haupt and H. H. Strehblow, "A combined surface analytical and electrochemical study of the formation of passive layers on FeCr alloys in 0.5 M H_2SO_4," *Corrosion Science*, vol. 37, no. 1, pp. 43–54, 1995.

[116] C. O. A. Olsson and D. Landolt, "Passive films on stainless steels—chemistry, structure and growth," *Electrochimica acta*, vol. 48, no. 9, pp. 1093–1104, 2003.

[117] K. Sugimoto and Y. Sawada, "The role of molybdenum additions to austenitic stainless steels in the inhibition of pitting in acid chloride solutions," *Corrosion Science*, vol. 17, no. 5, pp. 425–445, 1977.

[118] J. Horvath and H. Uhlig, "Critical potentials for pitting corrosion of Ni, Cr-Ni, Cr-Fe, and related stainless steels," *Journal of the Electrochemical Society*, vol. 115, no. 8, p. 791, 1968.

[119] W. Yang, R. C. Ni, H. Z. Hua, and A. Pourbaix, "The behavior of chromium and molybdenum in the propagation process of localized corrosion of steels," *Corrosion Science*, vol. 24, no. 8, pp. 691–707, 1984.

[120] H. Ogawa, H. Omata, I. Itoh, and H. Okada, "Auger electron spectroscopic and electrochemical analysis of the effect of alloying elements on the passivation behavior of stainless steels," *Corrosion*, vol. 34, no. 2, pp. 52–60, 1978.

[121] J. B. Lee, "Effects of alloying elements, Cr, Mo and N on repassivation characteristics of stainless steels using the abrading electrode technique," *Materials Chemistry and Physics*, vol. 99, no. 2–3, pp. 224–234, 2006.

[122] H. Hertz, "Ueber einen Einfluss des ultravioletten Lichtes auf die electrische Entladung," *Annalen der Physik*, vol. 267, no. 8, pp. 983–1000, 1887.

[123] A. Einstein, "Über einem die Erzeugung und Verwandlung des Lichtes betreffenden heuristischen Gesichtspunkt," *Annalen der Physik*, vol. 4, 1905.

[124] P. Innes, "On the velocity of the cathode particles emitted by various metals under the influence of Röntgen rays, and its bearing on the theory of atomic disintegration," *Proceedings of the Royal Society of London*, vol. 79, no. 532, pp. 442–462, 1907.

[125] K. Siegbahn, "Beta-and gamma-ray spectroscopy," *Indian Journal of Physics*, vol. 30, pp. 47–49, 1955.

[126] K. Siegbahn, "ESCA: atomic, molecular and solid state structure studies by means of electron spectroscopy," *Nova Acta Regiae Societatis Scientiarum Upsaliensis*, 1967.

[127] J. H. Scofield, "Hartree-Slater subshell photoionization cross-sections at 1254 and 1487 eV," *Journal of Electron Spectroscopy and Related Phenomena*, vol. 8, no. 2, pp. 129–137, 1976.

[128] J. J. Thomson, "XXVI. Rays of positive electricity," *The London, Edinburgh, and Dublin Philosophical Magazine and Journal of Science*, vol. 21, no. 122, pp. 225–249, 1911.

[129] R. Herzog and F. Viehböck, "Ion source for mass spectrography," *Physical Review*, vol. 76, no. 6, p. 855, 1949.

[130] A. Benninghoven, "Chemical analysis of inorganic and organic surfaces and thin films by static time-of-flight secondary ion mass spectrometry (TOF-SIMS)," *Angewandte Chemie International Edition in English*, vol. 33, no. 10, pp. 1023–1043, 1994.

[131] G. Binnig, H. Rohrer, C. Gerber, and E. Weibel, "Surface studies by scanning tunneling microscopy," *Physical Review Letters*, vol. 49, no. 1, p. 57, 1982.

[132] J. Tersoff and D. Hamann, "Theory and application for the scanning tunneling microscope," *Physical Review Letters*, vol. 50, no. 25, p. 1998, 1983.

[133] J. Bardeen, "Tunnelling from a many-particle point of view," *Physical Review Letters*, vol. 6, no. 2, p. 57, 1961.

[134] L. d. Broglie, "XXXV. A tentative theory of light quanta," *The London, Edinburgh, and Dublin Philosophical Magazine and Journal of Science*, vol. 47, no. 278, pp. 446–458, 1924.

[135] C. Davisson and L. H. Germer, "Diffraction of electrons by a crystal of nickel," *Physical Review*, vol. 30, no. 6, p. 705, 1927.

[136] "www.casaxps.com (2019)."

[137] G. Greczynski and L. Hultman, "X-ray photoelectron spectroscopy: towards reliable binding energy referencing," *Progress in Materials Science*, vol. 107, p. 100591, 2020.

[138] G. Greczynski and L. Hultman, "C 1s peak of adventitious carbon aligns to the vacuum level: dire consequences for material's bonding assignment by photoelectron spectroscopy," *ChemPhysChem*, vol. 18, no. 12, p. 1507, 2017.

[139] C. R. Brundle and B. V. Crist, "X-ray photoelectron spectroscopy: A perspective on quantitation accuracy for composition analysis of homogeneous materials," *Journal of Vacuum Science & Technology A: Vacuum, Surfaces, and Films*, vol. 38, no. 4, p. 041001, 2020.

[140] V. Maurice, L. Klein, H. H. Strehblow, and P. Marcus, "In situ STM study of the surface structure, dissolution, and early stages of electrochemical oxidation of the Ag (111) electrode," *The Journal of Physical Chemistry C*, vol. 111, no. 44, pp. 16351–16361, 2007.

[141] H. Grabke, R. Dennert, and B. Wagemann, "The effect of s, n, and c on the oxidation of ni-20% cr and fe-20% cr," *Oxidation of metals*, vol. 47, no. 5, pp. 495–506, 1997.

[142] L. Ma, B. Lynch, F. Wiame, V. Maurice, and P. Marcus, "Nanoscale early oxidation mechanisms of model fecrni austenitic stainless steel surfaces at room temperature," *Corrosion Science*, vol. 190, p. 109653, 2021.

[143] J. Burton, B. Berkowitz, and R. Kane, "Surface segregation in an engineering alloy: Hastelloy C-276," *Metallurgical Transactions A*, vol. 10, no. 6, pp. 677–682, 1979.

[144] R. Bricknell, R. Mulford, and D. Woodford, "The role of sulfur in the air embrittlement of nickel and its alloys," *Metallurgical Transactions A*, vol. 13, no. 7, pp. 1223–1232, 1982.

[145] J. Woodward and G. Burstein, "Surface segregation in a 3Cr-0.5Mo steel," *Metal Science*, vol. 14, no. 11, pp. 529–533, 1980.

[146] C. Uebing, V. Scheuch, M. Kiskinova, and H. Bonzel, "Segregation of ordered CrN and CrC surface phases on a Fe-15% Cr (100) crystal," *Surface Science*, vol. 321, no. 1-2, pp. 89–99, 1994.

[147] C. Müller, C. Uebing, M. Kottcke, C. Rath, L. Hammer, and K. Heinz, "The structure of the surface compound CrN formed by cosegregation on a Fe–15% Cr–N (100) single crystal surface," *Surface science*, vol. 400, no. 1-3, pp. 87–94, 1998.

[148] S. Tougaard, "Formalism for quantitative surface analysis by electron spectroscopy," *Journal of Vacuum Science & Technology A: Vacuum, Surfaces, and Films*, vol. 8, no. 3, pp. 2197–2203, 1990.

[149] G. Ilevbare and G. Burstein, "The role of alloyed molybdenum in the inhibition of pitting corrosion in stainless steels," *Corrosion Science*, vol. 43, no. 3, pp. 485–513, 2001.

[150] W. Fredriksson, S. Malmgren, T. Gustafsson, M. Gorgoi, and K. Edström, "Full depth profile of passive films on 316L stainless steel based on high resolution HAXPES in combination with ARXPS," *Applied Surface Science*, vol. 258, no. 15, pp. 5790–5797, 2012.

[151] L. Ma, *Premières étapes d'oxydation d'un acier inoxydable austénitique et influence sur la passivation*. PhD thesis, PSL University, Paris, France, 2019.

[152] P. Varga and M. Schmid, "Chemical discrimination on atomic level by STM," *Applied surface science*, vol. 141, no. 3-4, pp. 287–293, 1999.

[153] T. Duguet and P. A. Thiel, "Chemical contrast in STM imaging of transition metal aluminides," *Progress in surface science*, vol. 87, no. 5-8, pp. 47–62, 2012.

[154] F. Wiame, V. Maurice, and P. Marcus, "Initial stages of oxidation of $Cu_{0.7}Zn_{0.3}$(1 1 1)," *Surface science*, vol. 601, no. 18, pp. 4402–4406, 2007.

[155] F. Wiame, M. M. Islam, B. Salgın, J. Świątowska, D. Costa, B. Diawara, V. Maurice, and P. Marcus, "Zn effect on STM imaging of brass surfaces," *Surface Science*, vol. 644, pp. 148–152, 2016.

[156] F. C. Nascimento, C. E. Foerster, S. L. R. d. Silva, C. M. Lepienski, C. J. d. M. Siqueira, and C. Alves Junior, "A comparative study of mechanical and tribological properties of AISI-304 and AISI-316 submitted to glow discharge nitriding," *Materials Research*, vol. 12, pp. 173–180, 2009.

[157] P. L. Mangonon and G. Thomas, "The martensite phases in 304 stainless steel," *Metallurgical transactions*, vol. 1, no. 6, pp. 1577–1586, 1970.

[158] B. Lynch, S. Neupane, F. Wiame, A. Seyeux, V. Maurice, and P. Marcus, "An XPS and ToF-SIMS study of the passive film formed on a model FeCrNiMo stainless steel surface in aqueous media after thermal pre-oxidation at ultra-low oxygen pressure," *Applied Surface Science*, p. 149435, 2021.

[159] M. Chase, *NIST-JANAF Thermochemical Tables, 4th Edition*. American Institute of Physics, 1998-08-01 1998.

[160] E. Clauberg, J. Janověc, C. Uebing, H. Viefhaus, and H. Grabke, "Surface segregation on Fe–25% Cr–2% Ni–0.14% Sb–N, S (100) single crystal surfaces," *Applied Surface Science*, vol. 161, no. 1-2, pp. 35–46, 2000.

[161] P. Marcus and M. E. Bussell, "XPS study of the passive films formed on nitrogen-implanted austenitic stainless steels," *Applied surface science*, vol. 59, no. 1, pp. 7–21, 1992.

[162] Z. Wang, A. Seyeux, S. Zanna, V. Maurice, and P. Marcus, "Chloride-induced alterations of the passive film on 316L stainless steel and blocking effect of pre-passivation," *Electrochimica Acta*, vol. 329, p. 135159, 2020.

[163] L. Wang, S. Voyshnis, A. Seyeux, and P. Marcus, "Ion transport mechanisms in the passive film formed on 304L stainless steel studied by ToF-SIMS with 18O isotopic tracer," *Corrosion Science*, vol. 173, p. 108779, 2020.

[164] R. Natarajan, N. Palaniswamy, M. Natesan, and V. Muralidharan, "XPS analysis of passive film on stainless steel," *The Open Corrosion Journal*, vol. 2, no. 1, 2009.

[165] N. McIntyre and D. Zetaruk, "X-ray photoelectron spectroscopic studies of iron oxides," *Analytical Chemistry*, vol. 49, no. 11, pp. 1521–1529, 1977.

[166] H. Konno and M. Nagayama, "X-ray photoelectron spectra of hexavalent iron," *Journal of Electron Spectroscopy and Related Phenomena*, vol. 18, no. 3, pp. 341–343, 1980.

[167] B. J. Tan, K. J. Klabunde, and P. M. Sherwood, "X-ray photoelectron spectroscopy studies of solvated metal atom dispersed catalysts. Monometallic iron and bimetallic iron-cobalt particles on alumina," *Chemistry of Materials*, vol. 2, no. 2, pp. 186–191, 1990.

[168] R. Shalvoy, P. Reucroft, and B. Davis, "Characterization of coprecipitated nickel on silica methanation catalysts by X-ray photoelectron spectroscopy," *Journal of Catalysis*, vol. 56, no. 3, pp. 336–348, 1979.

[169] J. C. Klein and D. M. Hercules, "Surface characterization of model Urushibara catalysts," *Journal of Catalysis*, vol. 82, no. 2, pp. 424–441, 1983.

[170] P. Keller and H. H. Strehblow, "XPS investigations of electrochemically formed passive layers on Fe/Cr-alloys in 0.5 M H_2SO_4," *Corrosion Science*, vol. 46, no. 8, pp. 1939–1952, 2004.

[171] E. De Vito and P. Marcus, "XPS study of passive films formed on molybdenum-implanted austenitic stainless steels," *Surface and Interface Analysis*, vol. 19, no. 1-12, pp. 403–408, 1992.

[172] C. O. A. Olsson, H. J. Mathieu, and D. Landolt, "Angle-resolved xps analysis of molybdenum and tungsten in passive films on stainless steel pvd alloys," *Surface and Interface Analysis: An International Journal devoted to the development and application of techniques for the analysis of surfaces, interfaces and thin films*, vol. 34, no. 1, pp. 130–134, 2002.

[173] B. Brox and I. Olefjord, "ESCA studies of MoO_2 and MoO_3," *Surface and interface analysis*, vol. 13, no. 1, pp. 3–6, 1988.

[174] J. A. Hollingshead, M. T. Tyszkiewicz, and R. E. McCarley, "Sol-gel approach to synthesis of molybdenum (III) oxide. Molybdenum oxide hydroxide (MoO(OH)) and other intermediates from hydrolysis of molybdenum (III) alkoxides and $Mo_2(NMe_2)_6$," *Chemistry of Materials*, vol. 5, no. 11, pp. 1600–1604, 1993.

[175] Z. Wang, L. Zhang, X. Tang, Z. Zhang, and M. Lu, "The surface characterization and passive behavior of Type 316L stainless steel in H_2S-containing conditions," *Applied Surface Science*, vol. 423, pp. 457–464, 2017.

[176] A. G. Wren, R. W. Phillips, and L. U. Tolentino, "Surface reactions of chlorine molecules and atoms with water and sulfuric acid at low temperatures," *Journal of Colloid and Interface Science*, vol. 70, no. 3, pp. 544–557, 1979.

RÉSUMÉ

Le travail réalisé dans cette thèse a pour objet d'étudier l'influence des mécanismes initiaux d'oxydation sur le film passif formé à la surface d'un acier inoxydable austénitique modèle, FeCrNiMo(100). Cette étude a été réalisée en employant une approche combinée de science des surfaces et d'électrochimie, à l'aide de techniques analytiques telles que l'XPS, le STM, le ToF-SIMS et la voltampérométrie. Il était d'abord important d'analyser la surface FeCrNiMo sans oxyde. Le recuit à haute température de l'échantillon, nécessaire à la préparation de surface, entraîne la co-ségrégation du chrome et de l'azote. Cependant, des cycles répétés de bombardement et de recuit entraînent une diminution des quantités relatives de chrome et d'azote qui atteignent la surface. Ceci a un influence profonde, non seulement sur la cinétique d'oxydation, mais également sur la composition de l'oxyde au point où l'oxyde cesse de croître, comme observé par XPS. La structure de la surface propre a été étudiée par STM et LEED ; l'échantillon présente une surface reconstruite $(\sqrt{2} \times \sqrt{2})$R45°. Des lignes de lacunes traversent les terrasses dans deux directions perpendiculaires l'une à l'autre. La germination et la croissance de l'oxyde ont été suivies par des expositions progressives (0–100 L) d'oxygène à ultra-faibles pressions (10^{-8} mbar). Le rôle important de l'azote a été mis en évidence lors de la phase de nucléation (0–3 L), avec l'évolution d'espèces de chrome contenant de l'azote favorisant l'oxydation du chrome. Des oxydes de fer sont également formés pendant la nucléation alors que l'oxydation du molybdène métallique est plus tardive. Au fur et à mesure que le film d'oxyde s'épaissit, l'oxydation du fer devient le mode de croissance dominant en raison de la mobilité limitée des atomes de chrome. Une température plus élevée favorise l'oxydation de l'échantillon, résultant en un film plus épais et plus riche en fer. L'oxyde natif a été caractérisé par XPS et ToF-SIMS avant d'être passivé électrochimiquement dans H_2SO_4 0,05 M. La comparaison avec un échantillon pré-oxydé à 250 °C à des pressions ultra-faibles d'oxygène montre que la pré-oxydation améliore la protection contre la corrosion, notamment à la transition entre les domaines actif et passif. Les résultats XPS suggèrent que ceci est dû au plus fort enrichissement en molybdène du film passif formé avant polarisation anodique. La présence de 0,05 M d'ions chlorure dans l'électrolyte n'a pas d'influence sur le comportement du film passif préalablement pré-oxydé en conditions UHV.

MOTS CLÉS

Acier inoxydable, oxydation, film d'oxyde, passivation, corrosion, XPS, STM, LEED, ToF SIMS.

ABSTRACT

The work performed during this thesis has investigated the influence of the initial oxidation mechanisms on the passive film formed on a model, austenitic, single crystal stainless steel, FeCrNiMo(100). This was achieved using a combined surface science and electrochemical approach, using analytical techniques such as XPS, STM, ToF-SIMS and voltammetry. It was first important to analyse the oxide-free FeCrNiMo surface. High temperature annealing of the sample, necessary for surface preparation, results in the co-segregation of chromium and nitrogen. However, it was found that repeated cycles of sputtering and annealing result in a diminution of the relative amounts of chromium and nitrogen that reach the surface. This not only has a profound influence on the oxidation kinetics, as evidenced by XPS, but also on the composition of the oxide at the point where the oxide has stopped growing. The structure of the clean surface was investigated by STM and LEED, with the topmost surface plane displaying a $(\sqrt{2} \times \sqrt{2})$R45° reconstruction. Vacancy lines were found to run across the terraces in two directions, perpendicular to each other. The nucleation and growth of the oxide was followed by performing step-wise exposures (0–100 L) of oxygen at ultra-low pressures (10^{-8} mbar). The important role of nitrogen was highlighted during the nucleation phase (0–3 L), with the evolution of nitrogen-containing chromium species promoting chromium oxidation. Iron oxides are also found to form during the nucleation phase, whereas oxidation of metallic molybdenum is found to occur slightly later. As the oxide film becomes thicker, oxidation of iron becomes the dominant growth mode owed to the limited mobility of chromium atoms. Higher temperature promotes further oxide growth, resulting in a thicker, more iron-rich film. The native oxide was characterised by XPS and ToF-SIMS before being electrochemically passivated in 0.05 M H_2SO_4. Comparison with a sample that had been pre-oxidised at 250 °C at ultra-low pressures of oxygen shows that pre-oxidation improves corrosion protection, notably at the active-passive transition. XPS results suggest that this is due to enhanced molybdenum enrichment of the passive film prior to anodic polarisation. The presence of 0.05 M chloride ions in the electrolyte does not influence the behaviour of the passive film that had previously been pre-oxidised under UHV conditions.

KEYWORDS

Stainless steel, oxidation, oxide film, passivation, corrosion, XPS, STM, LEED, ToF SIMS.